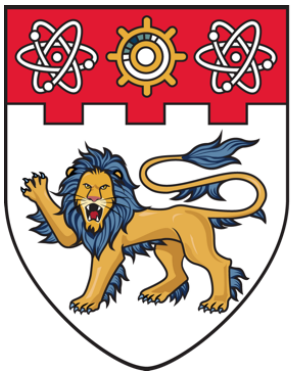

NANYANG TECHNOLOGICAL UNIVERSITY
SINGAPORE

PHOSPHORUS RECOVERY FROM SEWAGE SLUDGE THROUGH INTEGRATED THERMOCHEMICAL TREATMENT AND SEQUENTIAL WET EXTRACTION

TIWARI SATYA BRAT

INTERDISCIPLINARY GRADUATE PROGRAMME
NANYANG ENVIRONMENT & WATER RESEARCH INSTITUTE (NEWRI)

2024

PHOSPHORUS RECOVERY FROM SEWAGE SLUDGE THROUGH INTEGRATED THERMOCHEMICAL TREATMENT AND SEQUENTIAL WET EXTRACTION

TIWARI SATYA BRAT

INTERDISCIPLINARY GRADUATE PROGRAMME

NANYANG ENVIRONMENT & WATER RESEARCH INSTITUTE (NEWRI)

A thesis submitted to the Nanyang Technological University
in partial fulfillment of the requirement for the degree of
Doctor of Philosophy

2024

STATEMENT OF ORIGINALITY

I hereby certify that the work embodied in this thesis is the result of original research, is free of plagiarised materials, and has not been submitted for a higher degree to any other University or Institution.

29/06/2024

. . . . . .
Date

. . . . . .
Tiwari Satya Brat

SUPERVISOR DECLARATION STATEMENT

I have reviewed the content and presentation style of this thesis and declare it is free of plagiarism and of sufficient grammatical clarity to be examined. To the best of my knowledge, the research and writing are those of the candidate except as acknowledged in the Author Attribution Statement. I confirm that the investigations were conducted in accord with the ethics policies and integrity standards of Nanyang Technological University and that the research data are presented honestly and without prejudice.

30/06/2024

. . . . . .
Date

. . . . . .
Prof Lim Teik-Thye

AUTHORSHIP ATTRIBUTION STATEMENT

This thesis contains material from two papers published in the following peer-reviewed journal in which I am listed as an author. The other two papers are under revision/review.

Some parts of Chapters 1, 2, and 6 are constituents of the review manuscript which will be submitted for publication in a peer-reviewed journal.

Chapter 3 is published as Tiwari, S.B., Hooper, T.J., Veksha, A., Chan, W.P., Fei, X., Liu, W., Lisak, G. and Lim, T.T., 2023. Sequential wet extraction of phosphorus from sewage sludge using alum sludge: reassessing the aluminium-phosphorus speciation using experimental and simulation approach. Chemical Engineering Journal, 459, p.141569. https://doi.org/10.1016/j.cej.2023.141569

The contributions of the co-authors are as follows:

- Prof Lim provided the project direction and suggested revisions in the manuscript drafts.
- I designed the study, conducted it in my lab in NEWRI, and FACTS, processed the data, and prepared the manuscript drafts.
- Dr Hooper performed the solid-state NMR analysis at SPMS, processed the data, prepared the sections related to NMR in the manuscript drafts, and suggested improvements for my part.
- Dr Veksha and Dr Chan provided useful guidance for designing the study and revisions in the manuscript drafts.
- Prof Lisak and Prof Fei provided the resources for conducting the experiments and characterization, and suggestions for revisions in the manuscript drafts.

- Prof Liu provided initial project direction and suggestions for revisions in the manuscript drafts.

Chapter 4 is published as Tiwari, S.B., Chin, S.Y., Veksha, A., Chan, W.P., Fei, X., Lisak, G., Liu, W. and Lim, T.T., 2024. Synergistic application of alum sludge and sequential extraction for phosphorus recovery from sewage sludge char. Chemical Engineering Journal, 481, p.148574. https://doi.org/10.1016/j.cej.2024.148574

The contributions of the co-authors are as follows:

- Prof Lim provided the project direction and suggested revisions in the manuscript drafts.
- I designed the study, conducted it in my lab in NEWRI, and FACTS, processed the data, and prepared the manuscript drafts.
- Ms Chin performed the solid-state NMR analysis at SPMS, processed the data, and prepared the sections related to NMR in the manuscript draft.
- Dr Veksha and Dr Chan provided useful guidance for designing the study and revisions in the manuscript drafts.
- Prof Lisak and Prof Fei provided the resources for conducting the experiments and characterization, and suggestions for revisions in the manuscript drafts.
- Prof Liu suggested revisions in the manuscript drafts and provided contingency research facilities.

Chapter 5 was submitted as a research article in a peer-reviewed journal for publication. The preprint is available as: Tiwari, Satya Brat and Veksha, Andrei and Chan, Wei Ping and Fei, Xunchang and Liu, Wen and Lisak, Grzegorz and Lim, Teik Thye (T.T.), Directional Sewage Sludge Transformation Using Acidic Hydrothermal Carbonization for Enhanced Alkaline Extraction of Phosphorus. http://dx.doi.org/10.2139/ssrn.4848678. It has been published with

some modifications in the Resources Conservation and Recycling journal after peer review (https://doi.org/10.1016/j.resconrec.2024.107936).

The contributions of the co-authors are as follows:

- Prof Lim provided the initial project direction and suggested revisions in the manuscript drafts.
- I designed the study, conducted it in my lab in NEWRI, processed the data, and prepared the manuscript drafts.
- Dr Veksha and Dr Chan provided useful guidance for designing the study and revisions in the manuscript drafts.
- Prof Lisak provided the resources for conducting the experiments and characterization, and suggestions for revisions in the manuscript drafts.
- Prof Fei and Prof Liu suggested revisions in the manuscript.

29/06/2024

. . . . . .
Date

. . . . . .
Tiwari Satya Brat

ACKNOWLEDGEMENTS

I extend my deepest gratitude to my supervisor Prof. Lim for his unwavering support throughout my PhD journey. His guidance, provision of resources, and insistence on high standards in manuscript preparation have significantly enhanced my research capabilities and writing proficiency. I am also thankful to Dr. Andrei, Dr. Chan, Prof. Lisak, Prof. Fei, and Prof. Paul for their invaluable suggestions and access to crucial resources for experimentation.

I am grateful to my labmates, especially Vernette, Yinn Zhao, and Guicai, for their generous assistance during the initial stages of my PhD. I also extend my appreciation to Cyrus, Zhao Ke, Joewin, Rupendra, Ching Wei, and Wei Wei for their support in the lab. NEWRI analytical team's structured training protocols simplified my learning of sophisticated analytical instruments, while the CEE analytical team provided crucial support in sample analysis. I am particularly thankful to Ms. Eunice, whom I mentored for her FYP, for her assistance in experiments and her role in refining my mentoring skills.

I acknowledge the research and administrative staff at NEWRI, CEE, SPMS, and FACTS whose clear guidance facilitated the necessary paperwork for my research and teaching activities. Special thanks to Dr. Kai Xue from SPMS for his instrumental support in planning and conducting solid-state NMR analysis, and Dr Teddy for XPS analysis.

Lastly, my PhD would not be possible without the generous NTU Graduate Research Scholarship, and constant support from my family, spiritual teacher, and friends. This work is a tribute to my late father.

CONTENTS

STATEMENT OF ORIGINALITY i
SUPERVISOR DECLARATION STATEMENT ii
AUTHORSHIP ATTRIBUTION STATEMENT iii
ACKNOWLEDGEMENTS vi
LIST OF TABLES x
LIST OF FIGURES xiii
SUMMARY xix
ABBREVIATIONS xxi
1. INTRODUCTION 1
1.1. Background 1
1.2. Research motivation 2
1.3. Research objectives and scope 3
1.4. Organization of the thesis 4
2. LITERATURE REVIEW 5
2.1. About phosphorus 5
2.2. Phosphorus lifecycle in the wastewater treatment process 7
2.3. Qualitative and quantitative characterization of phosphorus in sewage matrices 11
2.3.1. Prospective characterization techniques 12
2.4. Phosphorus recovery from sewage sludge and its thermal residue 17
2.4.1. Acidic extraction 19
2.4.2. Alkaline extraction 24
2.4.3. Sequential extraction 24
2.5. Fate of phosphorus during pyrolysis 25
2.5.1. Effect of process parameters on P 26
2.5.2. Effect of feedstock properties on P 28
2.6. Fate of phosphorus during hydrothermal treatment 33
2.6.1. Effect of process parameters on P 34
2.6.2. Effect of feedstock properties on P 39
3. PHOSPHORUS TRANSFORMATION DURING ACIDIC PRETREATMENT OF SEWAGE SLUDGE WITH ALUM SLUDGE AND ITS ALKALINE EXTRACTION 43
3.1. Introduction 43

3.2. Experimental 45
3.2.1. Sample collection and processing 45
3.2.2. Sample characterisation 46
3.2.3. Experimental plan 47
3.2.4. Other analytical techniques 50
3.3. Results and discussion 51
3.3.1. Effect of acidic pretreatment 52
3.3.2. Phosphorus leaching in all the processes 57
3.3.3. Chemical equilibrium modelling of acidic pretreatment using Visual MINTEQ 57
3.3.4. SMT analysis of samples 60
3.3.5. Solid and liquid NMR analysis 61
3.3.6. Techno-economic feasibility 68
3.4. Conclusion 70
4. SYNERGIZING PYROLYSIS AND ACIDIC PRETREATMENT OF SEWAGE SLUDGE WITH ALUM SLUDGE FOR PHOSPHORUS RECOVERY 72
4.1. Introduction 72
4.2. Materials and methods 74
4.2.1. Sample preparation and acidic pretreatment 75
4.2.2. Pyrolysis and alkaline P extraction and its optimization 76
4.2.3. Sample characterization 76
4.3. Results and discussion 79
4.3.1. Acidic pretreatment optimization 79
4.3.2. Effect of SS amendment on P speciation 80
4.3.3. Effect of operational conditions on alkaline extraction of P 80
4.3.4. XRD of sludge and char samples 84
4.3.5. P speciation and its role in P extraction 85
4.3.6. Al speciation and its relationship with P 94
4.3.7. C speciation and its relationship with P 99
4.3.8. Trace element analysis 105
4.3.9. Morphology, surface area, and porosity of chars 106
4.3.10. Environmental implications 109
4.4. Conclusion 111

5. EFFECT OF ACIDIC PRETREATMENT IN HYDROTHERMAL CONDITIONS ON PHOSPHORUS TRANSFORMATION AND ITS RECOVERY 112
5.1. Introduction 112
5.2. Materials and methods 114
5.2.1. Sample preparation and characterization 114
5.2.2. Acidic hydrothermal carbonization and alkaline extraction 115
5.2.3. Other analyses 118
5.3. Results and discussion 119
5.3.1. Effects of HTC conditions on process outcomes 119
5.3.1.1. Effects on final pH and hydrochar yield 119
5.3.2. pH optimization of acidic HTC — effect of final pH of HTC on the extraction of major and trace elements 128
5.3.3. P and Al speciation and effects on its extraction 130
5.3.4. FTIR analysis for changes in functional groups 137
5.3.5. Process mechanism 139
5.4. Conclusion 141
6. CONCLUSIONS AND RECOMMENDATIONS 143
SUPPLEMENTARY INFORMATION 145
CHAPTER 2 145
CHAPTER 3 147
CHAPTER 4 151
CHAPTER 5 155
Multi-criteria optimization and model validation 156
REFERENCES 166

LIST OF TABLES

Table 2.1: Various P species in sewage sludge using SMT protocol in selected studies. 10

Table 2.2: Various P species in sewage sludge using ^{31}P liquid NMR in selected studies. 11

Table 2.3: Some of the analytical instruments generally applied in SS studies on the fate of phosphorus. 14

Table 2.4: Acid dissociation constant of acids used for P extraction from SS or its thermal products. 19

Table 2.5: Common reactions involving inorganic sludge components during acidic or alkaline extraction (modified from Levlin and Hultman). 20

Table 2.6: Studies on phosphorus (P) recovery from dried P-rich sludges (mainly sewage sludge). 21

Table 2.7: Some of the recent studies on co-pyrolysis of sewage sludge with chemicals or other wastes. 30

Table 2.8: Some studies on co-HT of SS with other feedstocks published in the last four years. 41

Table 3.1: Physico-chemical characteristics of sludge samples. 52

Table 3.2: Cost incurred for leaching per kg of dry SS to recover P using the sequential extraction process. 69

Table 3.3: Cost calculation for struvite precipitation from recovered P in this study. 69

Table 4.1: Physico-chemcial characteristics of sludge samples. 77

Table 4.2: P 2p XPS deconvoluted peak assignments for sludge and char samples, relative areas, and FWHM. 88

Table 4.3: Peak assignment for deconvoluted peaks of ^{31}P single pulse-magic angle spinning (SP-MAS) NMR spectra of sludge and char samples. 91

Table 4.4: Peak assignment[242,245,247–249] for deconvoluted peaks of ^{27}Al SP-MAS NMR spectra of sludge and char samples. 96

Table 4.5: Al 2p deconvoluted peaks with peak assignments[164,250–252] and relative area. 98

Table 4.6: Deconvoluted peaks of C 1s with their relative area and peak assignments[259–261]. 101

Table 4.7: Peak assignments for the spectra of sludge and char samples[263–267]. 103

Table 4.8: Trace element in sludge and char samples. 106

Table 5.1: Physico-chemical characterization of the sludge samples. 114

Table 5.2: Trace elements in the sludge samples. 115

Table 5.3: Hydrothermal carbonization runs conducted using SS and MS as feedstocks. 117

Table 5.4: Selection of runs for qualitative analysis. 119

Table 5.5: P 2p XPS deconvoluted peak assignments with their peak energy, relative area and full width at half maximum (FWHM) for SS and hydrochar samples. 134

Table 5.6: Al 2p XPS deconvoluted peak assignments with their peak energy, relative area and full width at half maximum (FWHM) for AS, hydrochar, and hydrochar (B) samples. 137

Table S 1: Key chemical properties of phosphorus. 145

Table S 2: Standard protocols useful for sewage sludge characterization. 145

Table S 3: Specification of sample weight and volume of leachant in all the processes. M3 represents the mixture of SS and AS in the ratio 3:2 (w/w). ... 147

Table S 4: The concentration of trace elements (mg/kg) in the dried sludge samples. 147

Table S 5: The extent of trace elements released into the acid leachates after the acidic pretreatment of SS (SSA(aq)) and M3 (M3A(aq)). M3 represents the sewage sludge (SS) and alum sludge (AS) mixture in the ratio 3:2 (w/w). 148

Table S 6: ^{31}P SSNMR fitting parameters and assignments for non-pretreated (sewage sludge (SS) and M3) and acid-pretreated SS (SSA) and M3 (M3A) sludges. M3 represents the SS and alum sludge (AS) mixture in the ratio 3:2 (w/w). 148

Table S 7: ^{27}Al SSNMR fitting parameters and assignments for non-pretreated (sewage sludge (SS), alum sludge (AS) and M3) and acid-pretreated SS (SSA) and M3 (M3A) sludges. M3 represents the SS and AS mixture in the ratio 3:2 (w/w). 149

Table S 8: The calculations for the acidic pretreatment of DSS and MS (DSS + AS). 151

Table S 9: Illustrative table showing the calculation steps for the weight of P and samples in the process flow (with clarifications in the footnote). Average values of the replicates were used for the calculations. 151

Table S 10: Molar ratio of major ions in the samples that form inorganic compounds with P. The values for MS are based on mass balance. 152

Table S 11: Total carbon (TC) in the solid sludge and char samples. 152

Table S 12: Total carbon (TC) and dissolved organic carbon (DOC) in the filtered liquid extracts obtained from acidic pretreatment and alkaline extraction. 152

Table S 13: The main parameters for BET fitting to quantify surface characteristics. 152

Table S 14: Surface characteristics of the char samples. 153

Table S 15: Illustrative example of mass balance of P and other major and trace elements in this study using hypothetical values. 155

Table S 16: HTC runs conducted during the pH optimization experiment in this study. 155

Table S 17: ANOVA and fit statistics for the response variables. 156

Table S 18: The optimized factor and response variables as per the models obtained using the CCD. 158

Table S 19: The outcome of the confirmation runs of the CCD to validate the prediction models. 158

Table S 20: Trace element concentration in hydrochar corresponding to each run. Ba, Sn and Sr were not analyzed. As per EU regulation for organic fertilizers, the maximum allowable concentration (mg/kg) of As (inorganic), Cd, Hg and Pb are 40, 1.5, 1 and 120, respectively. 159

Table S 21: Trace element concentration in hydrochar (B) corresponding to each run. Ba, Sn and Sr were not analyzed. As per EU regulation for organic fertilizers, the maximum allowable concentration (mg/kg) of As (inorganic), Cd, Hg and Pb are 40, 1.5, 1 and 120, respectively. 160

Table S 22: Concentration of trace elements in hydrochar and hydrochar (B) during pH optimization experiment. The mass balance was not calculated for these elements. As per EU regulation for organic fertilizers, the maximum allowable concentration (mg/kg) of As (inorganic), Cd, Hg and Pb are 40, 1.5, 1 and 120, respectively. 161

LIST OF FIGURES

Figure 1.1: The recovery of phosphorus from sewage sludge for land fertilization. 2

Figure 2.1: Important chemical and biochemical properties of phosphorus. 5

Figure 2.2: The major processes undertaken for recovering phosphorus from phosphate rock for various applications. 6

Figure 2.3: Classification of P species based on their properties. 8

Figure 2.4: P species in waste activated sludge and chemical enhanced primary sedimentation sludge. Here, the concentration of P species is with reference to total P (TP): high means >50% TP; moderate means 10-50% TP; low means <10% TP. Reproduced from Yu et al.[32] with permission from Elsevier. 10

Figure 2.5: P recovery from various matrices of sewage (reproduced from Jupp et al.[1] under Creative Commons license). 17

Figure 2.6: Solubility of ionic compounds of phosphate in water. Modified from Sigma Aldrich[60]. 18

Figure 2.7: The stages of pyrolysis of sewage sludge along with the by-products. Reproduced from Zhu et al[80] with permission from Elsevier. 26

Figure 2.8: The reactions during hydrothermal treatment of sewage sludge. Reproduced from D. Lachos-Perez et al. [113] with permission from Elsevier. 34

Figure 3.1: Experimental plan showing reference cases and design cases. The design cases involve alum sludge (AS) as an amendment in the leaching process. M3 represents the sewage sludge (SS) and AS mixture in the ratio of 3:2 (w/w) and TEs means the trace elements. The notation system for the relevant solid and liquid samples is also indicated. 48

Figure 3.2: XRD spectra of non-pretreated (sewage sludge (SS), alum sludge (AS) and M3) and acid-pretreated SS (SSA) and M3 (M3A) sludges. M3 represents SS and AS mixture in the ratio of 3:2 (w/w). 53

Figure 3.3: Ortho-P concentration in acidic and alkaline leachates and ortho-P recovery (process or effective) obtained in all the processes. The error bar represents the standard deviation. 54

Figure 3.4: SEM mapping of sludge samples: (a) sewage sludge (SS) (b) acid-pretreated SS (SSA) (c) M3 (d) acid-pretreated M3 (M3A). M3 represents SS and alum sludge (AS) mixture in the ratio 3:2 (w/w). The relative weight fraction (%) of each element along with the standard deviation obtained using SEM-EDS is also presented (Ca in SSA and M3A has a concentration below the detection limit of the instrument). All the images are at 5000 times magnification. 55

Figure 3.5: FTIR spectra of non-pretreated (sewage sludge (SS), alum sludge (AS) and M3) and acid-pretreated SS (SSA) and M3 (M3A) sludges. M3 represents the SS and AS mixture in the ratio 3:2 (w/w). 56

Figure 3.6: Simulated speciation of P and Al during acidic pretreatment of (a, b) sewage sludge (SS) and (c, d) M3. Speciation of Ca is not presented as it existed solely as Ca^{2+} in the 3<pH<7 range. M3 represents SS and alum sludge (AS) mixture in the ratio of 3:2 (w/w). Visual MINTEQ utilized for chemical equilibrium modeling. 59

Figure 3.7: SMT analysis of sewage sludge (SS), acid-pretreated SS (SSA) and M3 (M3A) sludges. M3 represents SS and alum sludge (AS) mixture in the ratio of 3:2 (w/w). Phosphorus species are organic phosphorus (OP), apatite phosphorus (AP), non-apatite inorganic phosphorus (NAIP), inorganic phosphorus (IP) and total phosphorus (TP). The error bar represents the standard deviation. 60

Figure 3.8: A simplified schematic illustrating P speciation during acidic pretreatment and alkaline leaching based on the data obtained from SSNMR and LSNMR. (a) inorganic ortho-P bound to the water of hydration via hydrogen bonds in the organic matrix (b) water of hydration or adsorbed water inside the organic matrix (c) amorphous calcium phosphate (d) binuclear bidentate inner-sphere surface complexation of ortho-P on aluminium hydroxide (e) AlO_6 coordination structure of $Al(OH)_3$ (in each octahedron, six OH^- surround one Al^{3+} and each OH^- is common between the two adjoining octahedrons, thus the chemical formula $Al(OH)_3$) (f) ortho-P monoester (g) ortho-P diester. This schematic is not to scale. 61

Figure 3.9: ^{31}P MAS NMR spectra of non-pretreated (sewage sludge (SS) and M3) and acid-pretreated SS (SSA) and M3 (M3A) sludge samples. M3 represents SS and alum sludge (AS) mixture in the ratio of 3:2 (w/w). Experimental spectra, simulated spectra and deconvoluted resonances are shown in solid line, dotted line and multicolor, respectively. The spectrum for AS is not shown as it had negligible P, hence a poor signal-to-noise ratio. 63

Figure 3.10: ^{27}Al MAS NMR spectra of non-pretreated (sewage sludge (SS), alum sludge (AS) and M3) and acid-pretreated SS (SSA) and M3 (M3A) sludge samples. M3 represents SS and AS mixture in the ratio of 3:2 (w/w). 65

Figure 3.11: ^{31}P-^{1}H CP-HETCOR MAS NMR spectra of the sewage sludge (SS) and acid-pretreated SS (SSA) and M3 (M3A). M3 represents SS and alum sludge (AS) mixture in the ratio of 3:2 (w/w). The $^{31}P(^{1}H)$ CP projection is presented on the top axis in red, alongside the ^{31}P MAS NMR spectra. 66

Figure 3.12: ^{31}P liquid-state NMR (LSNMR) of sewage sludge (SS) and leachate samples. The ortho-P peak shows a rightward shift at the reduced pH of the samples (*i.e.*, SSA(aq) and M3A(aq)). 67

Figure 4.1: Experimental schematic of this study showing (a) reference and (b) design processes. Dewatered sewage sludge (DSS) and alum sludge (AS) were

mixed in a ratio of 4:1 (w/w) to obtain MS before acidic pretreatment in the design process. The sample notation in this study is also indicated. 74

Figure 4.2: (a) The fraction of major ions extracted during acidic pretreatment of SS and MS at various pH (b) molar ratio of inorganic phosphate forming elements (Al, Ca, Fe, and Mg) with P after acidic pretreatment of SS (labeled SSA) and MS (labeled MA). 80

Figure 4.3: (a) Phosphorus extracted from chars using 0.5 M NaOH at L/S of 100:1 for 1 h. (b,c,d) represent one-factor-at-a-time (OFAT) optimization of the alkaline P extraction from SC400 and MC400. The error bar represents the standard deviation. 81

Figure 4.4: The mass balance for the entire process in the (a) reference and (b) design cases based on the average values of the replicates. The results are summarized in the table below the schematics. 83

Figure 4.5: XRD peaks of (a) SS and its chars and (b) MA and its chars. 85

Figure 4.6: (a) P species in the sludge and char samples determined using the SMT protocol. (b) Ratio of P species in sludge and char samples. P species are apatite phosphorus (AP), non-apatite inorganic phosphorus (NAIP), organic phosphorus (OP), and inorganic phosphorus (IP). The error bar represents the standard deviation. 86

Figure 4.7: P 2p spectra of (a,b,c,d) SS and its chars (e,f,g,h) MA and its chars. Experimental, simulated, and deconvoluted spectra are shown in multicolor solid lines, black dashed lines, and blue solid lines, respectively. 88

Figure 4.8: ^{31}P liquid-state NMR (LSNMR) of sludge (SS and MA) and char samples.....90

Figure 4.9: ^{31}P single pulse- magic angle spinning (SP-MAS) NMR spectra of (a) SS and its chars, (b) MA and its chars, (c) the approximate peak range for some important P species in this study (M^+ and M^{2+} represent alkali and alkaline earth metals, respectively) (d) fractional distribution of P species in the samples. Experimental spectra, simulated spectra, and deconvoluted resonances are shown in multicolor solid lines, black dotted lines, and black solid lines, respectively. Some of the peaks were in the overlapping region and hence assigned with an overlap in (d). The spinning sideband is marked with *.....91

Figure 4.10: ^{27}Al SP-MAS spectra of (a) SS and its chars, (b) MA and its chars, (c) the approximate resonance range for various Al coordination states relevant to this study, and (d) fractional distribution of Al coordination states in the samples. Experimental spectra, simulated spectra, and deconvoluted resonances are shown in multicolour solid lines, black dotted lines, and black solid lines, respectively. The spinning sideband is marked with *. 96

Figure 4.11: Al 2p spectra of (a,b,c,d) SS and its chars (e,f,g,h) MA and its chars. 98

Figure 4.12: C 1s spectra of (a,b,c,d) SS and its chars (e,f,g,h) MA and its chars. 101

Figure 4.13: FTIR spectra of the sludge and char samples. 103

Figure 4.14: $^{13}C\{^{1}H\}$ CP-MAS spectra of (a) SS and its chars (b) MA and its chars. ^{13}C SP-MAS of SC900 and MC900 are shown with black lines and compared with their respective $^{13}C\{^{1}H\}$ CP-MAS spectra (multicolor) in the inset of (a) and (b), respectively. 105

Figure 4.15: SEM images of the char samples (2500x magnification). 107

Figure 4.16: Adsorption-desorption isotherm of the char samples. The pore size distribution is provided in the inset. 108

Figure 4.17: The process mechanism is summarized highlighting the changes in P (black font), Al (dark red font), and C (navy blue font) speciation during the entire process. The predominant species are indicated with a bigger font and in bold. The acidic pretreatment and pyrolysis temperature had a critical effect on P speciation. 110

Figure 5.1: Experimental plan in this study showing the (a) reference process to assess the business-as-usual scenario and (b) design process showing the amended scenario. The parameters varied in process (b) are the SS:AS mixing ratio (2.8 – 11.5) to achieve the Al/P molar ratio (APMR) of 1.6 – 4.4 in the mixture (MS), pH at the start of HTC (1 – 3), and HTC temperature (158 – 242^{o}C). In process (a), HTC temperatures are in the range of 158 – 242^{o}C, while other parameters are constant. 116

Figure 5.2: pH of the feedstock after HTC (i.e., final pH) of (a) SS (b) MS and the hydrochar yield (%) via HTC of (c) SS and (d) MS. The shaded region in (b) represents the upper and lower bounds of the 95 % confidence interval. The error bar represents the standard deviation. 121

Figure 5.3: The fraction of total P in process water after acidic HTC of (a) SS and (b) MS. The alkaline extraction efficiency of P from hydrochars obtained from HTC of (c) SS and (d) MS. The overall P recovery efficiency after accounting for P loss via process water during the HTC of (e) SS and (f) MS. The shaded regions in (b) and (f) represented the upper and lower bounds of the 95 % confidence interval. The error bar represents the standard deviation. 122

Figure 5.4: The distribution of relevant major elements within the feedstock across both aqueous and solid phases in (a) reference (SS HTC) and (b) design (MS HTC) processes. The error bar represents the standard deviation. 125

Figure 5.5: The distribution of relevant trace elements within the feedstock across both aqueous and solid phases in (a) reference (SS HTC) and (b) design (MS HTC) processes. The error bar represents the standard deviation. 127

Figure 5.6: The distribution of some of the (a) major and (b) trace elements in the solid and liquid phases during the pH optimization experiment of acidic HTC of MS. The error bars represent the standard deviation. 129

Figure 5.7: (a, b) ^{31}P and (c, d) ^{27}Al SSNMR spectra of selected hydrochar and hydrochar (B) samples. SS and AS spectra are also provided for reference. The asterisk (*) represents the spinning sideband. 132

Figure 5.8: P 2p XPS spectra of (a) SS and selected hydrochars corresponding to HTC runs (b) 200-3, (c) 242-4.4, (d) 158-1.6, (e) 242-4.4-2, and (f) 242-4.4-2.5. The spectra of corresponding hydrochar (B) samples are not shown due to poor signal/noise ratio. Experimental, simulated, and deconvoluted spectra are shown in yellow solid lines, black dashed lines, and blue solid lines, respectively. 134

Figure 5.9: Al 2p XPS spectra of (a) AS and selected hydrochars corresponding to HTC runs (b) 200-3, (c) 242-4.4, (d) 158-1.6, (e) 242-4.4-2, (f) 242-4.4-2.5. For the HTC runs 242-4.4-2 and 242-4.4-2.5, the hydrochars after their alkaline extraction had an appreciable signal/noise ratio and hence represented as (h) 242-4.4-2 (B), and (i) 242-4.4-2.5 (B). Other hydrochar (B) samples had poor signal/noise ratios. The spectra of salts (j) $Al(OH)_3$ and (k) Al_2O_3 are also provided for reference. Experimental, simulated, and deconvoluted spectra are shown in yellow solid lines, black dashed lines, and blue solid lines, respectively. 136

Figure 5.10: FTIR spectra of (a) SS, AS, and hydrochars of selected HTC runs, (b) hydrochar (B) samples of the corresponding HTC runs. 139

Figure 5.11: The process mechanism is shown via the approximate partitioning trend of P, some major and trace elements along the process. The green and red arrows indicate the increase and decrease in the proportion of the species in the design process (MS HTC) compared to the reference process (SS HTC), respectively. The thicker the arrow, the higher the extent of increase or decrease compared to the reference process. 141

Figure S 1: Al 2p XPS spectra of M3 and acid-pretreated M3 (M3A) solid samples. M3 represents the SS and AS mixture in the ratio 3:2 (w/w). 149

Figure S 2: ^{1}H MAS NMR spectra of non-pretreated (sewage sludge (SS), alum sludge (AS) and M3) and acid-pretreated SS (SSA) and M3 (M3A) sludges. M3 represents the SS and AS mixture in the ratio 3:2 (w/w). 150

Figure S 3: ^{1}H SP-MAS NMR spectra of (a) SS and its chars (b) MA and its chars. 153

Figure S 4: ^{31}P SP-MAS NMR spectra of (a) SS chars and (b) MA chars after alkaline extraction of P from them. The spinning sideband is marked with *. 154

Figure S 5: The extracts obtained after the alkaline extraction of chars for P recovery 154

Figure S 6: Circumscribed central composite design (CCD) illustrating the actual values and coded values of the factors in the entire design space. 162

Figure S 7: Concentration of relevant major elements, i.e., (a) P, (b) Al, (c) Ca, (d) Fe, and (e) Mg in hydrochar and hydrochar (B) samples. The error bar represents the standard deviation. 163

Figure S 8: Concentration of selected trace elements, i.e., (a) Cr, (b) Cu, (c) Ni, (d) Ti, and (e) Zn in hydrochar and hydrochar (B) samples. The horizontal dashed lines represent the maximum allowable concentration in organic fertilizer as per EU regulation (no specification for Ti and Cr corresponds to Cr (VI) in the regulation). The error bar represents the standard deviation. 164

Figure S 9: Concentration of relevant (a) major and (b) trace elements in hydrochar and hydrochar (B) samples. The horizontal dashed lines represent the maximum allowable limit for concentration in organic fertilizer as per EU regulation (no specification for Ba, Mn, Ti, and V; Cr corresponds to Cr (VI) in the regulation). The error bar represents the standard deviation. 165

Figure S 10: SSNMR spectra of Al salts. The spinning sidebands are denoted by an asterisk (*). 165

SUMMARY

Phosphorus (P) is extracted from its natural mineral phosphate rock, which is finite and has a skewed geographical distribution. It is critical for the survival of life on earth and is mainly used for fertilizer production. P recovery from sewage sludge (SS) is critical for addressing the dual challenges of unsustainable fertilizer production and increasing eutrophication. However, the most prominent approach to P recovery from SS, i.e., acidic extraction of P from thermally treated SS residues (such as ash and char) is complicated by toxic trace element (TE) contamination. This PhD thesis investigates a novel approach combining integrated thermochemical treatment and sequential wet extraction to enhance P recovery from SS without TE contamination. The research is structured around three core studies, each addressing specific aspects of the process, collectively offering a comprehensive understanding of this novel method for P recovery.

The first study assessed the feasibility of the novel process and explored the underlying mechanisms for high P recovery efficiency. In this process, dry powdered SS was mixed with dry powdered alum sludge (AS) and subjected to acidic extraction in the pH range of 3 – 4. The amendment with AS under acidic conditions aimed to convert apatite phosphorus (AP) (mainly calcium phosphate (Ca-P)) to non-apatite inorganic phosphorus (NAIP) (mainly aluminum phosphate (Al-P)). Subsequently, the solid residue was extracted with an alkali at high pH (>12). Amending SS with AS reduced orthophosphate loss during acidic pretreatment by 59% compared to unamended SS. The highest orthophosphate alkaline recovery achieved was 74% for the amended SS. Various analytical techniques, including, solid-state NMR, and XPS; and modelling tools such as Visual MINTEQ and central composite design were employed to elucidate the mechanisms underlying the improved recovery. The findings demonstrated that the conversion of Ca-P to Al-P during acid pretreatment through Ca-P dissociation and adsorption of released orthophosphate onto $Al(OH)_3$, significantly boosted alkaline P recovery, making this method applicable to diverse sludge compositions globally.

Building on these findings, the second study explored an integrated approach combining sequential wet extraction and pyrolysis for P recovery from SS. SS+AS mixture underwent acid pretreatment, pyrolysis at varying

temperatures, and subsequent alkaline extraction from char. The highest alkaline P recovery efficiency, 88%, was achieved from the amended SS char prepared at 400°C. Pyrolysis at high temperatures (> 600°C) led to the conversion of NAIP to AP and immobilization of P in the char matrix, resulting in lower alkaline P recovery (< 60%). Most TEs were encapsulated in the char matrix, except for Zn, which partially volatilized above 600°C. This study highlighted that AP to NAIP conversion during acidic pretreatment and optimal pyrolysis conditions were crucial for maximizing P recovery. Advanced characterization techniques, including solid and liquid-state NMR, XPS, XRD, and FTIR, were applied to investigate the underlying mechanism, indicating that this integrated approach effectively isolated P from TEs, enhancing the viability of the method for practical applications.

Addressing the challenges associated with processing dry sludge and pyrolysis, the third study investigated the effects of hydrothermal conditions in the acidic pretreatment of SS with AS. This process involves acidic hydrothermal carbonization (HTC) followed by alkaline extraction from the residual solids (called hydrochar). A central composite design experiment optimized HTC conditions, achieving a maximum alkaline P recovery of 82% under optimal conditions. Solid-state NMR analysis revealed that P associated with aluminum in the hydrochar occurred via surface complexation rather than $AlPO_4$ formation. Detailed analysis using ICP-MS indicated that most TEs were retained in the hydrochar, resulting in a P-rich and TE-deficient extract. This approach potentially offered a cost-effective and energy-efficient pathway for P recovery, with the scope for further refinements to meet regulatory standards for TE concentrations in fertilizers.

In conclusion, this thesis presents a robust framework for P recovery from SS through integrated thermochemical treatment and sequential wet extraction. The studies collectively demonstrate that appropriate amendments and extraction conditions can significantly enhance P recovery while addressing TE contamination issues. This integrated methodology offers a sustainable solution for P recovery, aligning with global efforts towards resource recovery and environmental sustainability, and presents a promising avenue for large-scale implementation.

ABBREVIATIONS

Al-P	Aluminum Phosphate
AP	Apatite Phosphorus
APMR	Aluminum/Phosphorus Molar Ratio
AS	Alum Sludge
ATR	Attenuated Total Reflection
Ca-P	Calcium Phosphate
CCD	Central Composite Design
CP	Cross-polarization
CP-HETCOR	Cross-Polarisation-2D Heteronuclear Correlation
CP-MAS	Cross-Polarization-Magic Angle Spinning
CPS	Chemical Precipitation Sludge
Diester-P	Phosphate Diester
df	degree of freedom
DOC	Dissolved Organic Carbon
DSS	Dewatered Sewage Sludge
EBPR	Enhanced Biological Phosphorus Removal
EDTA	ethylenediamine tetraacetic acid
ER	Effective Recovery
Fe-P	Iron Phosphate
FTIR	Fourier Transform Infrared (spectroscopy)
HT	Hydrothermal Treatment
HTC	Hydrothermal Carbonization
HTG	Hydrothermal Gasification
HTL	Hydrothermal Liquefaction

IC	Ion Chromatography
ICP-MS	Inductively Coupled Plasma-Mass Spectrometry
ICP-OES	Inductively Coupled Plasma-Optical Emission Spectroscopy
IP	Inorganic Phosphorus
ISSA	Incineration Sewage Sludge Ash
L:S	Liquid-to-Solid
LSNMR	Liquid-State Nuclear Magnetic Resonance
M3	sewage sludge and alum sludge mixed in a 3:2 ratio (w/w)
M3A	solid residue obtained after acidic pretreatment of M3
M3A(aq)	acidic leachate of M3
M3AB(aq)	alkaline leachate of M3A
M3B(aq)	alkaline leachate of M3
MA	solid residue obtained after acidic pretreatment of MS
MAS	magic angle spinning
MC	pyrolysis char of MA
Meta-P	Metaphosphate
Monoester-P	Phosphate Monoester
MS	Mixed Sludge (sewage sludge + alum sludge)
NAIP	Non-Apatite Inorganic Phosphorus
ND	Not Determined
NMR	Nuclear Magnetic Resonance
OCP	octacalcium phosphate
OFAT	One-Factor-At-a-Time
OP	Organic Phosphorus
Ortho-P	Orthophosphate
Poly-P	Polyphosphate
PR	Process Recovery
PTFE	polytetrafluoroethylene

PVDF	polyvinylidene fluoride
Pyro-P	Pyrophosphate
RP	Reactive Phosphate
SC	pyrolysis char of sewage sludge
SEM-EDS	Scanning Electron Microscopy with Energy-Dispersive X-ray Spectroscopy
SI	Supplementary Information
SLR	Solid-to-Liquid Ratio
SMT	Standards Measurements and Testing
SP-MAS	Single Pulse-Magic Angle Spinning
SS	Sewage Sludge
SSA	solid residue obtained after acidic pretreatment of sewage sludge
SSA(aq)	acidic leachate of sewage sludge
SSAB(aq)	alkaline leachate of SSA
SSAl(aq)	alkaline leachate obtained after leaching of sewage sludge in Al ion-rich alkali solution
SSB(aq)	alkaline leachate of sewage sludge
SSNMR	solid-state nuclear magnetic resonance
TC	Total Carbon
TE	Trace Element
TIC	Total Inorganic Carbon
TOC	Total Organic Carbon
TP	Total Phosphorus
XPS	X-ray Photoelectron Spectroscopy
XRD	X-Ray Diffraction (spectroscopy)
WRP	Water Reclamation Plant
WWTP	Waste Water Treatment Plant

Dedicated to those who believe that virtue is its own reward

1. INTRODUCTION

1.1. BACKGROUND

Phosphorus (P) is an indispensable part of the food-energy-water nexus and it plays a pivotal role in our sustainable future. Being a plant macronutrient, it is critical for synthetic fertilizer production worldwide. However, fertilizer overuse and the increasing commercialization of agriculture have broken the natural phosphorus (P) cycle leading to a dual problem of P scarcity and eutrophication. 75% of the world's phosphate rock supply comes from Morocco and Western Sahara[1], while a populous country such as India is almost entirely dependent on imports to meet its phosphate rock demand. In 2014, the European Commission added phosphate rock to the critical raw material list due to increasing demand (from growing population and food security), lack of alternatives, and skewed geographical availability[2]. On the other hand, eutrophication has induced more than 400 ecosystems "dead zones", spanning more than 245,000 sq. km[3]. Hence, there has been an increasing research focus in the last two decades on the technologies for minimizing P loss and recovering from P from P-rich wastes[4]. The US National Academy of Science enunciates a research breakthrough in P reuse by 2030[5], as it has effects beyond food security such as co-recovery of energy, nitrogen, and precious metals, along with improved environmental quality and social equity[6].

Sewage sludge (SS) is a reclaimable P source for fertilizer production or application in soil as biochar. It has one of the highest P contents among biomass wastes (~2.5%)[7] and is produced in massive quantities globally (1.4 – 38.7 kg dry sludge/capita/year)[8]. Unlike in the past, SS cannot be applied on agricultural land directly in many countries due to strict regulations regarding toxic trace elements (TEs), persistent organic pollutants (POPs), and pathogens. Consequently, in the last two decades, many innovative approaches for P recovery from SS have been proposed and studied. Out of these, wet extraction and thermal treatment are most common[8,9]. It is estimated that recovered P from human waste can meet 22 % of the total global P demand[10]. The options for P recovery from SS for land fertilization are depicted in Figure 1.1.

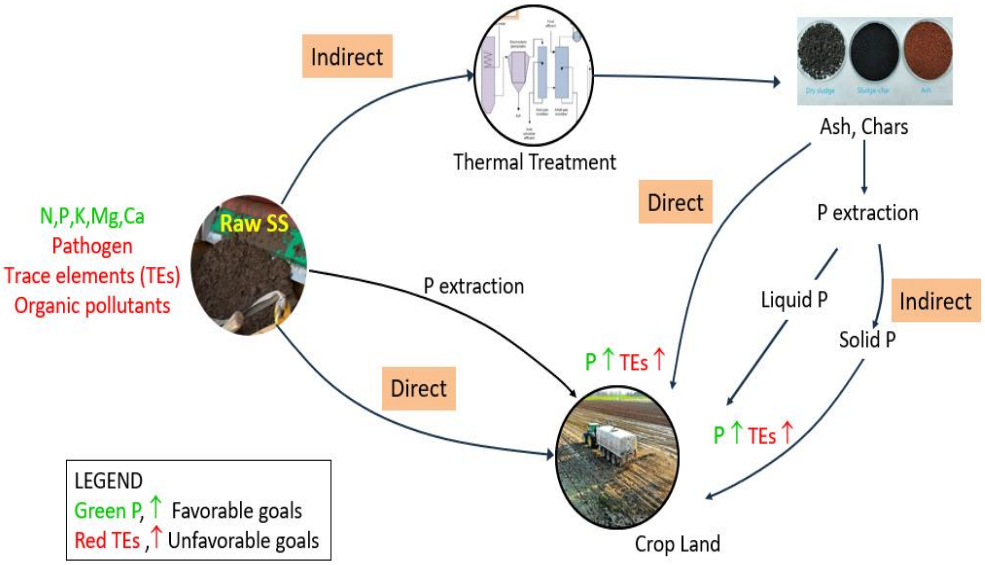

Figure 1.1: The recovery of phosphorus from sewage sludge for land fertilization.

1.2. RESEARCH MOTIVATION

In the past, incineration sewage sludge ash (ISSA) has been preferred for research on P recovery because many developed countries dispose of SS through incineration, and P concentration in ISSA is comparable to phosphate rock with medium P concentration[11]. However, trace element (TE) concentration in ISSA is above the legal limit for its direct application as fertilizer. P recovered after acidic extraction of ISSA (in the aqueous phase or as P salt obtained from the extract) requires additional purification steps before application as fertilizer, as TEs are concomitantly extracted with P (Figure 1.1). In alkaline conditions, most P compounds (and TEs) precipitate, hence a lower P recovery efficiency (30 – 40%)[8].

Alternate thermochemical treatment processes for SS have gained prominence in recent years owing to the drawbacks of incineration such as high operational cost and carbon footprint. However, P recovery from pyrolysis char or hydrochar (solid residue after hydrothermal treatment of SS) has received lesser research attention compared to ISSA. The studies on P recovery from SS or its char using alkaline extraction are rarer due to low recovery efficiency. High P recovery (> 70 %) from SS or its solid residue after thermal treatment is possible if the non-apatite inorganic phosphorus (NAIP) (mainly aluminum phosphate (Al-P)) content in SS is high[12–14]. But this is an intrinsic property of SS and varies with the SS source, and treatment process in the wastewater treatment plant (WWTP). While there are multiple studies on promoting NAIP

to apatite phosphorus (AP) conversion using pure salts[15], there are very few studies attempting vice versa, especially using waste material. Also, these studies do not quantify the P recovery from the SS directly and compare it with P recovery from ISSA or char. Thus, setting a reference is essential to ascertain the cost-benefit of P extraction after thermal treatment rather than before it. Moreover, direct P extraction from SS could be the relevant strategy for P recovery for developing countries where thermal treatment of SS is not an option.

1.3. RESEARCH OBJECTIVES AND SCOPE

The aim of this thesis was to propose a novel approach to the wet acidic treatment of SS with alum sludge (AS) to promote AP to NAIP conversion so that high P extraction efficiency can be achieved using alkaline wet extraction of SS. Because AP and most TEs tend to precipitate, while NAIP dissolves in alkaline conditions, this conversion was essential for efficiently recovering P without simultaneously extracting TEs. The main objectives of the studies in this thesis were as follows:

1. Quantify the effect of acidic pretreatment of SS with AS in promoting AP to NAIP conversion, P loss due to acidic pretreatment, and overall P recovery from the entire process.
2. Investigate the mechanism of P transformation during extraction and thermochemical treatment using the quantitative and qualitative characterization of P.
3. Study the fate of major metal cations such as Al, Ca, Fe, and Mg which form phosphate compounds in SS and its thermal treatment residue.
4. Investigate the effects of sequential extraction and thermochemical treatment on TEs.
5. Optimize the P recovery process for various operational parameters and understand the underlying reasons for high/low extraction efficiency.

The scope of this thesis is limited to:

1. P recovery from SS and its thermal residue.
2. Amendment of SS via acidic pretreatment using AS.

3. Final extraction of P in an aqueous state using an alkali.
4. Air drying, pyrolysis, and hydrothermal treatment were the thermal processes for SS treatment.
5. The baseline condition, i.e., P recovery from unamended SS was also investigated for comparison with the proposed novel process.

Previous studies have shown that SS can be a sustainable source to meet the industrial P demand[1]. However, there is only one prominent full-scale implementation of alkaline P extraction from ISSA, i.e., in Gifu, Japan[16], while most other industrial processes rely on acidic extraction. Thus, there is a need to develop diverse innovative methods to increase P recovery efficiency from SS suited to local conditions. This research project is an attempt in this direction.

1.4. ORGANIZATION OF THE THESIS

The thesis consists of six chapters. Chapter 1 provides a brief background of challenges associated with P, the advantages of P recovery from SS, the research motivation, and the research objectives and scope of this thesis. In Chapter 2, the detailed literature review is presented to gauge the research developments relevant to this project, especially recent developments. The fate of P during acidic pretreatment of SS with AS using experimental and modelling approaches is presented in Chapter 3, along with recovery efficiencies in five different methods for P recovery. Chapter 4 presents the effect of pyrolysis at three different temperatures after acidic pretreatment of SS on P speciation and its recovery in varying alkaline extraction conditions. In Chapter 5, the study on acidic pretreatment in hydrothermal conditions is presented which sought to assess whether hydrothermal conditions accentuated/inhibited AP to NAIP conversion. Finally, in Chapter 6, the principal findings of this project are summarized, and a prospective outlook for future research is presented. The terms leaching, extraction and their associated terms have been used interchangeably in this thesis.

2. LITERATURE REVIEW

2.1. ABOUT PHOSPHORUS

The recorded evidence suggests that P was first isolated in 1669 by the alchemist Hennig Brand who heated the solid residues of urine with sand and coal to obtain white phosphorus (P_4). He named it from the Greek word phosphoros ("light-bearer") because the isolated P_4 gave off a pale green glow. The important properties of P are illustrated in Figure 2.1.

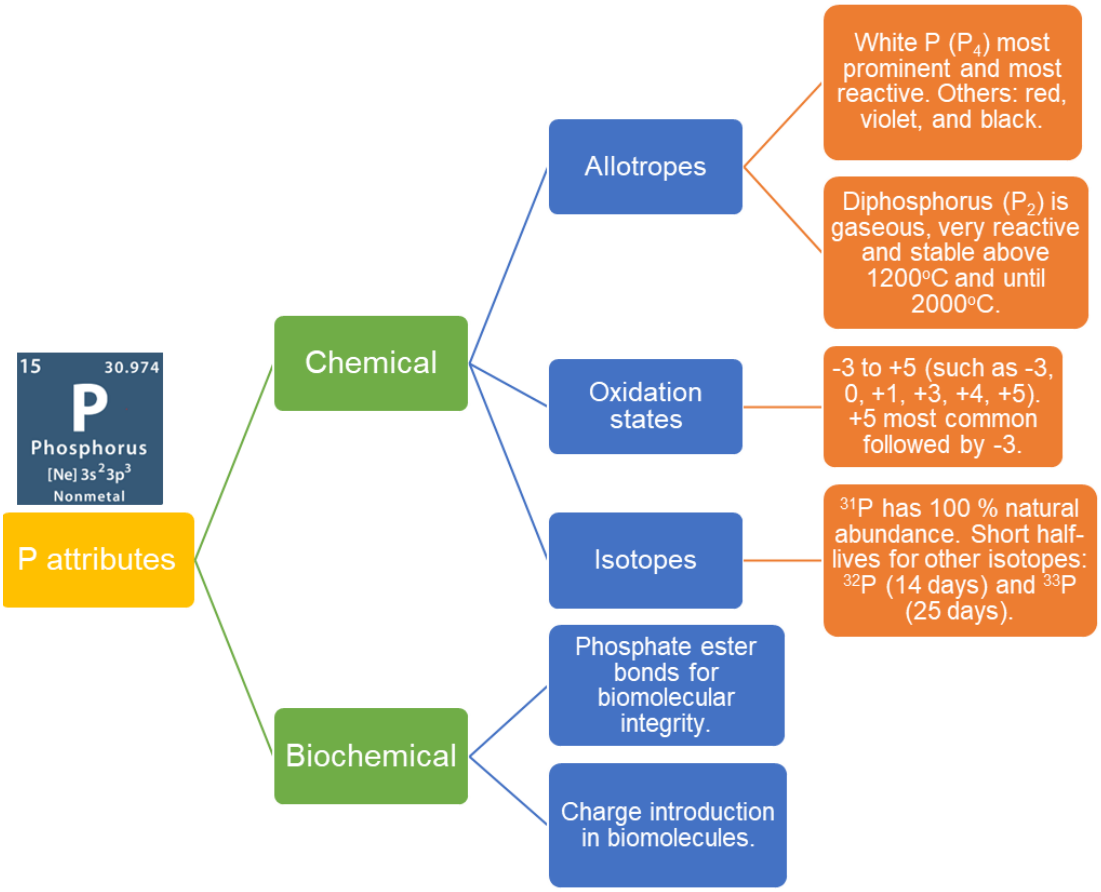

Figure 2.1: Important chemical and biochemical properties of phosphorus.

Like other elements, the properties of P are significantly influenced by parameters such as atomic size, ionization enthalpy, electron gain enthalpy, and electronegativity. The details of its chemical properties are listed in Table S 1. Its unique biochemical properties explain "why nature chose phosphates"[17] as the basic building block of life on earth (Figure 2.1). Briefly, phosphates possess unique properties crucial for cellular functions, including ion containment within the cell, charge introduction in biomolecules, and linkage formation in

biomolecules like deoxyribonucleic acid (DNA). Their stable phosphate ester bonds, essential for biomolecular integrity, are favoured by natural selection, though enzymatic catalysis allows controlled modification of these bonds. The lifecycle of P from phosphate rock till its application is presented in Figure 2.2.

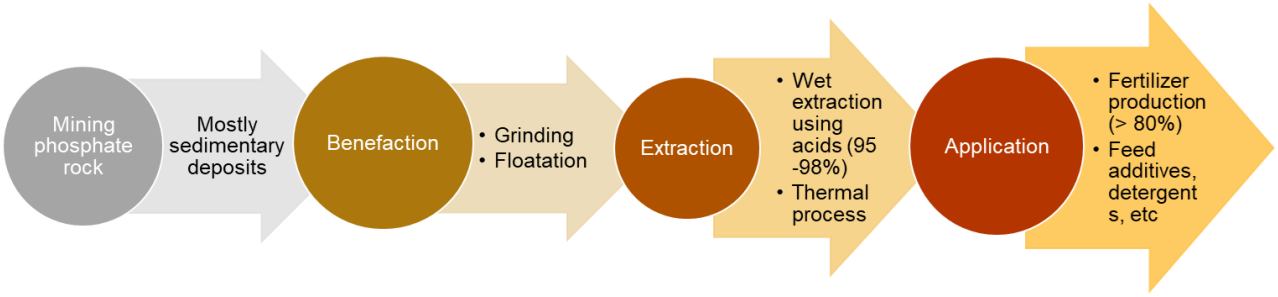

Figure 2.2: The major processes undertaken for recovering phosphorus from phosphate rock for various applications.

P for industrial use is primarily sourced from phosphate rock (mainly apatite phosphate, ($Ca_5(PO_4)_3X$, (X = OH, F, Cl)), with sedimentary deposits contributing over 80% of the total mined P, contains 7.8 – 40% phosphorus pentoxide equivalent (P_2O_5)[1,18]. The global phosphate rock consumption in 2016 was 44.5 million tonnes[18]. Post-mining, phosphate rock undergoes mechanical separation such as grinding and floatation for concentrating P, followed by P recovery using wet or thermal processes as phosphate rock usually contains impurities such as TEs. For instance, the world's largest phosphate rock reserves (three-quarters of the total) are in Morocco and the Western Sahara[18], where P coexists with Cd. The wet process, employed for about 95 – 98% of phosphate rock processing, involves acidulation using H_2SO_4 to produce H_3PO_4 along with phosphogypsum as a by-product[1,18] (Eqn.(1)).

$$Ca_5(PO_4)_3F+5H_2SO_4 +5nH_2O \rightarrow 3H_3PO_4 + 5CaSO_4.nH_2O +HF \text{ (n = 0, 0.5 or 2)} \quad (1)$$

The remaining 2 % phosphate rock is processed using the thermal (or Wöhler) process, i.e., heating phosphate rock with coke and SiO_2 at 1500 – 1600^{o}C to obtain elemental white P (P_4) (Eqn.(2)), a method strikingly similar to Hennig Brand's approach more than 350 years ago.

$$4Ca_5(PO_4)_3F + 18SiO_2 + 30C \rightarrow 3P_4 + 30CO + 18CaSiO_3 + 2CaF_2 \quad (2)$$

This process has large energy consumption (12.5 – 14 MW h/ tonne P_4)[1], and produces highly toxic white P, and thus there has been a call for more

sustainable alternatives[19]. However, this approach is currently the sole industrial method for obtaining fine P compounds[19], such as the production of high purity H_3PO_4 via oxidation (Eqn.(3)) and hydrolysis (Eqn.(4)) (though As contamination (5 – 30 ppm) is possible[1]).

$$P_4 + 5O_2 \rightarrow P_4O_{10} \quad (3)$$

$$P_4O_{10} + 6H_2O \rightarrow 4H_3PO_4 \quad (4)$$

Most of the phosphate rock is utilized for fertilizer production (> 80%) while another fraction is used for manufacturing feed additives, detergents, and technical P[20]. The key fertilizers being produced are diammonium phosphate (DAP), monoammonium phosphate (MAP), single superphosphate (SSP), and triple superphosphate (TSP). P flux due to anthropogenic factors such as the use of fertilizers, food trade, wastewater treatment, and food waste dominate over natural P flux (fluvial flux) in watersheds and landscapes[21]. The earth system boundary for P has been breached due to anthropogenic activities[22]. With the increasing global population and commercialization of agriculture, and diverse applications of P such as in spintronics and electric vehicles (lithium iron phosphate batteries), the broken P biogeochemical cycle will have serious repercussions for humanity. Thus, a two-pronged approach of efficient utilization of existing P resources and recycling P is essential for a sustainable future.

2.2. PHOSPHORUS LIFECYCLE IN THE WASTEWATER TREATMENT PROCESS

Sewage is considered a key point source of nutrient pollutants on a global scale[23]. P enters the sewage mainly through human excretory waste, food additives, and cleaning agents (dishwashing detergent and laundry products)[24]. P in sewage exists primarily as phosphates, including orthophosphates (ortho-P), condensed phosphates, and organically bound phosphates or organic phosphorus (OP), though it can exist in the reduced form as well [25,26]. The classification of P species based on various criteria is illustrated in Figure 2.3.

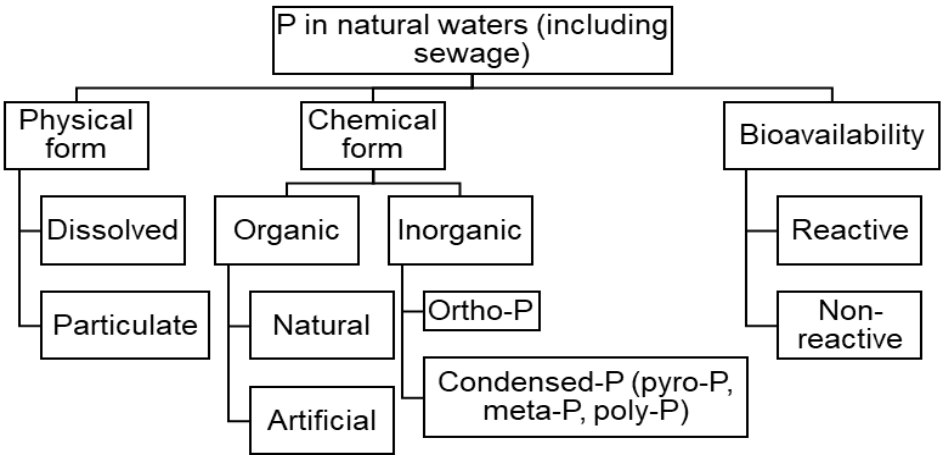

Figure 2.3: Classification of P species based on their properties.

OP means the P bound to organic compounds (for e.g., through P-O-C or P-C bonds) such as phosphate monoester (monoester-P), phosphate diester (diester-P), organic polyphosphate (poly-P), and phosphonate[27]. Condensed-P is generally inorganic and includes species such as pyrophosphate (pyro-P), triphosphate, metaphosphate (meta-P), and inorganic poly-P. P in sewage exists in an aqueous state, bound to solid matrices (adsorbed onto suspended metal hydroxides and/or clay particles) or in bodies of aquatic organisms. Total P concentration in sewage can be 5 – 20 mg/L[28] (average in the range 6 – 8 mg/L[29]), though values as high as 34.5 mg/L have been reported owing to temporal and geographical variations[30]. Th effluent P concentration depends on the local regulation, but it is generally ≤ 1 mg/L.

During the sewage treatment, P undergoes speciation transformation depending on the process. There are two major methods of P removal from sewage: chemical P removal and biological P removal. Chemical P removal is mainly conducted through Al, Fe, and Ca salts (generally sulfate and chloride), among which the order of best precipitants are aluminum sulfate (alum), Fe (III), Fe (II), and Ca[30]. Chemicals are generally added before or after the primary clarifier[31]. Some of the reactions for P precipitation are as follows (Eqn.(5)-(8)):

$$Al_2(SO_4)_3.14H_2O + 2PO_4^{3-} \rightarrow 2AlPO_4\downarrow + 3SO_4^{2-} + 14H_2O \quad (5)$$

$$Fe_2(SO_4)_3.9H_2O + 2PO_4^{3-} \rightarrow 2FePO_4\downarrow + 3SO_4^{2-} + 9H_2O \quad (6)$$

$$3FeSO_4.7H_2O + 2PO_4^{3-} \rightarrow Fe_3(PO_4)_2\downarrow + 3SO_4^{2-} + 7H_2O \quad (7)$$

$$10Ca^{2+} + 6PO_4^{3-} + 2OH^- \leftrightarrow Ca_{10}(PO_4)_6(OH)_2\downarrow \quad (8)$$

P precipitate formation is complex and depends on operational conditions, most importantly pH and alkalinity. P forms complexes with metals, and between metals and other ligands in sewage, and might get adsorbed on metal hydroxide formed due to alkalinity in sewage. Consequently, diverse metal phosphate precipitates can form during chemical P removal such as $AlPO_4$ and $Al_x(OH)_y(PO_4)_3$ from Al^{3+}, $FePO_4$ and $Fe_x(OH)_y(PO_4)_z$ from Fe^{3+}, $Fe_3(PO_4)_2$ and $Fe_x(OH)_y(PO_4)_3$ from Fe^{2+}, and $Ca_3(PO_4)_2$, $Ca_5(OH)(PO_4)_3$ and $CaHPO_4$ from Ca^{2+}. These species get concentrated in SS at the end of the sewage treatment and influence the P speciation and transformation during SS thermochemical treatment.

Biological P removal also depends on the operational conditions and generally occurs via microbial growth, precipitation, and adsorption[30]. Two common biological P removal approaches are the activated sludge process and enhanced biological P removal (EBPR). In the activated sludge process, biochemical oxygen demand (BOD) removal is the primary objective while P removal is secondary. Microbes consume P along with C and N for metabolism and cell growth, which is eventually released in sludge via cell disintegration as ortho-P/poly-P/OP. In EBPR, poly-P accumulating (PAO) bacteria operate in the anaerobic-aerobic-anoxic process to separate and accumulate P from sewage. The waste activated sludge from biological P removal has a relatively higher fraction of poly-P and OP than primary sludge obtained after chemical P removal[32]. Thus, SS is mainly composed of metal-bound ortho-P, condensed phosphates, and OP, their proportion dependent on the composition of raw sewage and the treatment process. After sewage treatment, P content in SS can be in the range of <0.1% to ~14% with a mean of 2.5%, depending on the influent P concentration and treatment process[7]. P species in SS corresponding to characteristics of raw sewage and sewage treatment is graphically presented in Figure 2.4, while their quantities in SS, as reported in some studies are enumerated in Table 2.1 and Table 2.2.

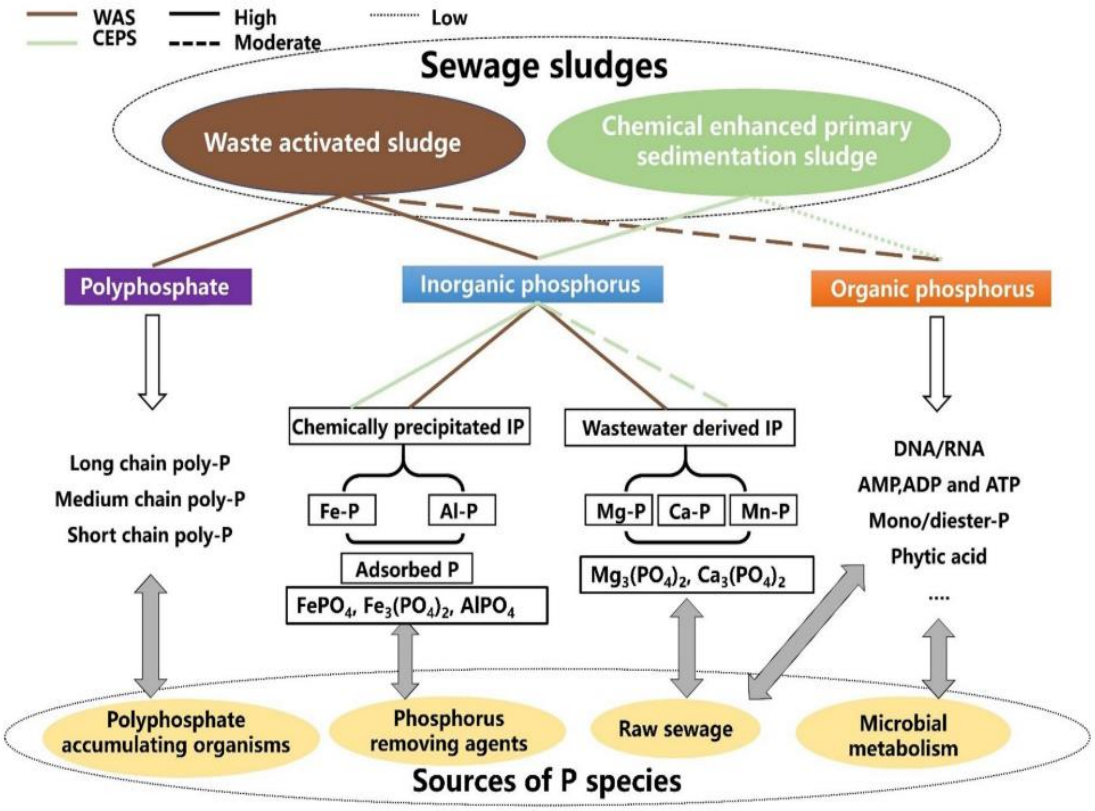

Figure 2.4: P species in waste activated sludge and chemical enhanced primary sedimentation sludge. Here, the concentration of P species is with reference to total P (TP): high means >50% TP; moderate means 10-50% TP; low means <10% TP. Reproduced from Yu et al.[32] with permission from Elsevier.

Table 2.1: Various P species in sewage sludge using SMT protocol in selected studies.

Feedstock	P species in solid fraction (%)	Reference
WAS	NAIP (43-50), AP (20-28), OP (16-20)	[33]
WAS	NAIP (71), AP (16), OP (10)	[34]
Mixed sludge (WAS + CPS)	NAIP (64), AP (6.4), OP (23.4)	[35]
WAS	NAIP (63), AP (20), OP (11)	[36]
WAS	NAIP (37), AP (20), OP (18)	[37]
WAS	NAIP (47), AP (24), OP (18)	[38]
SS	NAIP (91), AP (4), OP (3)	[39]

AP: apatite phosphorus; CPS: chemical precipitation sludge; NAIP: non-apatite phosphorus; OP: organic phosphorus; SMT: standards measurements and testing; SS: sewage sludge; WAS: waste activated sludge.

Table 2.2: Various P species in sewage sludge using ^{31}P liquid NMR in selected studies.

Feedstock	P fraction (%)				Ref.
	Ortho-P	Phosphate monoester	DNA	Pyro-P	
WAS	68-73	14-17	3-5	9-11	[33]
WAS	71	13	2	14	[38]
AGS	74	22	NR	2	[40]
WAS	73	11	5	11	[41]

AGS: aerobic granular sludge; DNA: deoxyribonucleic acid; EDTA: ethylenediamine tetraacetic acid; NMR: nuclear magnetic resonance; NR: Not reported; Ortho-P: orthophosphate; Pyro-P: pyrophosphate; WAS: waste activated sludge.

2.3. QUALITATIVE AND QUANTITATIVE CHARACTERIZATION OF PHOSPHORUS IN SEWAGE MATRICES

The prerequisites for accurate P analysis are proper sample collection, preservation and storage, and processing. This entails planning, adherence to protocols, and the use of appropriate apparatus and equipment to ensure that the sample is representative and has minimal contamination/losses[42]. For instance, it is recommended that the quantification of reactive P in sewage must be conducted within 48 h. P concentration and speciation in the samples can be maintained by physical (storing at temperature $\leq 4^{o}C$) and chemical (adding chloroform, mercuric chloride, H_2SO_4 (for pH < 2)) techniques[42]. However, the sample preservation would depend on experimental conditions, and for SS studies, refrigeration or freezing is generally sufficient. Some of the standard protocols for sample preparation and physico-chemical analysis of SS are provided in Table S 2. P species can be operationally determined using various fractionation techniques[27,43], out of which standards measurements and testing (SMT)[44] and Hedley[45] methods are the most prominently used SS studies. These extraction methods are useful only for semi-quantitative assessment of P species because of the subjective identification of P species[32]. For instance, in SMT protocol, total P is determined using 3.5 M HCl, assuming that strongly acidic conditions transform all the P species into ortho-P which is not necessarily true. Besides, P species fraction in the sample and chemicals for extraction also affect the analytical results. For example, Na_2S extraction is more suitable when SS has higher iron phosphate (Fe-P) content, while NaOH should be preferred when Al-P is higher[32]. Solid samples (including ash/char) are

generally digested in microwave acid digester using strong acids to extract P (some digestion protocols are listed in Table S 2). Complete digestion is dependent on the chemical composition of the sample and not always achieved, especially for char which has recalcitrant carbonaceous matrix. Eventually, different P species are transformed into ortho-P in aqueous state in all these methods and measured using analytical instruments. Aqueous sample should be filtered using highly resistant polytetrafluoroethylene (PTFE) or polyvinylidene fluoride (PVDF) filters if it is strongly acidic/alkaline.

There are many analytical instruments/approaches for analyzing P[46,47], but the commonly used approaches in SS studies are summarized in Table 2.3, with their advantages and disadvantages. Inductively coupled plasma-optical emission spectroscopy (ICP-OES) has been recommended as the most reliable for quantifying P in SS after microwave acid digestion[48]. OP might be overestimated in molybdate colorimetry due to poly-P or complexes between ortho-P and humic substances[27]. For quality control, the percentage recovery of the analyte using blank, blank spiked and matrix spiked samples must be determined[25] and preferably should be within 70 – 130%. Certified reference materials (CRMs) can be useful in cases where TEs in SS must be quantified as well[49]. The data must be reported along with standard deviation/standard error (calculated directly from the replicates or indirectly using the propagation of uncertainty technique[50]) wherever possible, and outliers, if any, should be cautiously identified using statistical approaches such as discordancy test (applicable for experiments with at least 3 replicates)[25]. P assessment using nuclear magnetic resonance (NMR) is not applicable if paramagnetic ions (such as Fe, Mn, and Cu) concentration in the sample are high, though some studies selectively separated P from paramagnetic ions using reagents such as dithionite, diethylenetriamine pentaacetate (DTPA), oxalate, chelax, and ethylenediamine tetraacetic acid (EDTA)[51]. However, there is a risk of hydrolysis or removal of some P species such as poly-P and meta-P during the extraction process[51].

2.3.1. Prospective characterization techniques

Some techniques that have not been applied/rarely applied in SS studies can provide insightful information on the fate of P. There are few studies on the source apportionment of P in sewage. The techniques deployed in watershed studies for source apportionment of P such as inventory analysis, receptor model,

or even machine learning[52] might be useful in this regard. Many techniques applied for soil P analysis[47] might be useful for SS as well. For instance, high-resolution resonant x-ray photoelectron spectroscopy (ResXPS) can be conducted to obtain brilliant spectral signals even from samples with low P content[47]. Spatially resolved data of P distribution and association can be obtained using emerging technologies for soil P research such as μ-x-ray fluorescence (μ-XRF), μ-x-ray absorption near edge structure (μ-XANES), and μ-extended x-ray absorption fine structure (μ-EXAFS)[47]. There are many studies exploring the fertilization potential of ash/char obtained from SS, but most do not utilize ^{33}P isotope exchange[53] and stable oxygen isotope ratios using isotope ratio mass spectrometer (IRMS) to ascertain the P cycling in soil/plant. P *K*-edge x-ray absorption spectroscopy (XAS) and isotopic (^{33}P and ^{18}O) can be combined to obtain dynamic insight on P cycling in soil[54]. The speciation transformation of dissolved OP can be deciphered using Fourier transform-ion cyclotron resonance mass spectrometry (FT-ICR-MS)[55]. Thus, there are various complementary approaches for P characterization, but their availability, cost of analysis, and skilled workforce might impede their wider application in the scientific community.

Table 2.3: Some of the analytical instruments generally applied in SS studies on the fate of phosphorus.

Analytical technique	Sample phase	P assessment type	Advantage	Disadvantage
IC	Liquid	Quantification	Simple sample preparation method; less interference from other ions; suitable for cation-rich solution such as alkaline extract.	Only aqueous ortho-P determined; not suitable for samples with very high halogen content.
UV-Vis	Liquid	Quantification	Widely used; fast data acquisition; protocol established for most analytes; relatively inexpensive equipment; ready-made kits available for various analytes.	Probability of error due to interference from multiple ions; sample preparation is cumbersome; reagents with Hg are discouraged for application.
ICP-OES	Liquid	Quantification	More than 26 analytes can be analyzed simultaneously; high accuracy; fast analysis.	Not suitable for very high (for instance, > 500 mg/L) and very low (for instance, < 0.5 mg/L) concentrations of analyte in the sample; expensive instrument; not suitable for cation-rich solutions; possibility of spectral interference (must select most appropriate spectral wavelength based on instrument manufacturer recommendation).
ICP-MS	Liquid	Quantification	Multiple isotopes of most analytes can be determined with high accuracy; generally applied for trace elemental quantification.	Not suitable for very high (for instance, > 500 µg/L) and very low (for instance, < 0.5 µg/L) concentrations of analyte in the sample; expensive instrument; not suitable for cation-rich solutions; possibility of spectral interference (must select most appropriate isotope based on sample characteristics).

XRF	Liquid and solid	Quantification	Fast and simple method; bulk analysis; non-destructive; high accuracy when reference matrix available; multiple analytes quantified simultaneously.	About 10 g sample needed; sample should be homogenous and have fine particle size (for example, < 50 μm); qualitative determination if no reference matrix available (such as sludge, and solid waste); not suitable for light elements.
^{31}P liquid NMR	Liquid	Association	Detailed P speciation (ortho-P , pyro-P, poly-P, various OP species); less sample required (< 1 g); fast data acquisition; high spectral resolution.	Sample preparation cumbersome; operational skills required; extraction protocol not well established; fractionation is semi-quantitative due to inefficient extraction of P species; P peak assignment dependent on pH of the solution[12] (preferably alkaline solution)[51].
^{31}P solid NMR	Solid	Association	Direct analysis of solid sample; detailed P speciation with coordination state; very less sample amount required (< 50 mg); non-destructive; no/minimal sample preparation.	Low spectral resolution; ambiguity in peak deconvolution and assignment due to diverse SS/ash/char composition; not suitable if paramagnetic ions in sample high; unreliable P quantification[56].
XRD	Solid	Association	Obtain crystalline P phases with high accuracy; ~ 2 mL sample volume; no/minimal sample pre-treatment required; generally $10^{o} < 2\theta < 60^{o}$ sufficient for SS studies; non-destructive.	Only crystalline phases identified; ambiguity in peak assignment due to diverse SS/ash/char composition; prior knowledge of elemental composition in sample required (qualitative); expensive; fine particle size required (~1 – 10 μm).
XPS	Liquid and solid	Association	Minimal sample required (< 1 mg); fast method; simultaneous analysis of multiple analytes; non-destructive; no/little sample preparation; depth profiling.	Only surface characteristics; peak deconvolution and curve fitting are ambiguous[57] due to proximity of peaks of various P species; prior knowledge of elemental composition required; subjectivity in peak assignment, and fractional distribution.
XAS	Liquid and solid	Association	Non-destructive; no/little sample preparation; little sample requirement (a few mg); both quantitative and	Not suitable for low P concentration samples; very expensive; fit result ambiguity.

			qualitative information of P speciation with other elements.	
FTIR and Raman spectroscopy	Liquid and solid	Association	Attenuated total reflection (ATR)-FTIR is non-destructive; fast and require no sample preparation; minimal sample requirement (< 1 mg); relatively inexpensive.	P peaks masked by other functional groups in SS and ash/char samples; peak assignment ambiguous due to diverse compounds in SS/ash/char.
SEM, TEM, EDS, WDS, EBSD	Solid	Distribution and association	Minimal sample requirement (< 1 mg); high-resolution images; multiple analytes simultaneously analyzed (EDS); crystals phases (EBSD)	Surface property only; expensive; require cumbersome sample preparation (only dry non-volatile sample).

EBSD: electron backscatter diffraction; EDS: energy-dispersive x-ray spectroscopy; FTIR: fourier transform infrared (spectroscopy); IC: ion chromatography; ICP-MS: inductively coupled plasma-mass spectrometry; ICP-OES: inductively coupled plasma-optical emission spectroscopy; NMR: nuclear magnetic resonance; SEM: scanning electron microscopy; TEM: transmission electron microscopy; UV-Vis: ultraviolet–visible spectroscopy; WDS: wavelength-dispersive x-ray spectroscopy; XAS: x-ray absorption spectroscopy; XPS: x-ray photoelectron spectroscopy; XRD: x-ray diffraction; XRF: x-ray fluorescence.

2.4. PHOSPHORUS RECOVERY FROM SEWAGE SLUDGE AND ITS THERMAL RESIDUE

Theoretically, P can be extracted from all the waste streams of a WWTP (such as sewage, primary/secondary sludge, waste activated sludge, dewatered sludge, etc.). However, to recover P from sewage directly, the aqueous phase concentration of P should be at least 50 – 60 mg/L, which is much higher than the average concentration practically found[1,58]. Besides, P recovery efficiency from sewage can be a maximum of 40 – 50%, but from SS and ISSA, it can be up to 90%[58]. Thus, P recovery from SS ash/char is considered the most economically feasible. The recovery options from sewage matrices are shown in Figure 2.5. This thesis focuses on P extraction from SS and its thermal residues.

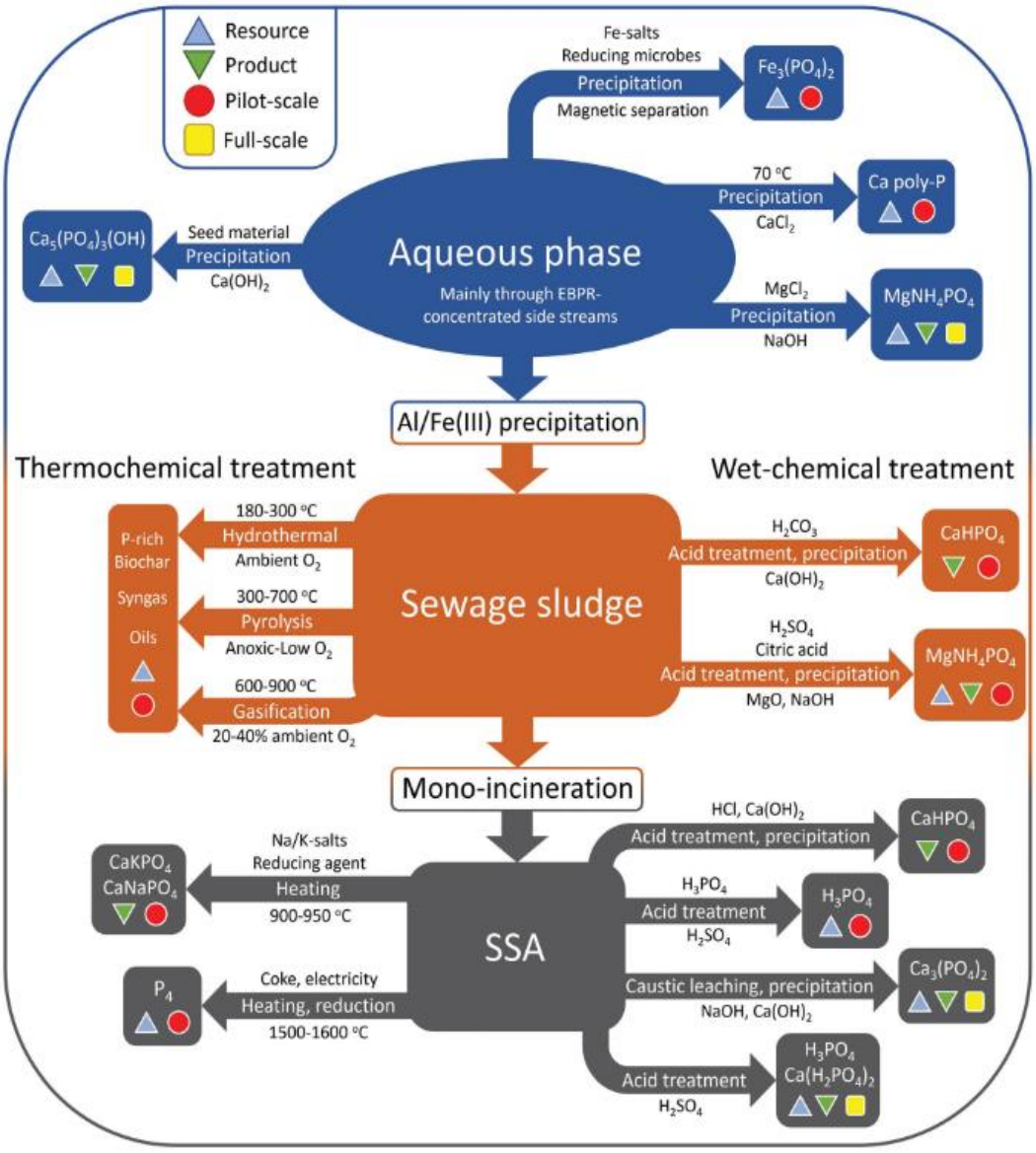

Figure 2.5: P recovery from various matrices of sewage (reproduced from Jupp et al.[1] under Creative Commons license).

Among various P species, the water-soluble fraction is readily utilized by plants and hence considered bioavailable. The dissolution of P in water is dependent on the nature of P species (such as ortho-P and poly-P) and the association with other elements[59]. For example, phosphates of sodium (Na_3PO_4), potassium (K_3PO_4), and ammonium ($(NH_4)_3PO_4$) are considered bioavailable. However, phosphates strongly bound to aluminum, calcium, or iron are retained in the solid matrix and do not dissolve easily[59]. The solubility of various metal compounds of phosphate in water is depicted in Figure 2.6. Some of these compounds are considered slow-release fertilizers (especially Ca-P) due to their low solubility in water. Hence, their use is advocated for fertilization as well as for the prevention of eutrophication. P transformation to a more bioavailable form is essential before applying SS or its thermal product (such as ash, char, or hydrochar) on the soil.

		Group I Alkali Metals			Group II Alkaline Earth Metals			Transition Metals					Post-transition Metals	
	Ammonium NH_4^+	Lithium Li^+	Sodium Na^+	Potassium K^+	Magnesium Mg^{2+}	Calcium Ca^{2+}	Barium Ba^{2+}	Iron (II) Fe^{2+}	Iron (III) Fe^{3+}	Copper (II) Cu^{2+}	Silver Ag^+	Zinc Zn^{2+}	Lead (II) Pb^{2+}	Aluminum Al^{3+}
Phosphate PO_4^{3-}	soluble	insoluble	soluble	soluble	insoluble	insoluble	insoluble	insoluble	insoluble	insoluble	insoluble	insoluble	insoluble	insoluble

Description	Approximate volume of water in mL/g of substance
Very soluble	less than 1
Easily soluble	from 1 to 10
Soluble	from 10 to 30
Sparingly soluble	from 30 to 100
Slightly soluble	from 100 to 1,000
Very slightly soluble	from 1,000 to 10,000
Practically insoluble	more than 10,000

Figure 2.6: Solubility of ionic compounds of phosphate in water. Modified from Sigma Aldrich[60].

Alternately, extracting P as PO_4^{3-} using wet extraction (alkaline or acidic) and using it for fertilizer manufacturing or direct application as a liquid fertilizer is another option. P can be extracted from SS directly or from the products after thermal treatment (such as ash and char) using acidic or alkaline extraction. P recovery efficiency is strongly dependent on P species in SS or its thermal residue (discussed in Sections 2.5 and 2.6), and operational parameters such as pH,

liquid-to-solid ratio, presence of interfering ions, and duration of extraction. Studies suggest that acidic treatment promotes the conversion of particulate reactive phosphate (RP) and non-RP into soluble RP, but alkaline treatment only mainly dissolves non-RP to soluble RP[61]. However, inorganic phosphorus (IP) dominates in the liquid phase after acidic/alkaline/sequential extraction[36]. After P extraction, precipitation of phosphate compounds (mainly struvite ($MgNH_4PO_4.6H_2O$) and hydroxyapatite ($Ca_5(PO_4)_3(OH)$)) is the most common method of P recovery from SS[11].

2.4.1. Acidic extraction

Acidic extraction of P from SS or its thermal products can be carried out using inorganic acids or organic acids [8], as shown in Table 2.4. Inorganic acids are highly efficient in dissolving the alkali metal oxides and all phases containing P in ISSA, while organic acids promote chelation which increases the dissolution of metal/metalloids from ash and soil matrices[62]. For acidic extraction, pH and acid type are among the most crucial factors controlling P recovery efficiency[8]. Some of the important reactions involving the dissolution of metal oxides and phosphates are given in Table 2.5 (modified from Levlin and Hultman[63]). Given the heterogeneity of P species in sludge and its thermal products, these equations portray a simplified explanation of the extraction process.

Table 2.4: Acid dissociation constant of acids used for P extraction from SS or its thermal products.

Acid type	Acid	Acid dissociation constant (K_a or K_{a1})*
Inorganic	Hydrochloric acid (HCl)	1.3×10^{6}
Inorganic	Sulfuric acid (H_2SO_4)	$1x10^{3}$
Inorganic	Nitric acid (HNO_3)	24
Inorganic	Phosphoric acid (H_3PO_4)	$7.1x10^{-3}$
Organic	Oxalic acid ($C_2H_2O_4$)	$5.9x10^{-2}$
Organic	Citric acid ($C_6H_8O_7$)	$8.4x10^{-3}$
Organic	Gluconic acid ($C_6H_{12}O_7$)	$2.5x10^{-4}$
Organic	Formic acid (CH_2O_2)	$1.8x10^{-4}$
Organic	Acetic acid ($C_2H_4O_2$)	$1.8x10^{-5}$

* K_a for monoprotic acid and K_{a1} for polyprotic acid

Table 2.5: Common reactions involving inorganic sludge components during acidic or alkaline extraction (modified from Levlin and Hultman).

Component	Extraction reaction	pH range
$Fe(OH)_2$	$Fe(OH)_2 + 2H^+ \rightarrow Fe^{2+} + 2H_2O$	
$Fe_3(PO_4)_2$	$Fe_3(PO_4)_2 + 4H^+ \rightarrow 3Fe^{2+} + 2H_2PO_4^-$	pH>2.2
$Fe_3(PO_4)_2$	$Fe_3(PO_4)_2 + 6H^+ \rightarrow 3Fe^{2+} + 2H_3PO_4^0$	pH<2.2
$Fe(OH)_3$	$Fe(OH)_3 + 3H^+ \rightarrow Fe^{3+} + 3H_2O$	
$Fe(PO)_4$	$Fe(PO)_4 + 2H^+ \rightarrow Fe^{3+} + H_2PO_4^-$	pH>2.2
$Fe(PO)_4$	$Fe(PO)_4 + 3H^+ \rightarrow Fe^{3+} + H_3PO_4^0$	pH<2.2
$Al(OH)_3$	$Al(OH)_3 + 3H^+ \rightarrow Al^{3+} + 3H_2O$	
$AlPO_4$	$AlPO_4 + 2H^+ \rightarrow Al^{3+} + H_2PO_4^-$	pH>2.2
$AlPO_4$	$AlPO_4 + 3H^+ \rightarrow Al^{3+} + H_3PO_4^0$	pH<2.2
$CaCO_3$	$CaCO_3 + 2H^+ \rightarrow Ca^{2+} + CO_2 + H_2O$	
$MgCO_3$	$MgCO_3 + 2H^+ \rightarrow Mg^{2+} + CO_2 + H_2O$	
$FePO_4$	$FePO_4 + 3OH^- \rightarrow PO_4^{3-} + Fe(OH)_3$	
$Al(OH)_3$	$Al(OH)_3 + OH^- \rightarrow Al(OH)_4^-$	
$AlPO_4$	$AlPO_4 + 4OH^- \rightarrow Al(OH)_4^- + PO_4^{3-}$	

There are relatively fewer studies on the direct extraction of P from dry SS than ISSA. Stark[64] extracted sludge samples (primary sludge, digested sludge, and deep-bed filter sludge) using a solution with a pH range of 2 – 12 and found that lower pH promoted P extraction than higher pH. Lesser organic content enhanced P recovery among the three sludge types investigated in that study. Other studies with their significant findings are given in Table 2.6.

Table 2.6: Studies on phosphorus (P) recovery from dried P-rich sludges (mainly sewage sludge).

Leaching method	Sample collected from WWTP	P removal technique at WWTP	Sample treatment	Leaching conditions	Max. leaching efficiency (%)	Significant findings	Ref
Acid	Dried sludge	No specific process for P removal. Treated both municipal and industrial wastewater.	Sample used as collected.	Acid type (HCl, H_2SO_4, HNO_3), acid conc., leaching time and L/S ratio optimised. Leaching done at 100°C. Outcome: 1 M H_2SO_4, 20 mL/1 g and 2 h.	82	• H_2SO_4 superior to HCl and HNO_3 for higher P recovery. • Higher H_2SO_4 conc. (>1 M) lead to lower P recovery. • P recovery reduces beyond 2 h of leaching possibly due to crystallization and precipitation. • Zeta potential used to ascertain viscosity and mass transfer. Contradictory result obtained. • Leaching kinetics shows diffusion controls the rate limiting step.	[65]
Acid	P-saturated dewatered aluminum sludge cake (DASC)	DASC used as a P-adsorbent in a lab-scale constructed wetland for the treatment of animal farm wastewater.	Dried at room temp.	0.063 M H_2SO_4, 177 L/S ratio (mL/g), 1 h duration,	98	• P-rich leachate had high Al and total organic carbon (TOC). Leachate treated using H_2O_2 to remove TOC. • TOC-free leachate used for $AlPO_4$ precipitation. pH increased to 5-6 using NaOH and a salt precipitate mixture of $AlPO_4$+$Al(OH)_3$ obtained.	[66]

						• SO_4^{2-} in the acid leachate did not influence the precipitation of Al, P.	
Acid and base	Dried sewage sludge	Biological P removal only	Re-dried at 105^{o}C for 1 h.	HCl or NaOH conc. (N): 0.1,0.2,0.4,0.6,0.8,1; Duration (h): 1,2,24,30; Temp. (^{o}C): 23,30,70; L/S ratio (mL/g): 25,50,75,100,150; pH: 0.3-13.8	Acid: 97.9 Base: 70.3	• pH most important factor for P leaching. Negligible effect of temperature and plateauing effect of leaching duration. • Almost complete leaching of P from below pH 1.5 but not in alkaline leaching. • Acid conc. is important but L/S not crucial for acidic leaching of P. For alkaline leaching, both conc. and L/S important.	[67]
Acid and base	Dewatered sludge cake	4 stage-BNR for P removal and gravity thickening with PAC.	Dried at 105^{o}C for 18 h.	HCl, H_2SO_4 and NaOH conc. (M): 0.1, 0.5 and 1. Duration: 2 h.	-	• P leaching efficiency: H_2SO_4> HCl>NaOH. • 15 g/L calcium silicate hydrates (CSH) could remove 90% of the leached P.	[68]
Acid and base	P-saturated dewatered aluminum sludge cake (DASC)	DASC used as a P-adsorbent in a lab-scale constructed wetland for the treatment of animal farm wastewater.	Dried at room temperature	Effect of leaching duration, acid/base type and conc., and L/S ratio assessed. HCl, H_2SO_4, HNO_3, NaOH and KOH conc. (M): 0.01-0.1; Duration (h): 1-6; L/S ratio (mL/g): ~42-250.	Acid: 98 (H_2SO_4) Base: 70 (NaOH)	• P leaching efficiency assessed using response surface methodology (RSM). Optimum condition: 0.8 g solid, 0.063 M H_2SO_4 and 142 mL acid. Duration: 1 h • No significant difference in P extraction efficiency due to acid/base type.	[69]

						• At low conc. (<0.05 M), base more efficient than acid for P extraction and vice versa. • Other metals leached concomitantly with P during acid leaching.	
Acid, base and sequential	Sewage sludge	PAC	Dried at 105^{o}C for 48 h.	HCl and NaOH conc. (N): 0.1, 0.2, 0.5, 1 and 2	Acid: 78 Base: 80.5 Sequential: 91.7 (NaOH-HCl) and 84.5 (HCl-NaOH)	• P leaching efficiency higher for NaOH than HCl. • P leaching efficiency reduced after 2 h. • P leaching and sludge dissolution follows first order reaction kinetics. No direct relation between sludge dissolution and P release.	[39]
Acid, base and reduced.	Sludge deposit from the vertical flow constructed wetland.	Wastewater treated with $FeCl_3$ for P precipitation. It treated domestic and winery effluents.	Dried at 35^{o}C.	Acid: 0.01 M HCl Base: 0.01 M NaOH Reducing agent: 0.05 M sodium ascorbate ($C_6H_7NaO_6$) Duration: 24 h Leaching temperature: 16 ± 5°C	Acid: 20 Base: 34 Reduced: 39.5	• 27 successive leaching experiments conducted using the same solid sample. • Higher buffering capacity of sludge in acidic and redox condition than in alkaline. • Redox potential (Eh) more influential than pH in P recovery when Fe-P predominant in sample. • OP more easily leached in alkaline conditions.	[70]

2.4.2. Alkaline extraction

Some researchers consider alkaline treatment better than acidic treatment because it has the added advantage of higher hydrolysis, which improves anaerobic digestion [33]. Generally, NaOH is used for alkaline treatment of SS because of higher organic fraction solubilization efficiency but at a higher operational cost [71,72]. Inorganic P is predominantly released during alkaline extraction of SS, and higher pH (12 or more) leads to a significant increase in extraction efficiency [33]. Bashir et al. [33] found re-immobilization of P when extraction pH was reduced from 12 to 8. Al and Fe ions tend to enhance P solubilization in alkaline conditions, while Ca does so in acidic conditions [33,34,73]. Sludge organic content can prevent organic P release, but the highly alkaline condition can lead to sludge disintegration leading to the dissolution of OP [34]. At lower alkalinity, only sludge flocs disintegrated, but at very high pH (11 and above), cell structure disintegrated, resulting in hydrolysis of nucleic acids and decomposition of the phospholipid bilayer, which increases phosphorus concentration [74,75]. Other studies with their significant findings are given in Table 2.6.

2.4.3. Sequential extraction

Acid and base can be applied sequentially to extract and precipitate P without concomitantly extracting interfering ions and trace elements. Seaborne process, Stuttgart process, Budenheim process, and Krepro process are some of the well-known sequential processes that have reached pilot or full-scale implementation [9,64]. Stuttgart process uses citric acid (10 – 12 L 50% citric acid per m^3 of extract) to promote the complexation of interfering ions and prevent precipitation along with phosphate [9]. Seaborne process does the same by increasing the pH to 5.7 using NaOH and Na_2S [9]. He et al. did a comparative study on acidic, alkaline, and sequential (acidic-alkaline and alkaline-acidic) anaerobic fermentation of waste activated sludge[36]. They found the acidic-alkaline treatment more effective than other methods for P migration from the solid to the liquid phase. Alkaline-acidic sequential treatment was the worst performer in this regard. Some studies with their significant findings are given in Table 2.6.

2.5. FATE OF PHOSPHORUS DURING PYROLYSIS

Pyrolysis entails the thermal decomposition of SS at temperatures 400 – 600^{o}C in an oxygen-free environment (utilizing N_2 and/or CO_2), to yield the desired products (char, bio-oil, and gas (H_2, CO, and other light gases))[76]. The details of the pyrolysis process, especially for SS can be found elsewhere[76], though a summary illustration is provided below (Figure 2.7). The pyrolysis of sewage sludge (SS) can be characterized by three distinct phases: (i) an initial stage involving dehydration and the release of light volatile compounds, which occurs between room temperature and 200 °C; (ii) the degradation and de-volatilization of both low and high molecular weight hydrocarbon compounds, taking place in the temperature range of 200–600 °C; and (iii) a final stage where inorganic materials decompose, accompanied by the formation of stable gases at temperatures exceeding 600 °C[77]. The gaseous by-product consists of light gases such as H_2, CO, CO_2, H_2O and C_1-C_4 hydrocarbons[78] (CH_4, C_2H_2, C_2H_4, C_2H_6, and C_3H_8). These gases can form via multiple reactions such as partial oxidation (Eqn.(9)), water gas reaction (Eqn.(10)), Boudouard (Eqn.(11)), hydrogasification (Eqn.(12)), and methanation (Eqn.(13))[79].

$$C + 1/2O_2 \rightarrow CO \qquad (9)$$

$$C + H_2O \rightarrow CO + H_2 \qquad (10)$$

$$2CO \rightarrow C + CO_2 \qquad (11)$$

$$C + 2H_2 \rightarrow CH_4 \qquad (12)$$

$$CO + 3H_2 \rightarrow CH_4 + H_2O \qquad (13)$$

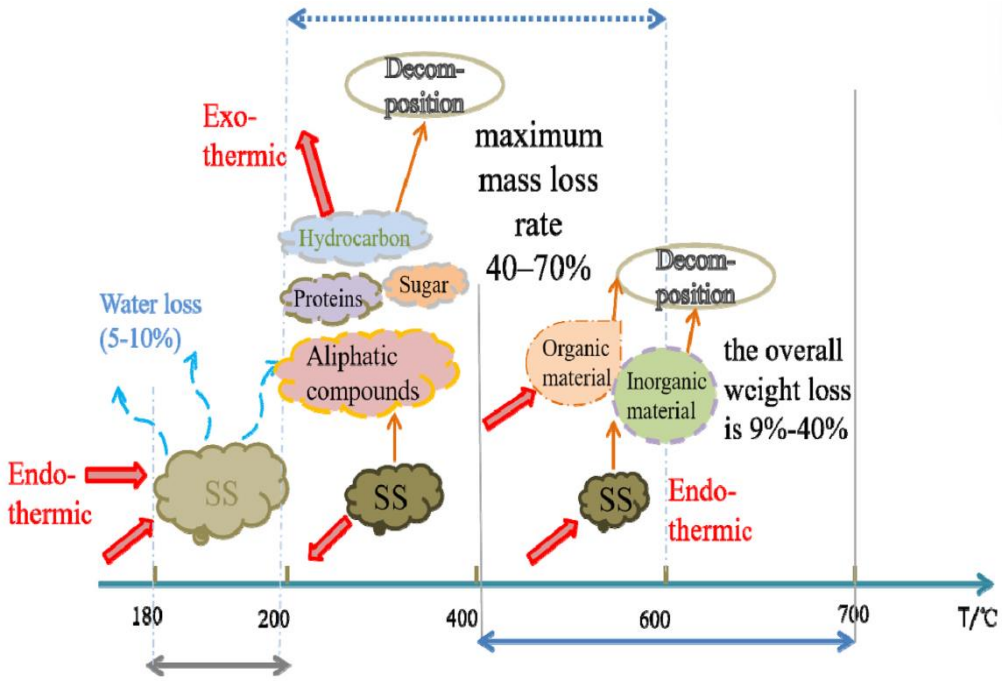

Figure 2.7: The stages of pyrolysis of sewage sludge along with the by-products. Reproduced from Zhu et al[80] with permission from Elsevier.

P is predominantly retained in the char (80 – 100 %) after pyrolysis, with minimal distribution in the gas and bio-oil[13,15,81], though P release to gas/liquid phase(s) in the range ~22 – 49% has been reported[82]. Generally, feedstocks rich in OP tend to release P in the gaseous phase[81], and SS is deficient in OP. P content in SS char (pyrolysis char and hydrothermal treatment (HT) char) is 2.9 – 10.6% (with an average of 7.7%), which is higher than in chars from other feedstocks such as manures (0.4 – 5%), woody residues (0.02 – 0.5%), grasses (0.05 – 0.5%), and agri-residues (0 – 1.7%)[83,84].

2.5.1. Effect of process parameters on P

2.5.1.1. Temperature

The transformation of P during pyrolysis is similar to incineration[85] (except for the reactions involving oxygen and the role of carbon in char[13,86]) and temperature plays a critical role. P concentration in char increases with increasing temperature[87] due to mass loss (due to loss of volatiles) while P is largely non-volatile. OP is most susceptible to decomposition during pyrolysis, as reported by the majority of studies on SS pyrolysis. It can be decomposed at temperature ~250^{o}C to organic/inorganic poly-P with condensed functional groups (poly-P end groups), pyro-P, and ortho-P[81,88] depending on operational conditions. Within OP, ortho-P diester is likely to degrade first to

ortho-P monoester and pyro-P, with ortho-P monoester being stabler than pyro-P[89,90]. However, another study reported that ortho-P monoester and pyro-P were decomposed at 500^{o}C and 700^{o}C, respectively, but ortho-P diester (~2%) was found at even 800^{o}C[91]. Moreover, OP can exist in char prepared at higher pyrolysis temperatures. For instance, out of total P in char prepared at 450^{o}C, 20% was phytic acid[92], and when prepared at 900^{o}C, 39% was ortho-P monoester and 21% ortho-P diester[93], though the authors did not provide the suitable reasons for their presence. The presence of OP in such cases might be due to its stabilization through interactions with the ash components of the char, or formation of organo-mineral complexes, or bonding with aromatic carbon through electrostatic interaction and hydrogen bonding[13].

Pyro-P is most prominent at temperatures 300 – 600^{o}C, which breaks down to ortho-P minerals as the temperature increases[81]. Its formation during pyrolysis can be attributed to polymerization and condensation reactions of P species, OP degradation through hydrolysis (enhanced by H_2O from the decomposition of carboxylic acid), and dehydration of metal ortho-P such as Ca ortho-P[13]. Also, two adjacent ortho-P groups in phytic acid can combine via dehydration to form pyro-P[81], though phytic acid content in SS is generally low. The formation of short-chain meta-P was also reported when SS was pyrolyzed at 400^{o}C, and it was hypothesized that labile C compounds facilitated their formation[86]. Another study reported meta-P presence in SS char prepared at 500^{o}C, and 700 but not at 300^{o}C[94]. However, these studies reported meta-P based on XPS peaks which are often difficult to assign due to SS char composition and proximity of peaks of various P compounds (Table 2.3). ^{31}P NMR peak of metaphosphate is also difficult to assign due to its potential hydrolysis during extraction (liquid NMR) or overlap with Al-P species (solid-state NMR)[51]. Nevertheless, the general thermal stability order of various P species during pyrolysis is OP < meta-P < pyro-P < ortho-P. After the decomposition of OP, pyro-P and meta-P, IP (ortho-P associated with metal or minerals) is predominant because metal/mineral combines or complexes with ortho-P released during their degradation. Similar to incineration, the crystallinity and relative fraction of AP increases while NAIP reduces in char as temperature increases because of its thermodynamic stability[13] but the relative molar ratio of cation/P is crucial for P speciation. It was hypothesized that Ca and Mg would react with carboxyl and carbonyl groups rather than P until these groups are

volatilized at temperatures > 500°C and thus AP fraction would increase significantly at higher temperatures[95]. The hydroxyapatite formation is dependent on both the Ca/P molar ratio and temperature of pyrolysis and starts decomposing above 900°C[93] via the dihydroxylation reaction. The bioavailability of P in char reduces when char is prepared at a higher temperature (> 500°C)[96], though another study on co-pyrolysis of SS with Ca additives found that char prepared at 900°C had better fertilization effect than that prepared at 500°C[93]. Overall, P tends to immobilize in the char matrix with increasing pyrolysis temperature[81]. Thermodynamic modelling indicates that P is non-volatile till 800°C during SS pyrolysis[97]. Modelling also suggests the presence of P in slag above 650°C, whose fraction reduces when P volatilizes to P_2 and combined heat and power (CHP) gas species above 800°C[97]. This study reported discrepancies in modelling and experimental results and there is a need for further studies on P volatilization during pyrolysis.

2.5.1.2. Other process parameters

Heating rate, and feedstock residence time are also important parameters during SS pyrolysis[76]. In the temperature range of 400 – 600°C, a heating rate of 20°C/min led to more NaOH extractable P (i.e., NAIP) than at 5°C/min[95]. Also, higher residence time promoted NAIP to AP conversion, especially at pyrolysis temperatures above 500°C[95,98]. This trend implied that temperature was more important than other process factors in determining P speciation. Pyro-P was higher in the chars prepared with a shorter residence time (30 min) but the difference reduced at the pyrolysis temperature was increased from 400 – 600°C[95]. The reactors generally used and suggested for pyrolysis are fixed bed, bubbling fluidized bed, auger reactor, and rotary kiln, among others[99]. Rotary drum and rotary kiln reactors are commercially utilized for SS pyrolysis in the EU, in conjunction with gasification and incineration[100]. The effect of process parameters other than pyrolysis temperature on the fate of P in SS has not been well investigated.

2.5.2. Effect of feedstock properties on P

Feedstock composition has a critical influence on P speciation and partitioning. P speciation in char depends on the chemical composition of SS, which is affected by raw sewage composition and sewage treatment process (as discussed in Section 2.2). When primary sludge, secondary sludge, digested

sludge, and dewatered sludge were pyrolyzed at 300, 500, and 700^{o}C, AP fraction was highest in char from dewatered sludge prepared at 700^{o}C because it had the highest Ca concentration[96]. The particle size of dry SS affects the interaction of P with additive, for instance, soaking granulated SS against finer SS in K(CH_3COO) for enhancing water-extractable potassium phosphate (K-P)[101]. It was also observed that char with finer particle size ($\leq$ 0.25 mm) had higher water-extractable P than coarser particle size ($\leq$ 2 mm)[102]. To alter P physico-chemical characteristics, SS is blended with chemicals such as hydroxides, carbonates, bicarbonates, and chlorides of metals, and other waste materials and subsequently pyrolyzed. The goal of co-pyrolysis is generally a directional P transformation to increase its bioavailability or leachability using acid/bases or increase adsorption capacity for pollutant/nutrient removal from wastewater. There are many studies on co-pyrolysis of SS with other feedstocks and some of the recent ones are summarized in Table 2.7. Most co-pyrolysis studies aimed for enhanced AP fraction in char by adding Ca-rich substrates. Though AP fraction increases with increasing temperature without additives, this conversion is hindered if the Ca/P molar ratio is low (<1)[13,103]. AP fraction can increase significantly with increasing temperature by adding Ca-based additives. Very few studies focussed on AP to NAIP conversion to enhance the alkaline extraction of P from SS without co-extracting TEs[13].

Table 2.7: Some of the recent studies on co-pyrolysis of sewage sludge with chemicals or other wastes.

Sludge type	Sewage treatment	Sludge Pretreatment	Additive	Pyrolysis condition	Significant findings	Ref.
SS (mix to PS + SeS)	Conventional (with A/A/O process)	Fenton's reagent	KOH, NaOH, K_2CO_3, Na_2CO_3, $KHCO_3$, $NaHCO_3$	Horizontal tube furnace; 300 – 700^oC; 10^oC/min; 2 h; Ar	Fenton's reagent increased Fe-P in SS, which was converted to potassium phosphate during $KHCO_3$-activated pyrolysis, enhancing the water-soluble P in the resulting biochar. Water-soluble P increased from 0.5 to 96.2% due to $KHCO_3$ addition. Final recovery of vivianite.	[104]
SS (mix to PS + SeS after AD)	Conventional	-	$CaCO_3$	Tube furnace; 500 – 700^oC; 5^oC/min; 2 h; N_2	AP fraction in IP increased from ~68 to 98% due to $CaCO_3$ addition while AP concentration in char increased at higher temperature (700^oC) leading to increase of slow-release P in char.	[105]
SS	-	-	$CaCl_2$	Tube furnace; 500^oC; 15^oC/min; 2 h; N_2	Ca addition promoted decomposition of OP and pyro-P while calcium phosphate (Ca-P) increased on average by about 10% to ~90%, which was more bioavailable compared to unamended char.	[106]
SS	-		CaO, and MgO	Horizontal microwave furnace; 300 – 500^oC; 20^oC/min; 1 h, N_2	Increase in AP fraction due to CaO was more obvious than MgO and was 2.5 times higher than in unamended case. Besides, addition of CaO and MgO also inhibited the formation of pyro-P during pyrolysis.	[89]
SS	Undigested	Soaked in $K(CH_3COO)$ solution	-	Thermogravimetric analyzer; 400 – 900^oC; 50^oC/min; 10 min	High K-doping (5%) and low pyrolysis temperature (400^oC) suitable for enhancing water-extractable P (43% of TP)	[101]
SS	AD + $FeCl_3$	Sprayed with $K(CH_3COO)$ solution	-	PYREG continuous auger reactor; 500 –	Water-extractable P fraction trend in the char from lab-scale pyrolyzer similar to microscale pyrolysis via thermogravimetric analyzer. K-doping led to K_2HPO_4 formation during pyrolysis, which is easily	[101]

				700^{o}C; ~2 kg/h; ~20 min, N_2	water-extractable. But higher temperatures led to Ca-P fractional increase.	
SS	Modified sequential batch reactor + poly-aluminum chloride	Extraction of SS in K_3PO_4 solution	-	Muffle furnace; 300 – 500^{o}C; 10^{o}C/min; 3 h, N_2	SS rich in Fe, when spiked with K_3PO_4, led to higher fraction of $Fe_rPO_4(OH)_{3r-3}$ formation during pyrolysis. This trend enhanced P availability in char.	[107]
SS	-	-	CaO	Tube furnace; 500 – 800^{o}C; 10^{o}C/min; 2 h	NAIP to AP conversion due to addition of CaO and higher temperature pyrolysis. Fast wet P release from char inhibited by CaO addition leading to slow-release fertilizer production.	[108]
SS	-	-	CaO, $CaCl_2$	Horizontal tube furnace; 450 – 850^{o}C; 10^{o}C/min; 2 h; N_2	22.5 – 49% of P released from unamended SS when pyrolyzed at 850^{o}C. CaO addition inhibited P loss during pyrolysis while $CaCl_2$ facilitated P volatilization.	[82]
SS	-	-	CaO, $MgCl_2$, $MgCl_2$ + CaO	Microwave furnace; 300 – 700^{o}C; 20^{o}C/min; 1 – 2.5 h; N_2	Greater residence time and addition of CaO promoted NAIP to AP conversion while $MgCl_2$ addition promoted AP to NAIP conversion. When both additives were added simultaneously, CaO dominated leading to NAIP to AP conversion.	[98]
SS (PS + SeS)	-	-	PVC, NaCl, $MgCl_2$, and $CaCl_2$	Horizontal furnace; 300 – 900^{o}C; 5^{o}C/min; 4 h; N_2	P solubility in neutral ammonium citrate increased after chlorination, peaking at 700^{o}C for each series. After pyrolysis at 700^{o}C, P solubility rose significantly from 40.1% in sludge biochar to upto 76.6% in amended biochar (corresponding to $MgCl_2$, due to formation of $Mg_3(PO_4)_2$). Some of the trace elements were volatilized.	[109]
SS	Undigested	Sprayed with $K(CH_3COO)$ solution	-	Auger reactor; 700^{o}C; ~2 kg/h; ~21.5 min, N_2	K-doping increased the fraction of water-extractable P due to formation of K_2HPO_4 within the char matrix.	[110]

SS (PS + SeS after AD)	Activated sludge process	Extraction of SS with alum sludge at pH ~3 – 4 using HCl.	-	Horizontal tube furnace; 400 – 900^{o}C; 20^{o}C/min; 1 h; N_2	SS acidic pretreatment promoted AP to NAIP conversion in SS, selective removal of Ca and Mg, and enrichment with Al. Al-P species dominated in pretreated SS char compared to non-pretreated SS char, which led to subsequent high alkaline extraction efficiency (~75% overall) of P.	[13]
SS	-	-	Phosphate tailings	Tube furnace; 600 – 900^{o}C; 5^{o}C/min; 1 h; N_2	Ca from phosphate tailings increased the AP fraction in char and P bioavailability. Trace elements such as Zn, Pb, Mn, Ni, and Cu immobilized in char and were less bioavailable.	[103]
SS	A/A/O		Reed (Phragmites australis)	Modified muffle furnace; 300 – 700^{o}C; 10^{o}C/min; 2 h, N_2	NAIP to AP transformation and reduced toxicity due to trace elements in the char from the co-pyrolysis. OP fraction of TP higher in blended char than pristine SS due to high OP content in reed.	[111]
SS (influent was mainly industrial wastewater)	Interactive batch bioreactor deep treatment process.	-	Rice husk	Tube furnace; 300 – 700^{o}C; 10^{o}C/min; 2 h; N_2	Addition of rice husk promoted OP to IP transformation and immobilization of trace elements.	[112]
SS	A/A/O + aluminum sulfate	-	Calcined clam shell powder	Horizontal tube furnace; 500 – 800^{o}C; 10^{o}C/min; 1 h, N_2	The OP content was inhibited, AP/NAIP fraction increased, water-extractable P reduced, and trace elements were immobilized due to co-plyrolysis with calcined clam shell powder.	[91]

A/A/O: anaerobic-anoxic-oxic; AD: anaerobic digestion; PS: primary sludge; PVC: polyvinyl chloride; SeS: secondary sludge

2.6. FATE OF PHOSPHORUS DURING HYDROTHERMAL TREATMENT

During HT, wet SS is subjected to heating in a closed vessel under autogenous above-saturation pressure. Since moisture content in SS is high (70 – 80%), water is both reactant and solvent during HT. Depending on the operating conditions, HT is divided into three main categories, hydrothermal carbonization (HTC), hydrothermal liquefaction (HTL), and hydrothermal gasification (HTG), providing biochar, bio-oil, and syngas as their main products, respectively. The broad temperature range for HTC, HTL, and HTG are 180 – 250, 250 – 370, and > 400^{o}C, respectively, while the operational pressures are 2 – 5, 5 – 20, and >20 MPa, respectively[113–115]. HT is performed in either of two states: sub- or supercritical water. Subcritical water is defined by temperatures ranging from 100 – 374°C, with pressures sufficient to maintain the liquid phase. When the temperature surpasses 374.3°C and the pressure exceeds 22.1 MPa, water transitions into a supercritical state, exhibiting unique properties such as very low density, dielectric constant, and inorganic solubility, while high hydrocarbon solubility. P content in SS hydrochar is 0.2 – 8.1%, with an average of 4.1%[115]. The main reactions during HT are hydrolysis, dehydration, decarboxylation, condensation, and polymerization[116,117] (Figure 2.8). The fate of P during these reactions is not well established. In recent years, several studies have deciphered the effects of process parameters and feedstock properties on P transformation and partitioning.

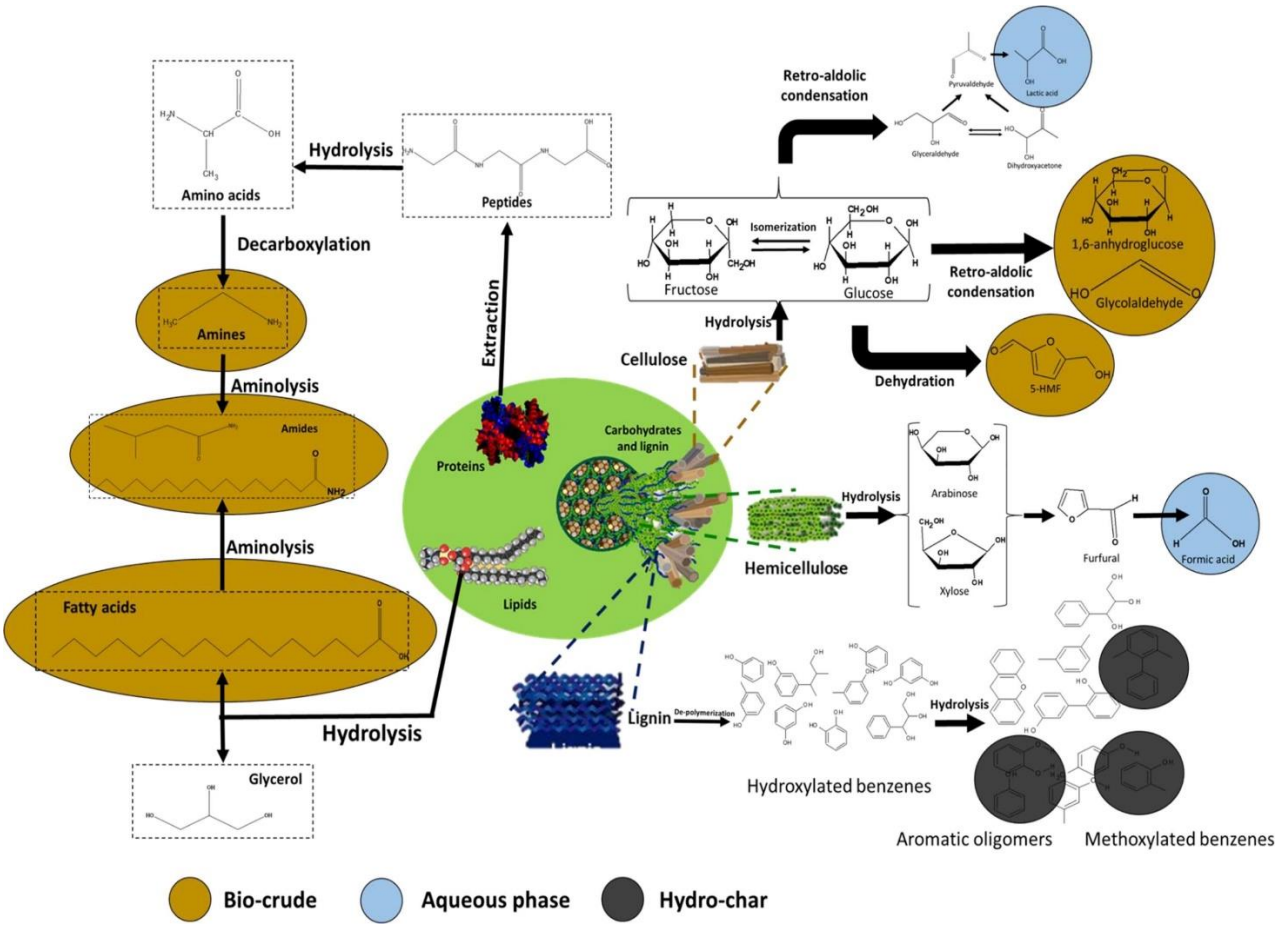

Figure 2.8: The reactions during hydrothermal treatment of sewage sludge. Reproduced from D. Lachos-Perez et al. [113] with permission from Elsevier.

2.6.1. Effect of process parameters on P

Like other thermochemical processes, temperature has a predominant role in P speciation and phase partitioning in the HT process. However, other factors such as solid/liquid ratio, and retention time might be important as homogeneity of mixed slurry and pressurized high-temperature operation can lead to extensive P conversions compared to other thermochemical processes. Random forest-based modeling suggests the following order of significance of process parameters for total phosphorus (TP) in hydrochar: temperature > retention time > initial pH of HT[118].

2.6.1.1. Temperature and retention time

The effect of HT temperature on the fate of P during SS HT is most widely investigated among all the operational parameters. This trend can be attributed to the critical effect of temperature in altering the properties of sub- and supercritical water. In subcritical conditions, hydrogen bond in water is weakened leading to the autoionization of water into hydronium and hydroxide ions[116].

Consequently, compounds in SS are transformed in acid-catalyzed reactions during HT. To assess the combined effects of temperature (T, in K) and reaction time (t, in s), severity factor f(T, t) is generally used (Eqn.(14)):

$$f(T, t) = 50t^{0.2}e^{-3500/T} \quad (14)$$

where f was originally conceptualized for hydrothermal coalification[119]. This model is based on time-temperature equivalence, i.e., a similar product can be generated with a shorter time and higher temperature or a longer time and lower temperature. In this review paper, the temperature and retention time effects are presented as per sub-categories of HT i.e., HTC, HTL, and HTG, though there are some studies on their comparative analysis[120,121].

2.6.1.1.1. Hydrothermal carbonization (HTC)

The studies on the fate of P during SS HTC are most common among the three sub-categories. In general, with increasing severity (f(T,t)), i.e., increasing HTC temperature and/or retention time, P concentration in hydrochar and AP/NAIP fraction increases (with temperature being a more important determinant than retention time)[115]. Most studies on HTC indicate that P fraction of SS in hydrochar is > 80% when f(T,t) < 0.6[115]. With increasing temperature (180 to 260^{o}C), the fraction of P in process water reduces (especially > 200^{o}C), while the effect of increasing retention time (1 to 5 h) has no clear trend[122]. However, some studies reported an increasing P fraction in hydrochar with increasing retention time (0.5 to 4.5 h) for the same HT temperature[123,124]. Another study found that P in process water was more dependent on temperature rather than retention time (> 220^{o}C)[125]. OP degradation during HT can start at 50^{o}C[55] and its complete degradation has been observed at temperatures > 175^{o}C[124], broadly consistent with the trend in most studies on HTC of SS. However, some monoester-P (< 5%) has been reported in hydrochar prepared at 200^{o}C[41,55]. Dissolved OP degradation has been explained via a two-stage process, i.e., stage I (50 – 120^{o}C) and stage II (120 – 200^{o}C)[55]. In stage I, the solubilization order with increasing temperature was: adenosine diphosphate (ADP) (50^{o}C) > diester-P (70^{o}C) > monoester-P (70^{o}C) and they were decomposed to dissolved OP hydrolysates[55]. These hydrolysates reacted with nitrogenous heterocyclic compounds generated via Maillard reactions, and other reactions such as reduction, decarbonization,

decarboxylation, and denitration aided the dissolved OP transformation to metal-OP (or IP) complexes and co-precipitates, especially above 180^{o}C[55]. Another study reported almost complete degradation of dissolved OP to ortho-P at f(T,t) > 0.18 (210^{o}C for 1 h)[126]. The release of phosphonates at temperatures >160^{o}C was also reported[55]. At the same HTC temperature, monoester-P is likely to degrade before pyro-P[41]. OP upon hydrolysis can transform to pyro-P and/or ortho-P, and other weaker metal-complexed/adsorbed/precipitated P with Ca, Al, Mg, and Fe as the process severity increases (especially temperature) [81,115,127]. Thus, the relative abundance of metal cations has a critical role in P repartitioning and fractionation, which in turn depend on feedstock properties. Pyro-P hydrolyses to ortho-P as the temperature and/or residence time increase(s)[88,127]. Overall, P in SS hydrochar predominantly exist as inorganic ortho-P. AP fraction in IP increases with increasing process severity (temperature being more crucial than retention time), especially above 220^{o}C[115], and thermodynamic modelling suggests that hydroxyapatite would be the largest fraction in IP due to its thermodynamic stability[125]. A study found no significant variation in bioavailability of P in hydrochar with change in temperature (180 – 200^{o}C) and retention time (4 – 8 h) on the plant availability of P in hydrochar[128]. Another study found the increase in plant-available P and decrease in water-extractable P with increasing HTC temperature (180 – 240^{o}C)[129]. Since plant availability of P depends on the soil environment (temperature, soil texture, pH, humidity, presence of oxides and carbonates, etc), the quantification based on extraction techniques might not be reliable and require pot/filed experiments[80]. Hence, the effect of HTC temperature and retention time on plant availability of P is inconsistent, though a general trend suggests that P transforms to a less labile form (i.e., extractable using acid/alkali) with increasing process severity[92,129].

2.6.1.1.2. Hydrothermal liquefaction (HTL)

About 85 – 99% of the P in SS is concentrated in hydrochar after HTL [127,130,131], followed by P in aqueous phase with negligible P in oil[132–134]. However, one study reported ~33% mass fraction of P in bio-oil, though in mineral form and filterable [135]. The containment of P in hydrochar after HTL was attributed to cations (Ca, Mg, Al, Fe) which bind to ortho-P (in-situ or released by OP)[132]. Given the temperature range of HTL (~280 – 370^{o}C), OP

is unlikely to be present in hydrochar, as evident in some studies[127,131]. Species such as octacalcium phosphate and hydroxyapatite increased while $AlPO_4$ and $Mg_3(PO_4)_2$ reduced as the HT temperature increased from 170 to 320^oC, indicating the increase in AP/NAIP fraction as the HT temperature increased from 260 – 320^oC [127]. However, another study found insignificant variation in AP/NAIP fraction during HTL (325 – 360^oC)[131]. The increase in retention time from 30 – 120 min at 350^oC led to an increase of P in hydrochar[136]. In conclusion, the general trend of P transformation with increasing temperature and retention time during HTL indicates that P is concentrated in hydrochar, OP is almost completely hydrolyzed to IP, and AP fraction might increase in TP.

2.6.1.1.3. Hydrothermal gasification (HTG)

During HTG, P in SS could be concentrated in hydrochar (~83 – 98%) [120,134,137] or in process water (~65 – 85%) (500 – 600^oC), but negligible in bio-oil[134]. The temperature increase led to an increase in P fraction in hydrochar[137,138]. OP fraction in TP reduced with increasing temperature and retention time[139]. OP has been reported in process water as well[120,139], and it could be as high as about 15% of TP[139]. Another study reported OP in hydrochar prepared at 400 – 500^oC, though the mass fraction was < 1%[138]. However, the presence of OP at such extreme conditions seems abnormal and requires further investigation. In supercritical conditions, NAIP precipitated, and AP hydrolyzed while OP converted to ortho-P[138]. Their relative fraction depended on the complex interplay of temperature, residence time, and solid-to-liquid ratio (SLR)[138]. The fraction of TP in hydrochar increased with increasing retention time[137].

2.6.1.2. Other process parameters

Unlike temperature, factors such as reaction pH, SLR, pressure, and gas composition in the HT vessel headspace prior to HT have not received great attention. The pH drops with increased dissolution of CO_2 in the aqueous phase during CO_2-purged HT[140], which might affect the P speciation and fractionation. However, the authors could not find any such study. HT encompasses a series of intermediate reactions, such as hydrolysis, decarboxylation, condensation, dehydration, and polymerization. These

processes contribute to the decomposition of biomacromolecules and the subsequent formation of organic acids, including formic, acetic, lactic, and levulinic acids[116] which could lead to a reduction in pH during HT. The formation of NH_4^+ via the hydrolysis of amino acids from the proteins and the dissolution of alkaline salts in SS could increase the pH[141–143]. The pH variation depends on operational conditions and the nature of the feedstock[126,144]. Some studies have explored the pH variation during HT via the addition of acid/base in the feedstock. Generally, P retention in the hydrochar is higher at medium pH (for instance, 3 – 11)[115,145]. At extreme pH (for instance, < 2 or > 12), the effect of temperature and retention time is not significant for P phase partitioning[146], and most of it will be released to process water (can be > 90%)[147,148]. A study found that H^+ releases both OP and IP effectively during acidic HT, while OH^- releases only OP effectively during alkaline HT[148]. It was reported that H^+ binds to the negatively charged tail while OH^- binds to the positively charged head of the phospholipid chain, and thus the mechanism of phospholipid disintegration is different during acidic and alkaline HT[148]. The OP/IP fraction in process water and hydrochar is low at extreme pH compared to medium pH[147,149]. Since P in SS is primarily IP (Ca-P, Al-P, Fe-P, etc) which dissolves in strong mineral acids[13], the fraction in process water is high at low pH. A study found that inorganic acids such as H_2SO_4 are more effective in releasing P in process water compared to organic acids such as HCOOH and CH_3COOH[150]. In strongly alkaline conditions, NAIP dissolves which might increase P in process water. Generally, Ca-P precipitates in alkali but it might dissolve as well if CO_3^{2-} is high, which competes with PO_4^{3-} for Ca precipitation[115]. NAIP to AP conversion at pH > 9 was reported in a study suggesting the precipitation of Ca-P when Ca is sufficiently abundant in the feedstock[149].

The aqueous phase before HT can be altered using oxidants such as H_2O_2, $K_2S_2O_8$, and $Na_2S_2O_8$, ethanol-water cosolvent[151], and deep eutectic solvent for P transformation and phase partitioning. The addition of oxidant led to enhanced degradation of OP[137,152], retention of P in hydrochar[152], or release in process water[153]. Deep eutectic solvent ($CaCl_2$-lactic acid) promoted the conversion of poly-P to pyro-P and ortho-P leading to its concentration in hydrochar[154]. The AP/NAIP fraction increased while OP/IP in process water had a mixed outcome with the application of deep eutectic solvent[154]. The

variation in SLR (2.5 – 30% w/w) led to a minor variation in the fractional phase distribution of P in solid and liquid (with the major fraction in solid)[125,141]. Though P concentration in process water increased with increasing SLR[141,155], owing to reduced quantity of water. It was observed that the reaction medium was more alkaline with increasing SLR (5 – 10% w/w)[125,141], which led to the precipitation of Ca-P and dissolution of Al-P, consequently increasing the AP and decreasing NAIP in hydrochar[125]. In HTG as well, higher SLR led to higher content of NAIP in hydrochar, though it was detrimental to the decomposition of OP[138]. Due to autogenous pressure build-up during HT, it is difficult to decouple the effect of temperature and pressure on P speciation and phase distribution. A study reported that TP and OP were reduced with increasing pressure[138]. Thermodynamic modeling indicated that the conversion of condensed phase P to gaseous P and the formation of hydroxyapatite would be inhibited with increasing pressure[125,156].

2.6.2. Effect of feedstock properties on P

The feedstock chemical composition has a significant bearing on the fate of P during HT, especially since it homogenizes the feedstock and thus allows greater contact between chemical species. SS may be rich in IP or OP depending on the sewage treatment process, but most P forms convert to ortho-P during HT[92]. Several studies reported a decline in P recovery in the hydrochar with rising temperatures, indicating that ortho-P remained dissolved in the process water[115]. It was likely due to a lack of metal cations or unfavorable pH conditions for metal phosphate precipitation. Conversely, if sufficient metal ions are present, P will be retained in the hydrochar even in acidic HTC[144]. A study compared thickened sludge, digested sludge, and dewatered sludge, and found that P was concentrated in hydrochar in all the cases, with dewatered sludge having the highest concentration (~11 mg/g)[157]. Random forest-based modeling suggested that TP in SS strongly and positively influenced the TP in hydrochar[118]. Hence, the HT of dewatered SS is most suitable for P recovery, as it generally has the highest P content among various sludge types. Another study compared the HTC of activated sludge and anaerobic sludge and observed that relative abundance and form of metal ions in sludge affected the P forms in hydrochar[92]. For instance, Fe existed mainly as a hydroxide mineral while Ca formed carbonate and sulfate minerals in sludge[92]. Thus, PO_4^{3-} precipitation

with Ca^{2+} would be impeded if SO_4^{2-} and/or CO_3^{2-} concentration in sludge is high. The relative fraction of major metal ions with affinity of bonding with P such as Ca, Al, and Fe can be altered using chemicals or other wastes. Some of studies on co-HT of SS with chemicals or wastes are summarized in Table 2.8. Majority of these studies reported that P was concentrated mainly in hydrochar, and AP/NAIP fraction in hydrochar depended on prominent metal cation in the additive.

Table 2.8: Some studies on co-HT of SS with other feedstocks published in the last four years.

Sludge type	Sewage treatment	Sludge Pretreatment	Additive	HT condition	Significant findings	Ref.
SS	Sequencial batch reactor	-	Complexation agent (ascorbic acid (AS), citric acid (CA), N, N-bis (carboxymethyl) glutamic acid (GLDA), and EDTA)	HTC	EDTA most effectively facilitated P release to the process water during the hydrothermal treatment of SS, followed by GLDA, CA, and AS. EDTA complexation with Ca, Fe, and Al in SS facilitated P release. Temperature above 160^{o}C led to thermal decomposition of Al and Fe complexes which promoted P precipitation in hydrochar.	[158]
SS	Anaerobic digestion. P precipitated using aluminum dichloride or sodium aluminate	-	$MgCl_2$	HTC	P enrichment in hydrochar and its higher solubility in water, citric acid, and alkaline ammonium citrate due to $MgCl_2$ addition.	[159]
SS	Anaerobic/Anoxic/Oxic (A/A/O)	Dewatering using flocculants (polyacrylamide, polyaluminum chloride and $FeCl_3$)	-	HTC	P enriched in hydrochar due to flocculant addition, which provided metal ions for precipitation of ortho-P.	[160]
SS	-	-	CaO	HTC	High-temperature HTC and CaO addition promoted almost complete conversion of NAIP to AP. Hydroxyapatite ($Ca_5(PO_4)_3OH$) formation was reported via experimental and simulation data.	[161]
SS	-	-	$CaCl_2$	HTC	$CaCl_2$ dosage and higher feedwater pH promoted NAIP to AP conversion.	[162]

					$Ca_3(PO_4)_2$, and $Ca_2P_2O_7$ rather than $Ca_5(PO_4)_3OH$ were main products after HTC.	
SS	A/A/O and poly-aluminum sulfate for chemical P removal	-	$FeCl_3$	HTC	Low pH and high Fe content due to $FeCl_3$ facilitated AP to NAIP conversion during HTC. Around 92% of P in SS recovered as K-struvite after alkaline extraction of P from hydrochar.	[41]
SS	Polymer flocculant	-	K_2CO_3	HTL	Most P (> 90%) concentrated in hydrochar rather than in process water or bio-oil when HTL was conducted with/without catalyst (K_2CO_3). P existed in hydrochar mainly as hydroxyapatite ($Ca_5(PO_4)_3(OH)$).	[133]
SS (PeS + SeS)	Activated sludge process	-	SS mixed with alum sludge at pH ~3 – 4 using HCl	HTC	AP to NAIP conversion promoted by alum sludge in acidic HTC conditions. Low trace elemental extraction during alkaline extraction of P from hydrochar. Optimized conditions for highest alkaline extraction of P from hydrochar identified.	[144]
SS	Biological treatment	-	Cheese whey	HTC	P retention in hydrochar and improved fuel property of hydrochar due to co-HT process. Hydrochar suitable as organic fertilizer despite trace element presence in it.	[163]
SS	Activated sludge process	-	Rice straw, cellulose, lignin, and KOH	HTC	Co-HTC facilitated the formation of Al-P and Fe-P compounds. The use of additives enhanced the bioavailability of P, with lignin proving to be the most effective and cellulose the least effective.	[164]

3. PHOSPHORUS TRANSFORMATION DURING ACIDIC PRETREATMENT OF SEWAGE SLUDGE WITH ALUM SLUDGE AND ITS ALKALINE EXTRACTION

The findings of this chapter have been published as an original research article:

Tiwari, S.B., Hooper, T.J., Veksha, A., Chan, W.P., Fei, X., Liu, W., Lisak, G. and Lim, T.T., 2023. Sequential wet extraction of phosphorus from sewage sludge using alum sludge: reassessing the aluminium-phosphorus speciation using experimental and simulation approach. Chemical Engineering Journal, 459, p.141569. https://doi.org/10.1016/j.cej.2023.141569.

Some minor modifications have been incorporated into the published version to ensure its consistency with this thesis.

3.1. INTRODUCTION

In 2014, the European Commission added phosphate rock to the critical raw material list due to increasing demand (from growing population and food security), lack of alternatives and skewed geographical availability [2]. Sewage sludge (SS) has one of the highest P concentrations among all biomass wastes [1] and hence it is a promising reclaimable source of P. It can be recovered directly from SS or the solid residues of SS thermal treatment (ash and char) using processes such as acidic or alkaline leaching, wet oxidation, thermal hydrolysis, super-critical water oxidation and bioleaching [9]. Acidic leaching of incineration sewage sludge ash (ISSA) for P recovery has been a major research focus in the last two decades. This focus is cogent as developed countries treat SS primarily through incineration [165] and acidic leaching has a high P recovery efficiency (upto 100%). However, toxic trace elements are concomitantly leached during acidic leaching and thus require an additional purification step for P recovery. In alkaline extraction, the leaching of the trace elements can be avoided but has a poor recovery efficiency (<50%) [63]. Consequently, there are fewer studies on alkaline leaching compared to acidic extraction [8,67].

Generally, a low P/Ca molar ratio (<2) leads to a low P recovery because apatite phosphorus (AP) (Ca-P) does not leach in alkaline conditions [8]. Petzet et al. [14] propose SESAL-Phos process in which acid leaching is performed prior to alkaline leaching of ISSA. Acidic leaching promotes AP to non-apatite inorganic phosphorus (NAIP) (such as Al-P and Fe-P) conversion in Al-rich ISSA, eventually leading to high alkaline P recovery. Ca-P dissolution and Al-P precipitate formation during acidic leaching (pH 3-5) in the SESAL-Phos process are elucidated using these representative equations (Eqn.(15)-(17)):

$$Ca_9(Al)(PO_4)_7 + 21HCl \rightarrow 9Ca^{2+} + Al^{3+} + 7H_3PO_4 + 21Cl^- \quad (15)$$

$$6Al(OH)_3 + 18H^+ \rightarrow 6Al^{3+} + 18H_2O \quad (16)$$

$$7Al^{3+} + 7H_3PO_4 \rightarrow 7AlPO_{4\,(s)} + 21H^+ \quad (17)$$

Few other sequential extraction processes achieved high P recovery by promoting AP to NAIP conversion in Al-rich ISSA or char [8]. However, when Al- based coagulant is not used for P removal during wastewater treatment, SS produced might be deficient in Al, thus making these processes unsuitable for P extraction. In general, this dependence on intrinsic SS characteristics impedes wider application of these processes. It is unclear whether an ex-situ addition of Al in SS would promote AP to NAIP conversion via the same mechanism. This uncertainty is because Al-P and Ca-P might not solely exist and interact, as shown in the equations above, since the precipitation-dissolution and adsorption-desorption reactions in the environmental processes are highly complex. This complexity might accentuate during the leaching of dried sludge due to its complex chemical composition compared to ISSA (higher TEs and organic fractions). Currently, most studies on dried SS explored the optimum operational conditions for P recovery and a few have analyzed P conversion during acidic/alkaline extraction (Table 2.6). However, P speciation during dried SS leaching has not been comprehensively studied. Thus, there is an evident research gap.

This study aimed for an enhanced alkaline P recovery from the dried SS by amending it with alum sludge (AS). AS is a waste produced during drinking water treatment with alum coagulation and is mainly composed of $Al(OH)_3$ precipitate. Besides SS, global AS production faces a significant disposal challenge [166,167]. The two-fold objectives of amending SS with AS were: (a)

enriching SS with Al ions and (b) simultaneous processing of two waste streams for dual waste management. There are diverse applications of AS (including for phosphorus removal from wastewater) [167], but to the best of the authors' knowledge, this is the first study on P recovery from AS-amended SS. Five alkaline leaching experiments (with/without acidic pretreatment) of SS (with/without AS amendment) were conducted and the reasons for the highest P recovery among them (amended+pretreated) were investigated. The research questions being addressed were: (1) was an ex-situ Al-source (AS) useful for AP to NAIP conversion in dried SS (2) did acidic pretreatment led to $AlPO_4$ formation (3) did excess Al ions enhance alkaline leaching efficiency without acidic pretreatment. P speciation and the detailed mechanism of P conversion from AP to NAIP were investigated using experimental and theoretical analyses. Especially, Visual MINTEQ was utilised for the simulation of acidic pretreatment process and solid-state nuclear magnetic resonance (SSNMR) for the experimental validation of AP to NAIP conversion. The findings from this study might benefit regions that dispose of dried sludge rather than incinerating it. This includes not just developing countries but developed countries such as the US, where less than 45% of the generated sludge is incinerated [165]. Moreover, many studies on gasification or pyrolysis of SS for P recovery use dry SS as the feedstock. Hence, a study on dry sludge can provide complementary data for comparison, especially because there are fewer studies on P recovery from dried SS than ISSA [67].

3.2. EXPERIMENTAL

3.2.1. Sample collection and processing

Dewatered SS (mix of primary and digestate sludges) was collected from a water reclamation plant (WRP) and dewatered AS was collected from a waterworks in Sept-Oct 2020. In Singapore, WRP treats wastewater from domestic and non-domestic sources, while the waterworks treats water from the surface water reservoirs. Grab sampling was conducted and the collected samples were well preserved in sealed containers and stored in a cold room (below 4°C). Dewatered SS and AS were processed separately before characterisation and experimentation. The sample processing was as follows: the dewatered SS and AS were dried at 50 ^{o}C (should be less than 60 ^{o}C to preserve organic phosphorus compounds [44]) in a drying oven with forced air circulation for at least 24 h.

The drying conditions were suitable for practically removing all the moisture in the samples in this experiment. After drying, the samples were homogenised using a kitchen mixer (Kenwood Prospero) and then crushed to approximately 0.1-0.2 mm using a jaw crusher (Retsch BB50). Finer AS particles were obtained using a ball mill (Retsch PM100) with 5 mm zirconia balls. The samples were homogenised again using the kitchen mixer and sieved to approximately 63-150 µm particle size. Finally, the sieved samples were dried again at 50 ^{o}C for at least 24 h and stored in air-tight plastic bottles for characterisation and experimentation. Henceforth, the samples (SS and AS) would refer to the processed samples, not the as-received dewatered SS and AS, unless otherwise stated.

3.2.2. Sample characterisation

The physico-chemical characterisation of SS and AS was conducted. pH, conductivity, and total dissolved solids were determined using Mettler Toledo SevenGo Duo [168]. Elemental composition (C, H, N, S) was obtained using an elemental analyser (Elementar Vario El cube). Density, moisture content, Ash_{550}, Ash_{950} and higher heating value were determined according to the conventional methods [169]. Inorganic elemental analysis was performed by digesting in a microwave acid digester (Anton Parr Multiwave5000) [170]. Hydrofluoric acid (HF) was utilised for the 'complete' digestion of recalcitrant silicate and organic phosphorus compounds. The digestate and leachate samples were analysed using Inductively Coupled Plasma-Optical Emission Spectroscopy (ICP-OES) (Perkin Elmer Optima 8300 OES) for the quantification of major inorganic elements and Inductively Coupled Plasma-Mass Spectrometry (ICP-MS) (Thermo Fisher iCAP QC) for trace inorganic elements. Orthophosphate (ortho-P) concentration in the digestate and leachate samples was determined using Ion Chromatography (IC) (Dionex Aquion) [25]. Most studies in the literature use the molybdenum blue method for ortho-P quantification, which is prone to ionic interferences and relatively cumbersome, unlike the IC [25].

The leachate samples were filtered using 0.45 µm and 0.22 µm PVDF/PTFE filters prior to the analysis. Blank, blank spiked and matrix spiked samples were used to monitor the percent recovery in the IC, ICP-OES and ICP-MS analysis. In most cases, the percent recovery of analytes ranged from 90-110%, well within the acceptable limit for environmental samples [25]. The

concentration of analytes was reported as mg/kg (dry basis). The sample characterisation, microwave acid digestion, leaching experiments and the Standards Measurements and Testing (SMT) analysis were conducted at least in triplicate.

3.2.3. Experimental plan

The experimental plan is illustrated in Figure 3.1. SS and AS were mixed in a 3:2 ratio (w/w), resulting in an approximate P:Al molar ratio of 1:3 in the mixed sludge sample, which is hereafter referred to as M3. Trial experiments were conducted to verify if 1:3 molar ratio was sufficient for AP to NAIP conversion without significantly diluting P concentration in the mixture (as P concentration in AS is relatively low). The sample weight and leachant volume for all the processes are specified in Table S 3. Processes A and B represent the reference cases for non-pretreated and acid-pretreated SS, respectively. Process C was performed to observe the effect of solid Al on alkaline leaching; Process D was to investigate the effect of acidic pretreatment on alkaline P leaching due to AP to NAIP conversion. Process E was conducted to evaluate if the aqueous Al ion was more effective in alkaline P leaching than Al in solid form (as in Process C). Though various P species might exist in the leachate samples, only free ortho-P concentration was determined as it can be utilised for salt precipitation such as struvite and subsequent fertilizer production.

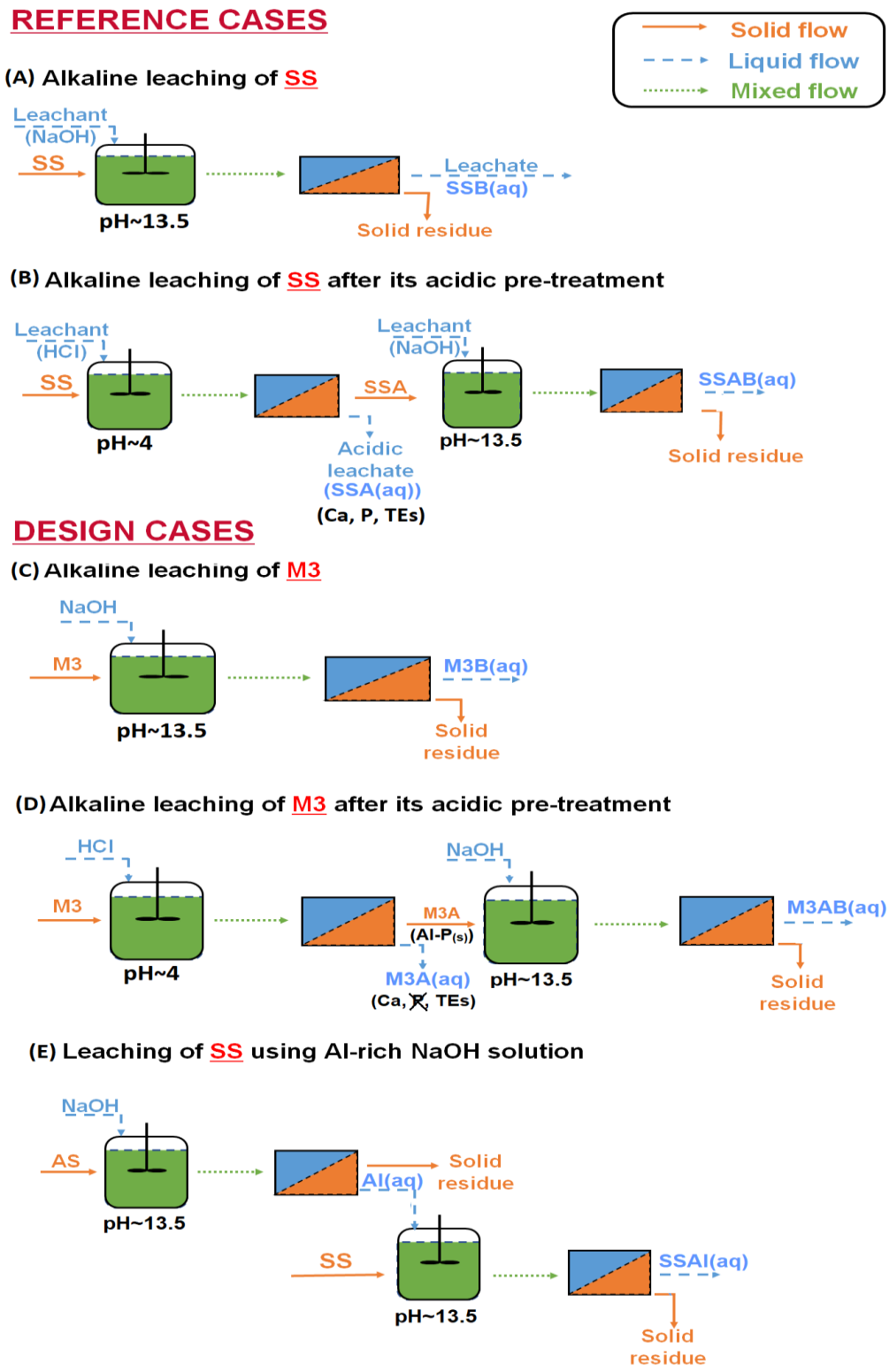

Figure 3.1: Experimental plan showing reference cases and design cases. The design cases involve alum sludge (AS) as an amendment in the leaching process. M3 represents the sewage sludge (SS) and AS mixture in the ratio of 3:2 (w/w) and TEs means the trace elements. The notation system for the relevant solid and liquid samples is also indicated.

3.2.3.1. Experimental procedure

SS and M3 were subjected to acidic pretreatment before alkaline leaching in Processes B and D (Figure 3.1). 0.4 g of sample was mixed with 40 mL of deionized (DI) water in a 50 mL centrifuge tube. Then, 10-20 µL of 6 M HCl was added dropwise using a 100 µL pipette to reduce the pH of the mixture to 3.5-4. Precise pH control is essential at the start of pretreatment to promote AP to NAIP conversion. A pH range of 3-4 is also recommended to reduce the concentration of interfering ions [9]. The mixture was agitated overnight (16 h) and centrifuged (Kubota 3700) for phase separation. Acidic leachate was filtered and analysed as explained above (Section 3.2.2). The solid residue was dried at 50 ^{o}C in a drying oven with forced air circulation for at least 24 h. The dried sample was crushed into powder and used for alkaline P leaching.

In Process E, an Al-rich alkaline solution (Al(aq)) was prepared by adding AS to 1 M NaOH at a 250:1 liquid-to-solid (L:S) ratio (mL/g) and the mixture was agitated overnight. Subsequently, the mixture was centrifuged to obtain the leachate, which was filtered for further use. This L:S ratio was selected to keep the liquid (ml):AS (g) ratio the same in Processes C and E. For alkaline leaching in all the processes, non-pretreated/pretreated SS or M3 was mixed with 1 M NaOH or Al-rich solution in 100:1 mL/g L:S and agitated for 16 h (overnight). The mixture was centrifuged and obtained leached was filtered before the analysis.

3.2.3.2. Calculation of phosphorus loss and recovery during the experiment

The ortho-P loss due to acidic pretreatment (Processes B and D, Figure 3.1) was calculated using (Eqn.(18)):

$$Loss = \frac{PO_{4\,(HCl)}^{3-}}{PO_{4\,(total)}^{3-}} \times 100\% \qquad (18)$$

where $PO_4^{3-}{}_{(HCl)}$ represents the PO_4^{3-} (ortho-P) concentration in acidic leachate of SS or M3 (Processes B and D). These leachates are represented as SSA(aq) and M3A(aq) in Figure 3.1. $PO_4^{3-}{}_{(total)}$ is the total PO_4^{3-} in SS or M3, as determined from the digestate of SS and AS and SS:AS mixture.

Process Recovery (PR) of PO_4^{3-} was calculated using (Eqn.(19)):

$$Process\ Recovery\ (PR) = \frac{PO_{4\,(NaOH)}^{3-}}{PO_{4\,(total)}^{3-}} \times 100\% \qquad (19)$$

where $PO_4^{3-}{}_{(NaOH)}$ represents PO_4^{3-} concentration in alkaline leachate (*i.e.*, SSB(aq), SSAB(aq), M3B(aq), M3AB(aq) or SSAl(aq), Figure 3.1).

Effective Recovery (ER) of PO_4^{3-} was calculated using the equation below account for the ortho-P loss during acidic pretreatment (Eqn.(20)):

$$Effective\ Recovery\ (ER) = \frac{PO_{4\ (NaOH)}^{3-}}{PO_{4\ (total)}^{3-} - PO_{4\ (HCl)}^{3-}} \times 100\% \qquad (20)$$

3.2.4. Other analytical techniques

SMT protocol [44,171] was conducted to operationally determine NAIP, AP, organic phosphorus (OP), inorganic phosphorus (IP) and total phosphorus (TP) in SS, SSA and M3A samples to observe the variation in P species before and after acidic pretreatment. SMT analysis was not performed on M3 due to the likely interference of excess Al ions in the sample. The concentrations of various P species in M3 are calculated using the values obtained for SS and mass balance. Speciation of P, Al and Ca during acidic pretreatment of SS and M3 was performed using Visual MINTEQ (VMINTEQ) version 3.1 [172]. The method proposed by Benjamin [173] was applied in VMINTEQ to quantify the dissolution and precipitation of various species. Owing to the complexity and heterogeneity of environmental samples, only PO_4^{3-}, Al^{3+} and Ca^{2+} concentration (Table 3.1) in SS and M3 was considered for the idealised modelling.

Solid state nuclear magnetic resonance (SSNMR) analyses of the non-pretreated and acid-pretreated sludges were performed using a Bruker Avance III HD 600 MHz (14.1 T) spectrometer with a Bruker 1.9 mm HXY magic angle spinning (MAS) probe. ^{31}P (ν_0 = 242.96 MHz), ^{27}Al (ν_0 = 156.39 MHz) and ^{1}H (ν_0 = 600.18) MHz single pulse analysis at a MAS frequency of 24 kHz was conducted with recycle delays of 180 s, 0.5 s and 5 s respectively. ^{31}P-^{1}H cross-polarisation (CP) 2D heteronuclear correlation (CP-HETCOR) analysis at a MAS frequency of 15 kHz was also conducted. High-power proton decoupling was employed during all ^{31}P NMR acquisitions. All spectra were processed using the Topspin software package and referenced to the unified scale using IUPAC recommended frequency ratios relative to the ^{13}C adamantane(s) methylene resonance (δ = 37.77 ppm) [174,175]. Spectral deconvolution was performed with Dmfit [176]. ^{31}P liquid-state NMR (LSNMR) of SS extract and leachate samples were performed on JEOL ECA400. A conventional extraction method was adopted [41] with some modifications to obtain SS extract. 0.8 g of dry SS

was mixed with 40 mL 0.05 M EDTA in a glass beaker using a magnetic stirrer at 100 rpm for 1 h. Thereafter, it was centrifuged, and the solid residue was mixed with 40 mL 0.25 M NaOH. After overnight agitation, the mixture was centrifuged, and the supernatant was lyophilised in a freeze dryer (CHRiST ALPHA 1-4 LD plus) for about two days. The freeze-dried sample was mixed with 2 mL 0.25 M NaOH and centrifuged to obtain the extract. 760 µL extract and 240 µL D_2O were transferred in a 5 mm NMR tube for ^{31}P LSNMR analysis. The spectrometer was operated at 162 MHz with 90˚ pulse, 32678 data points, 104 scans, 5 s relaxation delay and 1.62 s acquisition time. P species in the acidic (SSA(aq), M3A(aq)) and the alkaline (SSB(aq), SSAB(aq), M3AB(aq)) leachate were also determined using ^{31}P LSNMR. About 40 mL leachate was mixed with 40 mL 0.05 M EDTA at 100 rpm for 1 h using a magnetic stirrer. After that, the mix was filtered using a 0.45 µm PVDF filter and the filtrate was lyophilised. Post-lyophilisation steps were the same as above. All the samples were analysed as soon as possible to avoid hydrolysis of P species [27] and an external reference (85% H_3PO_4, δ=0 ppm) was used for precise peak identification.

Scanning electron microscopy with energy-dispersive X-ray spectroscopy (SEM-EDS) and SEM mapping was performed on JEOL JSM-7200F FESEM. X-ray photoelectron spectroscopy (XPS) was conducted on an AXIS Supra spectrometer (Kratos Analytical) operated at 5 mA using a monochromatic Al K-alpha source. Peaks were referenced using adventitious carbon, C 1s (284.8 eV). Samples for the SEM mapping and XPS were dried at 80 ^oC for four days to remove volatiles and moisture. X-ray diffraction (XRD) (PANalytical X'Pert PRO) analysis was conducted on sludge samples (SS, SSA, M3, M3A) to probe crystalline phases before and after the acidic pretreatment. The operational parameters were as follows: Cu Kα radiation (λ=1.54 Å) at 40 kV and 30 mA, with a step size of 0.1˚, step time of 100 s and $10^\circ < 2\theta < 80^\circ$ in Bragg-Brentanno geometry. Fourier transform infrared (FTIR) spectroscopy (Shimadzu IRPrestige-21) was performed on the same samples in attenuated total reflection (ATR) mode.

3.3. RESULTS AND DISCUSSION

The physico-chemical characterisation and major elements in the sludge samples are summarised in Table 3.1. The concentrations of trace elements are

listed in Table S 4. The P/Ca molar ratio in SS is low and hence alkaline leaching is challenging without any process modification.

Table 3.1: Physico-chemical characteristics of sludge samples.

Parameter	Sewage sludge (SS)	Alum sludge (AS)
Moisture content (%) *	85.9±0.21	66.2±0.1
pH	6.5±0.0	7.3±0.0
Dry density (g/mL)	0.9±0.1	0.6±0.0
Conductivity (mS/cm)	6.4±0.0	1.6±0.0
Total dissolved solids (g/L)	3.2±0.0	0.8±0.0
Ash_{550} (%)	23.5±2.8	59.7±0.6
Ash_{950} (%)	28.2±1.0	31.7±7.4
Higher heating value (J/g)	16527±387	ND
Carbon (%)	39.1±0.4	9.8±0.0
Nitrogen (%)	6.3±0.0	1.0±0.0
Hydrogen (%)	6.2±0.3	4.0±0.2
Silicon (%)	3.7±0.2	5.1±0.1
Phosphorus (PO_4-P) (%)	2.6±0.1	<0.5
Calcium (%)	2.4±0.2	0.5±0.0
Sulphur (%)	1.2±0.1	1.6±0.2
Magnesium (%)	1.5±0.1	<0.5
Iron (%)	1.2±0.1	1.6±0.1
Aluminium (%)	0.9±0.1	17.4±0.8

* As-received dewatered sludge samples.

ND: Not determined.

3.3.1. Effect of acidic pretreatment

SS and M3 sludge samples were subjected to acidic leaching (Figure 3.1, Processes B and D). The pH at the start and end of acidic pretreatment for SS is 3.8±0.2 and 4.8±0.2, respectively. For M3, it is 3.7±0.2 and 5.3±0.4 at the start and end, respectively. A higher pH shift for M3 indicates a higher H^+ consumption while leaching M3 than SS due to higher $Al(OH)_3$ concentration ($Al(OH)_3+3H^+ \rightarrow Al^{3+}+3H_2O$) [64,69].

Ca and Mg are found prominently in acidic leachate, their concentrations being 12862±870 and 8749±70 mg/kg, respectively in SSA(aq) and 9037±877 and 5484±164 mg/kg, respectively in M3A(aq). Ca and Mg losses through acidic leachate are 54% and 58% for SS, respectively, and 55% and 61% for M3, respectively. These results are in agreement with other studies that found high Ca and Mg leaching in acidic conditions [14,39,69]. XRD data (Figure 3.2) shows that struvite in SS and M3 is lost prominently during acidic pretreatment. No Ca-containing crystalline phases are observed in SS; hence, the dissolution of Ca phases cannot be inferred from the XRD spectra.

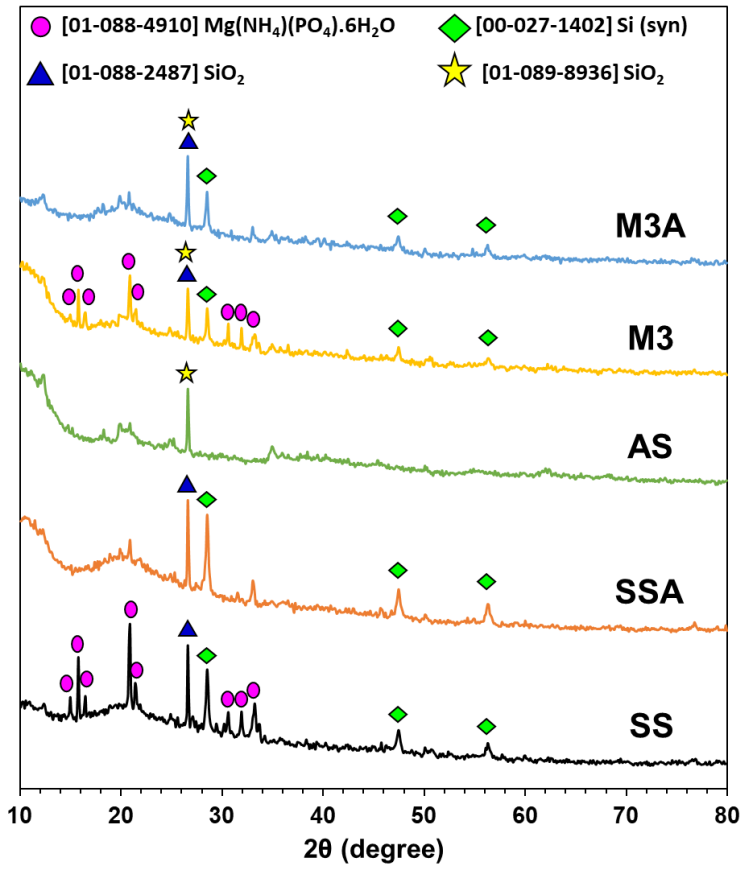

Figure 3.2: XRD spectra of non-pretreated (sewage sludge (SS), alum sludge (AS) and M3) and acid-pretreated SS (SSA) and M3 (M3A) sludges. M3 represents SS and AS mixture in the ratio of 3:2 (w/w).

Most importantly, there is negligible leaching of P when Al is abundantly available (*i.e.*, in M3) (Figure 3.3). The ortho-P loss through acidic leachate in Process B is significant (63%) compared to Process D, where ortho-P loss (4%) is inconsequential. Probably, excess Al in M3 is associated with the ortho-P released by the dissolution of Ca-P (indicating AP to NAIP conversion). Due to the selective leaching of Ca, the P/Ca molar ratio improved in M3A compared to

SS or M3. Though H_2SO_4 performed better than HCl or HNO_3 for acid leaching [65,68] and did not influence Al-P precipitation, it was not used in this study because of probable precipitation of $CaSO_4$ [8]. The P/Ca molar ratio would have remained unaltered due to $CaSO_4$ precipitation, which would have affected alkaline P leaching detrimentally.

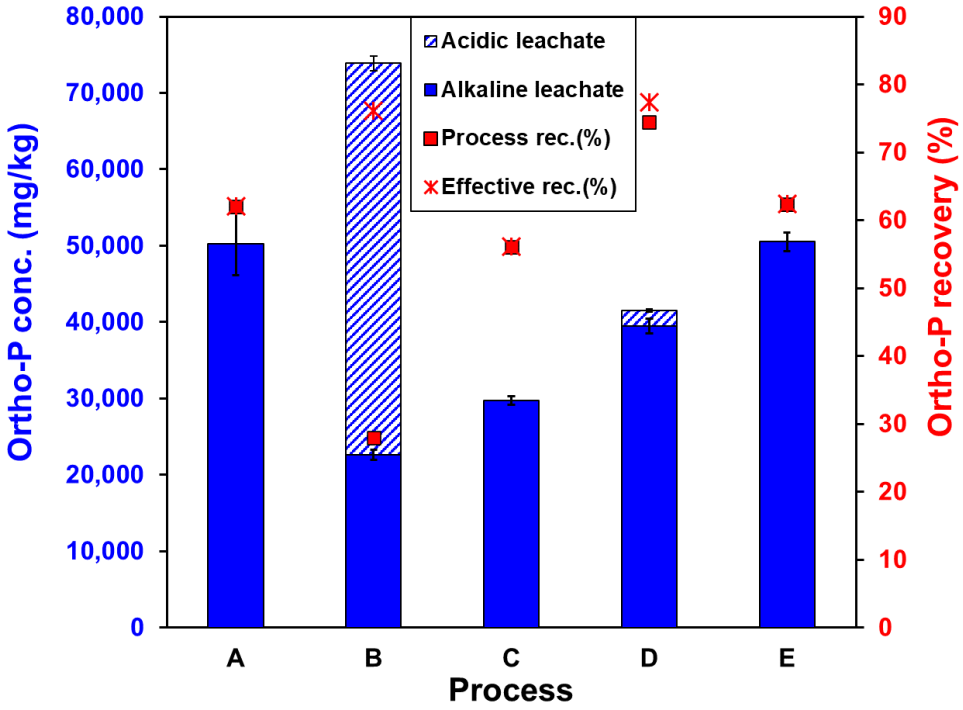

Figure 3.3: Ortho-P concentration in acidic and alkaline leachates and ortho-P recovery (process or effective) obtained in all the processes. The error bar represents the standard deviation.

SEM-EDS and SEM mapping also broadly corroborate the findings in this section (Figure 3.4). Al-P association in SS (Figure 3.4 (a)-(ii) and (a)-(iii)) and M3 (Figure 3.4 (c)-(ii) and (c)-(iii)) seems weak as they have a different spatial pattern. The spatial pattern association for Ca-P is visible in M3 (lump at the centre top, Figure 3.4 (c)-(ii) and (c)-(iv)) but not in SS, SSA or M3A. Nevertheless, a tangible association of P with Al after the acidic pretreatment is apparent (prominently in SS), indicating enrichment of Al-P after the acidic pretreatment (Figure 3.4 (b/d)-(ii) and (b/d)-(iii)). The concentrations of trace elements in acidic leachate (SSA(aq) and M3A(aq)) were below the detection limit for most of the elements (Table S 5). The data revealed that at around pH 4, most trace elements were bound to the solid residue. Also, the dissolution pattern of trace elements for SSA(aq) and M3A(aq) was similar.

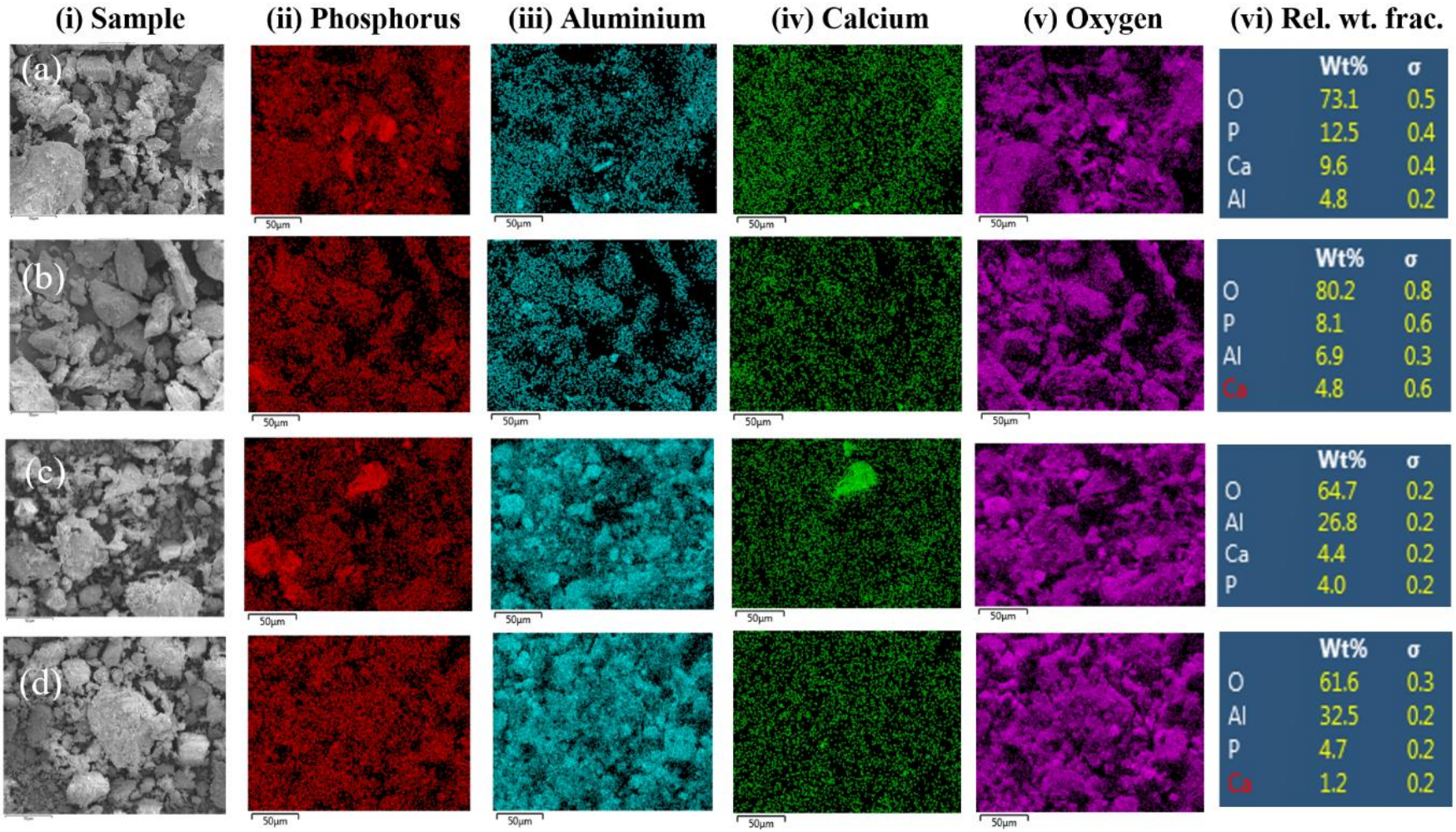

Figure 3.4: SEM mapping of sludge samples: (a) sewage sludge (SS) (b) acid-pretreated SS (SSA) (c) M3 (d) acid-pretreated M3 (M3A). M3 represents SS and alum sludge (AS) mixture in the ratio 3:2 (w/w). The relative weight fraction (%) of each element along with the standard deviation obtained using SEM-EDS is also presented (Ca in SSA and M3A has a concentration below the detection limit of the instrument). All the images are at 5000 times magnification.

FTIR analysis indicates various functional groups in the sludge samples before and after the acidic pretreatment (Figure 3.5). In environmental samples, a single peak can correspond to multiple functional groups; hence, an unambiguous peak determination is difficult. However, the information available from the literature is useful for qualitative assessment. In this study, the acidic pretreatment did not lead to any dramatic variation in the functional groups in SS and M3. The broad peak near 3300 cm^{-1} corresponds to the -OH stretching vibration for H-bonded alcohols and phenols. Two sharp but small peaks between 3000-2800 cm^{-1} represent vibration of aliphatic -CH_2-. Notably, these peaks are missing in AS, indicating a paucity of organic content. The stretching vibration of aromatic groups, C=O or C=C, is shown as a peak near 1650 cm^{-1}, which is also found in AS but with a broad peak. The bending vibration of N-H (primary, secondary amines and amides) is represented by a peak near 1550 cm^{-1} while that of aliphatic -CH_2 is at around 1450 cm^{-1}. These two peaks are missing in AS. There is a small peak at around 1230 cm^{-1} corresponding to the bending vibration of C-N, while a prominent peak for the inorganic functional groups in phosphates, silicates, sulphates and clay minerals near 1000 cm^{-1}. AS also has a small peak close to 1100cm^{-1} that might correspond to the stretching vibration of aromatic C-O [169,177,178]. Overall, it is clear that the functional groups did not play any significant role in the ortho-P adsorption during the acidic pretreatment.

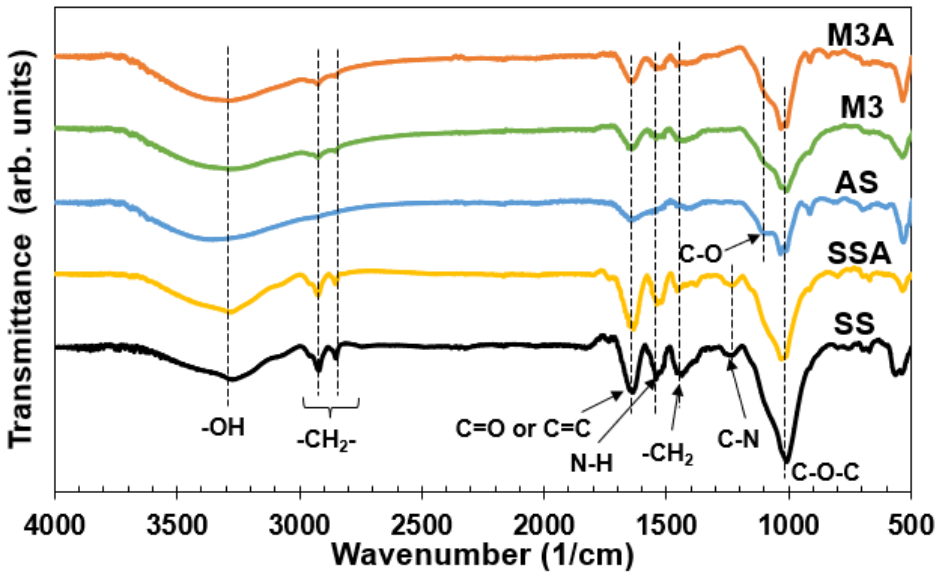

Figure 3.5: FTIR spectra of non-pretreated (sewage sludge (SS), alum sludge (AS) and M3) and acid-pretreated SS (SSA) and M3 (M3A) sludges. M3 represents the SS and AS mixture in the ratio 3:2 (w/w).

3.3.2. Phosphorus leaching in all the processes

The ortho-P concentration in acidic and alkaline leachate, PR and ER in all the processes are shown in Figure 3.3. Process D has the highest PR and ER (74% and 77%, respectively). Process B has the lowest PR (28%) but the second-highest ER (76%). A similar ortho-P recovery for Processes A, C and E indicate that the addition of Al in the solid or aqueous phase had a minor effect on P recovery. PR for Process C is lower than Process A, possibly due to some hydroxyl ion consumption by $Al(OH)_3$ ($Al(OH)_{3(s)}+OH^- \rightarrow AlO_2^- + 2H_2O$), thus sparing a lesser OH^- fraction for P dissolution. A higher ER of Processes D and B compared to the other Processes highlights that a higher alkaline P recovery is achieved after acidic pretreatment (possibly due to AP to NAIP conversion). Ali and Kim [39] also found higher recovery efficiency for sequential leaching compared to acid/ alkaline leaching and a significant role of Al in P dissolution. However, they have not investigated the reasons for this increased efficiency for sequential leaching. They postulated that P leaching in sequential extraction might be higher due to greater ionic dissolution using HCl than NaOH. Xu et al. [35] attributed the dissolution of $AlPO_4$ and $Al(OH)_3$ at high pH in NAIP-rich (64% of total P) excess sludge to the recovery of P. However, they did not characterise Al species directly; hence, conclusive evidence of $AlPO_4$ presence is missing. AP to NAIP conversion was also cited as a significant reason for high alkaline P recovery from the waste activated sludge [33,36].

It is suggested that alkaline P leaching would be more effective if in-situ Al content in SS is high (*i.e.*, Al-based coagulant is used for sewage treatment) [14]. This experiment shows that the addition of AS significantly ameliorates the challenge of alkaline leaching of AP in SS. Thus, AS-amended alkaline leaching might be useful for P recovery irrespective of the sewage treatment process or intrinsic properties of SS. NAIP is unstable in a wide pH range [36], thus offering an operational advantage of alkaline P recovery compared to acidic P recovery. However, there are techno-economic challenges (and opportunities) which are briefly discussed in Section 3.3.6.

3.3.3. Chemical equilibrium modelling of acidic pretreatment using Visual MINTEQ

Aqueous P concentration can be determined by the precipitation-dissolution and sorption-desorption effects of various chemical species in the

sludge matrix. Precipitation-dissolution of chemical species depends on pH, temperature, alkalinity, concentration and types (mono/multidentate) of ligands, metal ion types (valency) and concentration, particle size and system turbulence. Both kinetics and equilibrium influence precipitation; hence merely considering the solubility product (K_{sp}) can be erroneous. For instance, calcium phosphate ($Ca_3(PO_4)_{2(s)}$, $\log K_{sp}$=-28.92) is generally formed in natural waters (metastable equilibrium) owing to the slow formation kinetics of hydroxyapatite ($Ca_5(PO_4)_3OH$, $\log K_{sp}$=-58.33) and fluorapatite ($Ca_5(PO_4)_3F$, $\log K_{sp}$=-59.5) (true equilibrium) [179]. Hence, $Ca_3(PO_4)_{2(s)}$ is the controlling solid, which determines the concentration of other species in the aqueous and solid phases. Ca-P and Al-P solids commonly formed in natural waters are $Ca_3(PO_4)_{2(s)}$ and $AlPO_4 \cdot 1.5H_2O_{(s)}$ ($\log K_{sp}$= -20.46, from VMINTEQ) [179] and hence considered controlling solids in this modelling. In AS, Al^{3+} primarily exists as $Al(OH)_{3(s)}$ since alum reacts with alkalinity during water treatment [180] (Eqn.(21)):

$$Al_2(SO_4)_3 \cdot 14H_2O + 6HCO_3^- \leftrightarrow 2Al(OH)_3 \cdot 3H_2O(s) + 6\ CO_2 + 8H_2O + 3SO_4^{2-} \quad (21)$$

However, coagulation has rather complex chemistry and the state and speciation of Al are not well-known [180]. In this study, $Al(OH)_{3(soil)}$ is the controlling solid based on saturation index (= logIAP - $\log K_{sp}$, where IAP is ion activity product) calculated by VMINTEQ.

Modelling results indicate that in SSA(aq), more than 80% ortho-P exists as $H_2PO_4^-$ at pH less than 6 (Figure 3.6 (a)). The high abundance of $H_2PO_4^-$ is expected since, for pH<pK_{a2} (7.21), $H_2PO_4^-$ predominates in the ionisation equilibrium of H_3PO_4. In M3A (aq.), $H_2PO_4^-$ is the predominant ortho-P specie but with a significant concentration reduction in the 4<pH<5 range due to complexation with Al^{3+} (Figure 3.6 (c)). The complexation effect decreases with a higher pH due to the precipitation of $Al(OH)_{3(s)}$. There was no $AlPO_4$ precipitation (Figure 3.6 (b,d) and in both SSA(aq) and M3A(aq), ortho-P should have existed in aqueous form. However, experimental data reveal high aqueous ortho-P in SSA(aq) but not in M3A(aq) (Figure 3.3). Ca existed solely as Ca^{2+} in both cases for 3<pH<7 and contributed negligibly to the complexation and precipitation of ortho-P. Thus, the low ortho-P in M3A(aq) could be due to the adsorption of ortho-P on $Al(OH)_{3(s)}$ flocs [179] and consequent removal from the aqueous phase. $AlPO_4$ has a very low $K_{sp,}$ but ortho-P concentration has to be

sufficiently high in a solution for $AlPO_{4(s)}$ precipitation; otherwise, Al^{3+} would combine with the dissociation product of the solvent (*i.e.*, OH^-, in this case) [181]. Besides, $Al(OH)_{3(s)}$ has a high sorptive affinity for ortho, condensed and organic phosphates [181] and charge neutralisation and adsorption-bridging could be a plausible mechanism for adsorption [182].

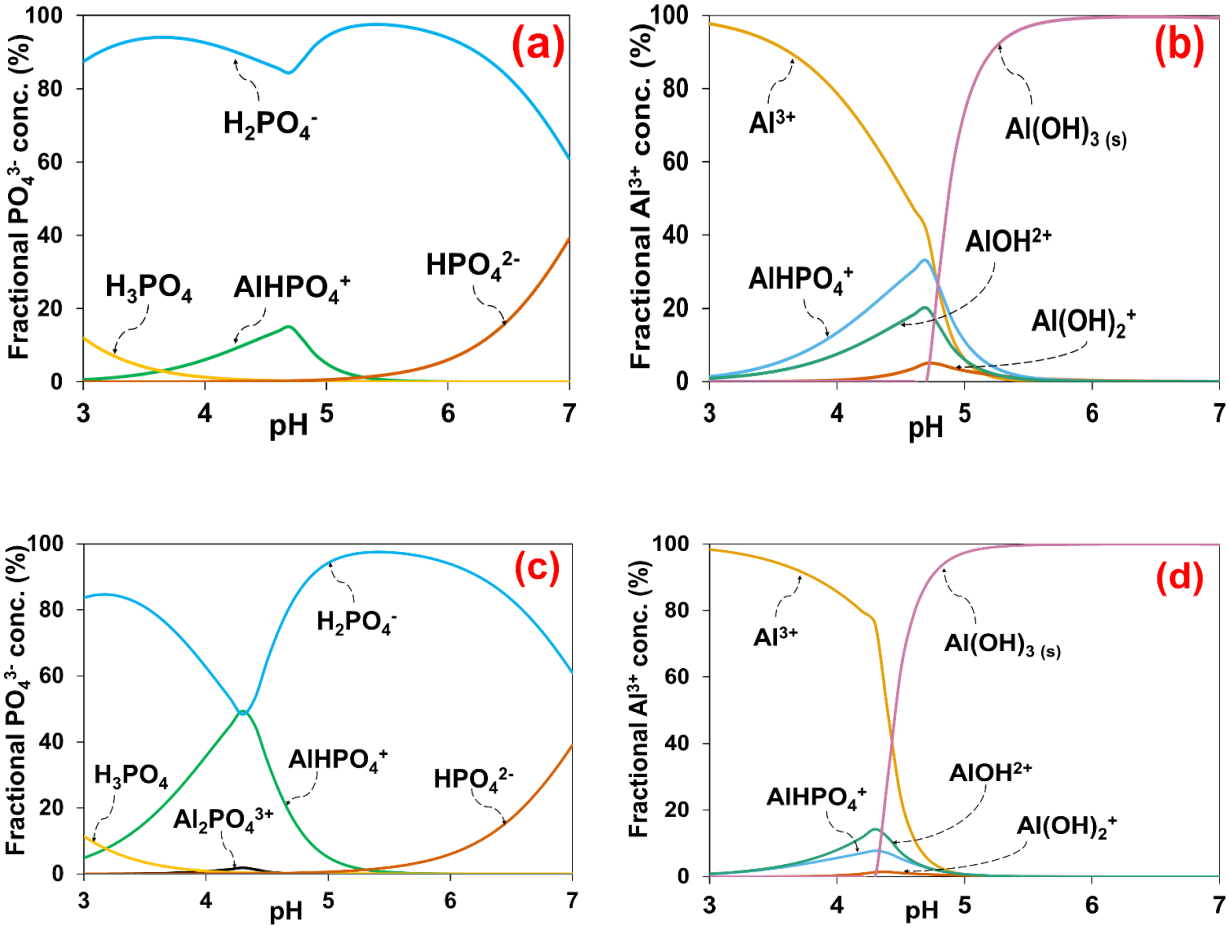

Figure 3.6: Simulated speciation of P and Al during acidic pretreatment of (a, b) sewage sludge (SS) and (c, d) M3. Speciation of Ca is not presented as it existed solely as Ca^{2+} in the 3<pH<7 range. M3 represents SS and alum sludge (AS) mixture in the ratio of 3:2 (w/w). Visual MINTEQ utilized for chemical equilibrium modeling.

$Al(OH)_{3(s)}$ floc formation starts at pH 4.8 during acidic pretreatment of SS, while it starts at pH 4.4 for M3 due to high Al enrichment in M3 (Figure 3.6 (b,d)). In both cases, pretreatment pH at the start and end were around 4 and 5, respectively. However, $Al(OH)_{3(s)}$ floc concentration was very high during and at the end of the pretreatment of M3. Modelling estimates that $Al(OH)_{3(s)}$ in the M3 acidic pretreatment mixture was 28 times higher than in SS at the end of acidic pretreatment. The Al XPS spectra of M3 before and after pretreatment indicate

no shift in peak (Figure S 1), thus suggesting no formation of $AlPO_4$ after acidic pretreatment. This Al $2p_{3/2}$ peak (74.8 eV) corresponds to $Al(OH)_3$ (though other Al oxides and hydroxide peaks have a statistical overlap) [183]. SSNMR data further corroborates the presence of $Al(OH)_{3(s)}$ in M3A and the adsorption of ortho-P on it (Section 3.3.5.1). Adsorbed ortho-P is released when $Al(OH)_{3(s)}$ dissolves in alkaline conditions forming $Al(OH)_4^-$ soluble complex.

3.3.4. SMT analysis of samples

SMT analysis was conducted to verify the conversion of AP (Ca-P) to NAIP (mainly Al-P in this case) in SS and M3 (Figure 3.7) due to acidic pretreatment. Though NAIP represents P bound to Al, Fe and Mn oxyhydrates [184], Al-P fraction in NAIP would predominate due to excess Al ions in M3. The analysis revealed negligible OP variation in SS and M3 before and after acidic pretreatment.

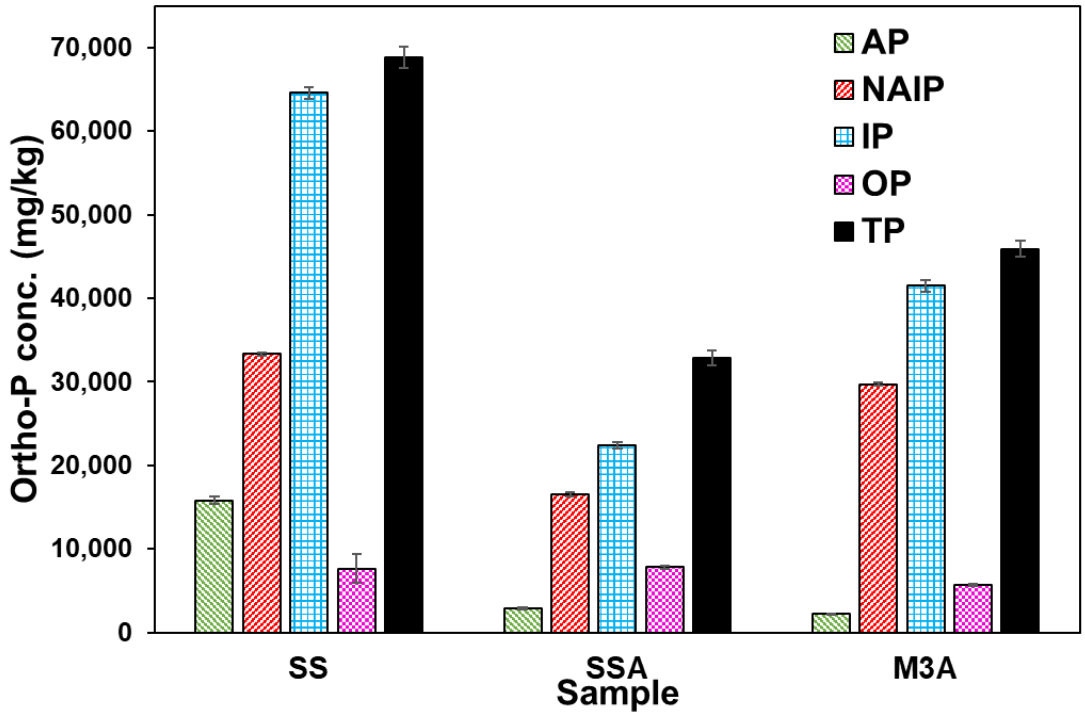

Figure 3.7: SMT analysis of sewage sludge (SS), acid-pretreated SS (SSA) and M3 (M3A) sludges. M3 represents SS and alum sludge (AS) mixture in the ratio of 3:2 (w/w). Phosphorus species are organic phosphorus (OP), apatite phosphorus (AP), non-apatite inorganic phosphorus (NAIP), inorganic phosphorus (IP) and total phosphorus (TP). The error bar represents the standard deviation.

The consistent OP concentration indicates that acidic hydrolysis is ineffective for the disintegration of OP to IP. A significant reduction of AP in the samples after pretreatment indicates a loss of Ca-P at low pH. This loss of Ca-P is also corroborated by Ca concentrations in SSA(aq) and M3A(aq). The AP loss is 81% for SS and 77% for M3. Interestingly, after acidic pretreatment, there is a 50% loss of NAIP for SSA (compared to SS) but a 49% increase for M3A (compared to M3), indicating the transformation of AP in M3 to NAIP in M3A. According to SMT protocol, AP+NAIP is equal to IP, but this was not the case in the present study. Another study found a similar inconsistency [185], possibly because the SMT protocol is a semi-quantitative technique prone to sample composition variation [32]. Hence, SMT analysis in this study operationally determined P speciation and other analytical techniques were used to validate the transformation of Ca-P to Al-P.

3.3.5. Solid and liquid NMR analysis

The major findings from SSNMR and LSNMR are illustrated in a simplified schematic (Figure 3.8), while the detailed analysis is elaborated in the subsequent sections.

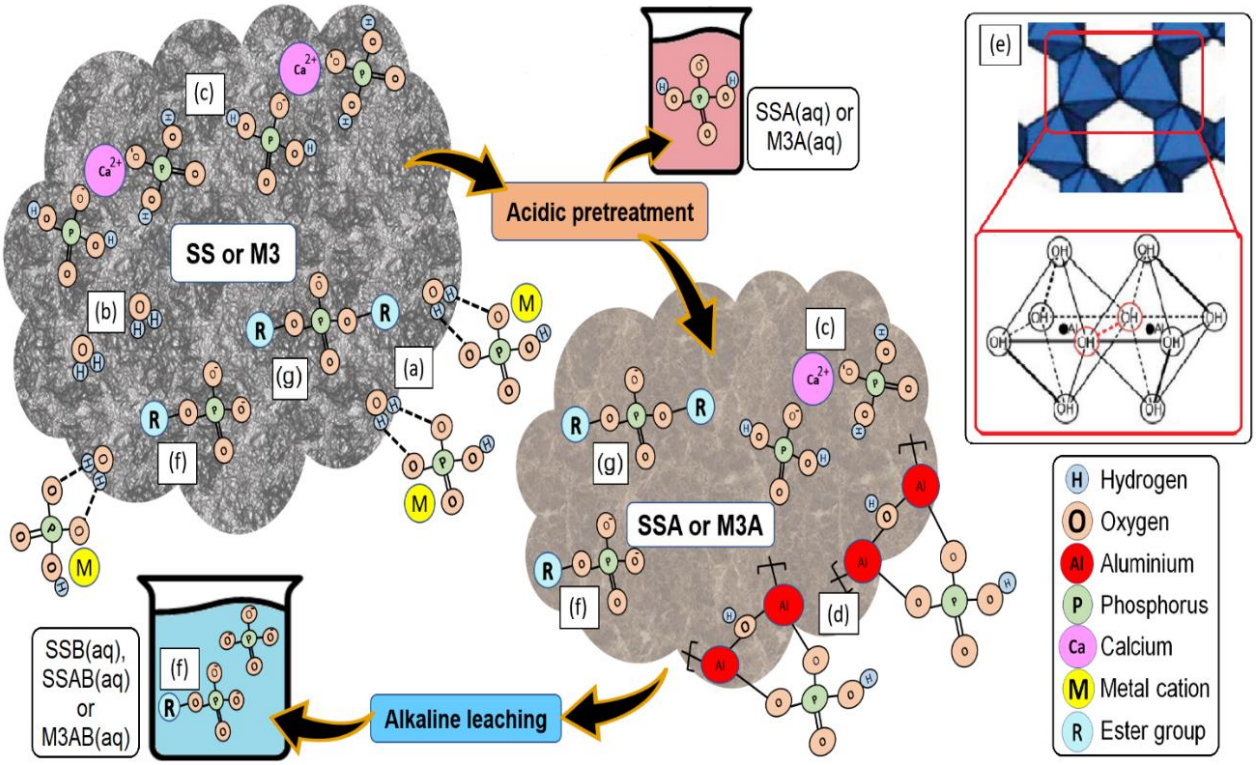

Figure 3.8: A simplified schematic illustrating P speciation during acidic pretreatment and alkaline leaching based on the data obtained from SSNMR and LSNMR. (a) inorganic ortho-P bound to the water of hydration via hydrogen

bonds in the organic matrix (b) water of hydration or adsorbed water inside the organic matrix (c) amorphous calcium phosphate (d) binuclear bidentate inner-sphere surface complexation of ortho-P on aluminium hydroxide (e) AlO_6 coordination structure of $Al(OH)_3$ (in each octahedron, six OH^- surround one Al^{3+} and each OH^- is common between the two adjoining octahedrons, thus the chemical formula $Al(OH)_3$) (f) ortho-P monoester (g) ortho-P diester. This schematic is not to scale.

3.3.5.1. Solid-state NMR (SSNMR) of sludge samples

The ^{31}P chemical shifts are dependent on the electronegativity, charge and radius of the next-nearest-neighbour cation [186]. Generally, the chemical shift anisotropy for ^{31}P NMR spectra has a linear relationship with P-O bond length and deviation in O-P-O bond angle in PO_4 [186]. Prior studies have reported the chemical shifts for cations of phosphate salts such as Al, Mg, Ca, Na, K and NH_4 [187]. The ^{31}P MAS NMR spectra of the non-pretreated (SS and M3) and acid-pretreated (SSA and M3A) sludges are presented in Figure 3.9, while the fitting parameters and determined relative integrals are given in Table S 6. Phosphorus concentration in AS was too small to detect and hence not reported in this section. Both SS and M3 spectra have a sharp resonance at 6.2 ppm and a broader resonance at around 2 ppm. SS and M3 have the same ^{31}P chemical shifts since P in M3 is sourced from SS. The resonance at 6.2 ppm might represent the inorganic HPO_4^{2-} anions bound to the physically adsorbed water through a hydrogen bond inside the organic matrix (Figure 3.8 (a, b)) [187]. The broader resonance might encompass amorphous Ca ortho-P (3-2 ppm) (Figure 3.8 (c)) [187] or protonated phosphates of ammonia (such as $NH_4H_2PO_4$ or $(NH_4)_2HPO_4$) [186]. Since apatite phosphorus is corroborated by SMT analysis, this peak predominantly corresponds to Ca-P. However, some fraction of ammonium phosphate might be present as SS is generally rich in ammonia. Sodium and potassium phosphates (such as $Na_4P_2O_7$, $Na_7P_5O_{16}$ and $K_4P_2O_7$) are unlikely to be present even though their chemical shifts are observed at around 1 ppm [188]. These compounds are highly soluble and less likely to precipitate when less soluble Ca, Fe and Mg phosphates can be formed [187].

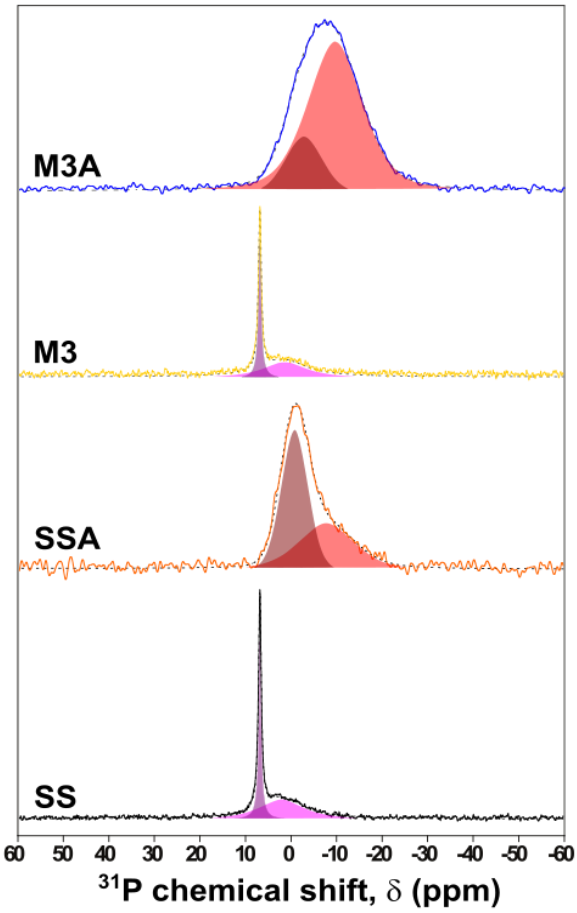

Figure 3.9: ^{31}P MAS NMR spectra of non-pretreated (sewage sludge (SS) and M3) and acid-pretreated SS (SSA) and M3 (M3A) sludge samples. M3 represents SS and alum sludge (AS) mixture in the ratio of 3:2 (w/w). Experimental spectra, simulated spectra and deconvoluted resonances are shown in solid line, dotted line and multicolor, respectively. The spectrum for AS is not shown as it had negligible P, hence a poor signal-to-noise ratio.

Acidic pretreatment strips phosphates from SS, with SSA containing 17% of the initial phosphorous concentration. The remaining phosphorus is represented by broad resonances at -1 and -8 ppm. In comparison, M3A retains 87% of the phosphorous concentration of M3, represented by similar broad resonances at -3 and -9 ppm. The P loss data of SSNMR and IC in this experiment are inconsistent due to differences in the analytical technique. Nevertheless, data from both instruments indicate a similar scale of P loss in SSA and M3A.

A sharp peak at 6 ppm is not present in SSA or M3A due to the removal of adsorbed water by acidic pretreatment. This removal is verified by the reduction of adsorbed water resonance in the ^{1}H spectrum (7 ppm, Figure S 2) [187]. As validated by SMT analysis, no signal remains at 2 ppm since a large fraction of Ca-P is removed. The higher frequency broad resonance at -2 ppm in

SSA and M3A might be protonated ortho-P adsorbed onto $Al(OH)_3$ [189]. This peak could also correspond to calcium or magnesium orthophosphate (such as $Ca(H_2PO_4)_2$ and $Mg_3(PO_4)_2$) [188,190]. Despite a significant loss during acidic pretreatment, 30-40% of Ca and Mg are retained in SSA and M3A. Since SSA and M3A have a high compositional heterogeneity (including OP and paramagnetic nuclei) and are acidified, it is difficult to assign the chemical shifts accurately. For both SSNMR and LSNMR, P peaks shift upfield (more negative) at a decreasing pH [187,189]. SSA and M3A also have a peak around -9 ppm; consistent with the ^{27}Al NMR, this might be amorphous $Al(OH)_2H_2PO_4$ or PO_4^{3-} adsorbed on $Al(OH)_3$ or both [187,189]. Thus, probably amorphous Al-P is present in SSA and M3A, with a larger proportion present in the latter, corresponding to more available Al. If $AlPO_4$ was present, a lower frequency resonance (around -30 ppm) would be expected [191].

The absence of this peak implies that acidic pretreatment eliminated apatite phosphate but could not promote the formation of $AlPO_4$. $Al(OH)_3$ is relatively unreactive, especially at about pH 5-6 [189,192] and the adsorption reaction seems much more plausible than the formation of $AlPO_4$ (contrary to the chemical equations in Section 3.1). The chemical equilibrium modelling data (Section 3.3.3) also indicate the abundance of $Al(OH)_3$ after pH 5. Nevertheless, adsorption onto $Al(OH)_{3(s)}$ is not the only reaction between aluminium and ortho-P, as some $Al(OH)_2H_2PO_4$ formation is evident. In acidic conditions (pH 3.5-6), surface complexation can proceed through ligand exchange, *i.e.*, ortho-P replacing surface -OH group in $Al(OH)_3$ and forming bidentate binuclear inner-sphere surface complexes (Figure 3.8 (d)) [189,193]. Overall, it is evident that adsorption and surface complexation dominate over the direct precipitation in the Al-P interaction in this study. Nevertheless, $AlPO_4$ formation is possible depending on the operational conditions and the concentrations of ortho-P and aluminium. The succeeding discussion provides further evidence regarding the mechanism explained above.

The ^{27}Al MAS NMR spectra of the sludge samples are presented in Figure 3.10, while the determined relative integrals are given in Table S 7. AS presents a dominant AlO_6 resonance, assigned as $Al(OH)_3$ (Figure 3.8 (e)), with smaller AlO_5 and AlO_4 resonances. SS has a low Al concentration (4% of AS), which is AlO_6 dominated with a smaller AlO_4 resonance. ^{27}Al spectrum of M3 is similar

to AS, with the lower frequency SS AlO_4 resonance (58 ppm) just visible. M3A spectrum is almost identical to the M3 spectrum, but an increased intensity in the low-frequency shoulder of the AlO_6 resonance (5 to -15 ppm) can be seen. This resonance could correspond to $Al(OH)_2H_2PO_4$ formation, which has been shown to have an AlO_6 resonance at a lower frequency than $Al(OH)_3$ [189]. However, the majority of the Al remains as $Al(OH)_3$. Al 2p XPS spectra of M3 and M3A also indicate negligible variation in the Al environment (Figure S 1). $AlPO_4$ contains tetrahedral Al, so the absence of an increased AlO_4 region confirms that it did not form. The ^{27}Al spectra of SS and SSA are almost identical, indicating a negligible change in the Al environment in SS after pretreatment. Al 2p XPS spectra of SS and SSA are not presented due to a poor signal-to-noise ratio.

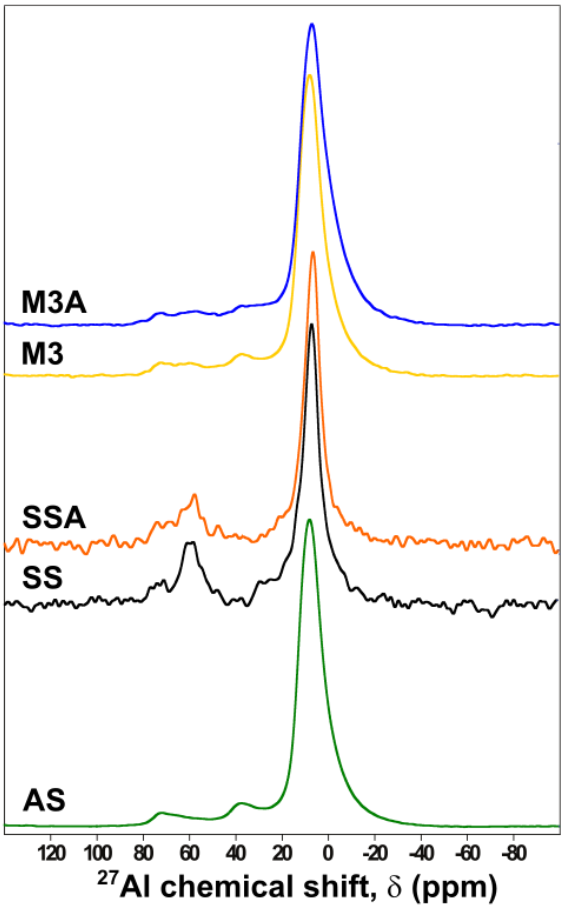

Figure 3.10: ^{27}Al MAS NMR spectra of non-pretreated (sewage sludge (SS), alum sludge (AS) and M3) and acid-pretreated SS (SSA) and M3 (M3A) sludge samples. M3 represents SS and AS mixture in the ratio of 3:2 (w/w).

The ^{31}P-^{1}H CP-HETCOR MAS NMR spectra of the sludges after acidic pretreatment are presented in Figure 3.11. This experiment shows resonances for ^{31}P and ^{1}H nuclei that are spatially close. The 2D spectrum of SS shows a

dominant environment at δ(^{31}P) = 6 ppm correlated to δ(^{1}H) = 7 ppm, which correlates to HPO_4^{2-}/$H_2PO_4^-$ anions [187,194]. However, SSA and M3A show a correlation to δ(^{1}H) = 4 ppm, which is related to $Al(OH)_3$. ^{1}H spectrum of AS shows $Al(OH)_3$ is represented by a broad resonance centred around 4 ppm (Figure S 2). SS inset also reveals a correlation between δ(^{31}P) = -1 ppm and δ(^{1}H) = 4 ppm, revealing some portion of PO_4^{3-} on $Al(OH)_3$ in SS [195]. Thus, the data from SSA and M3A corroborate that phosphates exist in hydrogenated environments. Notably, the functional groups do not affect the changes in P adsorption since there is no variation in functional groups during acidic pretreatment (Figure 3.5). Overall, the analysis in this section broadly concurs with the chemical equilibrium modelling data, elemental composition, XPS and SMT analysis.

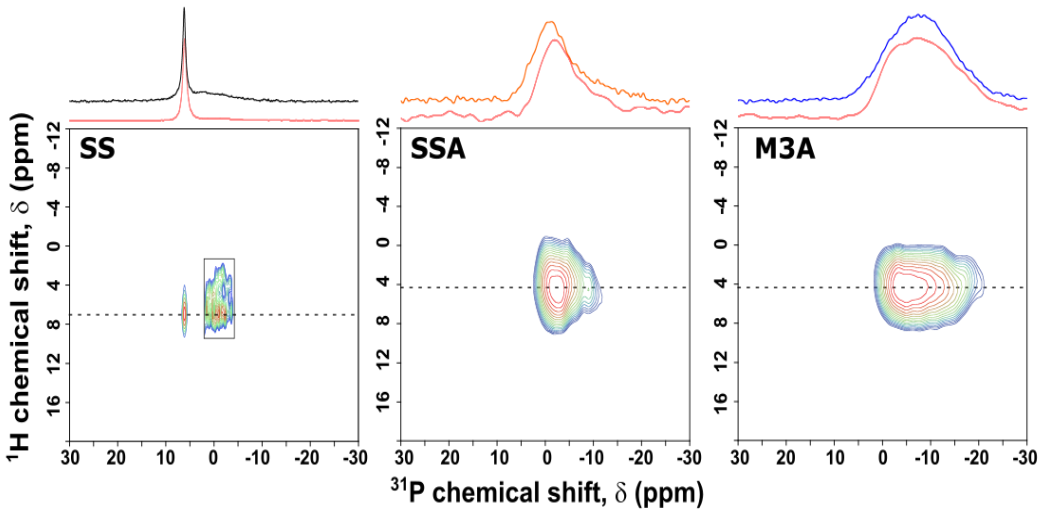

Figure 3.11: ^{31}P-^{1}H CP-HETCOR MAS NMR spectra of the sewage sludge (SS) and acid-pretreated SS (SSA) and M3 (M3A). M3 represents SS and alum sludge (AS) mixture in the ratio of 3:2 (w/w). The ^{31}P(^{1}H) CP projection is presented on the top axis in red, alongside the ^{31}P MAS NMR spectra.

3.3.5.2. Liquid-state NMR (LSNMR) of SS and leachate samples

Liquid NMR analysis was conducted to identify P species in SS and leachate samples (Figure 3.12). In this experiment, peaks were found within -1 to 8 ppm, though peaks of interest can range from -25 to 25 ppm in environmental samples [51,196]. In SS extract, ortho-P was prominently observed (6.5 ppm), but ortho-P monoester (including nucleotides, sugar phosphates and inositol phosphate) (5 to 6 ppm) (Figure 3.8 (f)) and ortho-P diester (such as phospholipids, DNA and ribonucleic acid (RNA)) (-0.2 ppm) (Figure 3.8 (g)) were also detected [27,51,196]. No polyphosphates were observed in SS,

probably due to their hydrolysis during the anaerobic digestion [88]. The proportion of inorganic ortho-P is much higher than organic phosphate (monoester and diester), concurring with SMT analysis. Although, liquid NMR should be preferably used for qualitative determination of OP because it is recalcitrant to solubilization [27].

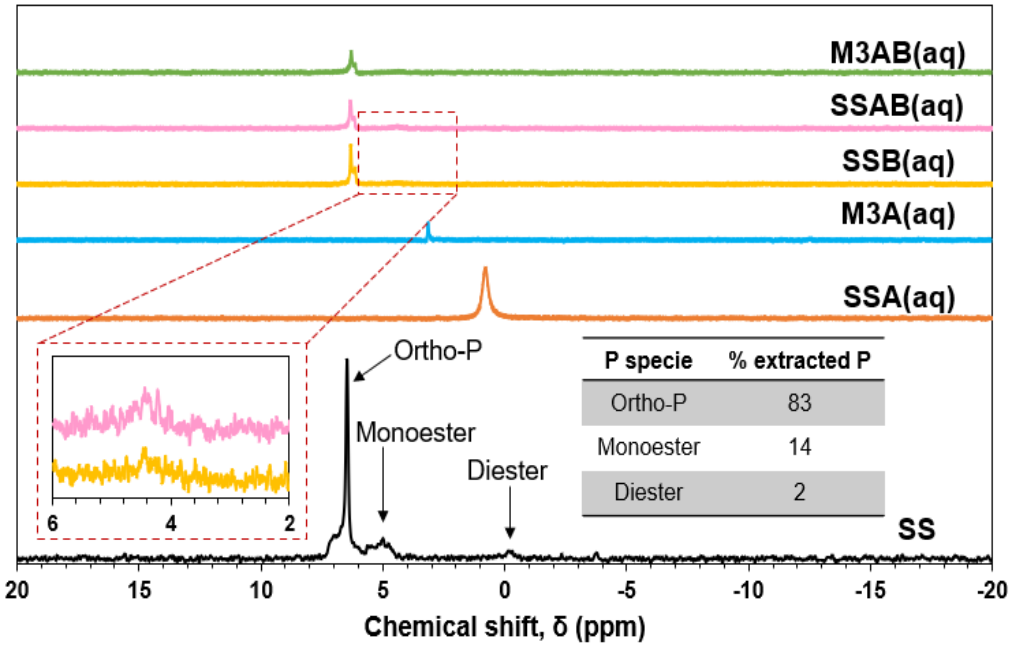

Figure 3.12: ^{31}P liquid-state NMR (LSNMR) of sewage sludge (SS) and leachate samples. The ortho-P peak shows a rightward shift at the reduced pH of the samples (*i.e.*, SSA(aq) and M3A(aq)).

P species in leachate samples were also determined, especially to observe OP dissolution. The dissolution of OP depends on both the operational conditions and OP species. Temperature and pH are essential parameters influencing acidic/alkaline hydrolysis of OP [61]. Also, compared to the ester (P-OCH_3) and anhydrite (P-O-P) bonds in OP compounds, the P-C bond is more recalcitrant to disintegration [61]. The absence of OP peaks in acidic leachates indicates that OP did not hydrolyse at pH 3-4. The chemical shifts of ortho-P in acidic leachates, SSA(aq) (0.8 ppm) and M3A(aq) (3.2 ppm) were more upfield (*i.e.*, more negative) than in alkaline leachate. Some other studies have reported a similar finding [88,197] because the chemical shift depends on the protonated forms of ortho-P, which in turn depend on the pH of the sample [51].

Alkaline leachates have similar spectra with a prominent ortho-P peak around 6.3 ppm. SSB(aq) and SSAB(aq) also have an ortho-P monoester peak just visible at around 4.4 ppm. This small ortho-P monoester peak can be

attributed to ortho-P monoester in SS or due to hydrolysis of ortho-P diester into ortho-P monester at high pH [198] or both. Interestingly, the ortho-P monoester peak is missing in the case of M3AB(aq), which might indicate the disintegration of some OP in the presence of excess Al. Possibly, some OP precipitated with $Al(OH)_3$ during acidic pretreatment, which eventually disintegrated during alkaline leaching. Lin and Li [199] found that alkaline pretreatment of Al-flocculated sewage sludge led to the dissolution of sludge flocs as well as organic compounds, as postulated below (Eqn.(22)):

$$HO\text{-}Al\text{-}PO_4\cdots\cdots Organic + OH^- \rightarrow AlO_2^- + PO_4^{3-} + Organic \qquad (22)$$

3.3.6. Techno-economic feasibility

This study was a "proof-of-concept" experiment and hence the operational parameters were chosen to minimize ambiguity in hypothesis testing. For instance, HCl was preferred over H_2SO_4 even though HCl is costlier since $CaSO_4$ might precipitate during acidic pretreatment (thus keeping the P/Ca molar ratio unaltered) [14,200]. Similarly, NaOH was preferred for alkaline P solubilization as it has an efficiency higher than $Ca(OH)_2$, albeit with a higher cost [71,201]. Nevertheless, a simplified cost assessment was conducted in this study to identify critical materials and operations influencing the viability of the proposed process for P recovery. Nättorp et al. [202] assessed nine P recovery processes (pilot and industrial) and quantified cost-benefit in the German context. The material cost of the process proposed in this study was compared with two processes in Nättorp et al. (Gifhorn and Stuttgart processes), which used digested sludge for P recovery as struvite. Assuming ~1.5% average inflation in Germany [203] after the publication of Nättorp et al., the material cost for these two processes would be ~7 USD/kg P currently. For the most efficient recovery process (Process D, 74% P recovery) in this study, the weight of the reagent required (Table S 3) and the weight of P recovered were calculated. Reagent prices vary regionally and seasonally, and currently, industrial grade HCl (31-37% w/w) is priced at ~40-140 USD/MT [204] and industrial grade NaOH (99% w/w) is priced at ~500-1000 USD/MT [205,206]. Thus, the cost for acidic pretreatment (HCl) would be ~0.07-0.23 USD/kg P, while it would be ~105-210 USD/kg P for alkaline leaching (NaOH) (refer Table 3.2). Besides, if the recovered P in the alkaline leachate is utilised for struvite precipitation, there would be an additional cost of $MgCl_2.6H_2O$ (~200-600 USD/MT) [207,208] and NH_4Cl (~100-500 USD/MT)

[209]. This implies an additional cost of ~1.5-5 USD/kg P for struvite production assuming Mg:N:P ratio requirement of 1:1:1 (refer Table 3.3). Thus, cost reduction would be necessary for the economic viability of this process.

Table 3.2: Cost incurred for leaching per kg of dry SS to recover P using the sequential extraction process.

Category	Acid leaching	Alkaline leaching
Sample wt. (kg)	1	1
Acid vol(L)	100	100
Conc. (M)	0.0015-0.003	0.4
P extraction (%)	NA	74
P content (%)	NA	2.6
P extracted (kg)	NA	0.02
Reagent molar wt. (g)	36.5	40
Reagent wt. (kg)	0.01	2
Reagent purity (w/w)	0.34	1
Reagent wt.(kg) (commercial)	0.03	1.62
Reagent cost (USD/kg) (min.)	0.04	0.5
Reagent cost (USD/kg) (max.)	0.14	1
Reagent cost (USD/kg P) (min.)	0.07	42
Reagent cost (USD/kg P) (max.)	0.23	84

NA: Not applicable

Table 3.3: Cost calculation for struvite precipitation from recovered P in this study.

Category	Value
$MgCl_2.6H_2O$ cost (USD/kg) (min)	0.2
$MgCl_2.6H_2O$ (USD/kg) (max)	0.6
$MgCl_2.6H_2O$ purity (w/w)	0.99
NH_4Cl (99%, USD/kg) (min)	0.1
NH_4Cl (99%, USD/kg) (min)	0.5
NH_4Cl purity (w/w)	1.00
$MgCl_2.6H_2O$ mol. wt. (g)	203.3
NH_4Cl mol. wt. (g)	53.5
Mg:N:P molar ratio in struvite	01:01:01
$MgCl_2.6H_2O$ needed (kg/kg P)	6.6
NH_4Cl needed (kg/kg P)	1.7
$MgCl_2.6H_2O$ cost (USD/kg P) (min)	1.3
$MgCl_2.6H_2O$ cost (USD/kg P) (max)	4.0
NH_4Cl cost (USD/kg P) (min)	0.2
NH_4Cl cost (USD/kg P) (max)	0.9

Apparently, there is a significant scope for cost reduction in this process, especially for alkaline leaching, which is a major cost contributor. For instance, ~0.4 M (instead of 1 M) NaOH can be utilized for alkaline leaching since P recovery is minimally affected by concentration beyond 0.4 M [67]. Simultaneously, the L:S ratio during alkaline leaching can be reduced from 100:1 to 10:1, albeit with a reduced P recovery. However, if the P fraction in SS is high (~4-5%), high P recovery can compensate for a slightly reduced recovery efficiency. Alternatively, alkaline leachate can be reused for multiple leaching cycles [210]. For instance, in Gifu, Japan, NaOH is recycled during alkaline leaching of P from ISSA in full-scale WRP [16]. NaOH can also be retrieved from alkaline leachate by precipitating Ca-P using lime and removing Al using precipitation or ion exchange [63]. This Al can be utilised as a precipitant in wastewater treatment [14]. Thus, Al from AS can be recovered along with P from SS, affording resource recovery from two waste streams. AS has a high disposal cost and its management is a serious nuisance [167].

There are proven commercial technologies for both acidic and alkaline leaching of P from waste streams [211] though P recovery efficiency is a concern. Given the price volatility of phosphate rock in the world market, unviable P recovery techniques might be feasible in the future [1]. In 2022, the price of diammonium phosphate (DAP) reached a record high of ~ 900 USD/MT [212], similar to the price in 2008 when it increased by almost 800% in a short duration [1]. A competitive P recovery scenario will spur investment in relevant technologies and promote research and development in this sector. Thus, future studies can explore the material and cost optimisation for the process proposed in this study and other promising approaches for P recovery.

3.4. CONCLUSION

This study demonstrates that high phosphorus recovery from dried sewage sludge (SS) is possible with suitable modifications in the feedstock and the leaching process. The highest orthophosphate (ortho-P) recovery is 74% for amended and acid-pretreated SS (due to the conversion of apatite to non-apatite phosphorus). This conversion prohibits the loss of P during acidic pretreatment and enhances the P/Ca molar ratio and, consequently, alkaline P leaching. Visual MINTEQ and solid-state NMR results indicate that ortho-P is adsorbed on $Al(OH)_3$ during acidic pretreatment rather than $AlPO_4$ formation from free ortho-

P and Al ion. Thus, the ionic concentration and operational parameters play a curial role in P speciation and recovery. The engineered approach in this study offers a dual waste management strategy and might make alkaline leaching feasible for SS with a low P/Ca molar ratio. However, there is a scope for further improvement in the proposed process. The solid residue after alkaline leaching would require processing for the removal/stabilisation of toxic trace elements, persistent organic pollutants and pathogens. With further refinements, the process might be technologically feasible and financially viable, thus realising the goal of decentralised P production and a circular economy.

4. SYNERGIZING PYROLYSIS AND ACIDIC PRETREATMENT OF SEWAGE SLUDGE WITH ALUM SLUDGE FOR PHOSPHORUS RECOVERY

The findings of this chapter have been published as an original research article:

Tiwari, S.B., Chin, S.Y., Veksha, A., Chan, W.P., Fei, X., Lisak, G., Liu, W. and Lim, T.T., 2024. Synergistic application of alum sludge and sequential extraction for phosphorus recovery from sewage sludge char. Chemical Engineering Journal, 481, p.148574. https://doi.org/10.1016/j.cej.2024.148574.

Some minor modifications have been incorporated into the published version to ensure its consistency with this thesis.

4.1. INTRODUCTION

Sewage sludge (SS) is a prospective source of reclaimable phosphorus (P) since it has one of the highest P concentrations among biomass wastes[1]. Among various approaches to P recovery from SS[1,9], acidic extraction of P from incineration SS ash (ISSA) has been a major research focus in the last two decades. The reason for this focus is high P content in ISSA (average 8% - comparable to medium phosphate deposits)[11] and potentially high P recovery efficiency during acidic extraction (> 80%)[8]. However, in acidic extraction, there is simultaneous extraction of toxic heavy metals/trace elements, necessitating an additional purification step before final P recovery[91]. Also, researchers are investigating alternatives to incineration, such as pyrolysis, gasification, and hydrothermal treatment for waste mass/volume reduction and stabilization, carbon sequestration, and biofuel recovery. SS pyrolysis can be utilized for P recovery since SS char is also rich in P (3-6%)[83]. However, the studies on P recovery from SS pyrolysis char are few[80]. P-related studies on SS pyrolysis have mainly focused on P speciation and transformation during pyrolysis and applying SS char as fertilizer[83]. Recent studies have focused on promoting non-apatite inorganic phosphorus (NAIP) (mainly aluminum

phosphates (Al-P)) to apatite phosphorus (AP) (mainly calcium phosphates (Ca-P)) conversion using Ca additives during SS pyrolysis[89–91,93,98,105,213] as AP is more bioavailable than NAIP[91]. Thus, the modified SS char is more beneficial for soil conditioning. However, plausible soil contamination due to TEs in SS char hinders its wider acceptance as a soil conditioner. Organic and emerging contaminants might also be present in SS char[214] (though some studies suggest their high removal efficiency (> 95% to > 99%) during pyrolysis[215]).

Thus, P recovery via its wet extraction from SS char seems more promising currently. The simultaneous TE extraction during wet P recovery can be largely avoided in alkaline extraction as TEs precipitate in alkaline conditions. But alkaline P extraction has a lower P extraction efficiency (< 50%)[8] due to precipitation of AP. Some studies suggested using $FeCl_3$ and Fenton's reagent for P transformation and its recovery in alkaline/neutral conditions[41,104]. Our previous study demonstrated that high alkaline P recovery (> 70%) from dry SS is possible if it is suitably amended (i.e., SS is mixed with alum sludge (AS) and then subjected to acidic wet extraction/pretreatment (pH 3-4) to get amended SS)[12]. SS amendment promoted AP to NAIP conversion, which enhanced alkaline P recovery, as NAIP readily dissolves in an alkali. AS is a waste by-product from water treatment plants; thus, the additional cost of SS amendment using pure chemicals can be avoided for P recovery. Additionally, Al from AS can be recovered simultaneously with P during alkaline extraction. This Al can be recovered as $Al(OH)_3$ or poly-aluminum chloride coagulant[216]. However, it remains unclear if similar/higher alkaline P recovery efficiency can be achieved from the char produced using amended SS. If achieved, investigating P transformation due to the combined effect of SS amendment and pyrolytic conditions might be interesting and insightful.

Thus, this study aimed to assess an alternative SS pyrolysis process for P recovery and the detailed investigation of P speciation to explain the improved P recovery efficiency. In this study, speciation means the "distribution of an element amongst defined chemical species in a system"[217]. SS was first amended (i.e., by mixing it with AS and then acidic pretreatment of their mixture) and then pyrolyzed at three different temperatures (400, 600, and 900˚C), and alkaline P recovery from chars was conducted. The critical research questions

being addressed in this study are (i) the effect of SS amendment and pyrolysis on alkaline P recovery, (ii) P speciation due to pyrolysis temperature and relative abundance of other major ions such as Al and Ca, and (iii) Al and C speciation and its effect on alkaline P extraction. Al and C were characterized due to their abundance in the sample and likely influence on P speciation and recovery. Various characterization techniques have been employed to ascertain these species quantitatively/qualitatively (such as NMR, XPS, XRD, and FTIR). To the best of authors' knowledge, this is the first study on co-treatment of SS and AS for enhanced P recovery using alkaline extraction. This study is a step towards simultaneous management of two waste streams and make alkaline P extraction more attractive for commercial application (irrespective of SS chemical composition).

4.2. MATERIALS AND METHODS

This study consisted of a reference (or baseline) process and a design process (Figure 4.1). The experimental details are explained in the subsequent sections. Dewatered SS and dewatered AS were collected from wastewater and water treatment plants in Singapore, respectively. Dewatered SS (DSS) was a mixture of primary and secondary sludges from domestic and non-domestic wastewater treatment. Dewatered AS was obtained after surface water treatment using alum as a coagulant.

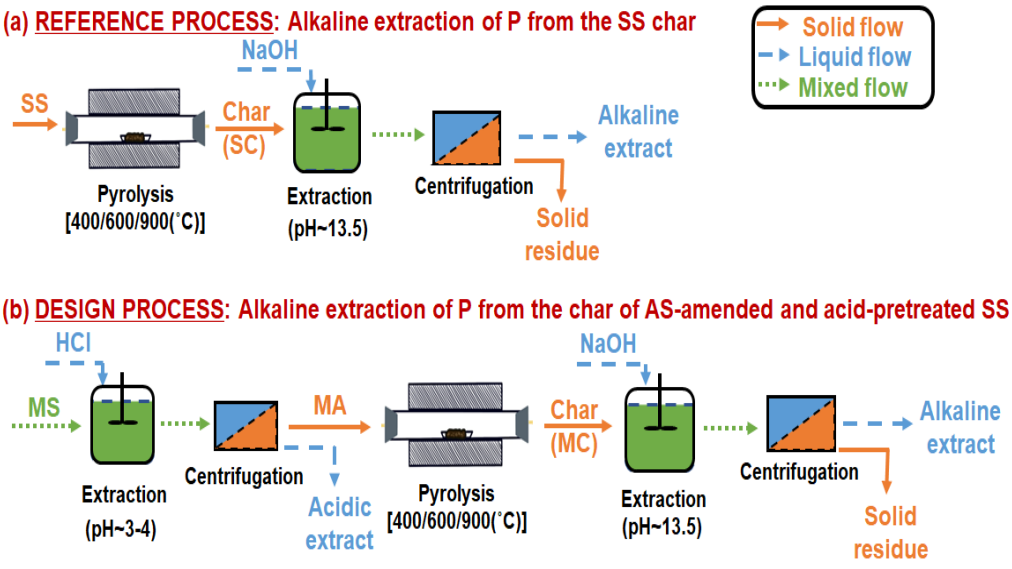

Figure 4.1: Experimental schematic of this study showing (a) reference and (b) design processes. Dewatered sewage sludge (DSS) and alum sludge (AS) were mixed in a ratio of 4:1 (w/w) to obtain MS before acidic pretreatment in the design process. The sample notation in this study is also indicated.

4.2.1. Sample preparation and acidic pretreatment

For the reference process (Figure 4.1), dewatered SS was dried and pulverized before pyrolysis. For the design process, dewatered AS was dried and pulverized to fine dry powder as in the previous study[12] (henceforth labeled AS) for amending SS. The amendment of SS (Figure 4.1) is as follows: DSS was mixed with AS in a 4:1 (w/w) ratio (resulting in an Al:P molar ratio of ~ 3:1 in the mixed sludge (MS)), and deionized (DI) water was added for homogeneous mixing using a magnetic stirrer. Al:P molar ratio of 3:1 was same as the previous study where this value was found optimum for AP to NAIP conversion[12]. Subsequently, the pH of MS was adjusted close to 3 using 6 M HCl and extraction was conducted for 1-2 h. Thereafter, the solid was separated, dried, and pulverized before pyrolysis. This amended SS was referred to as MA ("mixed sludge-acidified"). An optimization study was conducted to identify the optimum pH for acidic pretreatment. The pH at the start of acidic pretreatment of dewatered sewage sludge (DSS), and DSS + alum sludge (AS) (i.e., MS) was set at 1, 3, 5, and ~7 (no HCl added) in four distinct sets and extracted for 2 h to identify the most optimum pH for acidic pretreatment. The illustrative calculations for mixing DSS + AS + DI water + HCl (6 M) are shown in Table S 8. Subsequently, the mixture was centrifuged, the extract was filtered, and major inorganic elements in the acidic extracts were quantified using ICPOES.

In this study (unless stated otherwise), the solid-liquid separation was performed via centrifugation (Kubota 3700), wet solids were dried at 105˚C for at least 24 h, and liquid samples were filtered using 0.20/0.22/0.45 µm PTFE/PVDF syringe filters. Dried solid samples were pulverized using a kitchen blender or a ball mill (Retsch PM100) to particle size < 150 µm. All solid samples were kept in airtight containers and desiccators. The solid-liquid extraction was performed using a rotary agitator. A two-way analysis of variance (ANOVA) with replication ($\alpha = 0.05$) was performed to test the significance of the pyrolysis feedstock and pyrolysis temperature on the mean P recovered (mg/kg and % recovered). The normality and homoscedasticity assumptions were verified using the Shapiro-Wilk (SW) and Levene's tests ($\alpha = 0.05$), respectively. Data was also checked for possible outliers. Tukey's HSD (honestly significant difference) test ($\alpha = 0.05$) was applied as a post-hoc method. The analysis was conducted using

the Real Statistics tool pack[218] for Microsoft Excel. For extraction optimization results, two-way ANOVA ($\alpha = 0.05$) without replication (using mean of replicates) was conducted. Readers should note that the experiment was not completely randomized and that general cautions of statistical interpretation associated with a small sample size should be considered.

4.2.2. Pyrolysis and alkaline P extraction and its optimization

The pyrolysis was performed on a benchtop horizontal furnace. The sample (up to 10 g) was evenly placed in an alumina crucible (10 cm × 4 cm × 4 cm, thickness ~ 3.5 mm) and the crucible was placed at the center of the furnace. The furnace was purged with N_2 @ 500 mL/min for 5 min to remove residual O_2. After purging, the N_2 flow rate was reduced to 50 mL/min, the temperature ramping rate was set at 20°C/min, and the residence time at peak temperature was 1 h. Three peak pyrolysis temperatures, i.e., 400°C, 600°C, and 900°C, were adopted to investigate the effects of low, medium, and high-temperature pyrolysis on P, Al, and C speciation, and P recovery. After the completion of residence time, the furnace was allowed to cool naturally, and the obtained char was utilized for alkaline P extraction. Slow pyrolysis and longer residence time were intended to maximize char yield[219] so that P loss in the liquid/gaseous phase is minimized. The char from SS was labeled SCxxx, where xxx was the pyrolysis temperature, while the char from MA was called MCxxx (C stands for char).

Following pyrolysis, 0.1 g of char was mixed with 10 mL of 0.5 M NaOH for 1 h for P extraction. The chars from SS and MA with the highest P extraction efficiency (i.e., SC400 and MC400) were further investigated for optimum extraction conditions (NaOH concentration, extraction duration, and L:S ratio) using the one-factor-at-a-time (OFAT) method. OFAT approach was adopted for fine-grained investigation of three of the most critical parameters for extraction. The mass balance for the entire process was quantified based on the calculations explained in Table S 9.

4.2.3. Sample characterization

The physico-chemical characterization of SS and AS was performed: pH, wet density, moisture content, total dissolved solids, elemental composition (C, H, N, S), Ash_{550}, $Ash_{950,}$ and higher heating values were determined, as reported

in the previous study[12]. Some major and trace inorganic elements were quantified after digesting the samples in a microwave acid digester (Anton Parr Multiwave5000) using HCl + HNO_3 + HF + H_3BO_3 (EN13656:2020)[170]. Char sample (0.1 g) was mixed with 1 mL HCl (37%) + 8 mL HNO_3 (69%) + 2 mL H_2O_2 (30%) + 0.5 mL HF (40%). The temperature in the digestion vessels was increased from room temperature to 180˚C in 10 min and maintained at 180˚C for 20 min and thereafter allowed to cool naturally. After digestion, 3 mL H_3BO_3 (4.5%) was added to the digestion vessel, and the mixture was re-digested. For re-digestion, the temperature was ramped up from ambient to 150˚C in 10 min, maintained at 150˚C for 20 min, and then allowed to cool down naturally to room temperature. The inorganic elements were quantified using Inductively Coupled Plasma-Optical Emission Spectroscopy (ICP-OES, Perkin Elmer Optima 8300 OES). Blank, blank spiked, and matrix spiked samples were analyzed to assess the recovery percentage of analytes during ICP-OES analysis. The analysis was performed at least in triplicates (except for alkaline P extraction optimization, which was conducted at least in duplicate). The general physico-chemical characteristics of SS and AS are summarized in Table 4.1.

Table 4.1: Physico-chemcial characteristics of sludge samples.

Parameter	Sewage sludge (SS)	Alum sludge (AS)
Moisture content (wt.%)*	87 ± 0.1	66 ± 0.1
pH	6.7 ± 0.1	7.2 ± 0.0
Dry density (g/mL)	0.6 ± 0.0	0.6 ± 0.0
Higher heating value (J/g)	17044 ± 348	ND
Total dissolved solids (wt.%)	3.0 ± 0.0	1.2 ± 0.1
Ash_{550} (wt.%)	23.7 ± 0.3	59.7 ± 0.6
Ash_{950} (wt.%)	22.2 ± 0.4	31.7 ± 7.4
Al (wt.%)	1.1 ± 0.0	19.1 ± 1.6
C (wt.%)	38.2 ± 0.3	9.8 ± 0.0
Ca (wt.%)	2.4 ± 0.1	0.5 ± 0.1
Fe (wt.%)	1.4 ± 0.0	1.7 ± 0.0
H (wt.%)	6.2 ± 0.1	4.0 ± 0.2
Mg (wt.%)	0.8 ± 0.0	0.2 ± 0.0
N (wt.%)	6.0 ± 0.1	1.0 ± 0.0
P (wt.%)	2.0 ± 0.1	0.1 ± 0.0
S (wt.%)	1.2 ± 0.1	1.6 ± 0.2
Si (wt.%)	3.2 ± 0.2	4.2 ± 0.0

* As-received dewatered sludge samples.

ND: Not determined

Standards Measurements and Testing (SMT) protocol[44,171] was performed to operationally determine AP, NAIP, organic phosphorus (OP), and inorganic phosphorus (IP). Solid-state nuclear magnetic resonance (SSNMR) analyses were performed using a Bruker Avance III HD 600 MHz (14.1 T) spectrometer with a Bruker 3.2mm HXY magic angle spinning (MAS) probe for 27Al and 1H, and samples were spun at 15 kHz. The recycle delay for 27Al and 1H was 1 s and 1.5 s, respectively. 31P measurements were conducted using a 400 MHz (9.4 T) spectrometer with a Bruker 4 mm HXY MAS probe, and a recycle delay of 3 s. 13C{1H} cross-polarization (CP) was measured at MAS of 15 kHz, 1.5 ms contact time. 80 kHz TPPM high power decoupling was used during acquisition. All spectra were processed using Topspin software, and the chemical shift was calibrated using 13C adamantine methylene resonances (37.77 ppm). The spectral deconvolution was performed with Origin software, and the SSNMR spectra were normalized for their graphical presentation. 31P liquid-state nuclear magnetic resonance (LSNMR) was conducted using JEOL ECA400 spectrometer. The operational parameters of LSNMR analysis are as follows: 162 MHz frequency with 90° pulse, 32768 data points, 5 s relaxation delay, 2.03 s acquisition time, and 104 scans. The extracts for LSNMR analysis were obtained using a conventional method[41] with some modifications. Briefly, 0.8 g of SS and MA each and 0.4 g of char samples were mixed with 40 mL of 0.05 M EDTA separately for 1 h using a magnetic stirrer. Subsequently, the mixture was centrifuged, and the solid residue was mixed with 40 mL 0.25 M NaOH and left for overnight mixing. The supernatant was extracted from the mixture via centrifugation and filtration and left for lyophilization in a freeze dryer (CHRiST ALPHA 1-4 LD plus) for two days. The lyophilized sample was mixed with 2 mL 0.25 M NaOH and then centrifuged to obtain the final extract. 760 µL extract was mixed with 240 µL D2O in a 5 mm NMR tube for ^{31}P LSNMR analysis.

Fourier transform infrared (FTIR) spectroscopy (Shimadzu IRPrestige-21) analysis of the sludge and char samples was performed in attenuated total reflection (ATR) mode to identify the changes in some of the functional groups due to SS amendment and pyrolysis. Sludge and char samples were also subjected to x-ray diffraction (XRD) (Bruker D2 Phaser, Cu Kα radiation with $\lambda = 1.54$ Å at 30 kV and 10 mA) analysis to assess the changes in crystalline phases in the samples due to SS amendment and pyrolysis. The operational parameters are as

follows: time/step was 1s with a step size of 0.1°, 10°<2θ< 60°, and 496 steps in Bragg-Brentanno geometry. X-ray photoelectron spectroscopy (XPS) was conducted on AXIS Supra spectrometer (Kratos Analytical) operated at 5 mA using a monochromatic Al K-alpha source. Peaks for sludge samples (SS and MA) were referenced using adventitious carbon, C 1s (284.8 eV), while char samples were referenced using graphitic carbon (C=C) (284.5 eV). XPS peak deconvolution was performed using ESCApe software. Total carbon (TC) and total inorganic carbon (TIC) were determined using Shimadzu TOC-L_{CSH} for the liquid samples (after filtration) and Shimadzu SSM-5000 for the solid samples. Total organic carbon (TOC) was calculated by subtracting TIC from TC. TOC constitutes organic and elemental carbon, while TIC represents C species such as carbonate, bicarbonate, and dissolved CO_2. Scanning electron microscopy (SEM) was performed on JEOL JSM-7200F FESEM. The surface area and porosity of the char samples were determined using the N_2 adsorption method (QuadraSorb Station 2). About 0.5 g sludge and char samples were degassed at 200°C for 24 h, bath temperature being 77.3 K (-195.85°C), and saturation pressure (P_o) was 766.02 mm Hg (102.1 kPa). The surface area was determined using the BET (Brunauer-Emmett-Teller) model, while pore size and pore volume were based on the highest relative pressure (P/P_o) (~0.94-0.95) in the isotherm. Pore size distribution was based on QSDFT (Quenched Solid Density Functional Theory) adsorption model, assuming slit/spherical/cylindrical shaped pores.

4.3. RESULTS AND DISCUSSION

4.3.1. Acidic pretreatment optimization

After the acidic pretreatment of SS and MS, the acidic extracts were analyzed to quantify major ions and assess the fraction extracted (Figure 4.2). There was a sharp reduction in the fraction of Al and Fe extracted at pH ~3 and above. The reduction in P extraction was more prominent for MS at this pH range but not for SS, indicating the positive effect of AS addition and likely precipitation of aluminum phosphates (Al-P). There might also be some iron phosphate precipitation, but its proportion compared to Al-P was likely negligible due to the high Al/P molar ratio in MS. On the contrary, Ca and Mg did not show an abrupt drop in the fraction extracted. The molar ratio of major elements to P in the samples after acidic pretreatment of SS and MS (SSA and MA, respectively) are also shown in Figure 4.2. It shows that at pH>3, Ca/P molar ratio increased

while Al/P ratio was almost constant. Thus, to maximize P (via Al-P precipitation) and minimize Ca/P molar ratio in the acid-pretreated amended SS (MA), a pH range of 3-4 was recommended. Subsequently, acid pretreatment was conducted again to prepare the samples for pyrolysis.

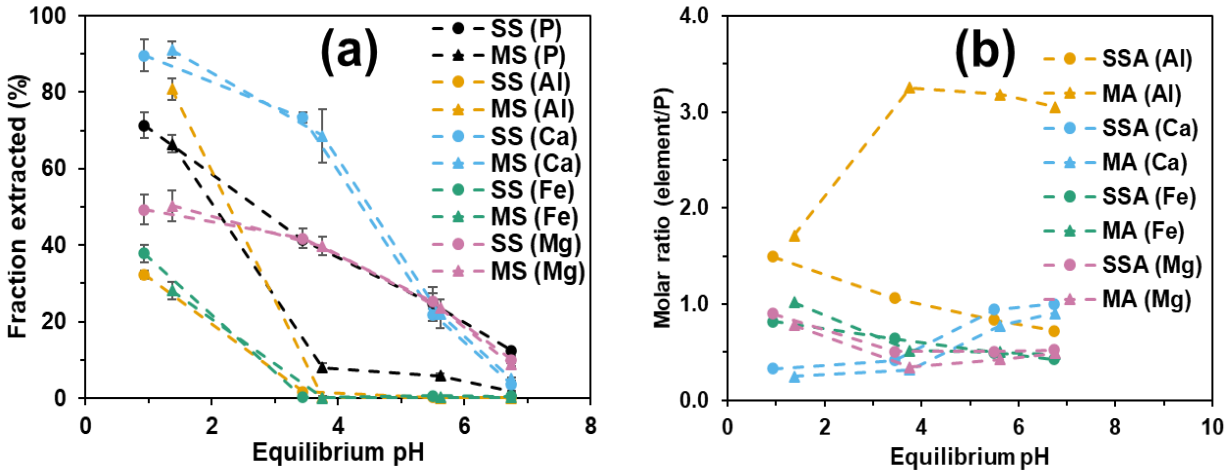

Figure 4.2: (a) The fraction of major ions extracted during acidic pretreatment of SS and MS at various pH (b) molar ratio of inorganic phosphate forming elements (Al, Ca, Fe, and Mg) with P after acidic pretreatment of SS (labeled SSA) and MS (labeled MA).

4.3.2. Effect of SS amendment on P speciation

SS amendment was conducted to promote AP to NAIP conversion in SS, and the conversion mechanism has been discussed in detail in the previous study[12] (but briefly explained here). Most of the Al (mainly from AS) and P precipitated and remained in solids during acidic pretreatment, while other major inorganic ions (such as Ca and Mg) dissolved and were discarded with the acidic extract. The molar ratio of major elements that form inorganic compounds with P was altered in the amended SS (Table S 10). Among these, reduction in Ca/P was most critical for improving the alkaline extraction of P from char. This aspect has been discussed in detail in the subsequent sections. Furthermore, it was reported that Al-P precipitated as $AlPO_4$ in acidic conditions[14,35], but it was found that Al-P association was through adsorption and surface complexation (bidentate binuclear innersphere) of orthophosphate (ortho-P) with $Al(OH)_3$[12].

4.3.3. Effect of operational conditions on alkaline extraction of P

P extraction (mg/kg and %) was significantly higher for MCs than SCs for all the pyrolysis temperatures (Figure 4.3) ($p < .001$, degrees of freedom (df) = 1)

despite higher P concentration in SCs. The higher alkaline P extraction efficiency for MCs (51-88%) than SCs (9-32%) was due to a higher fraction of NAIP (mostly Al-P) in them (discussed in detail in subsequent sections). Moreover, P recovered (mg/kg and %) was reduced significantly (p < .001, df = 2) for both SCs and MCs with increasing temperature, i.e., SC400 (32%) > SC600 (22%) > SC900 (9%) and MC400 (88%) > MC600 (66%) > MC900 (51%). Tukey's test confirmed this trend was significant (p < .001, total df = 12) for P recovery. This trend can be attributed to the increasing fraction of stable and less labile P minerals at higher temperatures and the immobilization of P during carbonization. This aspect has been discussed in detail in the subsequent sections. Two-way ANOVA also revealed a significant interaction effect (for both absolute P recovered (mg/kg) (p = .018, df = 2) and % recovered (p = .002, df = 2)) between two independent variables (i.e., pyrolysis feedstock type and temperature), but not as significant as the main effects of these variables.

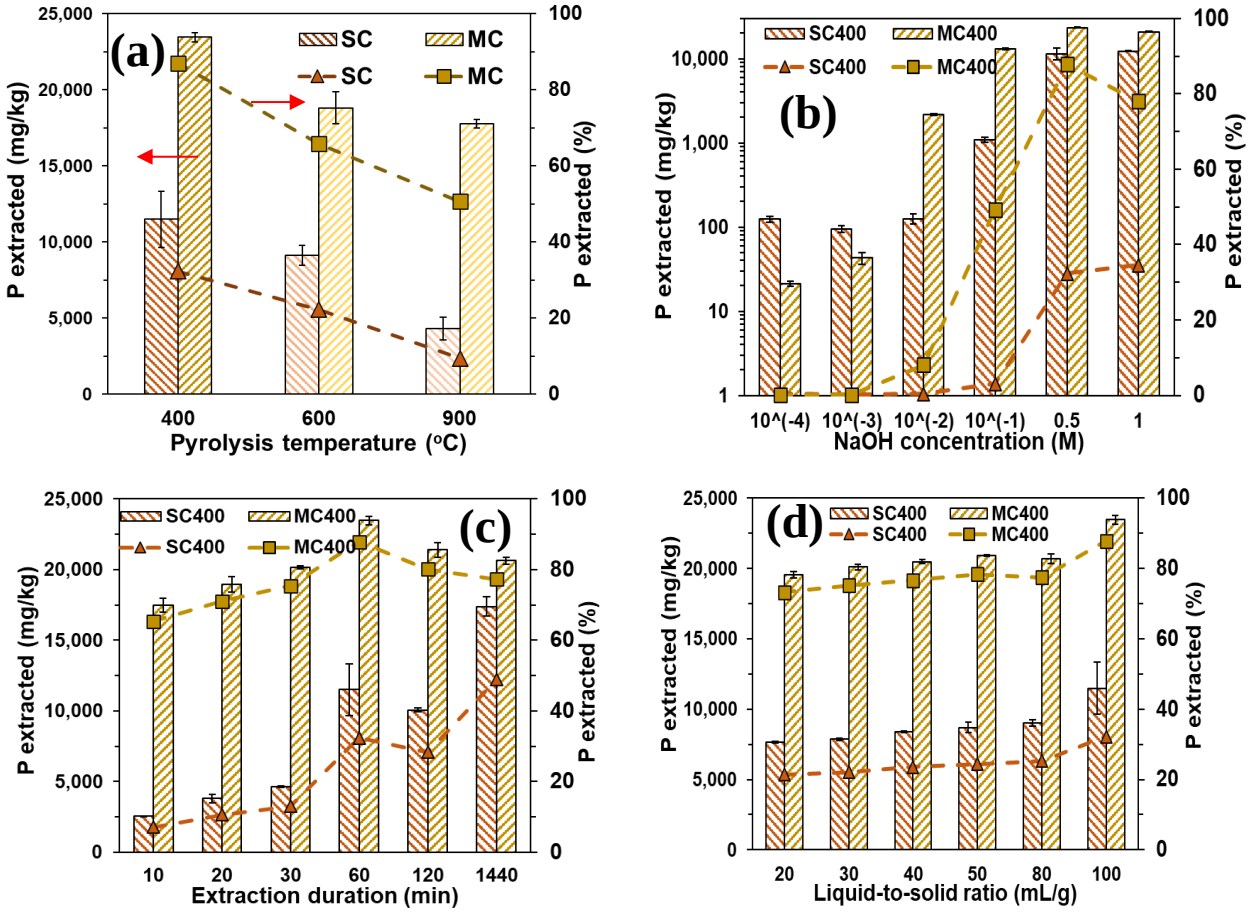

Figure 4.3: (a) Phosphorus extracted from chars using 0.5 M NaOH at L/S of 100:1 for 1 h. (b,c,d) represent one-factor-at-a-time (OFAT) optimization of the alkaline P extraction from SC400 and MC400. The error bar represents the standard deviation.

MC400 outperformed SC400 in P extracted (absolute value and %) for all three critical extraction operational parameters. For liquid-to-solid (L/S) ratio, the difference in P recovery (mg/kg and %) between SC400 and MC400 was significant ($p < .001$, df = 1) across the operation range. It was also significant within the individual cohorts of SC400 and MC400 ($p < .001$, df = 5). For other parameters normality/ homoscedasticity assumptions were not met and hence ANOVA results are not reported. However, it is apparent that NaOH concentration (or pH of the extractant) was important for P extraction in the investigated range of conditions. It was important because the change in P extracted with changing NaOH concentration was stark for both SC400 and MC400. At lower concentrations (10^{-4} and 10^{-3} M), the total P extracted was relatively higher for SC400 than MC400, as the latter lost labile P during acidic pretreatment (though the difference is inconsequential due to low absolute value of P extracted (~ 20-120 mg/kg)). However, with increasing concentration (> 10^{-3} M), MC400 outperformed SC400 (in both total P extracted, and percentage of P extracted), highlighting the critical role of NAIP proportion in char for alkaline extraction. The effect of extraction duration was more pronounced for SC400 than MC400, as the difference between the highest and lowest extraction efficiencies were 42% and 23%, respectively. The enhanced P dissolution kinetics in MC400 could be due to a higher proportion of NAIP than in SC400, which is easily extracted in alkaline conditions. The influence of L/S was practically insignificant in both SC400 and MC400, as alkaline P extraction is less influenced by the L/S ratio[220,221].

The mass balances for the entire process in the reference and design processes are shown in Figure 4.4. P concentration in char increased with increasing pyrolysis temperatures for both SS and MA as P in SS is largely non-volatile below 1100˚C[222]. The increase in P concentration in char is consistent with some other studies[105,223]. P loss in gaseous/liquid phases during pyrolysis was higher for SS (~ 14%) than MA (~ 2%, except for 600°C (~ 9%)) for all the temperatures. It was likely because OP volatilization was inhibited more during MA pyrolysis than during SS pyrolysis. In other words, Al abundance promoted the formation of metal phosphate complexes and minerals during the thermal decomposition of OP[81]. Moreover, these inorganic phosphate phases might have interacted with the organic fraction of char and stabilized further by organo-mineral interaction[224]. However, relatively higher

P loss during the MA pyrolysis at 600˚C than at 400/900˚C was unclear. Overall, the condensation of P on the solid char dominated the P volatilization even at high temperatures (~ 900˚C).

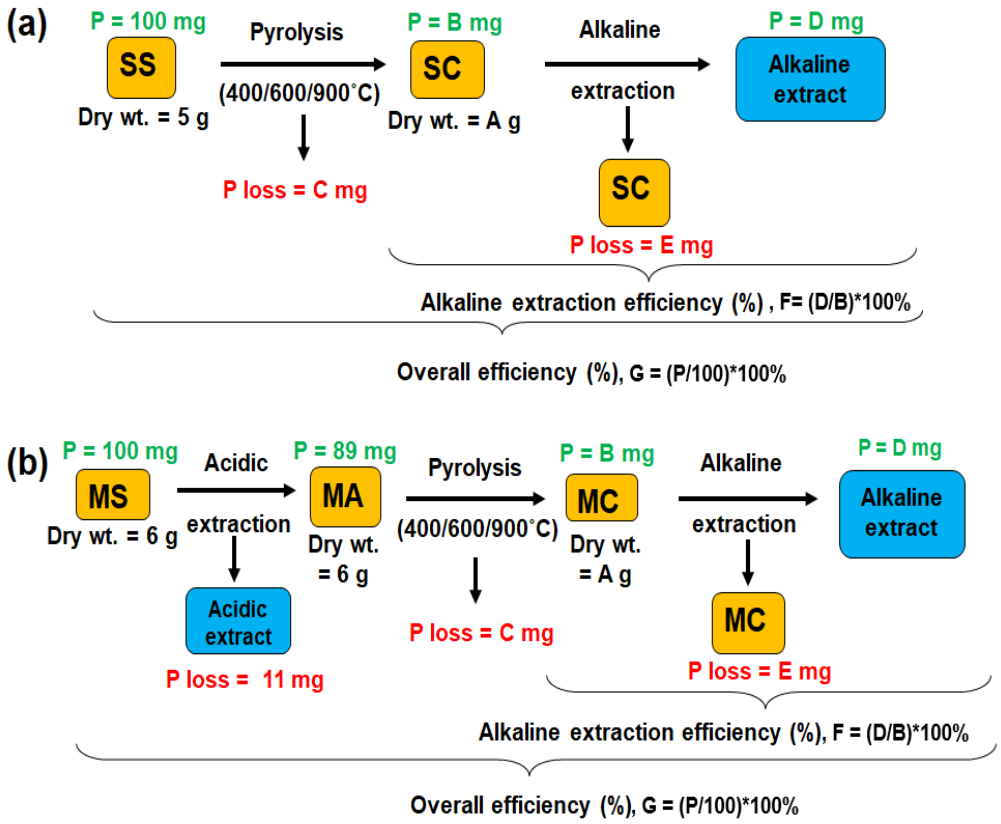

Feedstock	Pyrolysis temp. (T˚C)	Char wt. (A) (g)	P_{char} (B) (mg)	P loss via pyrolysis (C) (mg)	P_{alkali} (D) (mg)	P loss via char (E) (mg)	Alkaline extraction efficiency (F) (%)	Overall efficiency (G) (%)
SS	400	2.4	86	14	28	58	32	28
SS	600	2.1	87	13	19	67	22	19
SS	900	1.9	86	14	8	78	9	8
MA	400	3.2	87	2	76	11	88	76
MA	600	2.8	80	9	53	27	66	53
MA	900	2.5	87	2	44	43	51	44

Figure 4.4: The mass balance for the entire process in the (a) reference and (b) design cases based on the average values of the replicates. The results are summarized in the table below the schematics.

In conclusion, SS amendment followed by low-temperature pyrolysis was most suitable for alkaline P recovery from char. The proposed novel process engineered P transformation in SS using a waste, which led to relatively higher alkaline P recovery efficiency, hitherto unreported in prior literature. Some of the operational parameters, such as NaOH concentration, L/S, and extraction duration, might be adjusted to lower the economic and environmental cost of the

process (though detailed research is pertinent in this regard). P speciation had a critical role in its extractability from char, so it was investigated in detail and discussed in the subsequent subsections.

4.3.4. XRD of sludge and char samples

XRD analysis was conducted to identify the structural characteristics of major minerals in SS and MA and changes due to thermal treatment (Figure 4.5). Generally, identifying crystal phases in complex environmental samples is challenging due to overlapping peaks and amorphous phases (but useful, nonetheless). The broad hump in the range $14^\circ < 2\theta < 26^\circ$ in SS and MA spectra represents the amorphous phase. Similar spectra for SS and MA indicated that SS amendment did not lead to a change in crystal structures. With increasing pyrolysis temperature, the broad hump reduced, indicating the increasing crystallization of char samples. Regarding P compounds, the sludge samples and chars prepared at temperatures up to 600˚C did not exhibit P crystals (except SC600). The whitlockite peak was evident in SC600 and SC900, indicating the formation of Ca-P crystals at higher temperatures (≥ 600˚C). Conversely, $AlPO_4$ and augelite peaks rather than whitlockite peaks were detected in MC900 due to relatively higher Al/P and lower Ca/P molar ratios in MA than in SS. The formation of whitlockite partially explained the low alkaline P dissolution from SC900 (9%) compared to MC900 (51%). These findings concurred with the 31P SSNMR analysis in this study. The peak for aluminum phosphide (AlP) was also observed but not assigned, as its formation in this study was unlikely. AlP is highly reactive and thus likely to transform into other stable P compounds in the char samples. Besides, SiO_2 was a prominent mineral detected in all the samples. The increasing relative intensity of SiO_2 with increasing temperature could be attributed to changes in the ultrastructures of chars[225]. It could also be attributed to the reduction in the relative intensity of other crystal phases (such as FeS) due to thermal decomposition.

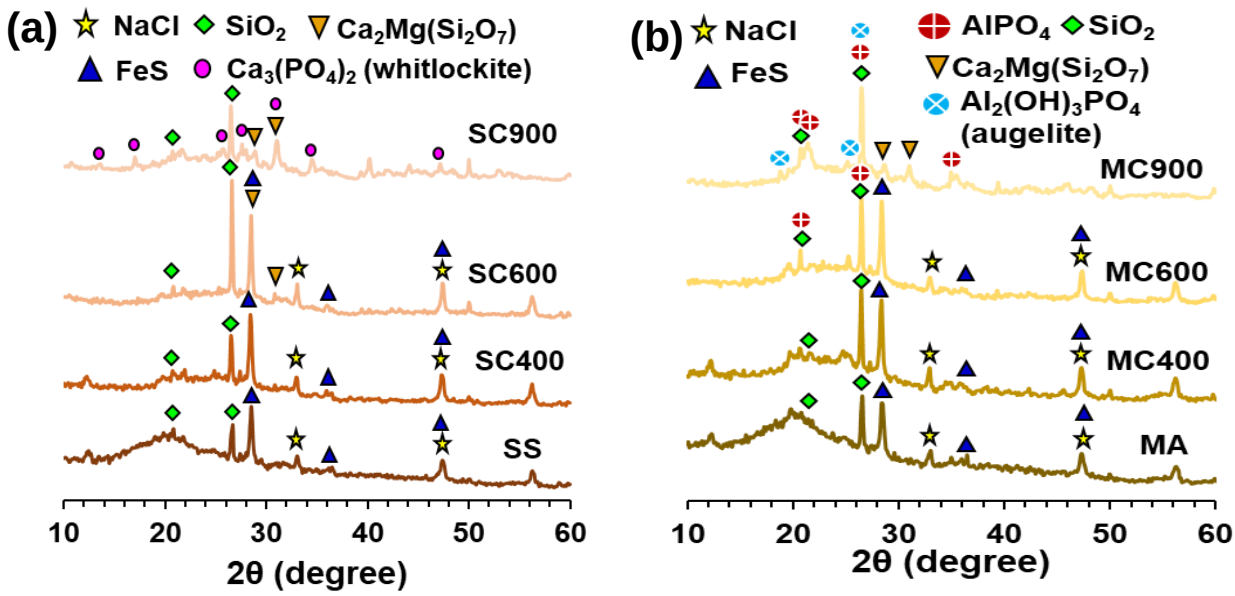

Figure 4.5: XRD peaks of (a) SS and its chars and (b) MA and its chars.

4.3.5. P speciation and its role in P extraction

4.3.5.1. SMT analysis

SMT analysis was conducted to ascertain the variation in P species (AP, NAIP, OP, and inorganic phosphorus (IP)) due to SS amendment and pyrolysis (Figure 4.6). The effect of SS amendment on AP to NAIP conversion was evident as AP/NAIP ratio in MA (0.04) was about 14 times lower than in SS (0.57). The reason for the conversion was explained in the preceding section. With increasing pyrolysis temperature, AP/NAIP ratio increased in SS chars, a trend observed in other studies as well[91,96,105]. This increase was due to the formation of thermodynamically more stable P species, such as apatite, as the pyrolysis temperature increased[222] (corroborated by XRD data in this study). The increasing AP/NAIP ratio from SC400 (0.84) to SC600 (1.67) to SC900 (2.19) partly explained the reduction in alkaline P extraction efficiency in SS chars with increasing temperature. Conversely, AP/NAIP stagnated or reduced with increasing pyrolysis temperature among MC chars. AP/NAIP in MC400, MC600, and MC900 was 0.22, 0.12, and 0.20, respectively. This trend was attributed to the deficiency of Ca and abundance of Al due to SS amendment. Multiphase, multicomponent thermodynamic equilibrium modeling using Gibbs free energy minimization also indicated that Al-P and iron phosphate species might dominate in the char if their concentrations were relatively high[226].

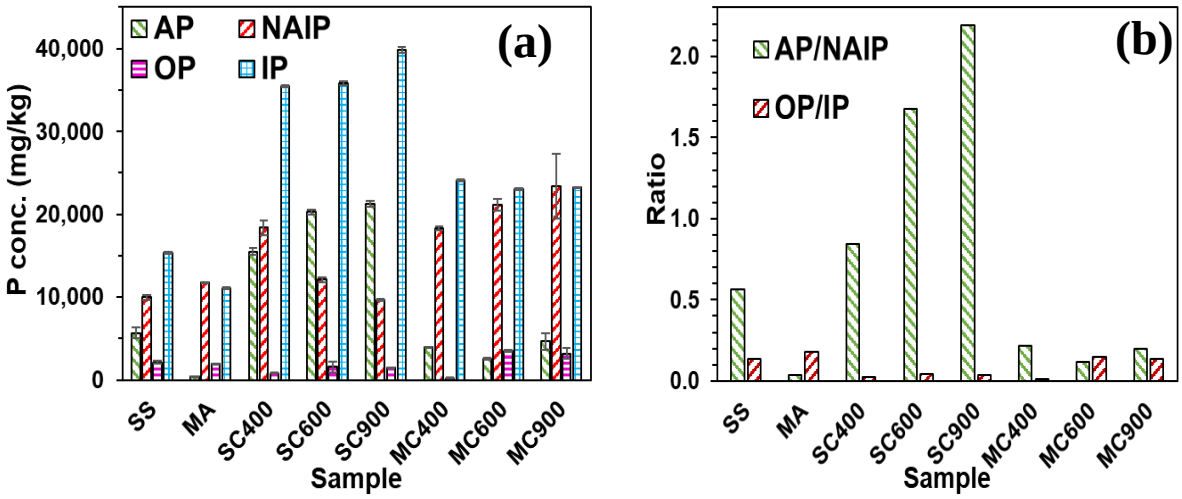

Figure 4.6: (a) P species in the sludge and char samples determined using the SMT protocol. (b) Ratio of P species in sludge and char samples. P species are apatite phosphorus (AP), non-apatite inorganic phosphorus (NAIP), organic phosphorus (OP), and inorganic phosphorus (IP). The error bar represents the standard deviation.

OP/IP ratio in MA (0.18) was higher than in SS (0.14) due to the loss of labile IP during acidic pretreatment of MS. OP was not lost as it is recalcitrant to acidic hydrolysis at pH 3-4[12]. Pyrolysis at 400˚C led to a reduction in OP/IP as it was 0.02 in SC400 and 0.01 in MC400. This reduction was due to the thermal decomposition of OP to ortho-P and the formation of IP when released ortho-P binds with inorganic elements. However, OP decomposition did not accentuate with increasing pyrolysis temperature in some cases (contrary to the general trend[81]), as evidenced by its finite presence in MC600 (OP/IP = 0.15), and MC900 (OP/IP = 0.14). Minor OP presence in MC900 was also corroborated by the LSNMR and SSNMR data. The decomposition of OP was further discussed in the sections on ^{31}P LS/SSNMR.

In conclusion, AP/NAIP ratio increased and stagnated with increasing pyrolysis temperature in SC and MC chars, respectively. SS amendment reduced AP in MA, affecting its concentration in char samples due to Ca deficiency. OP did not decompose completely, even at 900˚C. Overall, it was evident that SS amendment partially rectified the temperature effect to obtain P species in char that dissolved in an alkali (i.e., Al-P) rather than precipitated (such as Ca-P). It is worth noting that sequential fractionation techniques, including SMT, are limited by the nature of the sample (soil, lake sediment, and sludge), sample composition, and operational considerations[43]. Hence, it was supplemented with other

analytical techniques, such as P 2p XPS, ^{31}P LSNMR, and SSNMR analyses, for detailed P speciation in this study.

4.3.5.2. P 2p XPS analysis

XPS analysis was conducted to determine the oxidation states of P and correlate it with other data in this study (Figure 4.7). The deconvoluted peaks for all the samples with their relative areas and assignments are enumerated in Table 4.2. In SS, two major deconvoluted peaks possibly corresponding to HPO_4^{2-}, C-O-P, $(PhO)_3PO$ (where Ph is phenyl group, $-C_6H_5$) (133.9 eV) and metal-bound $PO_4^{3-}/P_2O_7^{4-}$ (such as with Ca) (133.1 eV) were identified. In MA, the fraction of C-O-P, HPO_4^{2-}, $(PhO)_3PO$ increased while the peak at 133.1 eV was missing, possibly indicating the loss of Ca-P during acidic pretreatment. Instead, a prominent peak at 135.1 eV in MA could correspond to $H_2PO_4^-$ bound to metal[227]. The presence of protonated ortho-P was confirmed by ^{31}P SSNMR analysis as well. Given the acidic pretreatment pH range of ~ 3 (less than pKa_2 (7.21) of H_3PO_4), $H_2PO_4^-$ dominates in the dissociation equilibrium and is more likely to associate with metal ions. Among char samples of SS, the area % of peak at around 133.2 eV increased from SS to SC400 to SC600 and then decreased for SC900, possibly indicating the changes in metal phosphate compounds. It could also imply the formation of pyrophosphate (133.2 eV) as the temperature increased up to 600˚C and then their destruction with further temperature increase (as corroborated by LSNMR data). SC900 also has a prominent peak at 135.7 eV, indicating the presence of phosphorus pentoxide (as P_2O_5 or P_4O_{10}). A similar trend of ortho-P, pyro-P, and C-O-P presence was observed among the chars of MA. Interestingly, metaphosphate (PO_3^-) was detected in some samples but not confirmed by other analytical techniques, possibly due to methodological limitations. For instance, it was not detected in LSNMR analysis because metaphosphate hydrolyses to ortho-P and pyro-P during dissolution[86].

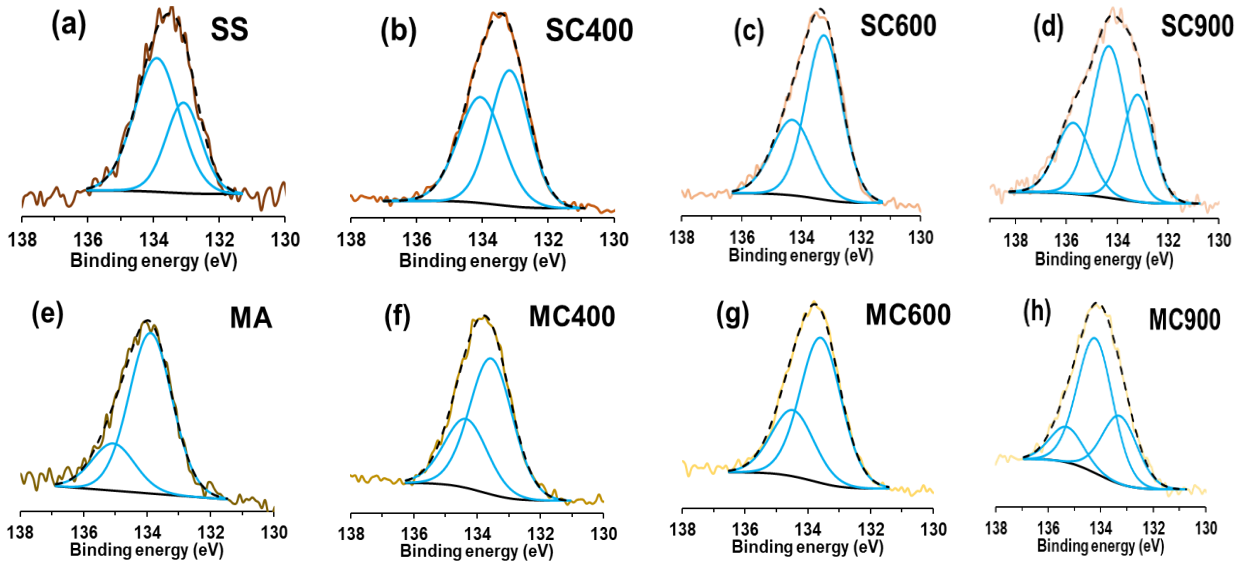

Figure 4.7: P 2p spectra of (a,b,c,d) SS and its chars (e,f,g,h) MA and its chars. Experimental, simulated, and deconvoluted spectra are shown in multicolor solid lines, black dashed lines, and blue solid lines, respectively.

Table 4.2: P 2p XPS deconvoluted peak assignments for sludge and char samples, relative areas, and FWHM.

Sample	Peak energy (eV)	Full width at half maximum (FWHM) (eV)	Area (%)	Peak assignment	Ref.
SS	133.1	1.25	34.79	PO_4^{3-}, $P_2O_7^{4-}$	[228,229]
	133.9	1.6	65.21	C-O-P, HPO_4^{2-}	[86,228,230]
SC400	133.2	1.41	53	PO_4^{3-}, $P_2O_7^{4-}$	[228,229]
	134.1	1.6	47	C-O-P, PO_3^-, $(PhO)_3PO$	[86,230,231]
SC600	133.2	1.41	65.9	PO_4^{3-}, $P_2O_7^{4-}$	[228,229]
	134.3	1.6	34.1	C-O-P, PO_3^-, $(PhO)_3PO$	[230,231]
SC900	133.2	1.4	29.54	PO_4^{3-}, $P_2O_7^{4-}$	[228,229]
	134.3	1.6	48.01	C-O-P, PO_3^-, $(PhO)_3PO$	[230,231]
	135.7	1.6	22.46	P_2O_5, P_4O_{10}	[232]
MA	133.9	1.6	77.32	C-O-P, HPO_4^{2-}	[86,228,230]
	135.1	1.6	22.68	$H_2PO_4^-$	[227]
MC400	133.6	1.6	66.47	C-P, C-O-P, HPO_4^{2-} or $P_2O_7^{4-}$	[230,232,233]
	134.3	1.6	33.53	C-O-P, PO_3^-, $(PhO)_3PO$	[230,231]
MC600	133.6	1.55	67.92	C-P, C-O-P, HPO_4^{2-} or $P_2O_7^{4-}$	[230,232,233]
	134.5	1.6	32.08	C-O-P, PO_3^-, $(PhO)_3PO$	[230,231]
MC900	133.3	1.6	28.74	PO_4^{3-}, $P_2O_7^{4-}$	[228,229]
	134.2	1.6	57.05	C-O-P, PO_3^-, $(PhO)_3PO$	[230,231]
	135.3	1.5	14.21	P_2O_5	[229]

Overall, the changes in P species were evident due to SS amendment and pyrolysis temperatures, even though P species can have overlapping peaks, and it might be hard to trace changes in specific P compounds. The presence of ortho-P, protonated ortho-P bound to a metal ion, and pyro-P were in conformity with NMR data. Besides, the detection of C-O-P, $(PhO)_3PO$, and C-P bonds indicated the association of P with carbon in the samples. It was likely that the association of P with aromatic carbon increased with increasing temperature (especially at 900˚C) (discussed in detail in the sections on carbon analysis).

4.3.5.3. ^{31}P LSNMR analysis

Figure 4.8 shows that almost the entire P in SS and MA was detected as ortho-P, as evident from one prominent peak in their spectra[196]. The abundance of ortho-P was confirmed by P 2p XPS analysis. A minor rightward shift in ortho-P peak for SS and MA compared to their chars was likely due to their lower pH than their chars[12] (as char can be more alkaline than SS[95]). In SC400, a prominent pyrophosphate peak at -4.3 ppm might be due to polymerization and condensation reactions of P compounds during pyrolysis[81,234,235]. It could also be due to the decomposition of OP via hydrolysis and facilitated by H_2O from the decomposition of carboxylic acid or dehydration of ortho-P[95]. However, OP content in SS was low; hence, pyrophosphate formation via degradation of OP was improbable. The pyrophosphate formation was likely due to dehydration of metal ortho-P, such as that of Ca[236,237]. Since MA had much lower Ca/P, the pyrophosphate formation was negligible in MC400. The pyrophosphate fraction in SC600 and SC900 was also low, possibly indicating the destruction of pyrophosphates and formation of inorganic P minerals at temperature $\geq$ 600˚C by the combination of ortho-P with metals such as Ca and Al[59]. Similar findings were reported in some other studies on SS pyrolysis[91,95,96]. Interestingly, both ortho-P monoester and pyrophosphate were detected in MC900 (though with minor peaks). As mentioned in the previous section, generally, OP decomposition accentuates with increasing pyrolysis temperature[81], but there are exceptions to this trend. The fractional content of OP species such as ortho-P monoester and diester has been reported to be as high as 39% and 21%, respectively, in char prepared at 900˚C[93]. In MC900, some pyrophosphate and ortho-P monoester were possibly stabilized by interaction with the ash component of the char or

formed a stable organo-mineral complex or bound to aromatic carbon through electrostatic and hydrogen bonding interactions[224,236,238]. The direct or indirect P bonding with C was also observed via P 2p XPS analysis in this study. However, it is likely that additives such as CaO, $Ca(OH)_2$, MgO[89,93] and AS (this study) had a greater role than carbon in preventing the decomposition of OP during pyrolysis. Otherwise, SS chars would also have OP content comparable to amended SS, which was not the case in this study.

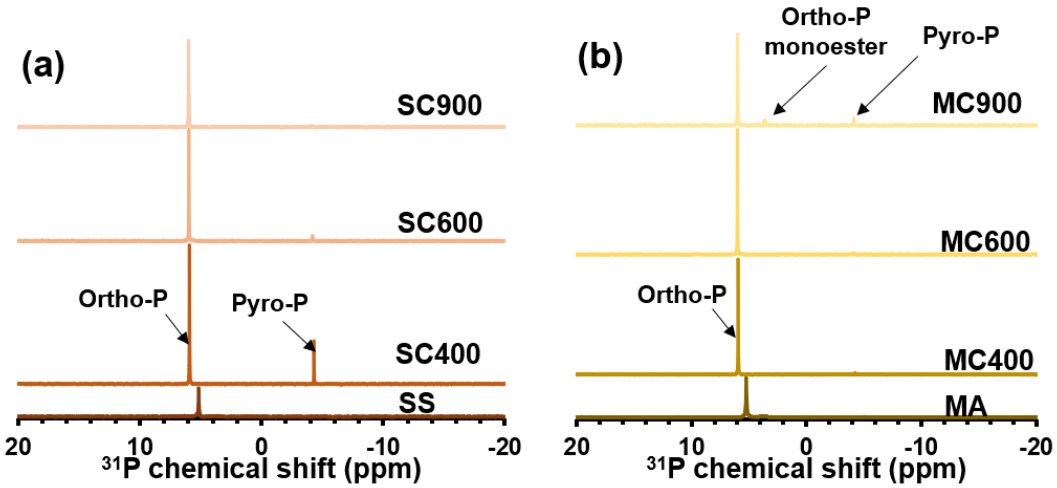

Figure 4.8: ^{31}P liquid-state NMR (LSNMR) of sludge (SS and MA) and char samples.

However, the OP data from the SMT protocol and LSNMR did not corroborate for some samples in this study. This is possibly due to the methodological limitation of LSNMR (hydrolysis of OP during NaOH-EDTA extraction or non-extraction of condensed organophosphates, making identification of P speciation difficult). In SSNMR, samples are analyzed directly in the solid samples; hence, it was helpful for the in-situ characterization of P species.

4.3.5.4. ^{31}P SSNMR analysis

^{31}P chemical shifts depend on the electronegativity, charge, and radius of the next-nearest-neighbor cation and generally have a linear relationship with P-O bond length and O-P-O bond angle in ortho-P[186]. ^{31}P SSNMR analysis of sludge (SS and MA) and char samples is shown in Figure 4.9, along with peak assignments to various P species and their fractional distribution. The peak assignments for deconvoluted peaks are tabulated in Table 4.3.

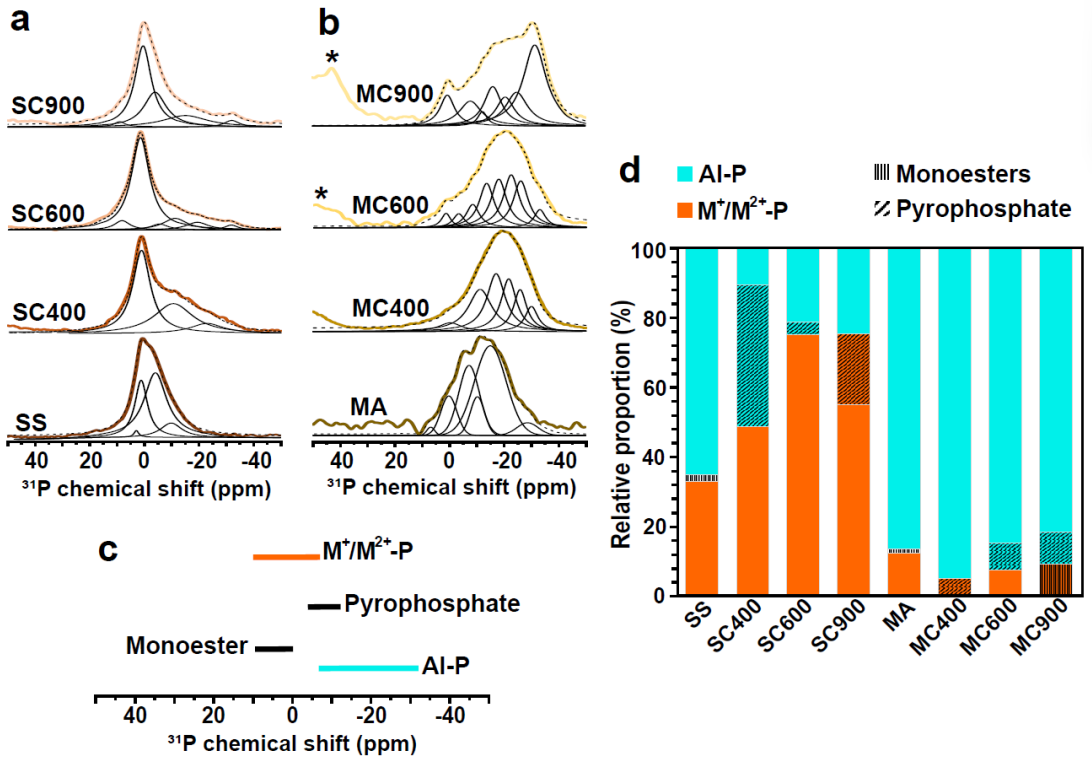

Figure 4.9: ^{31}P single pulse- magic angle spinning (SP-MAS) NMR spectra of (a) SS and its chars, (b) MA and its chars, (c) the approximate peak range for some important P species in this study (M^+ and M^{2+} represent alkali and alkaline earth metals, respectively) (d) fractional distribution of P species in the samples. Experimental spectra, simulated spectra, and deconvoluted resonances are shown in multicolor solid lines, black dotted lines, and black solid lines, respectively. Some of the peaks were in the overlapping region and hence assigned with an overlap in (d). The spinning sideband is marked with *.

Table 4.3: Peak assignment for deconvoluted peaks of ^{31}P single pulse-magic angle spinning (SP-MAS) NMR spectra of sludge and char samples.

Sample	Peak (ppm)	Peak assignment	Ref.
SS	4.1	Ortho-P monoester	[196,239]
	1.2	Octacalcium phosphate (OCP) ($Ca_8H_2(PO_4)_6{\cdot}5H_2O$), $NH_4H_2PO_4$,$(NH_4)_2HPO_4$	[186,187]
	-3.2	Protonated ortho-P adsorbed to $Al(OH)_3$,uncondensed aluminum phosphate	[187,189]
	-9.5	Protonated ortho-P adsorbed to $Al(OH)_3$,uncondensed aluminum phosphate	[187,189]
SC400	1.1	OCP ($Ca_8H_2(PO_4)_6{\cdot}5H_2O$), $NH_4H_2PO_4$	[186,187]
	-10.5	Pyrophosphate ($P_2O_7^{4-}$)	[196,239]
	-21.8	Lazulite ($MgA1_2(OH)_2(PO_4)_2$)	[240]

SC600	8.8	Inorganic ortho-P	[196]
	1.5	OCP ($Ca_8H_2(PO_4)_6 \cdot 5H_2O$), Brushite ($CaHPO_4.2H_2O$), $(NH_4)_2HPO_4$	[186,187]
	-7.5	Pyrophosphate ($P_2O_7^{4-}$)	[196,239]
	-11.2	Wavellite ($Al_3(OH)_3(PO_4)_2 \cdot 5H_2O$),unknown (likely Al-P)	[187,188,240]
	-19.8	Lazulite ($MgA1_2(OH)_2(PO_4)_2$)	[240]
	-31.8	Augelite ($Al_2(OH)_3PO_4$)	[240]
SC900	9.1	Inorganic ortho-P	[196]
	0.6	$Mg_3(PO_4)_2$	[187]
	-3.8	Pyrophosphate ($P_2O_7^{4-}$)	[196,239]
	-14.8	Unknown (likely Al-P)	[187,188]
	-31.8	Augelite ($Al_2(OH)_3PO_4$)	[240]
MA	6.7	Ortho-P monoester	[51,196,239]
	0.3	OCP ($Ca_8H_2(PO_4)_6 \cdot 5H_2O$), dicalcium phosphate anhydrous (DCPA, monetite ($CaHPO_4$))	[187]
	-5.0	Protonated ortho-P adsorbed to $Al(OH)_3$,uncondensed aluminum phosphate	[187,189]
	-10.2	Protonated ortho-P adsorbed to $Al(OH)_3$,uncondensed aluminum phosphate	[187,189]
	-16.1	Senegalite ($Al_2(OH)_3(PO_4).H_2O$, unknown (likely Al-P)	[188,240]
	-29.6	Augelite ($Al_2(OH)_3PO_4$)	[240]
MC400	0.11	Monetite ($CaHPO_4$)/ OCP ($Ca_8H_2(PO_4)_6 \cdot 5H_2O$), $Na_4P_2O_7$	[187,241]
	-11.2	Wavellite ($Al_3(OH)_3(PO_4)_2 \cdot 5H_2O$), unknown (likely Al-P)	[187,188,240]
	-17.0	Unknown (likely Al-P)	[187,188]
	-21.6	Lazulite ($MgA1_2(OH)_2(PO_4)_2$)	[240]
	-25.1	Berlinite ($AlPO_4$)	[187,240]
	-29.9	Augelite ($Al_2(OH)_3PO_4$)	[240]
MC600	1.4	OCP ($Ca_8H_2(PO_4)_6 \cdot 5H_2O$), Brushite ($CaHPO_4.2H_2O$) $(NH_4)_2HPO_4$	[186,187]
	-3.2	Protonated ortho-P adsorbed to $Al(OH)_3$,uncondensed aluminum phosphate	[187,189]
	-8.3	Pyrophosphate ($P_2O_7^{4-}$)	[196,239]
	-12.4	Unknown (likely Al-P)	
	-17.8	Unknown (likely Al-P)	[187,188]
	-21.4	Lazulite ($MgA1_2(OH)_2(PO_4)_2$)	[240]
	-25.2	Berlinite ($AlPO_4$)	[187,240]

	-32.8	Augelite ($Al_2(OH)_3PO_4$)	[240]
MC900	0.6	$Mg_3(PO_4)_2$, Ortho-P monoester	[187,239]
	-7.8	Pyrophosphate ($P_2O_7^{4-}$)	[196,239]
	-12.3	Unknown (likely Al-P)	
	-16.1	Senegalite ($Al_2(OH)_3(PO_4).H_2O$, unknown (likely Al-P)	[188,240]
	-20.6	Lazulite ($MgA1_2(OH)_2(PO_4)_2$)	[240]
	-24.8	Berlinite ($AlPO_4$)	[187,240]
	-31.4	Augelite ($Al_2(OH)_3PO_4$)	[240]

SS and SC samples had a prominent resonance at around 1 ppm and several weaker upfield resonances (ranging from -10 to -30 ppm). The peak at 1 ppm possibly indicated octacalcium phosphate (OCP), with upfield resonances encompassing various Al-P species and protonated phosphates adsorbed on $Al(OH)_3$. This peak sharpened with increasing pyrolysis temperatures in SC samples while the upfield shoulder of the spectrum reduced in prominence. This indicated an increase in the proportion of AP in SC samples, which is also corroborated by SMT analysis. In MA, a broad peak was observed encompassing various P species but mainly corresponding to the adsorption of phosphates on $Al(OH)_3$ and uncondensed Al-P, indicating AP to NAIP conversion due to SS amendment. Al-P species transformed with increasing pyrolysis temperature, more so beyond 600˚C, as evident from a few distinct peaks in MC900. More negative chemical shifts have been reported for aluminum phosphate precipitates that had been calcined[242]. Some of the minerals mentioned in Table 4.3 (such as whitlockite and augelite) were observed in the XRD spectra of these samples. Interestingly, some peaks in the ^{31}P SSNMR spectra of the chars could be assigned to hydrated compounds such as OCP, brushite, wavellite, and senegalite. However, their presence in this study was less likely as water of hydration peak was not apparent in ^{1}H single pulse-magic angle spinning (SP-MAS) SSNMR spectra of the char samples (further discussion in supplementary information (SI), Figure S 3). So, these peaks could be assigned to some unidentified compounds but broadly corresponding to M^+/M^{2+}-P or Al-P (Figure 4.9).

OP (such as orthophosphate monoester) was barely detected in SS. In the LSNMR of SS, OP was also not detected, though some of it was quantified in the SMT analysis. A small peak at 0.6 ppm in MC900 might correspond to monoester (also observed in LSNMR). Besides, small resonances (from -7 to -9 ppm) seen in SC/MC400 to SC/MC900 were likely associated with pyrophosphate, as

corroborated by the LSNMR of SC400 and MC900 as well (but not for other char samples). However, a clear assignment to OP was difficult as this resonance region overlapped with the Al-P region.

After alkaline extraction, SSNMR analysis of the char samples was conducted to identify unextracted P species (Figure S 4). All samples showed a peak at ~ 2.8 ppm, likely corresponding to Ca-P such as hydroxyapatite (HAP) ($Ca_5(PO_4)_3OH$), OCP ($Ca_8H_2(PO_4)_6{\cdot}5H_2O$) or $Ca_3(PO_4)_2$. Moreover, line sharpening in the spectra for all the samples indicated a higher degree of crystallinity of Ca-P species in the samples, as sharp lines represent the uniformity of the environment surrounding the P nuclei. The stable crystalline phases, such as apatite, are less labile than amorphous phases. Some of these crystalline phases were apparent in XRD spectra, especially when amorphous phases were thermally decomposed. The absence of resonance in the Al-P region was due to their dissolution during alkaline extraction.

Overall, the dominance of Ca-P in SC chars and Al-P in MC chars explained the higher alkaline P extraction efficiency in the latter. Moreover, increasing pyrolysis temperatures led to the formation of stable Ca-P species in SC and MC chars, further preventing their alkaline dissolution. To investigate the effect of Al on P extractability (especially from MC chars), Al speciation analysis was conducted in detail and elaborated in the subsequent section.

4.3.6. Al speciation and its relationship with P

4.3.6.1. ^{27}Al SSNMR analysis

^{27}Al spectra, the resonance range for various Al coordination states, and the fractional distribution of Al coordination states are presented in Figure 4.10. The deconvoluted resonance assignments are given in Table 4.4. In general, AlO_6 resonances in ^{27}Al spectra became less dominant with increasing temperatures, with a simultaneous increase in AlO_4 peak intensity, valid for both SC and MC samples. This corresponded to $AlPO_4$ formation in SC600, SC900, and MC600. Owing to the thermal treatment and sample type, different forms of $AlPO_4$ were formed, as confirmed by resonant peaks. Distinct resonance for berlinite, or the quartz form, was observed in MC600 at ~ 44 ppm, which is characteristic of the $AlPO_4$ environment in crystalline alumino-phosphate[243]. The tridymite form (38.8 to 39.8 ppm) was observed in SC600 and SC900. Both quartz and tridymite

forms exist in tetrahedral coordination. Another berlinite resonance (36 ppm) was observed in MC400 without the other resonance reported around 26 ppm[242,244], most likely due to its broad and weak nature. A corresponding berlinite peak was seen in ^{31}P SSNMR of MC400. In MC900, a prominent AlO_6 resonance (7 ppm) coupled with a smaller AlO_4 peak (64 ppm) were both assigned to γ-Al_2O_3[245]. Similar downfield resonances were seen in MA, MC400, and SC400; however, those were not assigned due to the lack of the dominant AlO_6 resonance at ~ 8 ppm. It indicated the formation of γ-Al_2O_3 by thermal dehydroxylation of boehmite (AlO(OH)) between 500-750˚C[246]. The abundance of Al_2O_3 over AlO(OH) in SC/MC900 was also evident from Al 2p XPS analysis (Section 4.3.6.2). Broad resonance for augelite (-31 ppm) in MC900 (^{31}P SSNMR spectrum) was consistent with prominent AlO_5 resonance in ^{27}Al spectra, while less prominent augelite peak in MC400 and MC600 show little to no AlO_5 resonance (possibly masked by more dominant $AlPO_4$ resonance). Augelite resonance in ^{31}P SSNMR spectra in SC600 and SC900 was too weak, corroborated by the absence of an AlO_5 peak in the ^{27}Al spectra. XRD analysis verified the presence of augelite in MC900 but not berlinite in char samples prepared at 400˚C. In conclusion, the Al environment in the samples was marked by the diversity of coordination states, especially for the chars prepared at 600˚C and above. ^{27}Al spectra were also helpful for confirming various P species determined using ^{31}P SSNMR (such as berlinite and augelite).

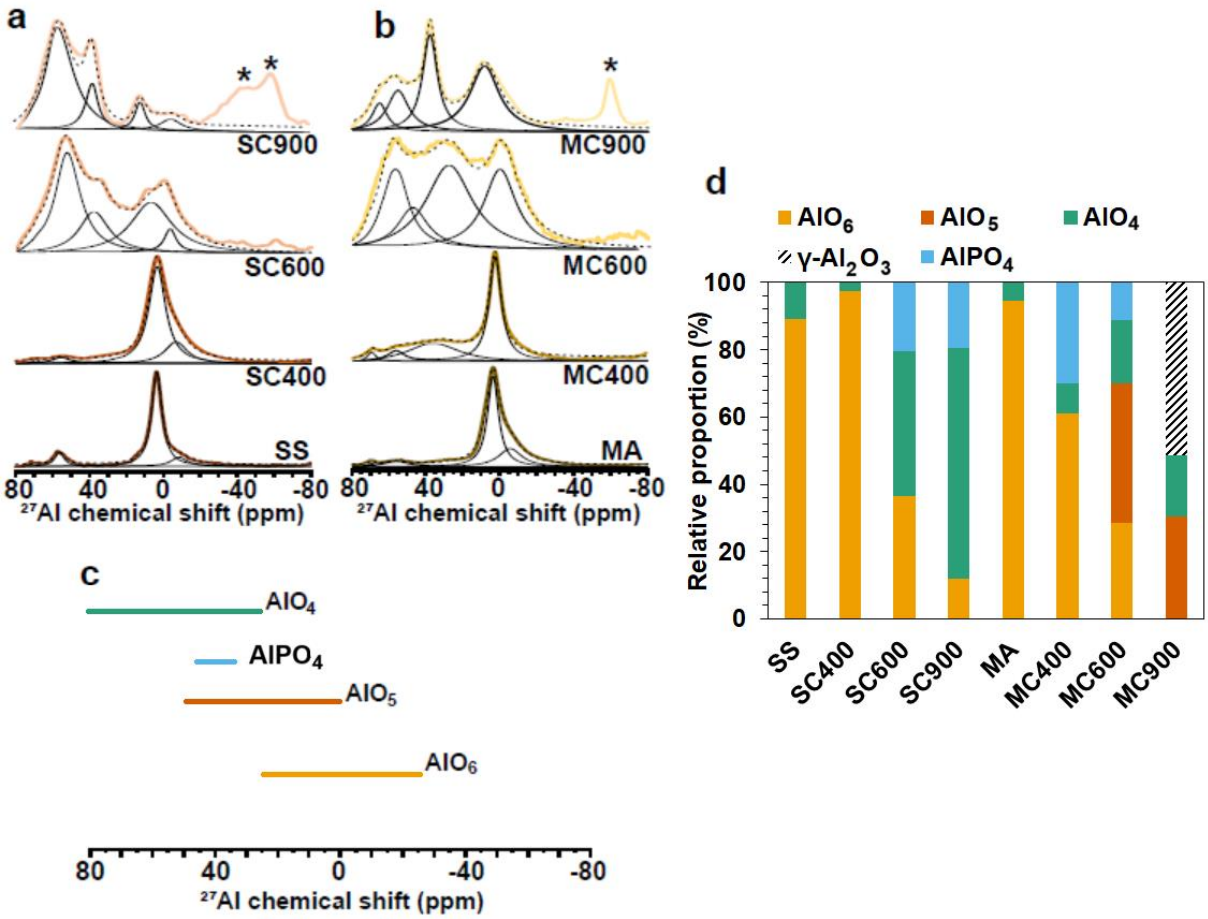

Figure 4.10: ^{27}Al SP-MAS spectra of (a) SS and its chars, (b) MA and its chars, (c) the approximate resonance range for various Al coordination states relevant to this study, and (d) fractional distribution of Al coordination states in the samples. Experimental spectra, simulated spectra, and deconvoluted resonances are shown in multicolour solid lines, black dotted lines, and black solid lines, respectively. The spinning sideband is marked with *.

Table 4.4: Peak assignment[242,245,247–249] for deconvoluted peaks of ^{27}Al SP-MAS NMR spectra of sludge and char samples.

Sample	Deconvoluted peak (ppm)	Peak assignment
SS	56.0	Tetra-coordinated Al
	3.3	Hexa-coordinated Al
	-8.7	Hexa-coordinated Al
SC400	68.9	Tetra-coordinated Al
	55.3	Tetra-coordinated Al
	3.4	Hexa-coordinated Al
	-6.4	Hexa-coordinated Al
SC600	57.0	Tetra-coordinated Al
	38.9	$AlPO_4$ (tridymite form)
	7.0	Hexa-coordinated Al
	-5.0	Hexa-coordinated Al

SC900	56.1	Tetra-coordinated Al
	38.8	$AlPO_4$ (tridymite form)
	12.5	Hexa-coordinated Al, Boehmite (AlO(OH))
	-4.3	Hexa-coordinated Al
MA	69.8	Tetra-coordinated Al
	56.1	Tetra-coordinated Al
	3.8	Hexa-coordinated Al
	-5.7	Hexa-coordinated Al
MC400	67.9	Tetra-coordinated Al
	55.3	Tetra-coordinated Al
	36.6	Berlinite ($AlPO_4$)
	1.7	Hexa-coordinated Al
MC600	59.1	Tetra-coordinated Al
	45.6	Berlinite ($AlPO_4$)
	27.9	Penta-coordinated Al
	0.8	Hexa-coordinated Al
MC900	64.3	γ-Al_2O_3 (tetra-coordinated, first peak)
	56.1	Tetra-coordinated Al
	36.5	Penta-coordinated Al
	7.1	Hexa-coordinated Al, γ-Al_2O_3 (second peak)

4.3.6.2. Al 2p XPS analysis

Al 2p spectra of the samples are presented in Figure 4.11 while XPS peak deconvolution and peak assignments with their relative area are summarized in Table 4.5. Unlike P 2p and C 1s, Al 2p XPS spectra of most samples were dominated by a single peak. Aluminum oxides and hydroxides were difficult to differentiate due to overlapping peak ranges. In this analysis, aluminosilicate and other minor Al compounds, which might have insignificant repercussions for P speciation and P extraction, were not considered for peak assignment. The peak at 74.4 eV in SS probably represented Al-O bonding, possibly due to Al-O-P innersphere complexation between Al and phosphate ion[250] during wastewater coagulation. It could also represent $Al(OH)_3$, Al_2O_3, or $AlPO_4$[251,252], though the last one was less likely since the peaks for $AlPO_4$ in ^{31}P and ^{27}Al SSNMR of SS were not detected in this study. SiO_2 and Al_2O_3 are generally significant constituents of the inorganic fraction of SS[253,254]. In MA, there were two peaks, among which the peak at 75 eV might be $Al(OH)_3$ and that at 74.3 eV might be Al_2O3 as $Al(OH)_3$ has higher binding energy than Al_2O_3. Al in MA was primarily sourced from AS, so MA was likely to have predominantly $Al(OH)_3$.

This is because AS primarily comprises $Al(OH)_3$ as alum reacts to form $Al(OH)_3$ during the coagulation-flocculation process[167]. However, AS can also have Al_2O_3 and SiO_2[166,253]. Aluminum oxide, hydroxide, and oxyhydroxide presence was ascertained in SCs and MCs. As the pyrolysis temperature increased, $Al(OH)_3$ was likely to dehydroxylate to various forms of Al_2O_3[255], some of which were confirmed by ^{27}Al SSNMR in this study. $AlPO_4$ presence was plausible (74.3 eV) in MC400/600, as corroborated by ^{27}Al SSNMR as well. However, $AlPO_4$ peak was not detected in SC600/900 in XPS spectra, contrary to ^{27}Al SSNMR findings. Possibly, $AlPO_4$ XPS peak was masked by the aluminum oxide/hydroxide peak in SC600/900.

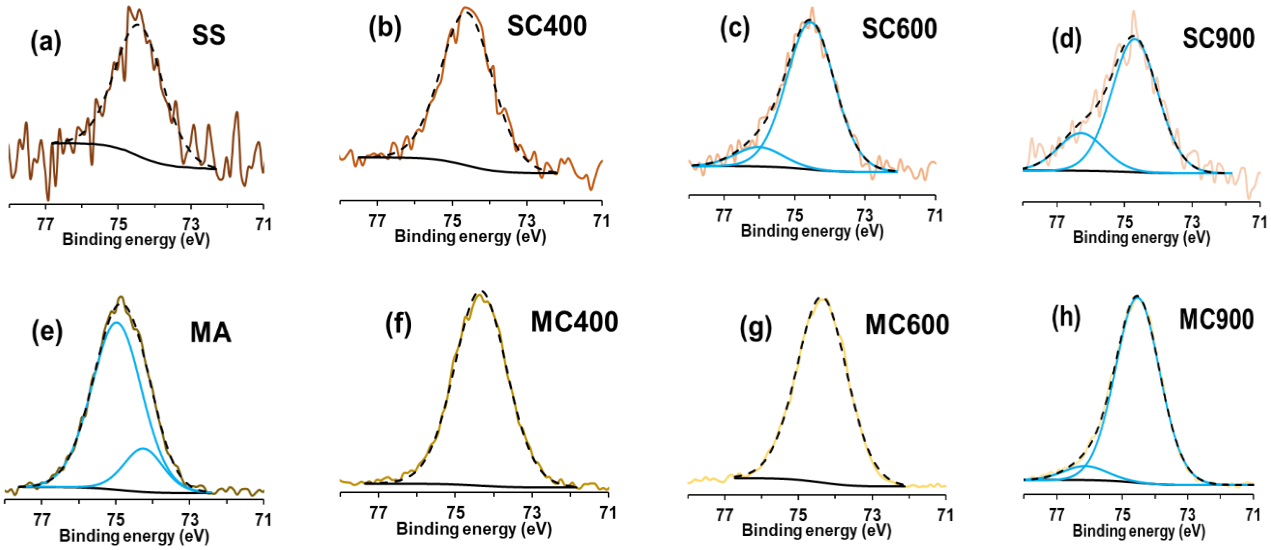

Figure 4.11: Al 2p spectra of (a,b,c,d) SS and its chars (e,f,g,h) MA and its chars.

Table 4.5: Al 2p deconvoluted peaks with peak assignments[164,250–252] and relative area.

Sample	Peak energy (eV)	Full width at half maximum (FWHM) (eV)	Area (%)	Peak assignment
SS	74.43	1.55	100	Al-O, $Al(OH)_3$, Al_2O_3
SC400	74.61	1.62	100	$Al(OH)_3$, Al_2O_3, AlO(OH)
SC600	74.54	1.6	88.32	Al-O, $Al(OH)_3$, Al_2O_3
	76.01	1.6	11.68	Al_2O_3, AlO(OH)
SC900	74.7	1.6	77.68	$Al(OH)_3$, Al_2O_3
	76.28	1.6	22.32	AlO(OH)
MA	74.26	1.24	16.66	$Al(OH)_3$, Al_2O_3
	74.98	1.6	83.34	$Al(OH)_3$, Al_2O_3
MC400	74.34	1.6	100	Al-O, $Al(OH)_3$, Al_2O_3, $AlPO_4$
MC600	74.36	1.6	100	Al-O, $Al(OH)_3$, Al_2O_3, $AlPO_4$
MC900	74.53	1.6	92.95	Al-O, $Al(OH)_3$, Al_2O_3
	76.12	1.6	7.05	AlO(OH)

4.3.7. C speciation and its relationship with P

Carbon constituted a significant fraction of sludge and char samples in this study (Table S 11). Besides, the alkaline extract of MC400 had a distinct dark color compared to the alkaline extracts of other char samples (Figure S 5). Since MC400 also had the highest alkaline P extraction efficiency; hence, carbon analysis was conducted to investigate the relation between P recovery and C speciation.

TOC analysis indicated that organic carbon and elemental carbon constituted the predominant majority in total carbon (TC) in solid and liquid samples (Table S 11 and Table S 12), as total inorganic carbon (TIC) was below the detection limit. Besides, dissolved organic carbon (DOC) in alkaline extracts (Table S 12) showed that carbon in chars produced at elevated temperatures (> 600˚C) was more recalcitrant to dissolution. Increasing pyrolytic temperatures can promote aromatization and formation of turbostratic graphite structures with poor crystallinity[256,257]. Possibly, elevated temperature induced structural changes in the carbon matrix leading to its consolidation, and P might have been trapped in the consolidated carbon, inhibiting its extraction from SC600/900 and MC600/900. Notwithstanding, P speciation was also vital for extraction. For instance, P dissolution efficiency from MC900 was > 50%, while it was < 10% in SC900 due to relatively higher NAIP in MC900 than in SC900. Thus, P transformation as NAIP played a predominant positive role in P dissolution over the inhibitory effects of carbon transformation during pyrolysis.

Interestingly, C dissolution from MC400 was ~ 5-25 times higher than other char samples and had the highest P recovery efficiency. As explained in the previous section, thermal treatment might have promoted the formation of organo-mineral complexes of P, especially in MA chars. High DOC and P extraction from MC400 could be due to the dissolution of these organo-mineral complexes. Additionally, high Al concentration in MA might have catalyzed pyrolytic reactions leading to the formation of easily extractable DOC, similar to biomass chars[258]. A study on chars from lignocellulosic feedstock reported the formation of weakly bound low molecular weight neutrals (uncharged small organics such as alcohols, aldehydes, ketones, sugars, and amino acids) and humic acids during low-temperature pyrolysis (≤450˚C)[258]. Humic acid and other negatively charged DOC could promote P solubility by enhancing ortho-P

desorption from char, and itself get adsorbed on minerals[177]. On the other hand, temperatures > 450˚C promoted secondary pyrolytic reactions, leading to the formation of poorly extractable carbon species[258]. Additionally, the C-O-P bond was possibly weak in MC400 but stronger in MC900 due to encapsulation in stable carbon compounds[86]. Hence, both P and C were poorly dissolved from SC900 and MC900. Stable carbon species (such as aromatic/graphitic carbon) were confirmed by C 1s XPS (Section 4.3.7.1) and FTIR analysis (Section 4.3.7.2) of char samples.

4.3.7.1. C 1s XPS analysis

C 1s spectra of sludge and char samples are shown in Figure 4.12, while the deconvoluted peaks, relative peak area, and peak assignments are summarized in Table 4.6. In general, coherence between C 1s XPS data and ^{13}C SSNMR data was evident. In SS and MA, the alkyl group (C-C, C-H) was predominantly present, followed by alcohol (C-OH)/ether (C-O-C) and minor amounts of carbonyl groups (C=O, O-C=O). The alkene (C=C)/ graphitic carbon fraction in char samples was higher than the other groups (alkyl, ether, amide, and carbonyl). With increasing temperature, the fraction of the alkyl group reduced and completely decomposed at ≥600˚C (as confirmed by ^{13}C SSNMR data as well). Besides, the increasing sharpness of the graphitic peak with increasing temperature indicated the enhanced orderliness/crystallization of the carbon structure. This might explain the higher stability of carbon and low DOC content in SC900 and MC900. P association with this recalcitrant carbon probably made it stable and less prone to dissolution, hence its immobilization. Overall, the thermal treatment increased the stable carbon matrix in both SS and MA chars.

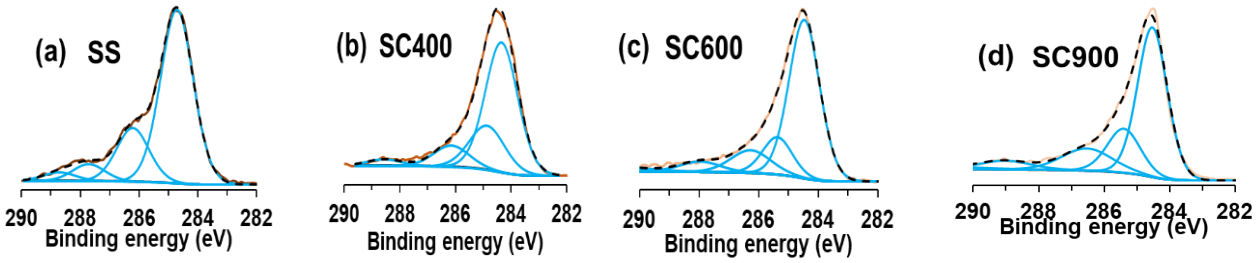

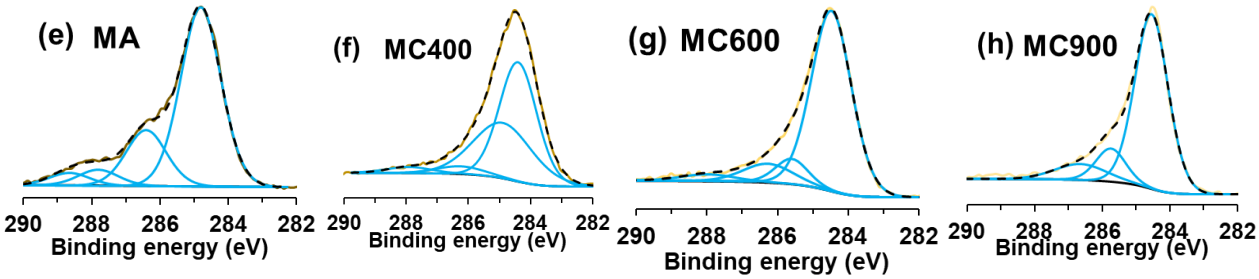

Figure 4.12: C 1s spectra of (a,b,c,d) SS and its chars (e,f,g,h) MA and its chars.

Table 4.6: Deconvoluted peaks of C 1s with their relative area and peak assignments[259–261].

Sample	Peak energy (eV)	Full width at half maximum (FWHM) (eV)	Area (%)	Peak assignment
SS	284.71	1.31	68.80	C-C, C-H
	286.21	1.31	21.08	C-OH, C-O-C
	287.71	1.31	6.81	C=O
	288.71	1.31	3.31	O-C=O
SC400	284.35	1.37	62.31	C=C
	284.87	1.5	23.03	C-C, C-H
	286.15	1.5	11.09	C-OH, C-O-C
	288.55	1.5	3.57	O-C=O
SC600	284.47	1.21	63.64	C=C
	285.37	1.17	14.59	C-N
	286.27	1.57	12.04	C-O-C
	287.97	1.6	5.5	C=O
	290.88	2.71	4.23	Satellite
SC900	284.53	1.07	58.69	C=C
	285.4	1.19	19.21	C-N
	286.53	1.8	14.55	C-O-C
	289.03	1.8	5.55	O-C=O
	290.94	2.71	2	Satellite
MA	284.81	1.39	67.85	C-C, C-H
	286.41	1.39	21.24	C-OH, C-O-C
	287.81	1.39	6.02	C=O
	288.65	1.39	4.88	O-C=O
MC400	284.4	1.41	53.44	C=C
	284.9	2.22	39.11	C-C, C-H
	286.24	1.8	4.44	C-O-C
	287.9	1.66	3.01	C=O
MC600	284.47	1.33	77.39	C=C
	285.6	1.08	8.59	C-N
	286.27	1.65	9.98	C-O-C
	287.97	1.8	4.05	C=O
MC900	284.54	1.16	76.26	C=C
	285.74	1.03	12.79	C-N
	286.64	1.8	10.95	C-O-C

4.3.7.2. FTIR analysis

Some of the important functional groups in the samples were identified (Figure 4.13, Table 4.7), though precise identification in carbonaceous materials was difficult due to the band overlap of functional groups. The effect of acidic pretreatment on the variation in the functional groups was not prominent, as SS and MA have similar spectra. Generally, the functional groups were removed with increasing temperature during the pyrolysis of SS and MA. The absence of a broad peak at 3279 cm^{-1} in char samples indicated the decomposition of inter/intramolecular H-bonded OH groups at 400˚C and above[262], likely leading to dehydration reactions. Similarly, aliphatic C-H (2924 cm^{-1}) and aliphatic CH_x (2853 cm^{-1}) peaks were absent, possibly due to lipid loss as CH_4, CO_2, and other gases or aromatic compounds during pyrolysis. Some of the reactions involving the formation of these gases are enumerated in Section 2.5. These findings were consistent with the ^{13}C SSNMR and C 1s XPS data in this study. The shift in peak at 1636 cm^{-1} in SS and MA to ~1600 cm^{-1} (in SC/MC400) could be due to conjugation (might be olefinic C=C conjugated with phenyl, alkene, and α, β-unsaturated carbonyls) and eventual loss due to heating at 600˚C and above. The aromatic ring peak at 1518 cm^{-1} was apparent in SS and MA but not so much in the char samples (but present nonetheless), possibly due to the high intensity of other functional groups in char. The peak at ~1420 cm^{-1} in SS, MA, SC400, and MC400 likely corresponded to aliphatic C-H stretching, as carbonate was less likely to be present in the samples (evident from TOC analysis in this study). With increasing pyrolysis temperature, the peak intensity in the range 850-1200 cm^{-1} was reduced but still predominant in the spectra. This trend indicated that while C-O was lost due to heating, P-O was retained as inorganic compounds (such as hydroxyapatite)[263,264]. Finally, Si-O vibration (~780 cm^{-1} and ~680 cm^{-1}) of inorganic minerals such as clay and quartz was observed in both sludge and char samples, as these compounds are found in sludge and are thermally stable. In conclusion, sludge samples had diverse functional groups, but with increasing pyrolysis temperature, aliphatic, hydroxyl, and carbonyl groups were lost, while aromatic and inorganic groups (such as P-O and Si-O) were retained.

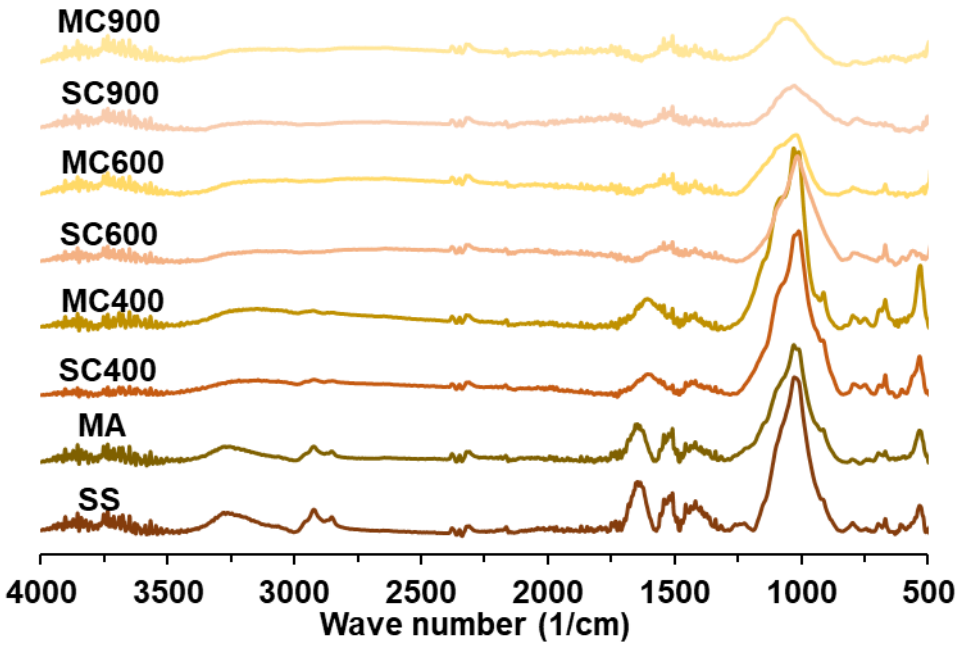

Figure 4.13: FTIR spectra of the sludge and char samples.

Table 4.7: Peak assignments for the spectra of sludge and char samples[263–267].

Peak (cm^{-1})	Peak assignment
3279	H-bonded OH, possibly OH-ether hydrogen bonds
2924	Aliphatic CH
2853	Aliphatic CH_x
1636	C-OH, C=O, C=C, amide I
~1600	Possibly olefinic C=C conjugated with phenyl, alkene, and unsaturated carbonyl
1518	Aromatic ring
~1420	Carboxyl-carbonate structure, aliphatic C-H stretching
850-1200	P-O, C-O
~780	Si-O vibration of inorganic compounds
~680	Si-O vibration of inorganic compounds

4.3.7.3. ^{13}C SSNMR analysis

$^{13}C\{^{1}H\}$ cross polarization – magic angle spinning (CP-MAS) NMR analysis of the sludge and char samples was conducted for detailed carbon assessment. However, only C species closer to H in space rather than all C species were assessed. In the alkyl region of 0-50 ppm, broad resonance from 10-40 ppm was observed in sludges (SS and MA) and SC400 and MC400. These groups could be $-CH_2$ or $-CH_3$, with the latter seen more upfield than the former. Alkyl groups started to disappear > 400°C (in SC600, the $-CH_2$ resonance was very

weak). It indicated the decomposition of organic fatty hydrocarbons into CH_4, CO_2, and other gaseous and aromatic compounds[268]. In the O-alkyl region of 60-110 ppm, resonance corresponding to carbohydrates[177] was present in SS, MA, SC400/900, and MC400/600 (chemical shift depended on what was directly bonded to the -OH). The trend was similar to alkyl groups; $-CH_3$ showed peaks more upfield, followed by $-CH_2R$, then $-CHR_2$ and $-CR_3$. O-CH-O resonance, possibly in SS, MA, and SC400 (too weak in MC400, hence not assigned), also confirmed the presence of carboxyl carbons. The abundance of alkyl and alcohol groups in the char prepared at 400˚C possibly explained their higher DOC, as explained in the previous section. It was found that OP associated with O-alkyl groups was more easily extracted than those associated with refractory alkyl and aromatic carbon groups[59,269]. Moreover, some carboxyl and hydroxyl groups may form organo-mineral with Ca and Mg and thus prevent the contact between Ca, Mg, and P and their consequent precipitation[59]. With increasing pyrolysis temperatures, such groups reduced (while aromatic carbon increased), which meant the formation of Ca and magnesium phosphate compounds[59], which were recalcitrant to dissolution in alkaline conditions. In the aromatic region of 110-160 ppm, broad resonance appeared in all the char samples (except MC900), and its prominence increased with the increasing temperature, indicating the conversion of alkyl and O-alkyl groups to aryl C. Carbon atoms existed primarily as RC=CR in MC900 (inset of Figure 4.14), with no H bonded or nearby (i.e., exists as an extended carbon network). However, in SC900, H-bonded carbon was predominant as $^{13}C\{^1H\}$ CP-MAS and ^{13}C SP-MAS had similar spectrum (inset of Figure 4.14). Nevertheless, increasing aromaticity with increasing pyrolysis temperatures was confirmed. A slight resonance corresponding to carboxylic C=O (170 to 180 ppm) in the protein region was also observed in SS and MA.

In conclusion, increasing pyrolysis temperature led to the loss of diverse functional groups and aromatization of carbon. P was encapsulated in a recalcitrant carbon matrix when pyrolysis was conducted at elevated temperatures (> 600˚C). Thus, low-temperature pyrolysis (~ 400˚C) was most suitable for P recovery from char.

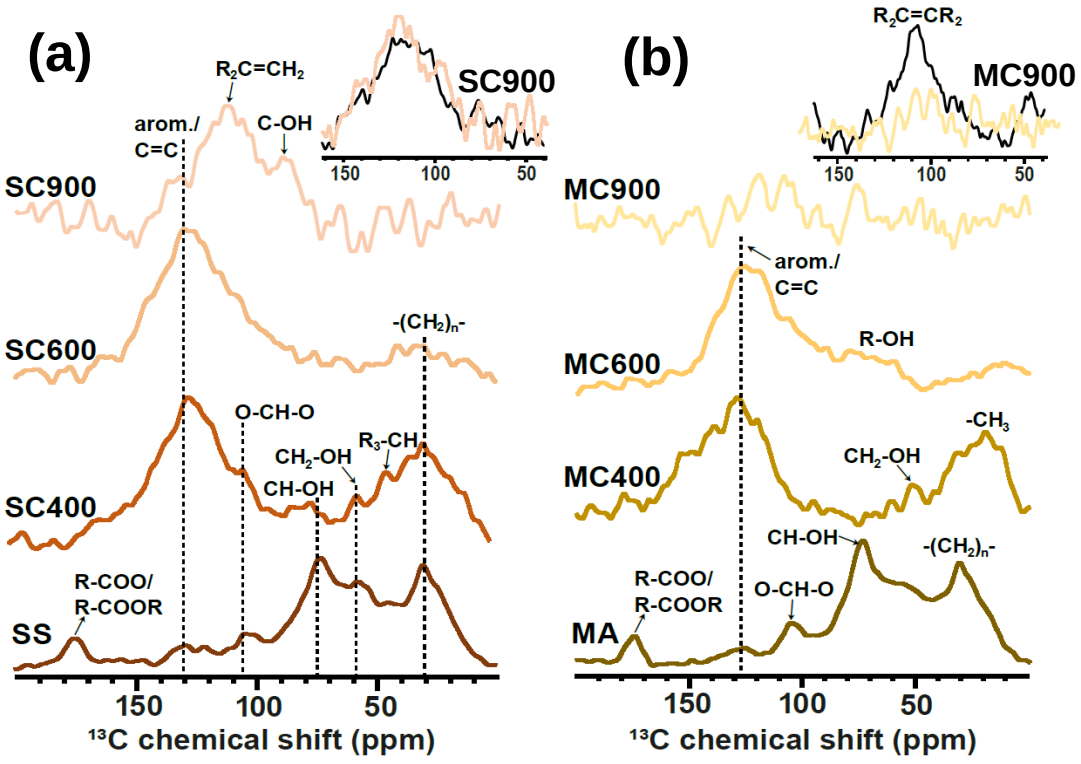

Figure 4.14: $^{13}C\{^{1}H\}$ CP-MAS spectra of (a) SS and its chars (b) MA and its chars. ^{13}C SP-MAS of SC900 and MC900 are shown with black lines and compared with their respective $^{13}C\{^{1}H\}$ CP-MAS spectra (multicolor) in the inset of (a) and (b), respectively.

4.3.8. Trace element analysis

Some major trace elements (TEs) detected in sludge and char samples were Ba, Cu, Ti, and Zn (Table 4.8). In general, TEs concentration increased with increasing pyrolysis temperature in the char samples. This enrichment was expected as TEs such as Cu and Zn do not volatilize easily even at high temperatures (~1000˚C), especially if thermally treated without chlorine-based additives[270,271]. However, in this study, Zn concentration in SC900 was lower than SC400/600, while in MC char, the trend was: MC400>MC600/900. It seems that excess Al ions in MA positively influenced the Zn volatilization, and hence, it was removed at a lower temperature compared to SS pyrolysis. High Zn volatilization (>70%) during SS pyrolysis above 750˚C has been reported in another study[272]. Though there are several studies on the co-pyrolysis of SS with organic and inorganic additives for TE stabilization/removal[273], the authors could not find any such study on the co-pyrolysis of SS with AS. Thus, this could be an interesting research avenue to explore.

Table 4.8: Trace element in sludge and char samples.

Sample	Trace element (mg/kg)			
	Ba	Cu	Ti	Zn
SS	<500	664 ± 21	1944 ± 71	1318 ± 51
AS	<500	<500	834 ± 10	<500
SC400	<625	1350 ± 37	3623 ± 29	2526 ± 63
SC600	729 ± 41	1532 ± 93	3631 ± 619	2945 ± 177
SC900	810 ± 29	1669 ± 72	4416 ± 176	960 ± 13
MC400	<1000	1525 ± 299	3450 ± 132	1679 ± 272
MC600	<1250	<1250	3154 ± 312	<1250
MC900	<1000	1465 ± 66	4186 ± 240	1092 ± 22

As per EU regulation of 2019/1009[274] for fertilizing products, the chars in this study exceeded the maximum allowable concentration for Cu and Zn. Thus, P extraction from char in this study was more prudent than the direct application of char on farms. In acidic or alkaline extract, the major TEs reported in this study were below the calibration limit of ICPOES. In other words, analyzed TEs were contained in the solid matrix during the entire operation, making their disposal easier. It would be interesting to analyze TEs using ICPMS for their more nuanced assessment in future studies.

4.3.9. Morphology, surface area, and porosity of chars

The surface characteristics of char affected the leachability of elements from it and its potential application as an adsorbent for environmental remediation. The morphology (Figure 4.15) and N_2 adsorption-desorption isotherms (Figure 4.16) are shown below. The main parameters for BET fitting are summarized in Table S 13, while the surface characteristics are summarized in Table S 14. Char samples had irregular surfaces, and there was no apparent distinction between chars of SS and MA in this regard (Figure 4.15). All the char samples had negligible micropores (pore diameter< 2nm). The surface area for the chars prepared at 900˚C was higher than those prepared at 400/600˚C (in their respective cohort), indicating the positive influence of high temperature on the surface area. SC900 and MC900 had the smallest pore size among their cohort, possibly due to the loss of volatiles leading to unblocking of micropores[263]. At lower temperatures (400/600˚C), these micropores might have been blocked due

to the recondensation of volatiles (especially when pyrolysis is conducted in a horizontal tube furnace). There was no clear trend of changes in surface area and pore size with temperature for SS chars. For MA chars, the surface area increased with temperature, but no clear trend in pore size was observed. These trends may be due to the complex interplay of factors such as the blocking of pores due to sintering and inorganic compounds[263] and pore enlargement during the intermediate thermoplastic stage (550-650˚C)[275]. Nevertheless, the positive influence of co-pyrolysis of SS with AS on the surface characteristics was apparent. The surface area and average pore diameter of MA chars were higher than SS chars for all the pyrolysis temperatures (except the average pore diameter of SC900 was greater than MC900). In conclusion, the pyrolysis temperature seemed to play a predominant role in determining the char surface characteristics, and co-pyrolysis of SS with AS led to improved surface area across the temperature range.

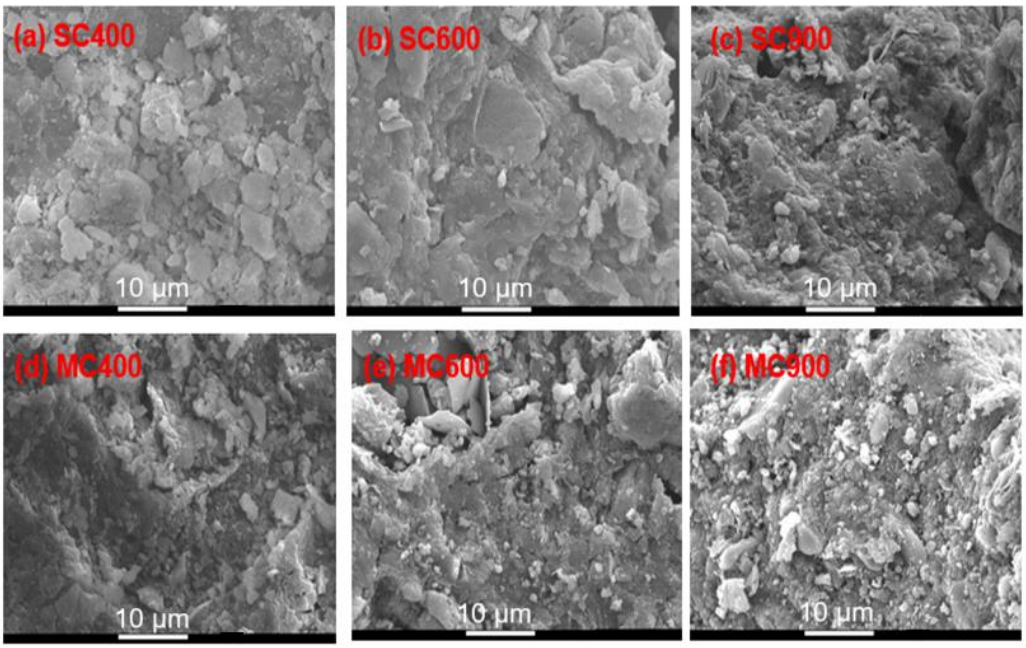

Figure 4.15: SEM images of the char samples (2500x magnification).

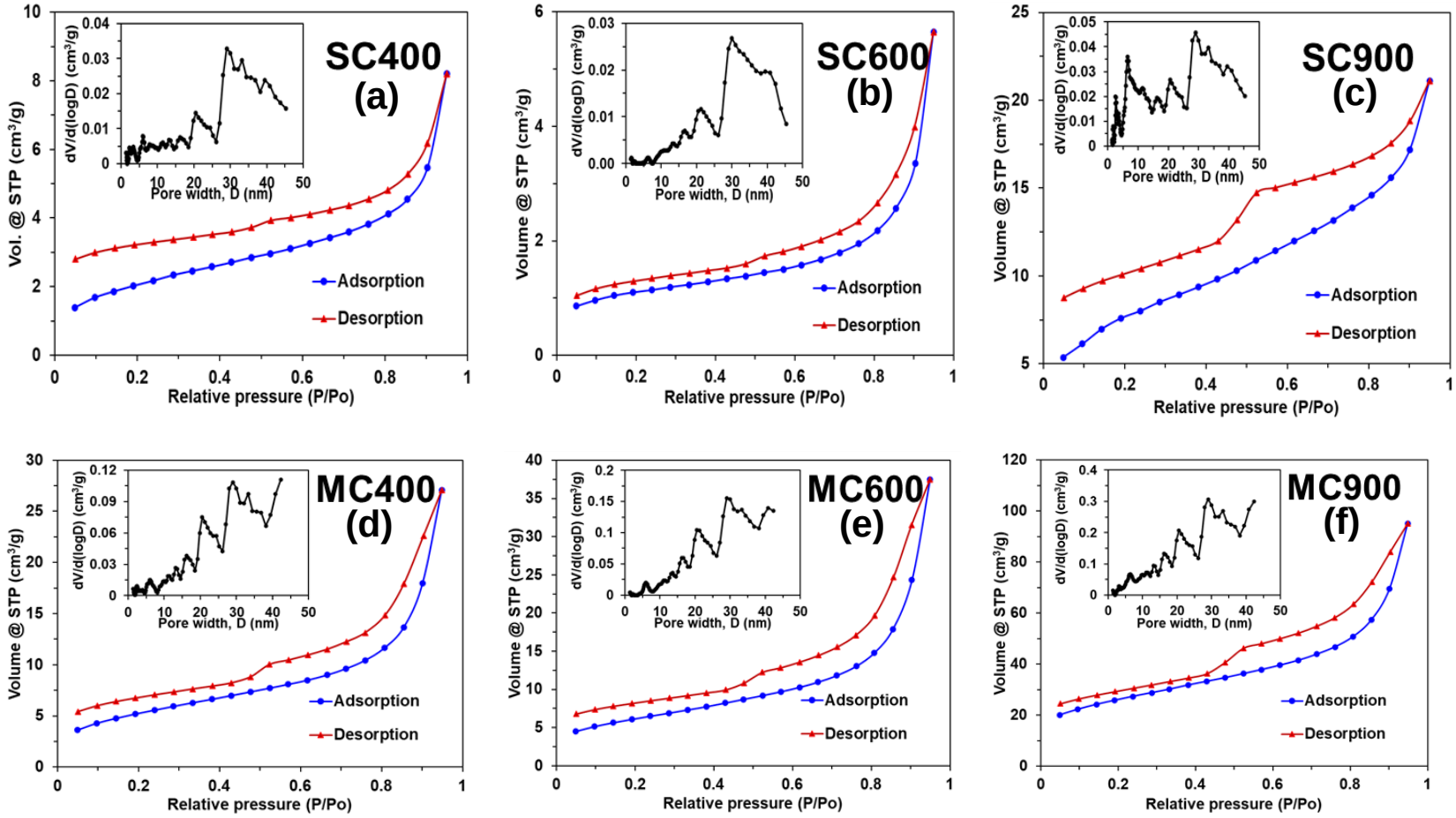

Figure 4.16: Adsorption-desorption isotherm of the char samples. The pore size distribution is provided in the inset.

4.3.10. Environmental implications

Most of AS worldwide is landfilled[166] (including in Singapore), which has a significant economic and environmental cost[166,167]. This study offered a dual waste management strategy along with P extraction. The P extraction efficiency from the char prepared using amended SS and low-temperature pyrolysis (400˚C) was highest due to the relative abundance of alkaline soluble P species and DOC compounds. The process mechanism is illustrated in Figure 4.17, summarizing the changes in P, Al, and C species in the char samples. SS char had a relative abundance of Ca ortho-P across various pyrolysis temperatures while Al ortho-P dominated in the MA chars. This trend is consistent with the relative abundance of these cations in the pyrolysis feedstock. SC400 had a relatively higher concentration of pyro-P compared to MC400 indicating that excess Al ions in MA prevented the formation of pyro-P and instead enhanced Al-P formation. The fraction of Ca-P in total P of MA chars increased when pyrolysis temperature increased to 900˚C which indicates that Ca-P is thermodynamically more stable at elevated temperatures. The changes in Al and C species in SC and MC samples are similar, with some exceptions such as the formation of $AlPO_4$ and γ-Al_2O_3. Higher pyrolysis temperature (> 600˚C) led to the formation of some graphitic carbon. Possibly, P was bound to recalcitrant aromatic and graphitic carbon which led to its lower alkaline extraction efficiency. As P and Al compounds are relatively non-volatile in the temperature range investigated in this study, their concentration in the char increased with increasing pyrolysis temperature leading to their consolidation in the solid phase. The crystallinity of the compounds was also more evident with increasing pyrolysis temperatures.

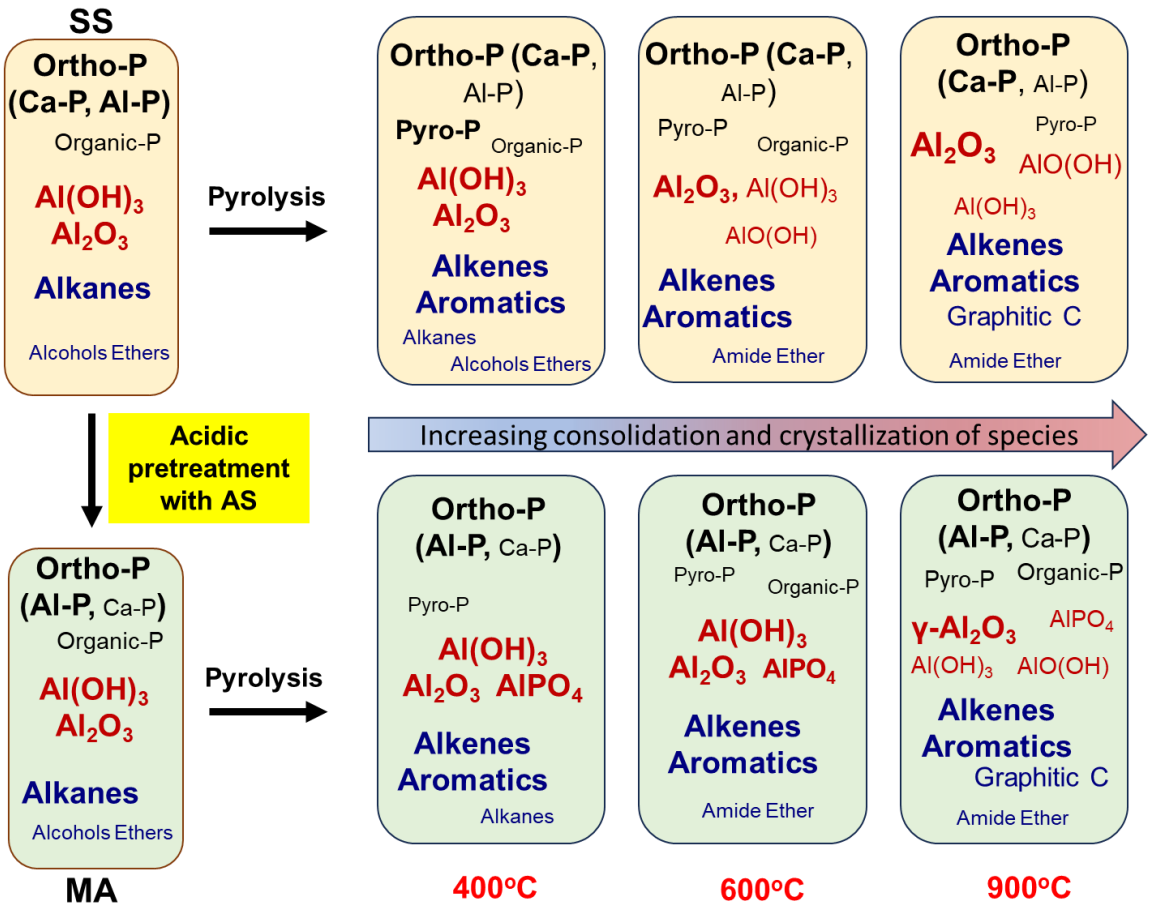

Figure 4.17: The process mechanism is summarized highlighting the changes in P (black font), Al (dark red font), and C (navy blue font) speciation during the entire process. The predominant species are indicated with a bigger font and in bold. The acidic pretreatment and pyrolysis temperature had a critical effect on P speciation.

Low-temperature pyrolysis meant a relatively lower energy requirement for pyrolysis. Further, the alkaline extract was rich in P and Al with low contaminant concentrations (e.g., trace elements). P can be recovered as fertilizer salts such as struvite, dicalcium phosphate, and hydroxyapatite[8], while Al as a polyaluminum chloride-based coagulant[14,216]. Other alternatives are recycling acidic and alkaline extract for multiple extraction cycles[210,276] and recovering NaOH after removing P and Al[63]. However, the additional economic and environmental cost and process sophistication might hinder the commercial exploitation of these alternatives. Thus, there is a need for further research in this direction.

The direct application of char as a fertilizer might not be feasible as TEs in char were above the regulatory limits. Being essentially free from TEs, the addition of AS aided the dilution of TEs in SS. But it also reduced the calorific

value of the mixture, affecting the potential recovery of biofuel using pyrolysis (though the quality of biofuel might improve[277]). Nevertheless, AS improved the surface properties of MC chars compared to SC chars. Thus, after alkaline extraction, the char might be useful as an adsorbent in primary wastewater treatment or other applications. However, further research is required in this direction to ascertain techno-economic feasibility. The eventual goal is to prevent CO_2 emission and resource loss via incineration and landfilling.

4.4. CONCLUSION

This study demonstrated that acidic pretreatment of SS with AS before pyrolysis led to higher alkaline P recovery from char than unamended SS. This high recovery was due to the conversion of apatite phosphorus (AP) to non-apatite inorganic phosphorus (NAIP) in amended SS. Speciation of P, Al, and C (the three most important elements in this study) using liquid/solid-state NMR (L/SSNMR), XPS, XRD, and FTIR indicated that P extraction from char prepared at high temperature (900˚C) was difficult due to its immobilization in the carbon matrix (mainly composed of aromatic/graphitic carbon). In unamended SS char (900˚C), P extraction was reduced further due to the formation of recalcitrant Ca-P crystalline phases such as whitlockite. Some of the major trace elements (TEs) in SS were concentrated in char irrespective of pyrolysis temperature, except Zn, which was partially volatilized beyond 600˚C. The approach proposed in this study might be helpful for the co-treatment of two sludges with resource recovery. Nevertheless, environmental and economic cost assessment, and pilot studies must be conducted to assess its potential for commercial application. With further refinement, this process might promote sustainable fertilizer production and efficient sludge management.

5. EFFECT OF ACIDIC PRETREATMENT IN HYDROTHERMAL CONDITIONS ON PHOSPHORUS TRANSFORMATION AND ITS RECOVERY

Chapter 5 has been submitted as a research article in Resources, Conservation and Recycling and it is currently under revision. The preprint is available as: Tiwari, Satya Brat and Veksha, Andrei and Chan, Wei Ping and Fei, Xunchang and Liu, Wen and Lisak, Grzegorz and Lim, Teik Thye (T.T.), Directional Sewage Sludge Transformation Using Acidic Hydrothermal Carbonization for Enhanced Alkaline Extraction of Phosphorus. http://dx.doi.org/10.2139/ssrn.4848678. It has been published with some modifications in the Resources Conservation and Recycling journal after peer review (https://doi.org/10.1016/j.resconrec.2024.107936).

Some minor modifications have been incorporated into the published version to ensure its consistency with this thesis.

5.1. INTRODUCTION

Sewage sludge (SS) stands out as a prospective source of reclaimable phosphorus (P) owing to its elevated P content relative to other biomass residues [1]. Among diverse strategies for P recovery from SS [1,9], acidic extraction of P from incineration SS ash has been well investigated and it has reached commercial application. However, incineration is both capital- and energy-intensive, has a substantial carbon footprint, and requires feedstock to be dried before operation. Most of these disadvantages plague other thermochemical treatment methods such as gasification and pyrolysis. Hydrothermal carbonization (HTC) offers direct treatment of SS with high moisture content, leading to SS valorization into biofuels and chemicals with potentially lower carbon footprint and operational cost [278]. Hence, HTC has attracted the attention of researchers in recent years.

During HTC, moist SS is subjected to heating at ~180 – 250 ^{o}C in a closed vessel in autogenous pressure. The end product is mainly the solid residue, often

called hydrochar, and process water rich in organics and elements such as P and N, depending on HTC operational. Prior P-related studies on HTC of SS mainly assessed the effect of HTC operational conditions on the fate of P [115,279]. HTC temperature stood out as the most critical parameter for P speciation in these studies [115]. A few studies aimed for directional P transformation i.e., its conversion to apatite phosphorus (AP) (mainly Ca-P) from non-apatite inorganic phosphorus (NAIP) (mainly Al-P) or vice versa. For instance, additives such as CaO and $CaCl_2$ in SS during HTC promoted NAIP to AP conversion [156,161,162,280,281]. Conversely, AP to NAIP transformation can be promoted by adding Al and Fe salts such as $AlCl_3$ and $FeCl_3$ [41,281], though such studies are relatively few. Nevertheless, the addition of salts for P transformation increases the HTC operational cost and natural resource consumption. The concentration of major cations (Al, Ca, Fe and Mg) can influence the precipitation/dissolution of phosphate and its speciation [84] but depends on other factors such as HTC temperature and pH, among others. Though these studies investigated the influence of major cations on P extraction, they did not quantify the concomitant extraction of trace elements (TEs). The studies on the co-dissolution of TEs with P from hydrochar using acidic extraction are rare while those using alkaline extraction are even rarer [8,80]. Thus, the research gap in identifying the P transformation strategy during HTC to enhance its recovery, while simultaneously reducing the contamination with TEs was apparent.

This study sought to bridge this gap by applying a two-step process of SS treatment for P recovery with reduced TE contamination. Instead of using a pure salt, Al-rich alum sludge (AS) from the water treatment plant was mixed with SS and thereafter subjected to acidic HTC. It was hypothesized that the abundant Al from AS could accentuate AP to NAIP conversion in SS during acidic HTC, leading to its increased proportion in hydrochar. Subsequently, P could be recovered from hydrochar using alkaline extraction as NAIP readily dissolves at high pH. Since most TEs precipitate in an alkaline environment, the proposed approach might be a cost-effective and convenient method of separating P from TEs. The main objectives of this study were to: (1) assess and optimize the effect of HTC temperature and Al/P molar ratio (APMR) in the feedstock on P conversion and subsequent P alkaline extraction from the hydrochar, (2) evaluate the fate of major cations that form phosphate compounds (i.e., Al, Ca, Fe, and

Mg) in the entire process, (3) quantify the distribution of targeted TEs in solid and liquid phases in the entire process, and (4) identify the optimum pH of acidic HTC to maximize P recovery and minimize the concentration of other elements of concern.

5.2. MATERIALS AND METHODS

5.2.1. Sample preparation and characterization

In this study, dewatered sewage sludge (SS) and dewatered alum sludge (AS) were collected from a wastewater treatment plant (WWTP) and a water treatment plant (WTP) in Singapore, respectively. WWTP treats wastewater from domestic and non-domestic sources[282] while WTP treats surface water[283]. Dewatered SS was a mixture of primary and secondary sludges after their digestion in an anaerobic digester while dewatered AS was obtained after the sedimentation process using alum. The collected samples were dried at 105^{o}C, pulverized to particle size < 150 µm and kept in airtight containers within desiccators. Henceforth, SS and AS samples in this study would mean processed SS and AS, respectively (unless stated otherwise). The physico-chemical characterization of SS and AS is presented in Table 5.1.

Table 5.1: Physico-chemical characterization of the sludge samples.

Parameter	Sewage sludge (SS)	Alum sludge (AS)
Moisture content (wt.%)*	87 ± 0.1	66 ± 0.1
pH*	6.7 ± 0.1	7.21 ± 0.04
Dry density (g/mL)	0.62 ± 0.02	0.58 ± 0.04
Higher heating value (J/g)	17044 ± 348	ND
Total dissolved solids (mg/kg)	29696 ± 389	11880 ± 462
Ash_{550} (%)	23.7 ± 0.3	59.7 ± 0.6
Ash_{950} (%)	22.2 ± 0.4	31.7 ± 7.4
C (wt.%)	38.2 ± 0.3	9.79 ± 0.04
H (wt.%)	6.2 ± 0.1	4.0 ± 0.2
N (wt.%)	6.0 ± 0.1	1.01 ± 0.03
S (wt.%)	1.2 ± 0.1	1.6 ± 0.2
Al (mg/kg)	11101 ± 429	190977 ± 15906
Ca (mg/kg)	23614 ± 896	4788 ± 1039
Fe (mg/kg)	13676 ± 499	16937 ± 227
Mg (mg/kg)	7938 ± 289	1764 ± 327
P (mg/kg)	20159 ± 786	1072 ± 37
Si (mg/kg)	32260 ± 1835	42204 ± 279

* As-received dewatered sludge samples.

ND: Not determined

Moisture content, pH, dry density, higher heating value, total dissolved solids, Ash_{550}, Ash_{950}, and CHNS analysis in SS and AS were analyzed as per the conventional methods[168,169]. The elemental composition in SS, AS, and hydrochar samples was determined after digesting them in a microwave acid digester (Anton Parr Multiwave5000) using a mixture of concentrated HCl, HNO_3, HF, and H_3BO_3[170]. Major elements such as P, Al, Ca, Fe, and Mg were quantified using Inductively Coupled Plasma-Optical Emission Spectroscopy (ICP-OES, Perkin Elmer Optima 8300 OES). The prominent TEs generally found in SS[77] were quantified using ICP-Mass Spectrometry (ICP-MS, Thermo Fisher iCAP QC) via the TE isotopes recommended in ISO 17294-1:2006[284]. During elemental quantification, blank, blank-spiked and matrix-spiked samples were also analyzed for quality control. The TEs in SS and AS are listed in Table 5.2.

Table 5.2: Trace elements in the sludge samples.

Trace element (mg/kg)	Sewage sludge (SS)	Alum sludge (AS)
As	13.8 ± 0.8	38.91 ± 0.05
Ba	256.3 ± 1.8	44.0 ± 21.2
Cd	< 10.0	< 10.0
Co	< 80.0	< 80.0
Cr	113.9 ± 2.9	18.2 ± 0.8
Cu	611.1 ± 10.0	40.1 ± 17.4
Hg	< 12.0	< 12.0
Mn	125.4 ± 3.0	272.9 ± 6.3
Mo	13.6 ± 0.3	25.3 ± 0.4
Ni	176.4 ± 38.2	49.4 ± 9.1
Pb	< 60.0	107.7 ± 4.1
Sb	< 10.0	< 10.0
Se	< 10.0	< 10.0
Sn	40.3 ± 1.1	< 10.0
Sr	56.0 ± 1.5	< 40.0
Ti	1902.2 ± 21.9	784.5 ± 19.2
V	11.6 ± 0.3	31.7 ± 0.9
Zn	1223.9 ± 53.4	91.6 ± 10.5

5.2.2. Acidic hydrothermal carbonization and alkaline extraction

The experimental plan of this study is illustrated in Figure 5.1. It consisted of a reference process to assess the baseline scenario and a design process

illustrating the proposed process for enhancing alkaline P recovery. Circumscribed central composite design (CCD) was applied to investigate the effect of the APMR in the SS + AS mixture (i.e., MS, "mixed sludge") and HTC temperature on alkaline P recovery. These factors were selected as they were most critical in this study. Other parameters such as residence time, and L:S ratio demonstrated a minor effect on P recovery[115].

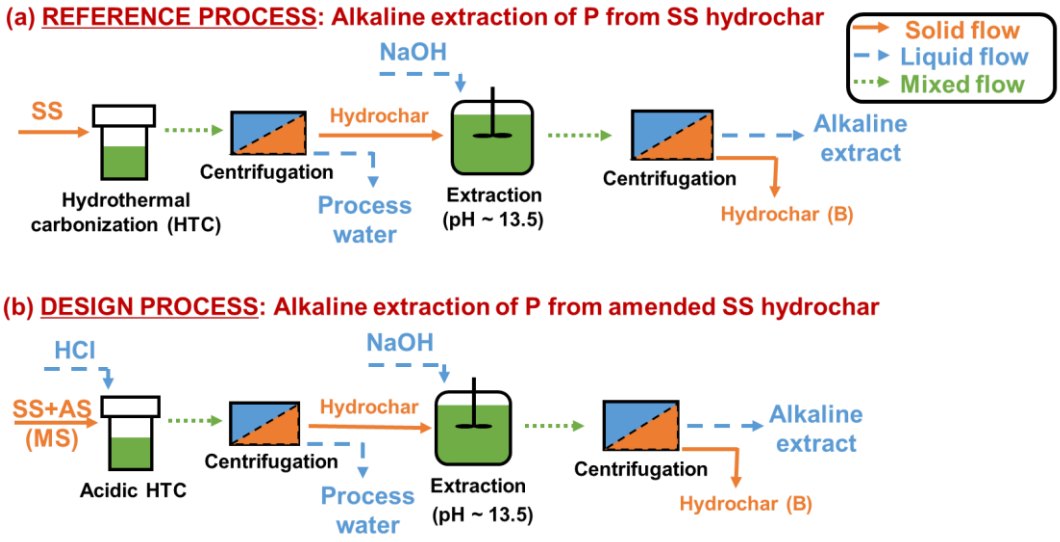

Figure 5.1: Experimental plan in this study showing the (a) reference process to assess the business-as-usual scenario and (b) design process showing the amended scenario. The parameters varied in process (b) are the SS:AS mixing ratio (2.8 – 11.5) to achieve the Al/P molar ratio (APMR) of 1.6 – 4.4 in the mixture (MS), pH at the start of HTC (1 – 3), and HTC temperature (158 – 242°C). In process (a), HTC temperatures are in the range of 158 – 242°C, while other parameters are constant.

HTC temperature can range from 180 – 250°C[113] but due to the absence of a specific boundary[115], 200°C was selected as a centre point of CCD to broadly encompass the temperature range of HTC. For APMR, 3 was the centre point within a CCD range of 1.6 to 4.4, suitable for examining the impact of Al on P transformation. The design space of CCD is detailed in Table 5.3 and depicted in Figure S 6, along with their notations for referencing. Factorial points and axial points were performed in duplicates while the centre point had four replicates. For the reference process, only temperature was varied as acidic HTC would have led to a disproportionate loss of P in the process water[115]. All the SS HTC runs were conducted in duplicates, and all the runs were independent and randomized.

Table 5.3: Hydrothermal carbonization runs conducted using SS and MS as feedstocks.

Run	Feedstock	Temp. (^{o}C)	Al:P molar ratio (APMR)	Notation	Point	Initial pH	pH after adding acid	pH after HTC or final pH	Vol. of 6 M HCl added (mL)
1S	SS	170	-	170	-	5.24	-	5.35	-
2S	SS	230	-	230	-	5.32	-	5.29	-
3S	SS	170	-	170	-	5.25	-	5.37	-
4S	SS	242	-	242	-	5.28	-	5.05	-
5S	SS	200	-	200	-	5.28	-	5.41	-
6S	SS	230	-	230	-	5.35	-	5.28	-
7S	SS	242	-	242	-	5.30	-	5.16	-
8S	SS	200	-	200	-	5.27	-	5.4	-
9S	SS	158	-	158	-	5.32	-	5.38	-
10S	SS	158	-	158	-	5.26	-	5.34	-
1M	MS	230	4	230-4	Factorial	5.54	3.04	3.64	0.17
2M	MS	230	2	230-2	Factorial	5.50	3.02	3.97	0.18
3M	MS	242	3	242-3	Axial	5.57	3.01	4.20	0.18
4M	MS	200	4.4	200-4.4	Axial	5.56	3.00	4.16	0.18
5M	MS	200	1.6	200-1.6	Axial	5.33	2.99	3.75	0.18
6M	MS	200	1.6	200-1.6	Axial	5.44	2.98	3.90	0.17
7M	MS	230	2	230-2	Factorial	5.33	2.99	3.87	0.18
8M	MS	200	3	200-3	Centre	5.35	2.99	4.08	0.17
9M	MS	200	3	200-3	Centre	5.48	2.97	3.97	0.18
10M	MS	230	4	230-4	Factorial	5.66	3.01	4.20	0.17
11M	MS	200	3	200-3	Centre	5.57	3.01	4.06	0.17
12M	MS	200	4.4	200-4.4	Axial	5.54	2.97	3.95	0.18
13M	MS	242	3	242-3	Axial	5.44	3.02	4.20	0.17
14M	MS	170	4	170-4	Factorial	5.54	3.00	3.93	0.18
15M	MS	170	2	170-2	Factorial	5.43	3.00	3.75	0.19
16M	MS	158	3	158-3	Axial	5.43	2.99	3.65	0.17
17M	MS	170	4	170-4	Factorial	5.54	3.00	3.90	0.17
18M	MS	200	3	200-3	Centre	5.48	3.01	4.03	0.17
19M	MS	170	2	170-2	Factorial	5.35	3.03	3.72	0.17
20M	MS	158	3	158-3	Axial	5.50	2.98	3.77	0.17

Each HTC run was conducted in a 45 mL PTFE-lined hydrothermal vessel (4744 General Purpose Vessel, Parr Instrument Company). SS or MS was mixed with ultrapure water using a magnetic stirrer in a ratio of 1:20 g/mL and the initial pH of the mixture was recorded. For acidic HTC, 6 M HCl was added incrementally to lower the pH to 3 (while inducing a negligible change in solid-

to-liquid ratio). Once pH 3 was reached, the vessel was immediately transferred (as pH increased slowly due to the ongoing reactions) to the oven and left for 1 h. After natural cooling, the final pH was recorded, and the process water was separated from hydrochar using centrifugation. The hydrochar was dried and pulverized, and it was mixed with 0.5 M NaOH in a ratio of 1: 50 g/mL for alkaline P extraction. The extraction was conducted in a rotary agitator for 1 hour and thereafter hydrochar was separated, dried, and pulverized. Hydrochar after alkaline extraction was called "hydrochar (B)" (B stands for base). The fractional distribution of major and trace elements of the feedstock in various phases during the entire process was quantified using the mass balance as explained in Table S 15. The experimental errors of > 100 % and < 0 % distribution in some cases could be due to the inadequacy of the microwave acid digestion method to quantify the "total" analyte concentration, sample dilution, and other random errors.

An one-factor-at-a-time (OFAT) experiment was conducted to explore how the final pH after acidic HTC affected the P transformation and overall P recovery, given that CCD runs achieving maximum P recovery had final pH levels exceeding the recommended 3 – 4 range[13]. With temperature and APMR optimized for maximum overall P recovery, pH at the start of HTC was set at 1, 1.5, 2, 2.5, and 3 but the analogous final pH was 1.97 ± 0.15, 2.52 ± 0.08, 3.29 ± 0.23, 3.88 ± 0.04, and 4.42 ± 0.01, respectively. All the runs in OFAT were duplicated, randomized, independent, and listed in Table S 16.

5.2.3. Other analyses

Statistical analysis of CCD was analyzed using the Stat-Ease 360 software (version: 22.0.8 64 bit). Before executing the runs, CCD was checked for the precision of the model, which meant its fraction of design space (FDS) > 0.95. The statistical significance of the model was evaluated using the analysis of variance (ANOVA) ($\alpha = 0.05$). The models obtained were also verified using confirmation runs conducted in duplicates. Some of the samples that exhibited the highest and lowest overall P recovery (as detailed in Table 5.4) were further analyzed for P and Al speciation. Solid-state nuclear magnetic resonance (SSNMR) analyses were performed using a Bruker Avance III HD 600 MHz (14.1 T) spectrometer with a Bruker 3.2 mm HXY magic angle spinning (MAS) probe for ^{31}P and ^{27}Al. The samples were spun at 10 kHz and the recycle delay

was 3 s for ^{31}P while it was 12.5 kHz and 1 s for ^{27}Al, respectively. 80 kHz TPPM high-power H decoupling was used during data acquisition and the chemical shift was calibrated using ^{13}C adamantine methylene resonances (37.77 ppm). All spectra were processed using Topspin software, and SSNMR spectra were normalized for their graphical presentation. X-ray photoelectron spectroscopy (XPS) was carried out using an AXIS Supra spectrometer (Kratos Analytical) with a monochromatic Al K-alpha source at 5 mA. The XPS spectra peaks were referenced to adventitious carbon at 284.8 eV for C 1s for charge correction and peak deconvolution was conducted using ESCApe software. Fourier transform infrared (FTIR) spectroscopy (Shimadzu IRPrestige-21) was conducted in attenuated total reflection (ATR) mode to investigate the changes in the functional groups before and after the alkaline extraction of hydrochars.

Table 5.4: Selection of runs for qualitative analysis.

Run	Description	Selection criteria
200-3	Centre point of CCD	For reference
242-4.4	CCD run with temp = 242 ^{o}C; APMR = 4.4 (confirmation run)	Highest overall P recovery in the CCD experiment
158-1.6	CCD run with temp = 158 ^{o}C; APMR = 1.6 (confirmation run)	Lowest overall P recovery in the CCD experiment
242-4.4-2	pH optimization run with temp = 242 ^{o}C; APMR = 4.4; final pH = 2	Lowest overall P recovery in the pH optimization experiment
242-4.4-2.5	pH optimization run with temp = 242 ^{o}C; APMR = 4.4; final pH = 2.5	Highest overall P recovery in the pH optimization experiment

5.3. RESULTS AND DISCUSSION

5.3.1. Effects of HTC conditions on process outcomes

5.3.1.1. Effects on final pH and hydrochar yield

pH was one of the most critical operational parameters influencing P speciation and repartitioning. The highest and lowest final pH for SS HTC (along with their runs) were 5.41 ± 0.01 (200) and 5.11 ± 0.01 (242), respectively. HTC involves various intermediate reactions, including hydrolysis, decarboxylation, condensation, dehydration and polymerization[285] leading to the breakdown of

biomacromolecules and the formation of organic acids such as formic, acetic, lactic, and levulinic acids[116]. For the temperature range 158 – 200 ^{o}C, the pH increase during SS HTC could be due to the formation of NH_4^+ via the hydrolysis of amino acids from the proteins in SS, while the accumulation of organic acids likely led to a reduction in pH above 200^{o}C (Figure 5.2 (a)). The dissolution of inorganic ions during HTC can also influence the final pH as it can have a buffering effect[115], leading to a pH increase with increasing temperature, as evident in MS HTC runs (Figure 5.2 (b)). For MS HTC runs, the highest and lowest final pH were 4.20 ± 0.00 (242-3) and 3.7 ± 0.1 (158-3), respectively. Possibly, severe HTC conditions at 242^{o}C induced relatively higher dissociation of $Al(OH)_3$ in MS leading to the highest final pH. Prior studies suggest OH^- ion increment after HTC when biomass feedstock was catalyzed using an alkali leading to an increase in final pH[116]. The statistical analysis indicated that the final pH in MS HTC was dependent on temperature, though R^2 was relatively low (< 0.5) (Table S 17).

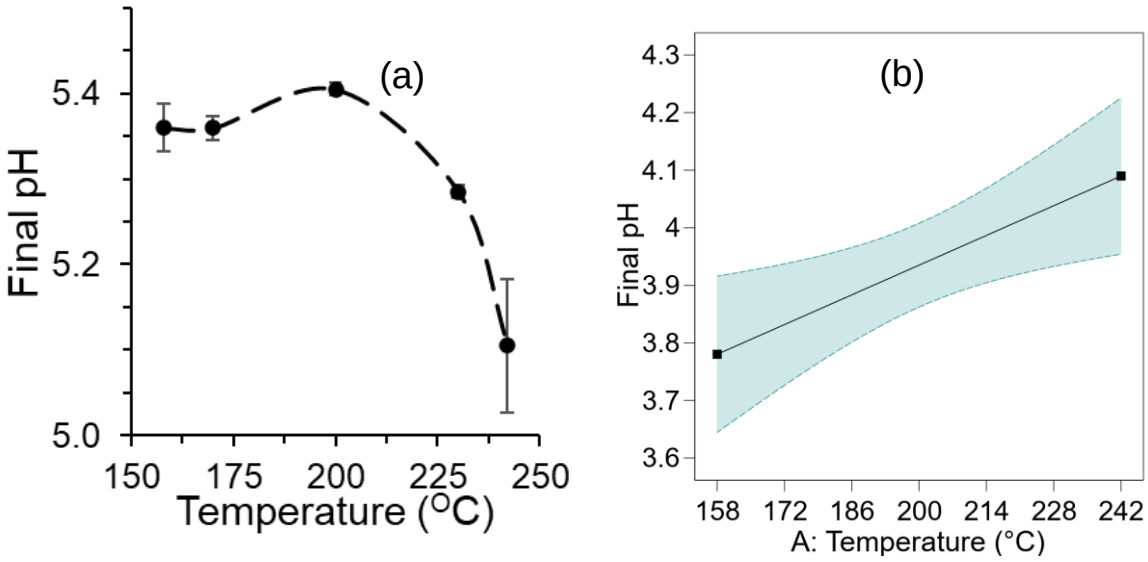

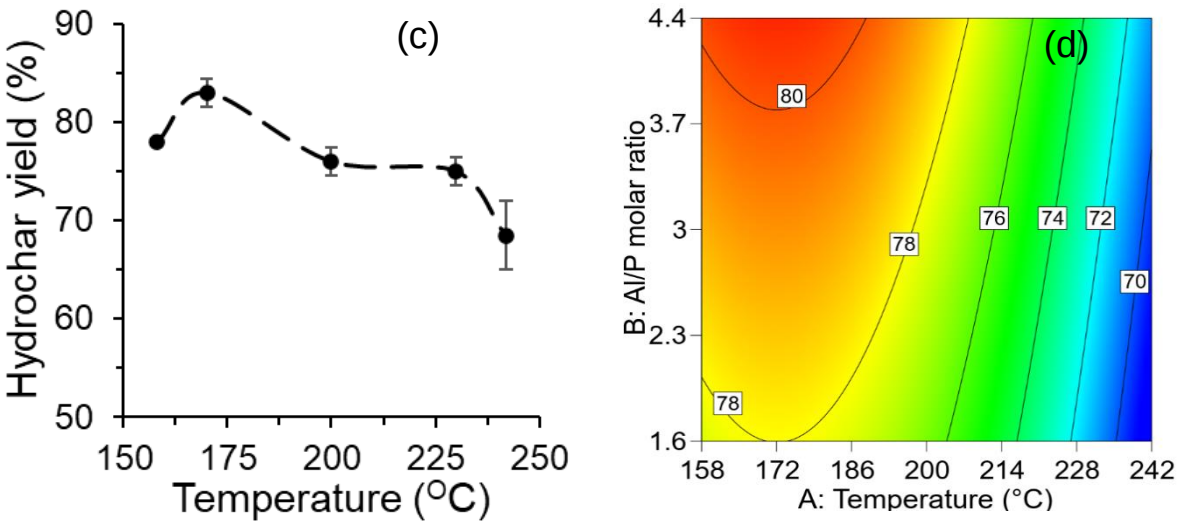

Figure 5.2: pH of the feedstock after HTC (i.e., final pH) of (a) SS (b) MS and the hydrochar yield (%) via HTC of (c) SS and (d) MS. The shaded region in (b) represents the upper and lower bounds of the 95 % confidence interval. The error bar represents the standard deviation.

The hydrochar yield trends (Figure 5.2 (c,d)) for both SS and MS indicated that higher temperatures promoted organic matter dissolution via decarboxylation and dehydration[113], and inorganic compound solubilization[115]. The highest and lowest hydrochar yields from SS HTC (with their corresponding runs) were 83 ± 1 % (170) and 69 ± 4 % (242), respectively. For MS HTC, the highest and lowest hydrochar yields were 81 ± 1 % (170-4) and 69.00 ± 0.00 % (242-3), respectively. The statistical analysis indicated that temperature had a negative influence on hydrochar yield while APMR had a positive influence (Table S 17). In conclusion, the pH variation was the opposite while the hydrochar yield variation was similar in SS and MS HTCs.

5.3.1.2. Effects on P recovery

During the entire process, P was distributed in process water, alkaline extract, and hydrochar (B). P extraction efficiencies based on this distribution are shown in Figure 5.3, while P concentrations (mg/kg) in hydrochars and hydrochars (B) are provided in Figure S 7 (a). For SS HTC, the highest P loss via process water was 27 ± 2 % (242) while the lowest was 15.9 ± 0.2 % (170). P loss increased with increasing temperature above 170^{o}C (Figure 5.3 (a)) which can be attributed to the scarcity of cations such as Al, Ca, Fe, and Mg in SS which generally form compounds with P. The cation/P molar ratio in SS was 0.6, 0.9, 0.4, and 0.5 for Al, Ca, Fe., and Mg, respectively.

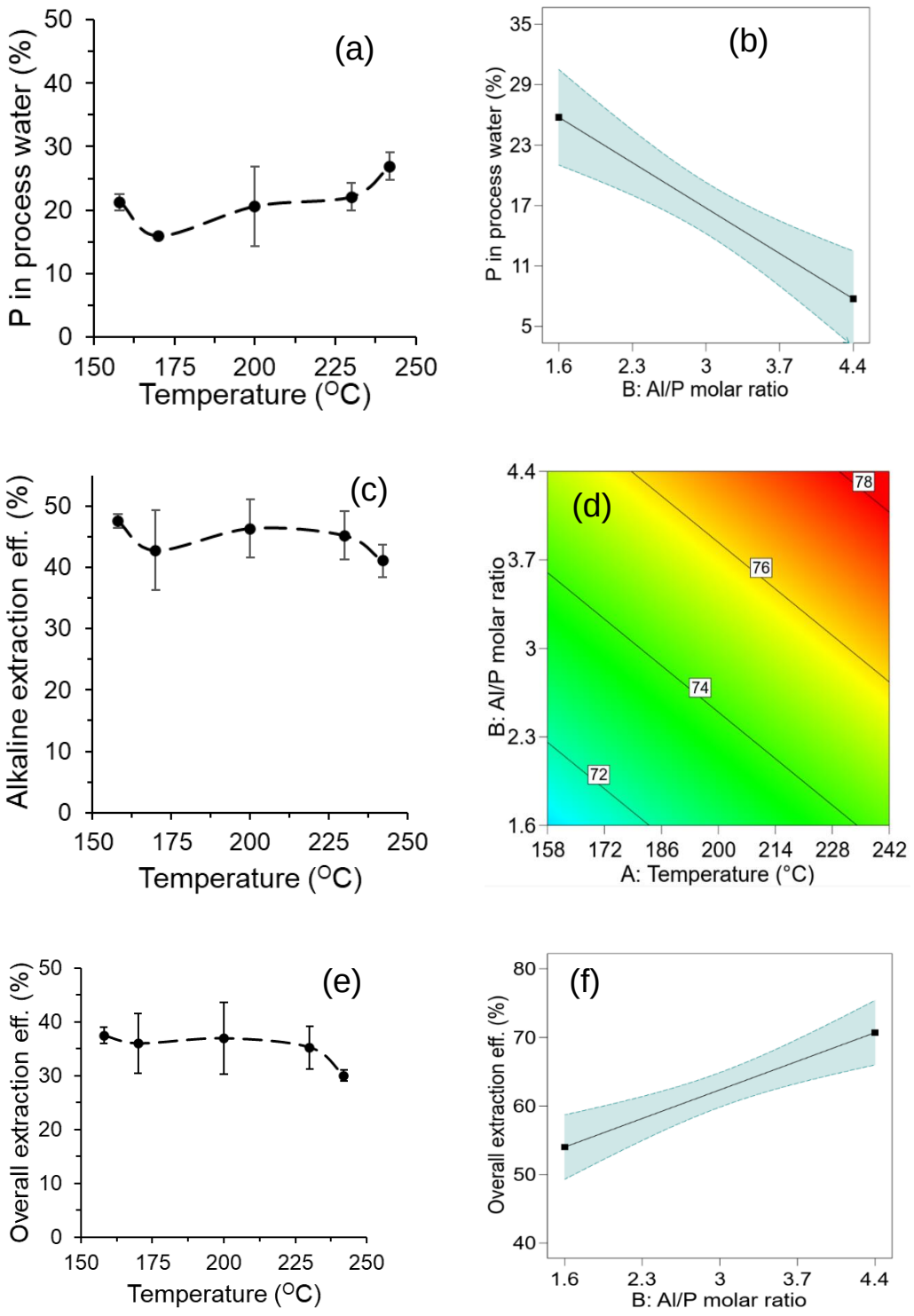

Figure 5.3: The fraction of total P in process water after acidic HTC of (a) SS and (b) MS. The alkaline extraction efficiency of P from hydrochars obtained from HTC of (c) SS and (d) MS. The overall P recovery efficiency after accounting for P loss via process water during the HTC of (e) SS and (f) MS. The shaded regions in (b) and (f) represented the upper and lower bounds of the 95 % confidence interval. The error bar represents the standard deviation.

Organic P decomposed to ortho-P during HTC and possibly the released P did not precipitate with these ions due to their insufficient

concentration[84,115]. The autogenous acidic medium during SS HTC might have also led to a repartitioning of inorganic ortho-P compounds to the aqueous phase leading to further loss of ortho-P, especially when competing anions such as SO_4^{2-} were abundantly present (generally so in SS) to bind with the cations. In MS HTC, P loss only depended on APMR (Figure 5.3 (b)), indicating the critical role of cation (Al) in binding P in hydrochar during HTC. As APMR increased, more Al ions were available to precipitate ortho-P ions released by organic P and AP in the acidic HTC conditions leading to the increase in NAIP. The precipitation of ortho-P with Al was through surface complexation rather than a combination reaction to form $AlPO_4$, as elaborated in the SSNMR analysis (Section 5.3.3).

The highest and lowest alkaline P extraction efficiencies (%) from SS hydrochars were 48 ± 1 % (158) and 41 ± 3 % (242), respectively (Figure 5.3 (c)). Due to the relative scarcity of NAIP in SS hydrochars, alkaline P extraction efficiency was < 50 %. With increasing temperature, AP increased while NAIP reduced[115] because the formation of AP is thermodynamically more favourable at higher HTC[125]. Besides, the Ca/P molar ratio was higher than APMR in SS. The alkaline P recovery efficiency (%) in MS HTC was dependent on both APMR and temperature because they contributed to the AP to NAIP conversion (Figure 5.3 (d)). The highest and lowest alkaline P extraction efficiencies (%) from MS hydrochars were 79 ± 1 % (242-3) and 74 ± 1 % (200-1.6), respectively.

The overall P extraction was lowest for SS HTC at 242^{o}C, i.e., 30 ± 1 % while the highest was at 158^{o}C, i.e., 37 ± 2 %. The results suggested that low temperature (~150 – 160^{o}C) HTC was most favourable for alkaline extraction of P from SS hydrochar (Figure 5.3 (e)). The highest and lowest overall P extraction efficiencies (%) from MS hydrochars were 75 ± 7 % (170-4) and 59 ± 8 % (200-1.6), respectively. The overall P extraction efficiency (%) depended only on APMR (Figure 5.3 (f)), as the effect of temperature was statistically insignificant ($p > 0.05$) (Table S 17). While a higher APMR was preferred, its increase was constrained by the reduction in total P extracted per unit mass of MS, given that AS contained negligible P (~0.1%). For instance, if the effect of temperature was disregarded in MS HTC, P recovered was highest when APMR was 4 (11.46 ± 0.73 mg P/g MS_{dry}) but lowest when APMR was 4.4 (10.62 ± 0.86 mg P/g MS_{dry}).

Moreover, since AS had a low calorific value (3390 ± 282 J/g) [286], MS hydrochar would not be a suitable biofuel if APMR was too high. The ANOVA and fit statistics indicated that the models describing the fate of P were adequate except for the significant lack of fit ($p < 0.05$) (Table S 17). Confirmation runs were conducted to verify the models, whose details are available in SI (Table S 18 and Table S 19). In conclusion, acidic HTC and the addition of AS with SS led to AP to NAIP transformation and consequently, ~22 – 45 % higher overall P extraction efficiency was achieved compared to SS HTC.

5.3.1.3. Effect on other relevant major elements

The distribution of Al, Ca, Fe, and Mg in the by-products of HTC are shown in Figure 5.4 while their concentrations in hydrochars are provided in Figure S 7. The fraction of these elements in the process water reduced with increasing temperature above 170^{o}C during SS HTC (Figure 5.4 (a)). The average Mg fraction in process water of SS HTC ranged from 36 to 46 % which was the highest among all the relevant major elements while Fe had the lowest (5 – 13 %). Al and Fe had relatively higher fractions of alkaline extractable species (~15 – 20 %) compared to Ca and Mg (~5 – 15 %). Overall, these elements were concentrated in hydrochar (B) (> 45 %), irrespective of temperature. Besides, the immobilization in hydrochar increased with increasing temperatures above 170^{o}C. For MS HTC, the average fraction in process water was highest for Ca (64 – 71 %) (Figure 5.4 (b)). This range was much higher compared to the Ca fraction in process water during SS HTC (13 – 33 %), indicating the critical role of low pH (~3 – 4) in accentuating Ca dissolution during HTC. The average Al fraction in process water was 14 – 23 %, which was much lower than Ca. The average alkaline extractable fraction of Al was 49 – 57 %, which was much higher than Ca, Fe, and Mg (< 17 %). The scarcity of Ca, Fe, and Mg in alkaline extracts for MS HTC cases meant that relatively purer salts such as struvite and $Al(OH)_3$ could be recovered from the alkaline extract[216] in the downstream process compared to SS HTC. Overall, the co-dissolution of P and Al and a relative scarcity of other major elements during alkaline extraction possibly indicated the Al-P association in the hydrochars of MS.

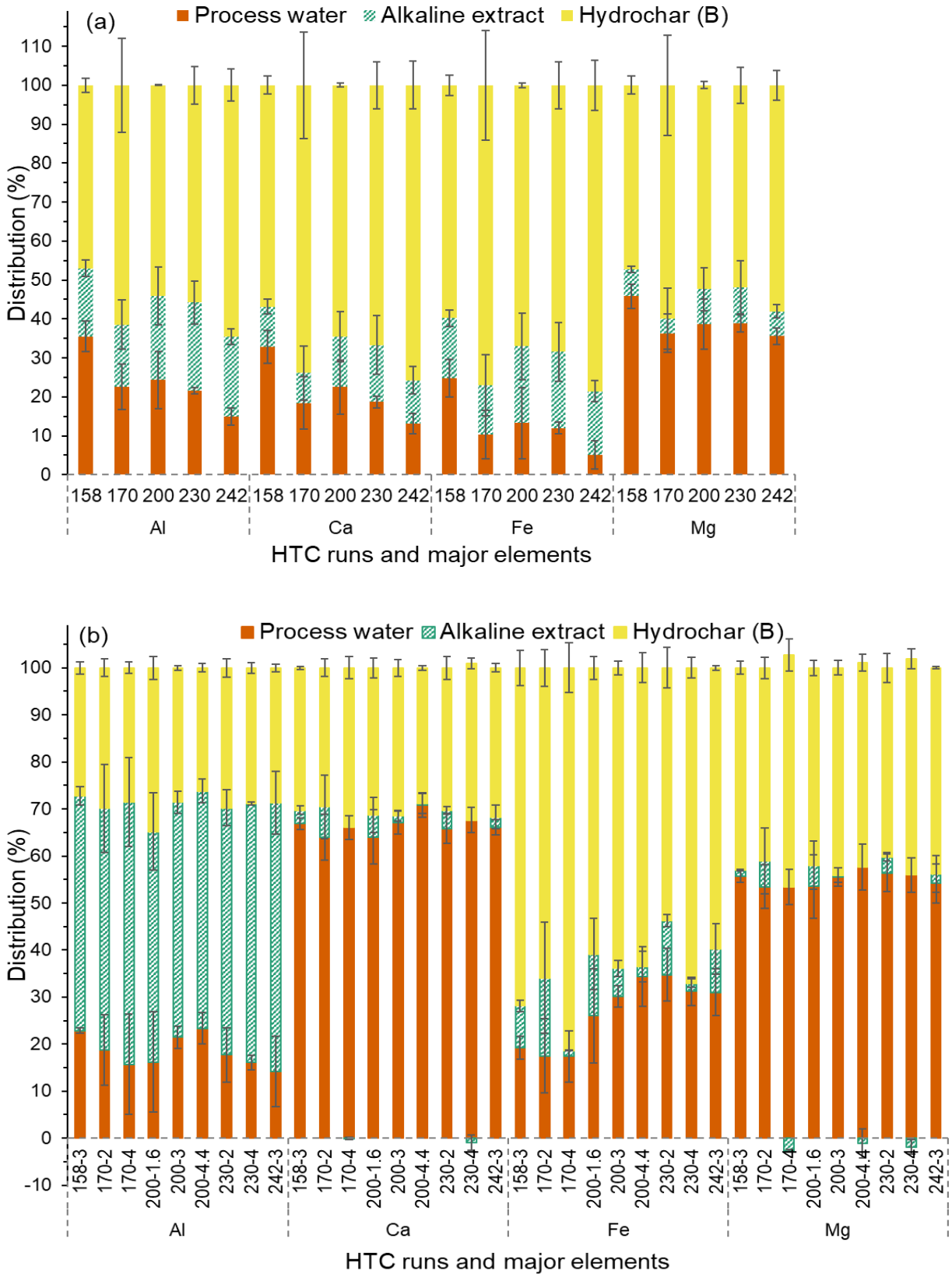

Figure 5.4: The distribution of relevant major elements within the feedstock across both aqueous and solid phases in (a) reference (SS HTC) and (b) design (MS HTC) processes. The error bar represents the standard deviation.

5.3.1.4. Effect on trace elements

Based on EU regulation[274] on fertilizing products (including those obtained from SS), solid organic fertilizer containing solely P as a macronutrient should have at least 2 % by mass of total P_2O_5 equivalent. Though N and K were present in hydrochar and hydrochar (B), they were not analyzed. SS hydrochars, SS hydrochars (B), and MS hydrochars had P concentration as P_2O_5 equivalent > 2% but the trace element concentration in them was unacceptable according to the EU regulation (Figure S 8). Therefore, P extraction from hydrochar was a safer approach for P recovery but it was pertinent to assess the partitioning of TEs in various phases during the extraction process. For SS HTC (Figure 5.5 (a)), Zn, had the lowest average dissolution in process water while Ni had maximum, i.e., 6 – 16 % and 33 – 46 %, respectively. In the alkaline extract, the average fraction was highest for Zn (28 – 40 %) while Cr had the lowest (4 – 26 %). Ti had the highest average fraction (62 – 66 %) in hydrochar (B), while Ni had the lowest (39 – 42 %) due to its dissolution in process water. For MS HTC (Figure 5.5 (b)), the lowest and highest average fraction in process water was for Cu and Ni, i.e., 8 – 23 % and 46 – 56 %, respectively. In the alkaline extract, Zn predominated with the average fraction of 27 – 42 % while Cr was < 5 %. Cr was primarily present in hydrochar (B) with an average fractional distribution of 74 – 82 % while Zn had the lowest fractional distribution in hydrochar (B) (29 – 40 %) owing to its extraction during acidic HTC and alkaline extraction.

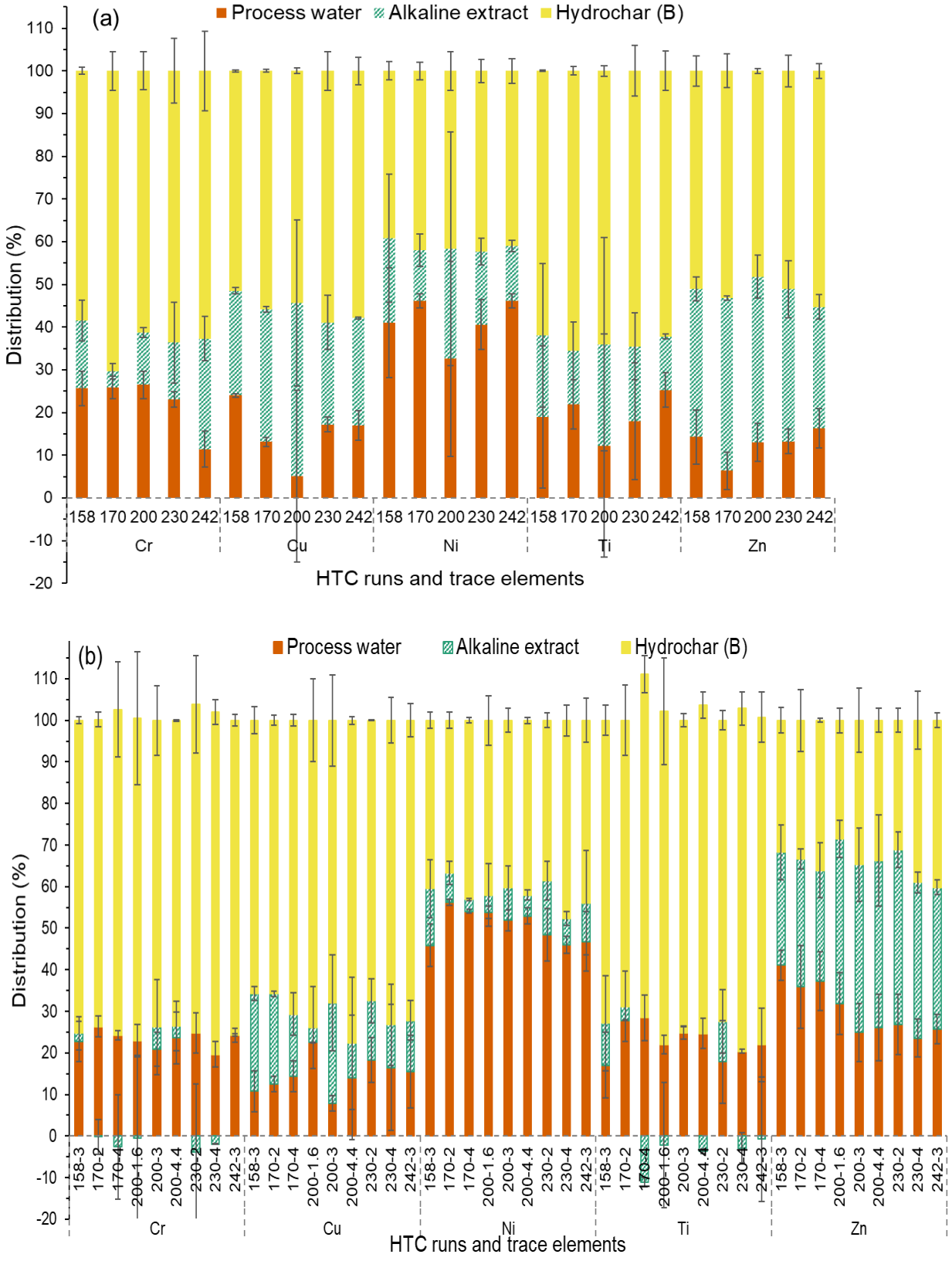

Figure 5.5: The distribution of relevant trace elements within the feedstock across both aqueous and solid phases in (a) reference (SS HTC) and (b) design (MS HTC) processes. The error bar represents the standard deviation.

The fate of TEs was dependent on the complex interplay of factors such as dissolution in acidic conditions, re-precipitation with anions, chelation with functional groups, and immobilization in the carbon matrix of hydrochar[287]. The addition of AS with SS diluted the concentration of most of the analyzed TEs. P content in alkaline extracts corresponding to SS HTC and MS HTC were ~0.04 % and ~0.1 % by mass of P_2O_5 equivalent. This is much lower than the EU regulation for liquid organic fertilizer (i.e., at least 1 % by mass of P_2O_5 equivalent if P is the only macronutrient in the fertilizer). Thus, P recovery via salt precipitation or other further processing methods is necessary though this aspect was beyond the scope of the current study. In conclusion, the fractional distribution of TEs in the alkaline extract was relatively less (except Zn) and the immobilization of TEs in hydrochar was more successful for MS HTC than SS HTC. The TEs with concentration below the calibration limit in hydrochar and hydrochar (B) are listed in Table S 20 and Table S 21.

5.3.2. pH optimization of acidic HTC — effect of final pH of HTC on the extraction of major and trace elements

Among the major elements, P and Al had similar dissolution patterns during acidic HTC and alkaline extraction (Figure 5.6 (a)). P fraction in hydrochar (B) increased (from 6 to 12 %) while that in process water reduced (from 21 to 17 %) with increasing final pH from 2.5 to 4.4. P fraction in the alkaline extract also reduced marginally (from 73 to 71 %) with increasing pH in the same pH range. This trend indicated that as the final pH increased, the AP to NAIP conversion was less efficient. The increasing concentration of Ca in hydrochar (B) with increasing final pH reaffirmed this conversion trend. Due to the higher acid volume needed to achieve a final HTC pH of ≤ 2.5, the suggested final pH for optimal P recovery in this scenario would be ~3 – 4, consistent with non-HTC conditions[13]. For the final pH in the range of 2.5 – 4.4, Al had the highest fraction in alkaline extract (52 – 63 %) while Ca and Mg were prominent in process water across the entire final pH range, i.e., 65 – 93 % and 60 – 69 %, respectively. Fe had distribution strongly dependent on the final pH.

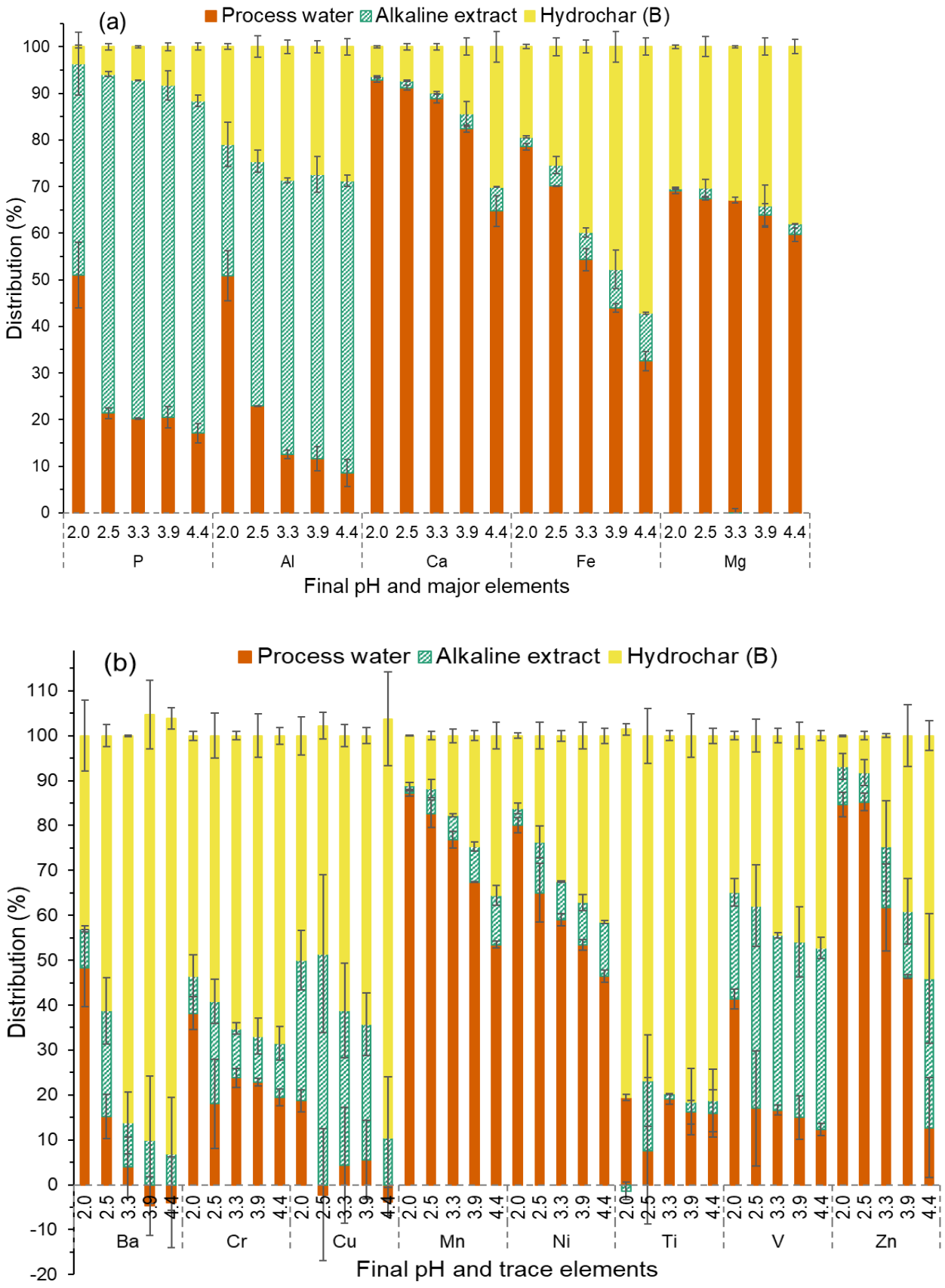

Figure 5.6: The distribution of some of the (a) major and (b) trace elements in the solid and liquid phases during the pH optimization experiment of acidic HTC of MS. The error bars represent the standard deviation.

Among the TEs (Figure 5.6 (b)), the lowest final pH led to maximum fractional distribution in process water, which was expected as the dissolution of elements is high at low pH. Mn, Ni, and Zn had ≥ 80% fraction in process water at pH 2. These elements were more sensitive to pH variation as evidenced by a steep gradient of fraction in process water as the final pH increased. For other TEs, the fraction in process water at pH 2 was < 50 % and the fraction in process water in the pH range of 2.5 – 4.4 was relatively stable. The fraction in the alkaline extract was relatively higher for Cu (10 – 51 %) while it was < 12 % for Cr, Mn, and Ni. Ba (43 – 97 %), Cr (53 – 68 %), Cu (50 – 93 %), and Ti (77 – 82 %) had the highest fraction in hydrochar (B). The absolute concentration of these TEs in different phases depended on their initial concentrations in MS and that determined the appropriate operational final pH. Overall, the final pH of ~3 – 4 was most desirable for P recovery and the immobilization of TEs in the hydrochar but the exact recommended pH would depend on the purity of the alkaline extract expected and other techno-economic considerations. The concentration of relevant major and trace elements in hydrochar and hydrochar (B) are provided in Figure S 9 while the TEs with concentrations below the calibration limit in hydrochar and hydrochar (B) are listed in Table S 22.

5.3.3. P and Al speciation and effects on its extraction

5.3.3.1. ^{31}P and ^{27}Al SSNMR analysis

^{31}P and ^{27}Al SSNMR analyses of the hydrochar and hydrochar (B) samples revealed the chemical state of P and Al in the samples. ^{31}P spectrum for AS was not reported as it had negligible P concentration (~0.1 %). SS had a sharp resonance at 3.4 ppm followed by an adjacent broad shoulder upfield (-10 – 2 ppm) (Figure 5.7 (a)). The peaks of various crystalline Ca-P species such as monetite, brushite, hydroxyapatite and octacalcium phosphate (OCP) have been reported in the range of -1.5 – 3.4 ppm[187]. The peak at 3.4 ppm likely corresponded to OCP but it could also encompass peaks of other amorphous Ca ortho-P (protonated or deprotonated) species, as evidenced by the adjacent broad shoulder. It could also include ammonium phosphate species such as $NH_4H_2PO_4$ and $(NH_4)_2HPO_4$[186] because SS is also rich in ammonia. The protonated ortho-P presence is affirmed by P 2p XPS analysis as well (Section 5.3.3.2). Generally, a more negative chemical shift is associated with protonated phosphate anion while positive values indicate deprotonated phosphate species[187]. The adjacent

shoulder in the range -10 – 0 ppm indicated the presence of protonated ortho-P adsorbed to $Al(OH)_3$ or uncondensed aluminum phosphate[13] or M^+ & M^{2+} aluminophosphate [188] (where M is metal). On comparing hydrochar spectra with the SS spectrum, it was clear that acidic HTC led to P transformation (Figure 5.7 (a)). The broad peak at -12.6 ppm in all the hydrochar samples before alkaline extraction represented Al orthophosphate and aluminophosphate of alkali (M^+) and alkali earth metals (M^{2+})[188]. Possibly, ortho-P formed bidentate binuclear inner-sphere surface complexes with Al[12]. The absence of a peak at -30 ppm implied that there was no $AlPO_4$ formation. Nevertheless, this shift from predominantly apatite phosphate to Al-P in hydrochar led to higher alkaline P recovery compared to SS. Further, the conversion from AP to NAIP in MS was accentuated by high APMR. For instance, the small peak corresponding to AP was present in 200-3 and 158-1.6 but absent in other hydrochar samples, which had APMR of 4.4 (Figure 5.7 (a)). In the spectra of hydrochar (B) samples, the only prominent peak at 3.6 ppm likely corresponded to Ca-P (Figure 5.7 (b)). It indicated that Ca-P remained undissolved in alkali and thus affected the overall P recovery. In essence, ^{31}P spectra indicated that high APMR promoted AP to NAIP conversion during acidic HTC and the AP that did not convert would remain undissolved during alkaline P extraction.

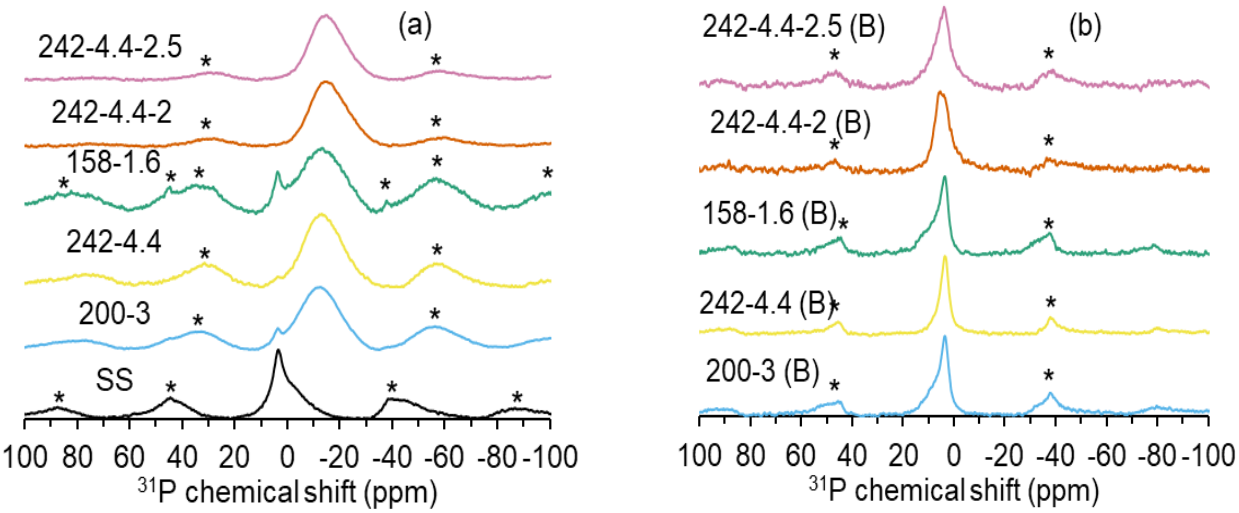

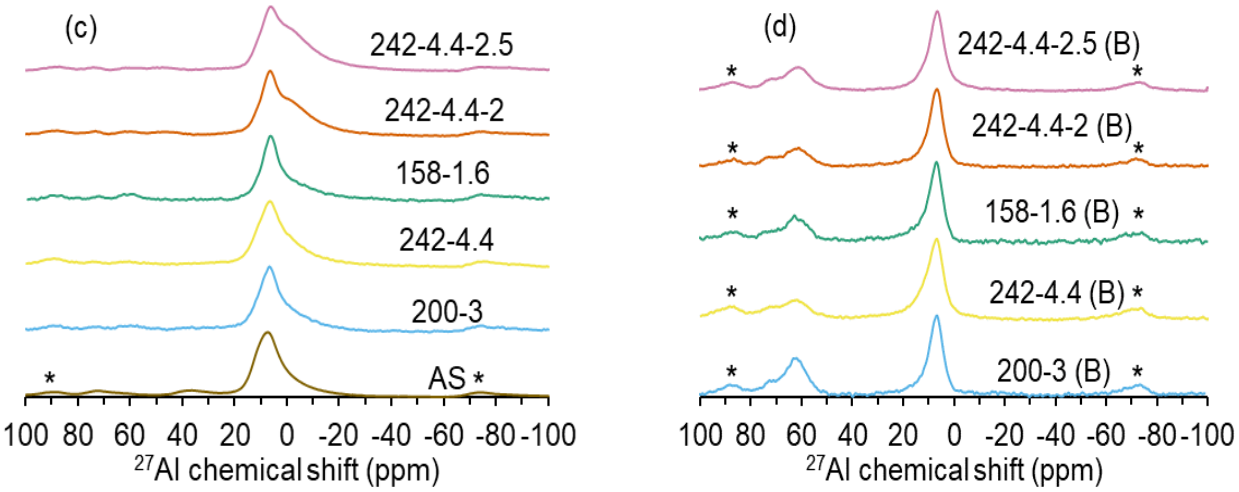

Figure 5.7: (a, b) ^{31}P and (c, d) ^{27}Al SSNMR spectra of selected hydrochar and hydrochar (B) samples. SS and AS spectra are also provided for reference. The asterisk (*) represents the spinning sideband.

The changes in the Al chemical environment were also assessed to complement the ^{31}P spectra data. In AS and hydrochar samples, AlO_6 (hexa-coordinated Al) was predominant as evident from a single major peak at 7.3 ppm (Figure 5.7 (c)). AS is expected to be predominantly composed of $Al(OH)_3$ as a result of the reaction of alum during the coagulation-flocculation process but it can also contain Al_2O_3 and SiO_2[13], or Al-Si compounds. However, the prominent peak of AS at 7.3 ppm neither corresponded to $Al(OH)_3$ (major peak at 8.2 ppm) nor to Al_2O_3 (peak at 16.0 ppm) (Figure S 10). Nevertheless, minor peaks at 38.2 ppm and 70.5 ppm in the AS spectrum closely resembled the minor peaks of $Al(OH)_3$. It was highly likely that the $Al(OH)_3$ signal was masked by other AlO_6 species in AS. These minor peaks of AS were absent in hydrochar species which indicated the depletion of $Al(OH)_3$ and probable complexation of Al with ortho-P, as mentioned for ^{31}P spectra. Alternatively, $Al(OH)_3$ could have dissociated and reprecipitated as Al (hydroxo) oxides as apparent from XPS data (Section 5.3.3.2). Also, in 242-4.4-2 and 242-4.4-2.5 (Figure 5.7 (c)), a low-frequency shoulder in the -15 – 5 ppm region was visible. This resonance could correspond to $Al(OH)_2H_2PO_4$ which has a resonant frequency lower than $Al(OH)_3$[189]. The presence of protonated ortho-P in 242-4.4-2 and 242-4.4-2.5 was corroborated by ^{31}P spectra as well. Other hydrochar samples did not have this lower frequency shoulder prominently because their final HTC pH was more than 3. As the pH increased, the deprotonated ortho-P form dominated the

dissociation equilibrium of H_3PO_4. Thus, the role of final pH was more important than temperature in determining Al speciation. AlO_4 coordination state corresponding to $AlPO_4$ was missing in hydrochar samples, which corroborates with the findings of ^{31}P spectra. All hydrochar (B) samples had similar spectra marked by the major resonant frequency at 6.7 ppm corresponding to AlO_6 and a minor peak at 62.0 ppm corresponding to AlO_4 (Figure 5.7 (d)). In conclusion, the variation in Al coordination states was influenced more by final pH than temperature and this was corroborated by the ^{31}P spectra data.

5.3.3.2. P 2p and Al 2p XPS analysis

P 2p XPS spectra of SS and hydrochar samples were meant to complement ^{31}P SSNMR analysis. P 2p spectra of hydrochar (B) samples are not shown due to poor signal/noise ratio. The details of the deconvoluted peaks such as peak energy, relative area, peak assignment and full width at half maximum can be found in Table 5.5. Due to the proximity of peaks and heterogeneity of the samples, accurate peak assignment was difficult. Nevertheless, the approximate assignment was useful for assessing the trend in P speciation. The deconvoluted peaks of SS (Figure 5.8 (a)) indicated the presence of HPO_4^{2-} at 133.2 eV and $H_2PO_4^-$ at 134.1 eV, mainly associated with Ca, Na and NH_4^+, as concurred by ^{31}P SSNMR data. The acidic HTC led to a peak shift to a higher binding energy value in the hydrochar samples (Figure 5.8 (b – f)), indicating the changes in P speciation. Most hydrochar samples have two deconvoluted peaks at 133.5 ± 0.1 eV and 134.6 ± 0.2 eV, corresponding to metal PO_4^{3-} and metal HPO_4^{2-}, such as with Ca, Fe and Al. Na and K ortho-Ps were not expected in hydrochar samples as they are highly reactive and labile in acidic conditions compared to other metal ortho-Ps. P could be linked directly or indirectly to C as well given the abundance of C in hydrochars. Thus, P linked to the phenolic group (Ph), C-PO_3 and C_2-PO_3 groups and C-O-P groups were possible. Some of these could correspond to organic phosphates in SS[13]. However, the presence of organic phosphates in the hydrochars was less likely as hydrothermal conditions generally led to the conversion of all the P species to ortho-P[81]. Thus, the presence of condensed phosphates such as metaphosphate (PO_3^{3-}) and pyrophosphates ($P_2O_7^{4-}$) in the hydrochars, was also less likely. However, some pyrophosphate and monoester-P (< 5 %) were reported in $FeCl_3$-assisted HTC of SS at 200^{o}C[41]. Hence, the peaks were assigned to meta-P and pyro-P but their presence was expected to be

minor. Interestingly, at low pH (< 3) HTC, phosphorus pentoxide (P_2O_5 or P_4O_{10}) and its compounds with metals were also detected. There is a need for further research to elucidate their presence.

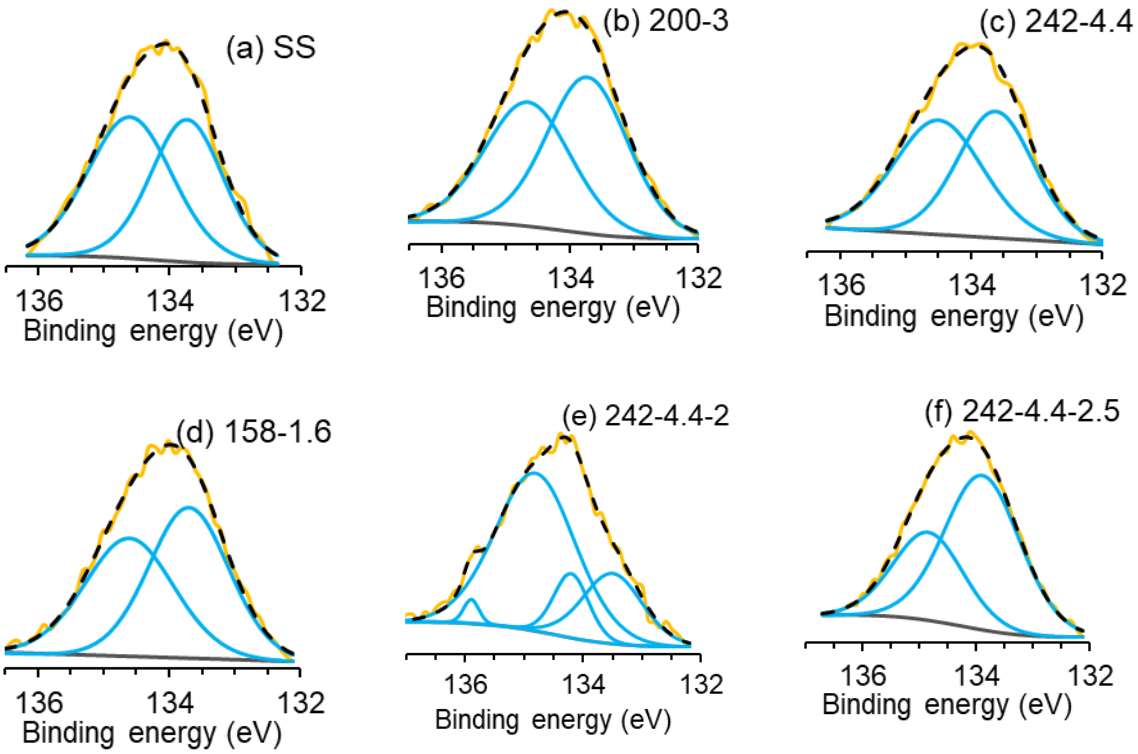

Figure 5.8: P 2p XPS spectra of (a) SS and selected hydrochars corresponding to HTC runs (b) 200-3, (c) 242-4.4, (d) 158-1.6, (e) 242-4.4-2, and (f) 242-4.4-2.5. The spectra of corresponding hydrochar (B) samples are not shown due to poor signal/noise ratio. Experimental, simulated, and deconvoluted spectra are shown in yellow solid lines, black dashed lines, and blue solid lines, respectively.

Table 5.5: P 2p XPS deconvoluted peak assignments with their peak energy, relative area and full width at half maximum (FWHM) for SS and hydrochar samples.

Sample	Peak energy (eV)	FWHM (eV)	Area (%)	Peak assignment	Reference
SS	133.2	1.29	46.3	$Ca_5OH(PO_4)_3$, $CaHPO_4$ $Ca_3(PO_4)_2$, Na_2HPO_4, C-PO_3 or C_2-PO_2 groups	[230,288]
	134.1	1.52	53.7	$Ca(H_2PO_4)_2$, $(NH_4)H_2PO_4$, $Ca(H_2PO_4)_2.H_2O$, NaH_2PO_4, C-O-P	[86,230,288]
200-3	133.7	1.50	54.5	$CaHPO_4$, $FePO_4$, $Ca_3(PO_4)_2$, $(PhO)_3PO$	[231,288]
	134.6	1.58	45.5	PO_3^{3-}, $(PhO)_3PO$, C-O-P	[230,231,288]

242-4.4	133.6	1.38	48.8	$CaHPO_4.2H_2O$, $CaHPO_4$, $FePO_4$, PO_3^{3-}, C-PO_3 or C_2-PO_2 groups, $(PhO)_3PO$	[230,231,233, 288]
	134.5	1.60	51.2	PO_3^{3-}, $(PhO)_3PO$, C-O-P	[231,288]
158-1.6	133.7	1.44	53.4	$CaHPO_4$, $FePO_4$, $Ca_3(PO_4)_2$, $(PhO)_3PO$	[231,288]
	134.6	1.60	46.6	PO_3^{3-}, $(PhO)_3PO$, C-O-P	[230,231,288]
242-4.4-2	133.5	1.19	21.4	$Ca_3(PO_4)_2$, $Ca_5(PO_4)_3Cl$, $CaHPO_4.2H_2O$, $CaHPO_4$, $P_2O_7^{4-}$, C-PO_3 or C_2-PO_2 groups	[230,233,288]
	134.2	0.70	11.7	$Ca(H_2PO_4)_2$, $(NH_4)H_2PO_4$, $Ca(H_2PO_4)_2.H_2O$, NaH_2PO_4, C-O-P, PO_3^{3-}	[230,231,288]
	134.8	1.60	65.1	P_2O_5 compounds	[288]
	135.9	0.30	1.83	P_4O_{10}	[230]
242-4.4-2.5	133.9	1.57	65.3	P_2O_5 compounds, $Ca_3(PO_4)_2$, $Ca(H_2PO_4)_2$, $(PhO)_3PO$, C-O-P	[230,231,288]
	134.8	1.46	34.7	P_2O_5 compounds	[288]

Al 2p peaks were also difficult to assign for the reasons stated above. For instance, $Al(OH)_3$ and Al_2O_3 had peak binding energies at 74.2 eV and 74.1 eV, respectively in this study (Figure 5.9 (j,k)). Nevertheless, approximate peak assignments for the deconvoluted peaks are presented in Table 5.6. SS and hydrochar samples with APMR < 4.4 had a poor signal/noise ratio and hence were not reported. AS had two peaks at 73.9 eV and 74.5 eV indicating the presence of mainly Al–Si compounds with some $Al(OH)_3$, AlOOH, and Al-OH bonding (Figure 5.9 (a)). The peak of $Al(OH)_3$ in the SSNMR spectrum was confirmed, corroborating with the Al 2p XPS data. The change in Al speciation due to acidic HTC was evident from peak energies shifting to higher values (Figure 5.9 (b – f)). The hydrochar samples had two peaks in the range of 74.4 ± 0.2 eV and 75.3 ± 0.3 eV. Al-Si compounds were likely to predominate in hydrochars as they are stable but in the pH range 3 – 5, $Al(OH)_3$ and AlOOH could be found, as evident from the thermodynamic equilibrium modelling[12]. Also, when pH was less than 3, $Al(OH)_3$ was not detected in the hydrochar samples, in confirmation with the thermodynamic modelling. In hydrochar (B) samples, Al-Si compounds were present along with some $Al(OH)_3$ (Figure 5.9 (g – i)). For hydrochar samples with APMR ≤ 3, Al concentration in hydrochar (B) was relatively low (~2 % or lower) and hence, the Al 2p peaks with appreciable signal/noise ratio could not be obtained. In conclusion, P and Al species changed

to acidic HTC and the final pH was more important than temperature for these changes.

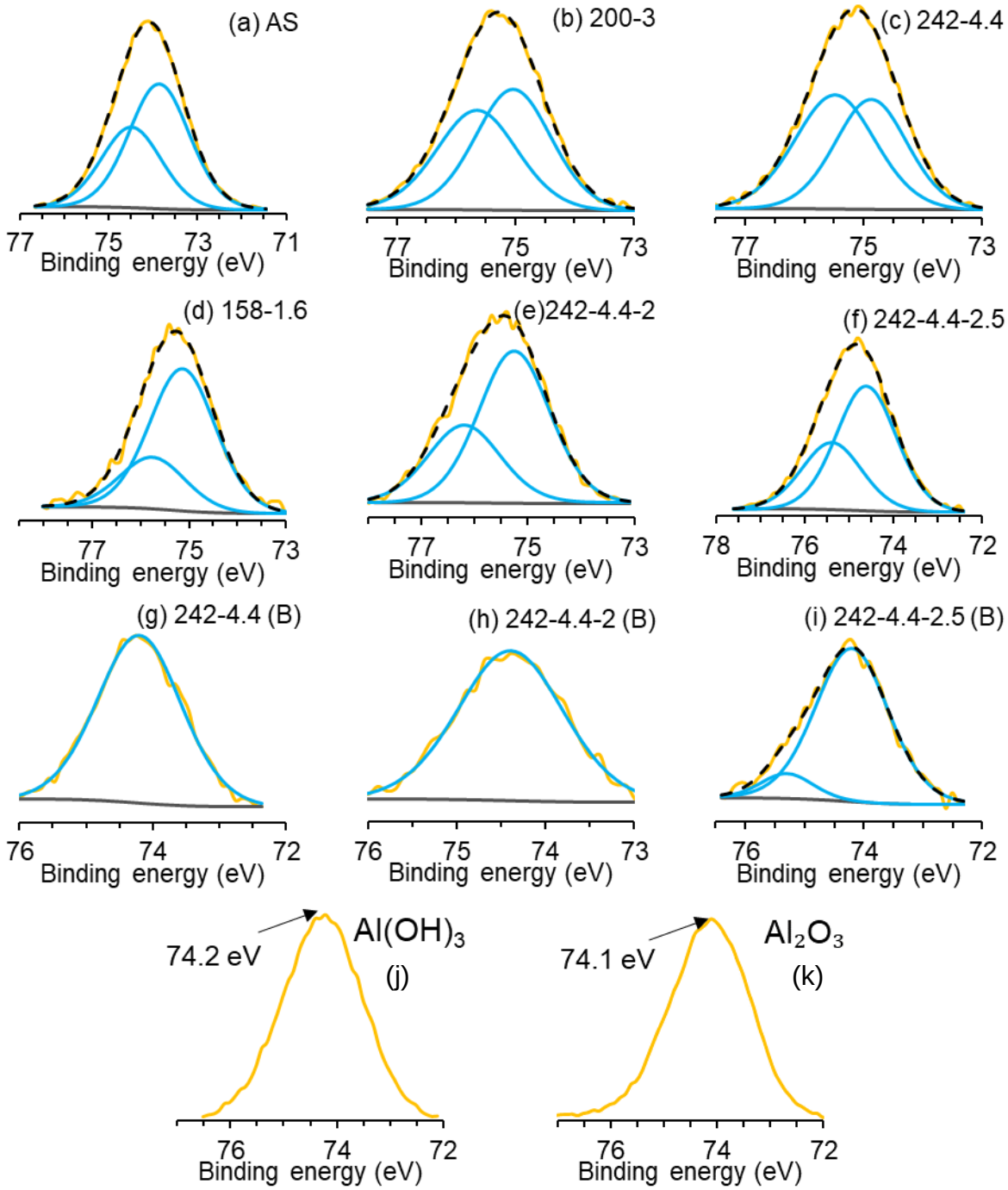

Figure 5.9: Al 2p XPS spectra of (a) AS and selected hydrochars corresponding to HTC runs (b) 200-3, (c) 242-4.4, (d) 158-1.6, (e) 242-4.4-2, (f) 242-4.4-2.5. For the HTC runs 242-4.4-2 and 242-4.4-2.5, the hydrochars after their alkaline extraction had an appreciable signal/noise ratio and hence represented as (h) 242-4.4-2 (B), and (i) 242-4.4-2.5 (B). Other hydrochar (B) samples had poor signal/noise ratios. The spectra of salts (j) $Al(OH)_3$ and (k) Al_2O_3 are also provided for reference. Experimental, simulated, and deconvoluted spectra are shown in yellow solid lines, black dashed lines, and blue solid lines, respectively.

Table 5.6: Al 2p XPS deconvoluted peak assignments with their peak energy, relative area and full width at half maximum (FWHM) for AS, hydrochar, and hydrochar (B) samples.

Sample	Peak energy (eV)	Full width at half maximum (FWHM) (eV)	Area (%)	Peak assignment	Ref.
AS	73.9	1.60	60.8	Al-OH, Al-Si compounds	[250,288]
	74.5	1.60	39.2	$Al(OH)_3$, AlOOH, Al-Si compounds	[288]
200-3	74.5	1.51	53.6	$Al(OH)_3$, AlOOH, Al-Si compounds	[288]
	75.1	1.60	46.4	Al-Si compounds	[288]
242-4.4	74.4	1.44	46.6	$Al(OH)_3$, Al-Si compounds	[288]
	75.0	1.60	53.4	$Al_2(SO_4)_3$, Al-Si compounds	[288]
158-1.6	74.6	1.60	73.2	Al-Si compounds, AlOOH	[288]
	75.2	1.60	26.8	Al-P-Si compounds	[288]
242-4.4-2	74.8	1.57	65.7	Al^{3+}, $Al_2(SO_4)_3$, Al-Si compounds	[164,288]
	75.7	1.60	34.3	$CaAl_2O_4$	[288]
242-4.4-2.5	74.6	1.60	64.9	Al-Si compounds, AlOOH	[288]
	75.4	1.60	35.1	Al-O-C bonding, Al-Si compounds	[288]
242-4.4 (B)	74.2	1.48	100	$Al(OH)_3$, Al-Si compounds	[288], this study
242-4.4-2 (B)	74.4	1.40	100	$Al(OH)_3$, Al-Si compounds	[288]
242-4.4-2.5 (B)	74.2	1.45	89.8	$Al(OH)_3$, Al-Si compounds	[288]
	75.3	1.03	10.2	Al-P-Si compounds	[288]

5.3.4. FTIR analysis for changes in functional groups

The functional groups in SS, AS, hydrochar, and hydrochar (B) samples are presented in (Figure 5.10). A precise functional group identification was difficult due to peak overlap and sample heterogeneity. Nevertheless, the trend based on previous studies was evident. Since carbon content in AS was much lesser than in SS, the peaks attributed to C-H (2924 cm^{-1}), aliphatic CH_x (2853

cm^{-1}) and aromatic ring (1516 cm^{-1})[13] were missing in AS (Figure 5.10 (a)). The overlapping peak at 1100 cm^{-1} possibly indicated a C-O functional group, but given the low C content in AS, it could also imply inorganic compounds, such as sulphates, phosphates and silica compounds[263]. The presence of these inorganic compounds was further evidenced by the peak at around 900 cm^{-1}. The presence of carbonate in this peak range (900-1100 cm^{-1}) in hydrochar samples was less likely because of the low pH (< 5) of hydrochar samples. Besides, AS had relatively more prominent inter/intramolecular H-bonded OH groups (~3300 cm^{-1}) indicating the presence of $Al(OH)_3$ which was confirmed by ^{27}Al SSNMR and Al 2p XPS spectra. Barring these differences, SS, AS and hydrochar samples had similar characteristics spectra, suggesting that acidic HTC did not lead to significant changes in functional group composition.

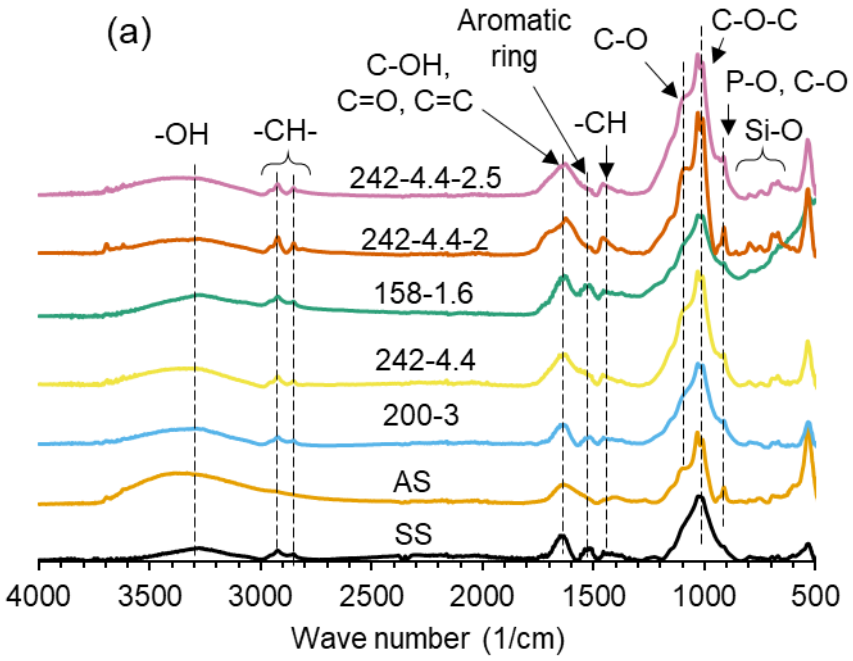

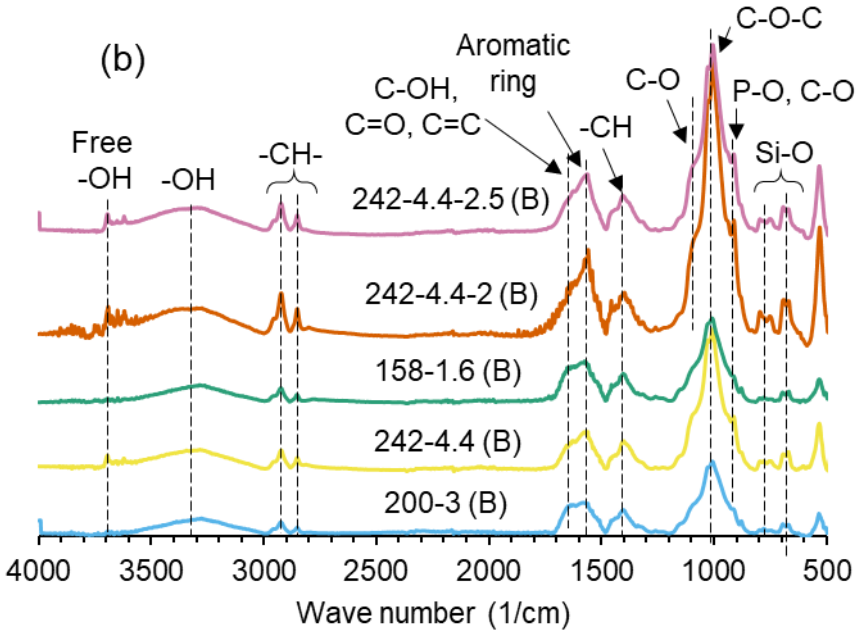

Figure 5.10: FTIR spectra of (a) SS, AS, and hydrochars of selected HTC runs, (b) hydrochar (B) samples of the corresponding HTC runs.

However, after alkaline extraction, some modifications in the spectra of hydrochars were apparent (Figure 5.10 (b)). The presence of the free -OH group at ~3700 cm^{-1}[263] might be due to residual OH ions after alkaline extraction. The relative increase in the intensity of the aromatic ring, carboxyl-carbonate structure, and aliphatic C-H stretching (~1420 cm^{-1}) probably suggested their recalcitrance to alkaline dissolution. The inorganic functional groups (< 1000cm^{-1}) in hydrochar (B) samples were relatively more prominent than in hydrochar samples, possibly due to their unmasking because some labile carbon functional groups were lost during alkaline extraction. In conclusion, FTIR spectra of samples indicated the diversity of functional groups whose composition was affected more by alkaline extraction rather than acidic HTC.

5.3.5. Process mechanism

As shown in this study, P recovery depended on multiple factors and definite generalization of the process mechanism is difficult. However, an approximate detailing of the process mechanism is possible and it is pictorially represented in Figure 5.11. P species and TEs were distributed in all the solid and liquid by-products of the entire process of SS. Consequently, it was challenging to recover relatively purer P from one of the by-products of the entire process (i.e., either hydrochar or liquid extract).

With the addition of AS with SS and acidic hydrothermal treatment, NAIP fraction of total P in hydrochar increased while AP fraction was reduced. The relative increase/decrease of P species was dependent on the fraction of AS in SS+AS mixture, HTC temperature and pretreatment pH. P concentration was inversely proportional to Ca and Mg concentrations in process water in the given operational conditions indicating their partitioning during acidic HTC. Some TEs were retained in hydrochar while others were extracted to process water during acidic HTC. Finally, after alkaline extraction, the relative fraction of AP and NAIP in hydrochar (B) of the amended process was lower than hydrochar (B) of the reference process and vice versa for TEs. In the alkaline extract of the amended process, P and Al were abundant compared to the reference process, which indicated that the conversion of AP to NAIP during acidic HTC was beneficial for higher alkaline extraction efficiency of P. Most TEs in the amended process were concentrated in hydrochar (B) and the alkaline extract was relatively free from TE contamination compared to the reference process. The addition of AS led to dilution of TE concentration in the HTC feedstock which also affected this trend. Overall, the proposed process achieved its objective of partitioning P from TEs and alkaline P extraction from hydrochar was enhanced due to acidic pretreatment.

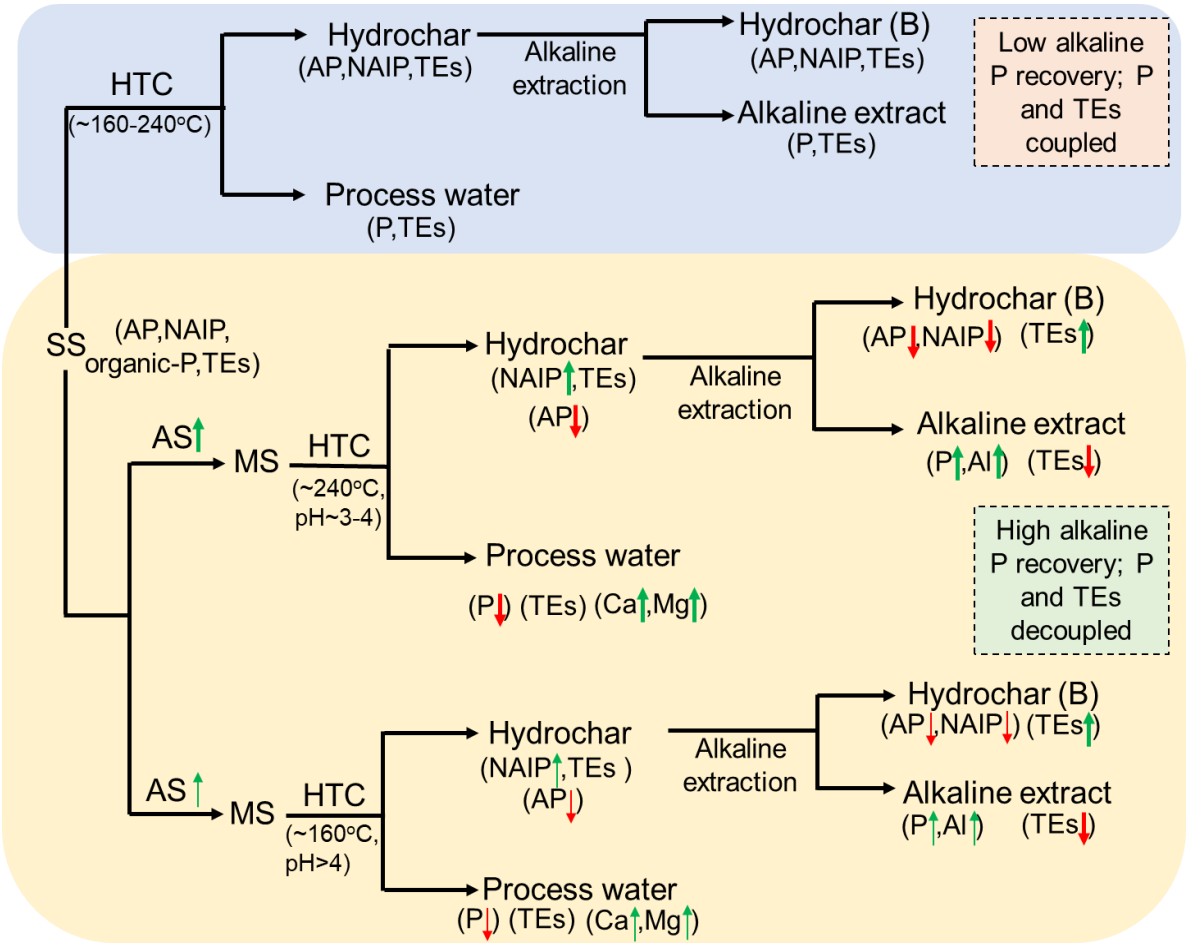

Figure 5.11: The process mechanism is shown via the approximate partitioning trend of P, some major and trace elements along the process. The green and red arrows indicate the increase and decrease in the proportion of the species in the design process (MS HTC) compared to the reference process (SS HTC), respectively. The thicker the arrow, the higher the extent of increase or decrease compared to the reference process.

5.4. CONCLUSION

This study demonstrated the positive effect of acidic HTC of SS mixed with Al-rich AS on AP to NAIP conversion. P conversion led to its enhanced recovery in aqueous form via alkaline extraction with reduced contamination from trace elements (TEs). High HTC temperature (~240 ^{o}C), high APMR (~4) in the feedstock and low final pH of feedstock post-HTC (~3 – 4) were recommended for maximizing P recovery. The highest alkaline P recovery was 82 % while the highest overall P recovery was 75 % for acidic HTC. For SS HTC, the highest alkaline and overall P recoveries were 48 % and 37 %, respectively. Solid-state NMR and XPS analyses revealed that APMR and final pH were more important determinants than temperature for P and Al speciation. Most analyzed TEs were concentrated in hydrochar (B) in the acidic HTC cases compared to SS

HTC cases. But more importantly, TEs such as Cr, Cu, and Ti were predominantly present in the hydrochar (B) (> 60%) for acidic HTC cases. Only Zn had an appreciable fraction in alkaline extract (27 – 42 %). Further techno-economic assessment is imperative for pilot/industrial application, and leachate management will be crucial for lowering the environmental impacts of this process. With refinements, the proposed process can be an effective strategy for P recovery with the circular management of the two major waste streams from wastewater and drinking water treatment plants.

6. CONCLUSIONS AND RECOMMENDATIONS

The studies conducted in this thesis investigated the synergistic effect of SS amendment using AS, thermochemical treatment, and sequential wet extraction for P recovery. The first study explored the mechanistic aspect of AP to NAIP transformation during acidic pretreatment of SS with AS at pH ~3 – 4. This transformation occurred via the dissociation of AP and adsorption of released ortho-P on $Al(OH)_3$ or other (hydroxo)oxide minerals of Al, as validated by Visual MINTEQ simulation and experimental data from SSNMR and XPS. The presence of AS inhibited the loss of P during acidic pretreatment via acidic extract. The overall alkaline extraction of P from the acid-pretreated and amended SS was ~12% higher than the control case (non-amended and non-acid-pretreated).

The second study assessed the synergistic role of acidic pretreatment and pyrolysis on the fate of P and its recovery using alkaline extraction. The findings indicated that low-temperature pyrolysis (400^{o}C) after acidic pretreatment was most suitable for P recovery. Increasing temperature from 400 to 900^{o}C led to NAIP to AP transformation in both unamended and amended cases as it was thermodynamically favourable. However, when Al was abundantly present, this transformation was inhibited significantly. Also, higher temperatures led to the formation of recalcitrant minerals and immobilization of P in the char matrix which inhibited its release during alkaline extraction.

The third study focussed on acid pretreatment in HTC conditions to explore the accentuating effect of high-temperature and high-pressure conditions on AP to NAIP transformation. The effect of various ratios of SS:AS in the sludge mixture, pH of acidic pretreatment, and HTC temperatures were investigated. Central composite design and one-factor-at-a-time experiment revealed that AS addition was redundant beyond a limit in promoting AP to NAIP conversion. Moreover, the optimum pH for acidic pretreatment was ~3 – 4. The higher temperature of HTC promoted the formation of AP in the non-amended case while excess Al in the amended case inhibited AP formation.

Some of the trends apparent from the three studies above are: (1) addition of AS with SS in mildly acidic conditions promoted AP to NAIP conversion with

or without HT (2) P loss during acidic pretreatment for SS + AS was within 5 – 25%, and HT condition did not accentuate AP to NAIP conversion relative to non-HT condition (3) optimized alkaline P recovery was highest for pyrolysis char (~88%), followed by hydrochar (~81%), and dry amended SS (~77%) (4) optimized overall P recovery (after accounting for acidic pretreatment loss and alkaline recovery) was approximately same for all the three process explored in this thesis (~75%) (5) most trace elements were concentrated in the solid matrix after the entire extraction process, though some amphoteric elements such as Zn could be present in the alkaline extract. Given the high extraction efficiency of P and low trace elemental contamination, this process might be one of the feasible strategies for P recovery in many locations worldwide and promote the co-treatment of two waste streams with resource recovery.

There are some recommendations for future studies. To assess the effectiveness of the process proposed in this thesis, pilot-scale studies should be conducted with feedstocks obtained from diverse sources. Process automation and modelling using software such as Aspen can be explored. If similar extraction efficiencies as bench scale studies are obtained, detailed techno-economic analysis and life cycle assessment should be performed to evaluate the commercial viability and environmental footprint of this process. To reduce the cost further, by-products from other industrial processes can be explored. For instance, HCl and NaOH might be obtained from the plant treating brine using direct electrosynthesis. Beyond this process, more studies are required on extractant management after P recovery. Most studies have focussed on final P recovery as salt such as struvite or hydroxyapatite which is not financially lucrative. In addition to the production of these P salts from alkaline extract, other chemicals such as flame retardants, salts for electric vehicle batteries and the electronic industry should be explored. The methods of integrating these recovery options with the existing wastewater treatment at the pilot/industrial scale should be studied as well. With integrated wastewater treatment and resource recovery, circularity in water and wastewater treatment can be achieved.

SUPPLEMENTARY INFORMATION

CHAPTER 2

Table S 1: Key chemical properties of phosphorus.

Property	Remark
Oxidation state	It can vary from -3 to +5 (such as -3, 0, +1, +3, +4, +5), though most transitional oxidation states disproportionate into +5 (most common in nature) and -3, both in alkali and acid[289].
Isotopes	^{31}P has 100% natural abundance as most other isotopes are highly radioactive (half-lives in seconds). Two other isotopes with relatively longer half-lives are ^{32}P (14 days) and ^{33}P (25 days)[290].
Allotropes	White (or yellow) phosphorus (P_4) is the most prominent and reactive allotrope of P, hence stored under water. Other allotropes are red, violet and black phosphorus. Diphosphorus (P_2) is gaseous phase of P, very reactive and stable above 1200^oC and until 2000^oC[290].
Compounds	Due to its large atomic radius (1.8 Å, non-bonded), P tends to form single bond with itself and other elements such as O, N and S. Besides, due to lower electronegativity (2.19, Pauling scale), P tend to exist more in positive oxidation states. The electronic configuration of P is $[Ne]3s^23p^3$ and has 5 valence electrons for bonding. However, due to empty 3d atomic orbitals, P can expand valence shell to incorporate 10 or more electrons (such as in compounds PF_5 and PF_6^-)[291].

Table S 2: Standard protocols useful for sewage sludge characterization.

Standard method	Title/ Utility	Originally applicable for	Ref.
ISO 11464:2006	Pretreatment of samples for physico-chemical analyses: drying, crushing, sieving, dividing and milling.	Soil	[292]
ISO 12404:2021	Screening methods for soil and waste characterization.	Waste (solid, liquid), soil and soil-such as materials.	[293]
ISO 16720:2007	Pretreatment of samples by freeze-drying for subsequent analysis	Soil	[294]
ISO 11465:1993	Moisture content on a mass basis using gravimetric method.	Soil	[295]
ISO 9963-1:1996	Determination of total and composite alkalinity	Water and wastewater	[296]
EN 15933:2012	pH determination.	Municipal sludge, compost, arable and forest soils.	[168]

ASTM D7582-15	Proximate analysis by macro thermogravimetric analysis (moisture, volatile matter, ash and fixed carbon).	Coal and coke	[297]
ISO 29541:2010	Total carbon, hydrogen and nitrogen by the instrumental method.	Coal and coke	[298]
EN 15170:2008	Calorific value.	Sludge and sludge products	[299]
ISO/TR 20736:2021	Sludge recovery, recycling, treatment and disposal - Guidance on thermal treatment of sludge.	Municipal and industrial sludge	[300]
ISO 18227:2014	Elemental composition using X-ray fluorescence (XRF). Applicable for major and trace elements with approximately 0.0001% to 100% concentration.	Homogenous solid waste, soil and soil-such as materials.	[301]
ISO 11885: 2007	Determination of selected elements using ICP-OES	Water, sludge, and sediments	[302]
ISO 17294-2:2016	Application of Inductively Coupled Plasma — Mass Spectrometry (ICP-MS) for selected elements	Water, sludge, and sediments	[284]
ISO / TS 16965: 2013	Trace element determination in soil extracts by ICP-MS	Municipal sludge, compost and sludge-amended soils.	[303]
ISO 54321: 2021	Digestion of sample with aqua regia for elemental composition determination.	Sludge (municipal and industrial), treated biowaste (compost), soil and solid waste.	[304]
EN 13656:2020	Digestion of sample with hydrochloric (HCl), nitric (HNO_3) and tetrafluoroboric (HBF_4) or hydrofluoric (HF) for elemental composition determination.	Sludge (municipal and industrial), treated biowaste (compost), soil and solid waste.	[170]
ISO 16729:2013	Digestion of sample with nitric acid for elemental composition determination.	Municipal sludge, compost and sludge-amended soils.	[305]
ISO 14869-2:2002	Digestion of sample by alkaline fusion for elemental composition determination.	Soil	[306]
ISO 6878:2004	Determination of phosphorus — Ammonium molybdate spectrometric method	Water, wastewater, seawater, etc	[307]
ISO 10304-1:2007	Determination of phosphate and other anions using liquid chromatography	Water, wastewater, seawater, etc	[308]

CHAPTER 3

Table S 3: Specification of sample weight and volume of leachant in all the processes. M3 represents the mixture of SS and AS in the ratio 3:2 (w/w).

Process	Sample for procedure before alkaline leaching (sample name, sample amount (g))	Vol. of acid or base before alkaline leaching (mL)	Sample for alkaline leaching (sample name, sample amount (g))	Vol. of base (mL)
A	-	-	SS, 0.25	25
B	SS, 0.4	40	SSA, 0.25	25
C	-	-	M3, 0.25	25
D	M3, 0.4	40	M3A, 0.25	25
E	AS, 0.1	25	SS, 0.25	25

Table S 4: The concentration of trace elements (mg/kg) in the dried sludge samples.

Element	Sewage sludge (SS)	Alum sludge (AS)
Barium (Ba)	255.4±5.2	98.1±8.7
Cadmium (Cd)	<20	<20
Cobalt (Co)	<100	<100
Chromium (Cr)	121.6±5.4	27.0±5.5
Copper (Cu)	597.1±41.5	<100
Mercury (Hg)	<20	<20
Manganese (Mn)	115.6±1.9	263.4±3.0
Molybdenum (Mo)	<20	<20
Nickel (Ni)	130.5±4.3	64.7±6.3
Lead (Pb)	20.7±1.1	44.0±2.6
Antimony (Sb)	<20	<20
Selenium (Se)	<20	<20
Tin (Sn)	26.4±0.5	<20
Strontium (Sr)	43.9±1.7	<20
Titanium (Ti)	1358.2±19.6	658.5±3.6
Vanadium (V)	<20	29.4±1.0
Zinc (Zn)	905.0±19.6	ND

ND: Not determined.

Isotope with the highest natural abundance was determined.

Table S 5: The extent of trace elements released into the acid leachates after the acidic pretreatment of SS (SSA(aq)) and M3 (M3A(aq)). M3 represents the sewage sludge (SS) and alum sludge (AS) mixture in the ratio 3:2 (w/w).

Element	SSA(aq)		M3A(aq)	
	Conc.(mg/kg)	% Released	Conc.(mg/kg)	% Released
Barium (Ba)	<4	<1.6	<4	<2.1
Cadmium (Cd)	<4	-	<4	-
Cobalt (Co)	<20	-	<20	-
Chromium (Cr)	<4	<3.3	<4	<4.8
Copper (Cu)	<20	<3.3	<20	-
Mercury (Hg)	<4	-	<4	-
Manganese (Mn)	51.5±6.2	44.6	54.6±10.8	31.3
Molybdenum (Mo)	<4	-	<4	-
Nickel (Ni)	19.4±1.7	14.9	10.8±3.1	10.4
Lead (Pb)	<4	<19.3	<4	<13.3
Antimony (Sb)	<4	-	<4	-
Selenium (Se)	<4	-	<4	-
Tin (Sn)	<4	<15.2	<4	-
Strontium (Sr)	15.6±2.3	35.5	12.2±3.6	-
Titanium (Ti)	20.6±2.1	1.5	18.1±3.0	1.7
Vanadium (V)	<4	-	<4	-
Zinc (Zn)	185.1±38.5	20.5	ND	-

ND: Not determined.

Isotope with the highest natural abundance was determined.

Table S 6: ^{31}P SSNMR fitting parameters and assignments for non-pretreated (sewage sludge (SS) and M3) and acid-pretreated SS (SSA) and M3 (M3A) sludges. M3 represents the SS and alum sludge (AS) mixture in the ratio 3:2 (w/w).

Sample	Assignment	δ_{iso} (ppm)	FWHM (ppm)	Relative integrals[a] (%)	Normalized integrals[b]	Normalized integral sum[c]
SS	HPO_4^{2-} on H_2O	6.16	0.72	39.51	0.395	1.000
	Amorphous ortho-P	1.17	11.89	60.49	0.605	
SSA	Adsorbed or amorphous ortho-P	-1.49	7.17	56.14	0.095	0.169
	$Al(OH)_2H_2PO_4$ and/or PO_4 on $Al(OH)_3$	-8.48	14.55	43.86	0.074	
M3	HPO_4^{2-} on H_2O	6.17	0.8	40.47	0.269	0.665
	Amorphous ortho-P	0.7	12	59.53	0.396	
M3A	Adsorbed or amorphous ortho-P	-3.14	9.62	17.6	0.101	0.576
	$Al(OH)_2H_2PO_4$ and/or PO_4 on $Al(OH)_3$	-10.02	14.56	82.4	0.475	

[a] Relative integrals of deconvoluted resonances in NMR line-shape.
[b] Integrals of deconvoluted resonances normalised to sum of SS integral
[c] Sum of normalised integrals for each spectrum.

Table S 7: ^{27}Al SSNMR fitting parameters and assignments for non-pretreated (sewage sludge (SS), alum sludge (AS) and M3) and acid-pretreated SS (SSA) and M3 (M3A) sludges. M3 represents the SS and AS mixture in the ratio 3:2 (w/w).

Sample	Assignment	δ_{iso} (ppm)	Relative integrals[a] (%)	Normalized integrals[b]	Normalized integral sum[c]
AS	AlO_4	80 > 50	6	0.067	
	AlO_5	50 > 30	7	0.081	1.000
	AlO_6	20 > -15	87	1.000	
SS	AlO_4	80 > 50	22	0.011	0.042
	AlO_6	20 > -15	78	0.037	
SSA	AlO_4	80 > 50	21	0.010	0.041
	AlO_6	20 > -15	79	0.037	
M3	AlO_4	80 > 50	7	0.030	
	AlO_5	50 > 30	8	0.034	0.396
	AlO_6	20 > -15	86	0.391	
M3A	AlO_4	80 > 50	7	0.037	
	AlO_5	50 > 30	6	0.032	0.448
	AlO_6	20 > -15	86	0.444	

[a] Relative integrals of deconvoluted resonances in NMR line-shape.
[b] Integrals of deconvoluted resonances normalised to sum of SS integral
[c] Sum of normalised integrals for each spectrum.

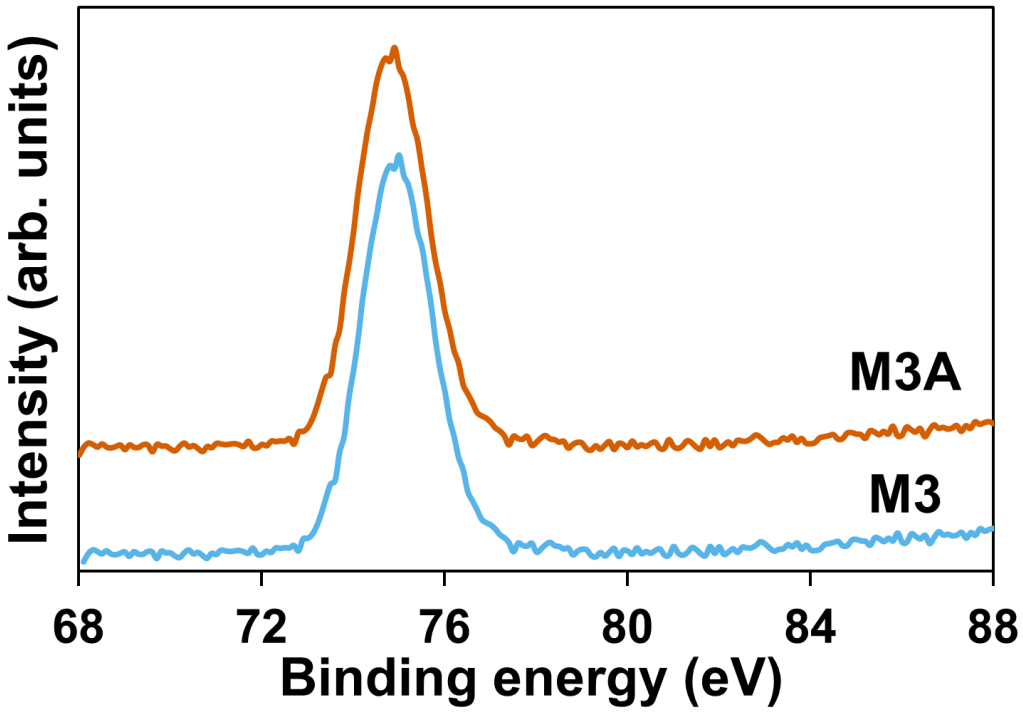

Figure S 1: Al 2p XPS spectra of M3 and acid-pretreated M3 (M3A) solid samples. M3 represents the SS and AS mixture in the ratio 3:2 (w/w).

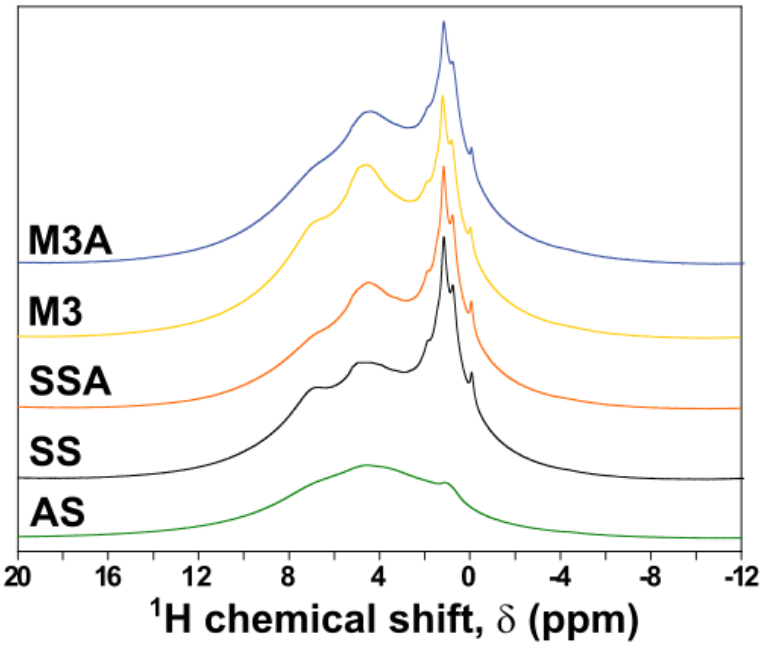

Figure S 2: ^{1}H MAS NMR spectra of non-pretreated (sewage sludge (SS), alum sludge (AS) and M3) and acid-pretreated SS (SSA) and M3 (M3A) sludges. M3 represents the SS and AS mixture in the ratio 3:2 (w/w).

Table S 8: The calculations for the acidic pretreatment of DSS and MS (DSS + AS).

Parameter	DSS	Amended DSS
Total solids of DSS (g) (1)	1	0.8
Total solids of AS (g) (2)	0	0.2
Total solids for acidic pretreatment (g) (3) [= (1) + (2)]	1	1
Wet weight of DSS (g) (4) [= (1)/{1-0.87}][a]	7.7	6.3
Total weight of sample for acidic pretreatment (g) (5) [= (2) + (4)]	7.7	6.5
Liquid-to-solid ratio ($L:S_W$) (mL:(g,wet)) (6)	5:1	5:1
DI water added to the sample (7) [= (5) × (6)]	38	32
Liquid-to-solid ratio ($L:S_D$) (mL:(g,dry)) (8) [= {(7) + (4) × 0.87}/(3)][a]	45:1	38:1

a. Moisture content of DSS = 87 %

Table S 9: Illustrative table showing the calculation steps for the weight of P and samples in the process flow (with clarifications in the footnote). Average values of the replicates were used for the calculations.

Parameter	SS	MS
P in the dry sample at the start of the process (mg) (1)	100	100
Dry sample wt. (g) [= (1)/P][a] (2)	5	6
P loss during acidic pretreatment (mg) (3) [= (2)*(P_{MS} - P_{MA})][b]	0	11
P in pyrolysis feedstock (mg) (4) [= (1) – (3)]	100	89
Char yield (%)[c] (5)	NA	NA
Char wt. (g) (6) [= (2)*(5)/100]	NA	NA
P in char (mg) (7) [= (6)*P_{char}][d]	NA	NA
P loss due to pyrolysis (mg) (8) [= (7) – (4)]	NA	NA
P in alkaline extract (9) [= (6)*P_{alkali}][e]	NA	NA
P lost after alkaline extraction (10) [= (7) – (9)]	NA	NA
Alkaline extraction efficiency (%) (11) [= (9)*100/(7)]	NA	NA
Overall efficiency (%) (12) [= (9)*100/(1)]	NA	NA

a. P (mg/g) in SS (P_{SS}) was determined using ICPOES and in MS (P_{MS}) using the mass balance (using mass fraction and P in SS and AS).
b. P_{MA} (mg/g) was determined using ICPOES. No mass loss was assumed during acidic pretreatment.
c. Char yield (%) = [Char wt. (g)/Feedstock wt. (g)]*100. Since the char yield for both processes differs for different pyrolysis temperatures, the entry is filled as NA in this row and subsequent rows.
d. P content in char (P_{char}) (mg/g) was obtained using ICPOES.
e. P content in alkaline extract (P_{alkali}) was obtained using ICPOES.

Table S 10: Molar ratio of major ions in the samples that form inorganic compounds with P. The values for MS are based on mass balance.

Molar ratio	SS	AS	MS	MA
Al/P	0.6	204.6	3.0	4.0
Ca/P	0.9	3.5	0.9	0.4
Fe/P	0.4	8.8	0.5	0.5
Mg/P	0.5	2.1	0.5	0.3

Table S 11: Total carbon (TC) in the solid sludge and char samples.

Sample	Total carbon (TC, %)	Sample	Total carbon (TC, %)
SS	39.6 ± 0.5	MA	36.8 ± 0.4
SC400	38.1 ± 0.2	MC400	34.1 ± 0.3
SC600	38.3 ± 0.2	MC600	33.6 ± 0.3
SC900	40.2 ± 0.5	MC900	31.2 ± 0.4

Table S 12: Total carbon (TC) and dissolved organic carbon (DOC) in the filtered liquid extracts obtained from acidic pretreatment and alkaline extraction.

Sample	Total carbon (TC, mg/kg))	Dissolved organic carbon (DOC, mg/kg)	Fraction of TC extracted from solid to liquid (%)
Acidic extract	5417 ± 88	5358 ± 116	1.5
Alkaline extract (SC400)	4666 ± 302	3277 ± 161	1.2
Alkaline extract (SC600)	4263 ± 879	3140 ± 208	1.1
Alkaline extract (SC900)	1166 ± 53	<1000	0.3
Alkaline extract (MC400)	24087 ± 649	22937 ± 652	7.1
Alkaline extract (MC600)	2792 ± 623	2028 ± 165	0.8
Alkaline extract (MC900)	1023 ± 402	<1000	NA

Table S 13: The main parameters for BET fitting to quantify surface characteristics.

Sample	C (unitless)	r (unitless)	Lowest P/P_o for fitting	Highest P/P_o for fitting
SC400	65.752	0.999	0.049	0.287
SC600	134.605	0.999	0.050	0.144
SC900	85.283	0.999	0.049	0.286
MC400	70.481	0.999	0.049	0.286
MC600	108.966	0.999	0.049	0.286
MC900	294.287	0.999	0.049	0.287

Table S 14: Surface characteristics of the char samples.

Sample	Surface area (m^2/g)	Avg. pore dia. (nm)	Pore vol (cm^3/g)	Highest pore dia. (nm) (for pore vol.)	P/Po for pore vol.	Micropore vol. (cm^3/g)
SC400	7.6	6.7	0.0	40.1	0.95	0.000
SC600	4.1	8.6	0.0	40.4	0.95	0.000
SC900	27.5	4.8	0.0	40.3	0.95	0.000
MC400	19.2	8.7	0.0	39.6	0.95	0.000
MC600	22.0	10.6	0.1	39.7	0.95	0.000
MC900	91.0	6.5	0.1	39.5	0.95	0.004

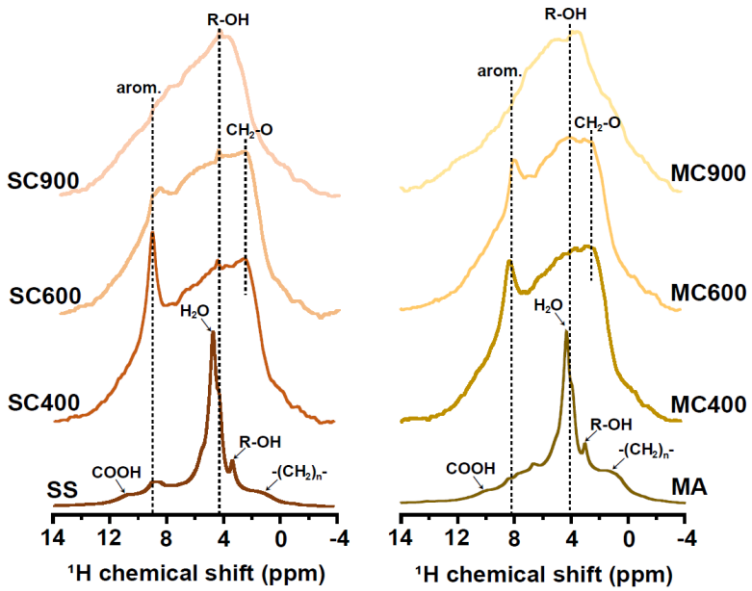

Figure S 3: ^{1}H SP-MAS NMR spectra of (a) SS and its chars (b) MA and its chars.

^{1}H SP-MAS NMR spectra of sludges and char samples confirmed the ^{13}C{^{1}H} CP-MAS findings. The spectra showed a general trend of decreasing alkyl and hydroxyl groups and increasing aromatic groups with increasing temperatures. SS and MA had similar ^{1}H spectra as samples contained alkyl, alcohol, water, and carbonyl groups. Peak around 9 ppm in SS, MA, SC400/600, and MC400/600 likely represented aromatic protons, which decreased with increasing temperatures. SS and MA had a small resonance (10 to 12 ppm) assigned as a carboxylic C=O peak (might be present in other samples, but the peaks were too weak). SS and SC samples likely contained R-OH, which

presented as a sharp resonance (4 ppm). A peak closer to 4.7 ppm in SS and MA was missing in char samples, indicating the absence of water of hydration.

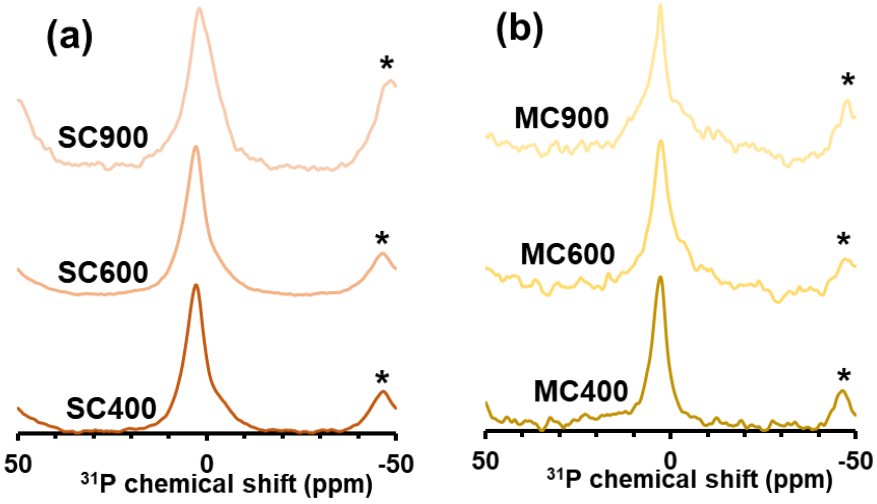

Figure S 4: ^{31}P SP-MAS NMR spectra of (a) SS chars and (b) MA chars after alkaline extraction of P from them. The spinning sideband is marked with *.

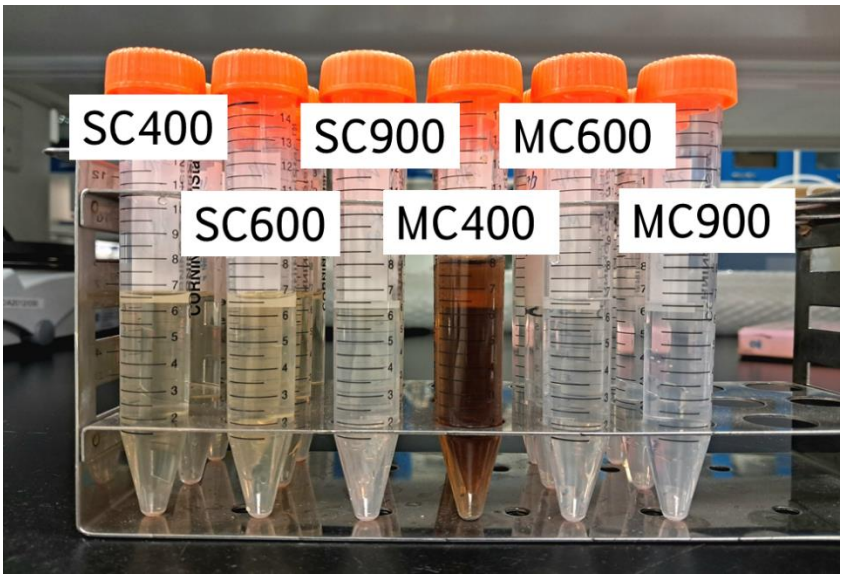

Figure S 5: The extracts obtained after the alkaline extraction of chars for P recovery.

Table S 15: Illustrative example of mass balance of P and other major and trace elements in this study using hypothetical values.

Parameter	Quantity
(1) Dry feedstock (SS or MS) wt. for HTC (g)	1
(2) P in feedstock [= (1)*$P_{SS\ or\ MS}$][a] (mg)	20
(3) Hydrochar yield [= (dry hydrochar wt. (g)/dry feedstock wt. (g))]	0.75
(4) P in hydrochar [= (1)*(3)*$P_{hydrochar}$)][a] (mg)	16
(5) P in process water [= (2) – (4)] (mg)	4
(6) Hydochar yield after alkaline extraction[b] [= dry hydrochar wt. (g)/ dry hydrochar (B) wt. (g)]	0.8
(7) P in hydrochar (B) [= (1)*(3)*(6)*$P_{hydrochar\ (B)}$][a] (mg)	4
(8) P in alkaline extract [= (4) – (7)] (mg)	12
(9) P in process water [= (5)*100/(2)] (%)	20
(10) P in hydrochar (B) [= (7)*100/(2)] (%)	20
(11) P in alkaline extract [= (8)*100/(2)] (%)	60
(12) Alkaline extraction efficiency [= (8)*100/(4)] (%)	75
(13) Overall extraction efficiency [= (11)] (%)	60

a. P_{SS}, $P_{hydrochar}$ and $P_{hydrochar\ (B)}$ were determined using ICP-OES after microwave acid digestion (MAD). P_{MS} was calculated using the mass fraction of SS and AS in MS, and P in them.
b. Hydrochar after alkaline extraction was named "hydrochar (B)". Hydrochar yield after alkaline extraction had a range of ~0.7 – 0.9 in this study. Therefore, in case of unavailability of data, 0.8 was assumed.

Table S 16: HTC runs conducted during the pH optimization experiment in this study.

Run	Initial pH	pH after adding acid	pH after HTC or final pH	Run notation	Vol. of 6 M HCl (mL)
1	5.38	3	4.41	4.4	0.17
2	5.38	2	3.45	3.3	0.32
3	5.57	3	4.42	4.4	0.18
4	5.49	1.49	2.57	2.5	0.65
5	5.49	2.02	3.13	3.3	0.34
6	5.34	2.52	3.9	3.9	0.23
7	5.37	1	1.86	2.0	1.1
8	5.35	2.5	3.85	3.9	0.24
9	5.38	1.5	2.46	2.5	0.6
10	5.36	0.99	2.07	2.0	1.1

Table S 17: ANOVA and fit statistics for the response variables.

	Final pH	Hydrochar yield (%)	P in process water (%)	Alkaline P extraction efficiency (%)	Overall P extraction efficiency (%)
Coded model	3.93 + 0.11*A	77.7-3.4*A + 0.9*B-1.8*A^2	16.8-6.4*B	74.8 + 1.2*A + 1.5*B	62.4 + 6.0*B
ANOVA: p-value					
Model	0.011	<0.0001	0.0002	0.0047	0.0003
A: Temperature (^oC)	0.011	<0.0001	-	0.028	-
B: APMR	-	0.042	0.0002	0.007	0.0003
A^2	-	0.002	-	-	-
Lack of fit	0.216	0.545	0.007	0.0043	0.0025
Fit statistics					
R^2	0.309	0.840	0.554	0.468	0.520
Adjusted R^2	0.271	0.810	0.529	0.406	0.493
Predicted R^2	0.144	0.744	0.447	0.241	0.397
Adequate precision	6.316	14.565	10.518	7.049	9.818

The model terms such as A, B, and A^2 were included in the model if they were statistically significant ($p < 0.05$). Insignificant lack of fit (i.e., $p > 0.05$) meant that the model fitted well with the experimental data. If the difference between predicted R^2 and adjusted R^2 was < 0.2, it suggested that there was no model overfitting. Adequate precision > 4 implied that the signal-to-noise ratio was adequate to navigate the design space using the model. A relatively low R^2 (< 0.5) indicated that the model did not explain much of the variability in the dependent or response variable.

Multi-criteria optimization and model validation

Using multi-criteria optimization, the best and worst conditions for alkaline and overall P recoveries were determined (Table S 18) and these runs were conducted in duplicate to verify the model predictions. The best condition for maximizing P recovery was computed to be at 242^{o}C and APMR of 4.4 while the worst condition was at 158 ^{o}C and APMR of 1.6. The experimental data

validated all the models except the hydrochar yield (%) model for a 99 % prediction interval (Table S 19). However, if the validation conditions were more stringent, for instance, confidence ≤ 95 %, the prediction interval would be narrower implying that some of the other models would be invalidated as well. Hence, the evaluation of the models depended on design criteria and the critical objectives of the process. In this study, the objective was to identify a broad trend in P extraction variation with HTC process parameters, which were met satisfactorily.

Table S 18: The optimized factor and response variables as per the models obtained using the CCD.

Objective	Factor variables		Response variables					Optimized factor condition	
	Temp. (°C)	APMR	Final pH	Hydrochar yield (%)	P in process water (%)	Alkaline P extraction (%)	Overall P extraction (%)	Temp. (°C)	APMR
Maximize P recovery	158 – 242	1.6 – 4.4	None	None	Minimize	Maximize	Maximize	242	4.4
Minimize P recovery	158 – 242	1.6 – 4.4	None	None	Maximize	Minimize	Minimize	158	1.6

Table S 19: The outcome of the confirmation runs of the CCD to validate the prediction models.

Response	Maximize P recovery			Minimize P recovery		
	Predicted values	99 % prediction interval	Experimental values	Predicted values	99 % prediction interval	Experimental values
Final pH	4.09 ± 0.16	3.72 – 4.46	4.37 ± 0.10	3.78 ± 0.16	3.41 – 4.15	3.83 ± 0.02
Hydrochar yield (%)	70.79 ± 1.64	66.20 – 75.39	60.45 ± 0.07	77.61 ± 1.64	73.02 – 82.21	73.90 ± 0.42
P in process water (%)	7.73 ± 5.42	-5.07 – 20.54	18.23 ± 1.44	25.76 ± 5.42	12.96 – 38.57	38.15 ± 3.19
Alkaline P recovery (%)	78.48 ± 1.95	73.43 – 83.53	82.05 ± 0.02	71.02 ± 1.95	65.97 – 76.07	68.89 ± 2.20
Overall P recovery (%)	70. 69 ± 5.37	58.00 – 83.39	67.09 ± 1.19	54.01 ± 5.38	41.31 – 66.71	42.64 ± 3.55

Table S 20: Trace element concentration in hydrochar corresponding to each run. Ba, Sn and Sr were not analyzed. As per EU regulation for organic fertilizers, the maximum allowable concentration (mg/kg) of As (inorganic), Cd, Hg and Pb are 40, 1.5, 1 and 120, respectively.

Feedstock	Run notation	As	Cd	Co	Hg	Mn	Mo	Pb	Sb	Se	V
SS	158	< 17	< 17	< 17	< 17	140.5 ± 27.0	< 17	94.1 ± 1.1	< 17	< 17	< 17
SS	170	< 17	< 17	< 17	< 17	< 133	< 17	83.8 ± 0.7	< 17	< 17	< 17
SS	200	< 17	< 17	< 17	< 17	152.9 ± 37.2	< 17	86.1 ± 1.3	< 17	< 17	< 17
SS	230	< 17	< 17	< 17	< 17	145.6 ± 13.4	< 17	92.7 ± 3.9	< 17	< 17	< 17
SS	242	< 17	< 17	< 17	< 17	147.0 ± 4.6	< 17	113.7 ± 0.8	< 17	< 17	19.3 ± 1.0
MS	158-3	< 17	< 17	< 17	< 17	< 133	< 17	91.5 ± 1.6	< 17	< 17	< 17
MS	170-2	< 17	< 17	< 17	< 17	< 133	< 17	88.1 ± 0.1	< 17	< 17	< 17
MS	170-4	< 17	< 17	< 17	< 17	< 133	< 17	92.1 ± 2.2	< 17	< 17	< 17
MS	200-1.6	< 17	< 17	< 17	< 17	< 133	< 17	90.9 ± 5.7	< 17	< 17	< 17
MS	200-3	< 17	< 17	< 17	< 17	< 133	17.0 ± 0.7	96.1 ± 0.7	< 17	< 17	< 17
MS	200-4.4	17.5 ± 0.4	< 17	< 17	< 17	< 133	17.2 ± 0.4	98.3 ± 1.8	< 17	< 17	< 17
MS	230-2	< 17	< 17	< 17	< 17	< 133	17.4 ± 0.7	100.5 ± 6.5	< 17	< 17	< 17
MS	230-4	18.1 ± 0.1	< 17	< 17	< 17	< 133	19.0 ± 0.7	102.9 ± 1.9	< 17	< 17	< 17
MS	242-3	< 17	< 17	< 17	< 17	< 133	18.0 ± 0.0	103.6 ± 1.1	< 17	< 17	< 17

Table S 21: Trace element concentration in hydrochar (B) corresponding to each run. Ba, Sn and Sr were not analyzed. As per EU regulation for organic fertilizers, the maximum allowable concentration (mg/kg) of As (inorganic), Cd, Hg and Pb are 40, 1.5, 1 and 120, respectively.

HT Feedstock	Run notation	As	Cd	Co	Hg	Mn	Mo	Pb	Sb	Se	V
SS	158	< 17	< 17	< 17	< 17	< 133	< 17	79.0 ± 2.0	< 17	< 17	< 17
SS	170	< 17	< 17	< 17	< 17	< 133	< 17	91.6 ± 4.9	< 17	< 17	< 17
SS	200	< 17	< 17	< 17	< 17	< 133	< 17	83.5 ± 5.6	< 17	< 17	< 17
SS	230	< 17	< 17	< 17	< 17	< 133	< 17	86.3 ± 10.5	< 17	< 17	< 17
SS	242	< 17	< 17	< 17	< 17	141.9 ± 5.0	< 17	92.9 ± 7.4	< 17	< 17	< 17
MS	158-3	< 17	< 17	< 17	< 17	< 133	< 17	113.9 ± 2.3	< 17	< 17	< 17
MS	170-2	< 17	< 17	< 17	< 17	< 133	< 17	107.3 ± 2.0	< 17	< 17	< 17
MS	170-4	< 17	< 17	< 17	< 17	< 133	< 17	130.6 ± 14.0	< 17	< 17	< 17
MS	200-1.6	< 17	< 17	< 17	< 17	< 133	< 17	108.3 ± 21.4	< 17	< 17	< 17
MS	200-3	< 17	< 17	< 17	< 17	< 133	< 17	105.9 ± 8.5	< 17	< 17	< 17
MS	200-4.4	< 17	< 17	< 17	< 17	< 133	< 17	113.0 ± 3.3	< 17	< 17	< 17
MS	230-2	< 17	< 17	< 17	< 17	< 133	< 17	122.1 ± 26.1	< 17	< 17	< 17
MS	230-4	< 17	< 17	< 17	< 17	< 133	< 17	123.7 ± 0.9	< 17	< 17	< 17
MS	242-3	< 17	< 17	< 17	< 17	< 133	< 17	120.1 ± 3.7	< 17	< 17	< 17

Table S 22: Concentration of trace elements in hydrochar and hydrochar (B) during pH optimization experiment. The mass balance was not calculated for these elements. As per EU regulation for organic fertilizers, the maximum allowable concentration (mg/kg) of As (inorganic), Cd, Hg and Pb are 40, 1.5, 1 and 120, respectively.

Final pH	As	Cd	Co	Mo	Pb	Sb	Se	Sn	Sr
					Concentration in hydrochar (mg/kg)				
2.0 ± 0.1	19.8 ± 1.2	< 17	< 17	28.7 ± 2.4	86.6 ± 0.5	< 17	< 17	56.8 ± 3.8	20.1 ± 0.7
2.5 ± 0.1	24.1 ± 4.5	< 17	< 17	27.5 ± 6.0	118.6 ± 14.2	< 17	< 17	56.5 ± 15.2	22.1 ± 3.4
3.3 ± 0.2	21.7 ± 1.3	< 17	< 17	21.2 ± 1.3	129.1 ± 7.5	< 17	< 17	44.1 ± 2.0	22.5 ± 0.6
3.9 ± 0.0	21.1 ± 0.5	< 17	< 17	20.9 ± 0.7	138.8 ± 0.2	< 17	< 17	43.0 ± 1.0	26.4 ± 1.3
4.4 ± 0.0	22.4 ± 0.0	< 17	< 17	21.5 ± 2.5	141.5 ± 6.7	< 17	< 17	48.7 ± 4.7	36.5 ± 3.2
					Concentration in hydrochar (B) (mg/kg)				
2.0 ± 0.1	< 17	< 17	< 17	17.9 ± 2.4	103.9 ± 0.9	< 17	< 17	34.5 ± 4.9	25.7 ± 0.8
2.5 ± 0.1	< 17	< 17	< 17	< 17	133.7 ± 2.5	< 17	< 17	29.1 ± 1.9	26.9 ± 1.3
3.3 ± 0.2	< 17	< 17	< 17	< 17	166.2 ± 4.4	< 17	< 17	31.1 ± 1.1	32.1 ± 0.8
3.9 ± 0.0	< 17	< 17	< 17	< 17	183.9 ± 0.2	< 17	< 17	34.1 ± 0.6	38.5 ± 1.4
4.4 ± 0.0	< 17	< 17	< 17	< 17	180.2 ± 2.7	< 17	< 17	33.1 ± 1.0	49.8 ± 2.4

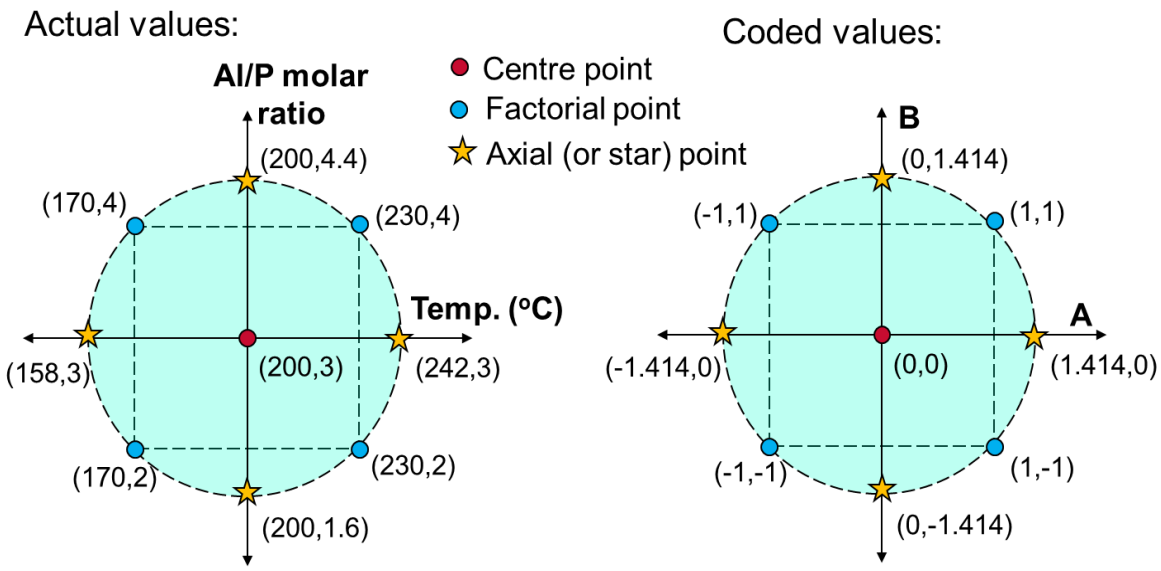

Figure S 6: Circumscribed central composite design (CCD) illustrating the actual values and coded values of the factors in the entire design space.

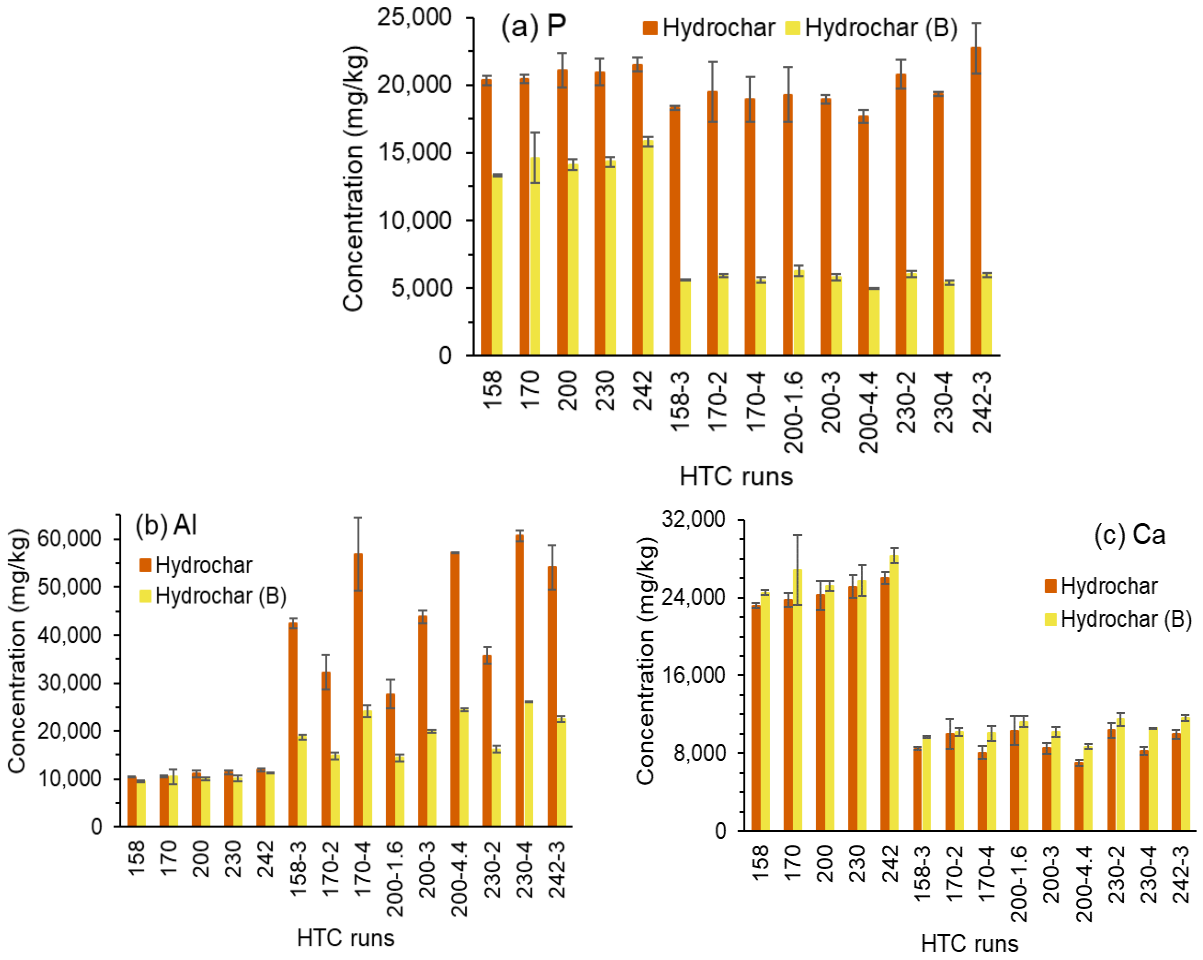

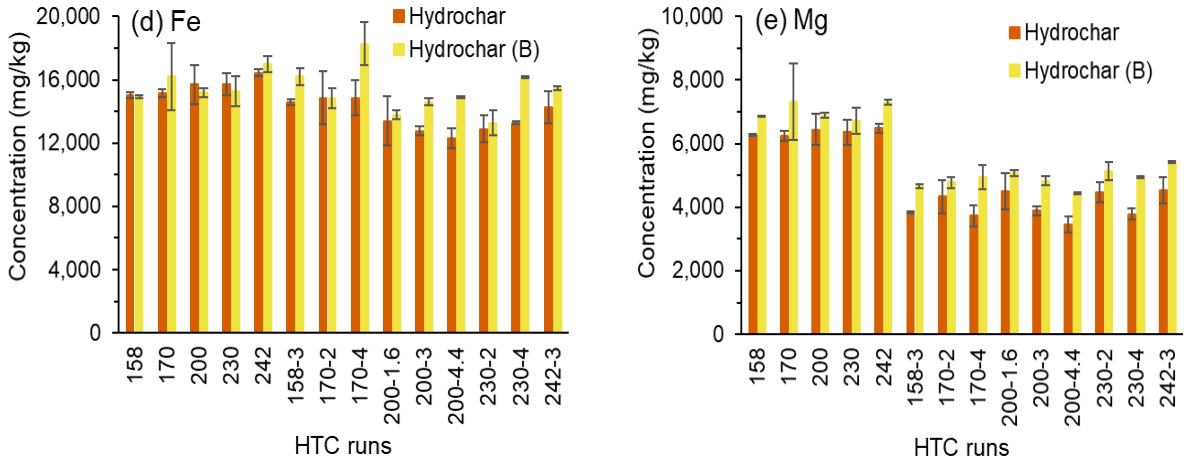

Figure S 7: Concentration of relevant major elements, i.e., (a) P, (b) Al, (c) Ca, (d) Fe, and (e) Mg in hydrochar and hydrochar (B) samples. The error bar represents the standard deviation.

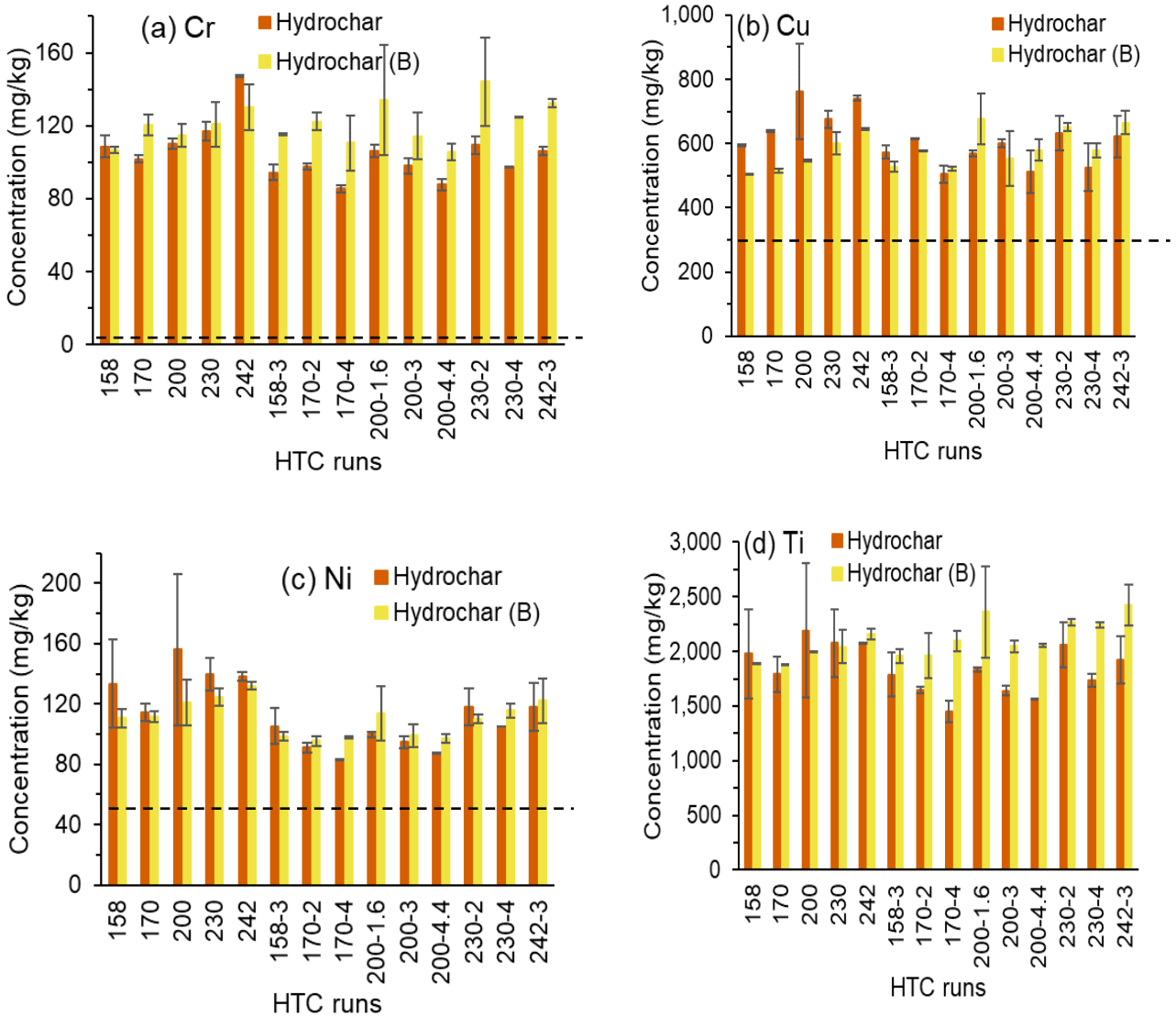

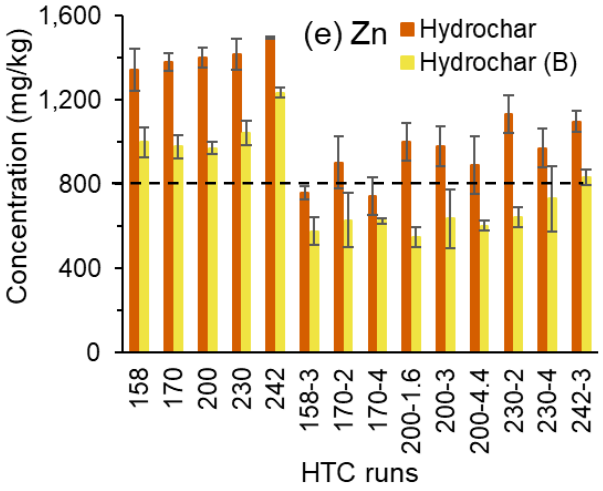

Figure S 8: Concentration of selected trace elements, i.e., (a) Cr, (b) Cu, (c) Ni, (d) Ti, and (e) Zn in hydrochar and hydrochar (B) samples. The horizontal dashed lines represent the maximum allowable concentration in organic fertilizer as per EU regulation (no specification for Ti and Cr corresponds to Cr (VI) in the regulation). The error bar represents the standard deviation.

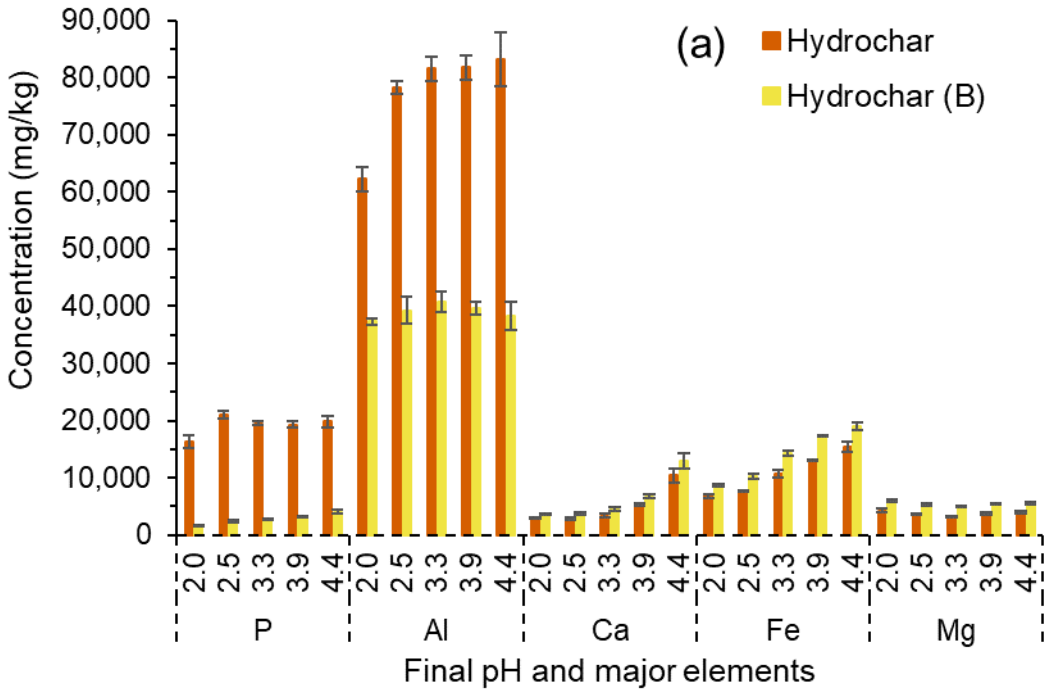

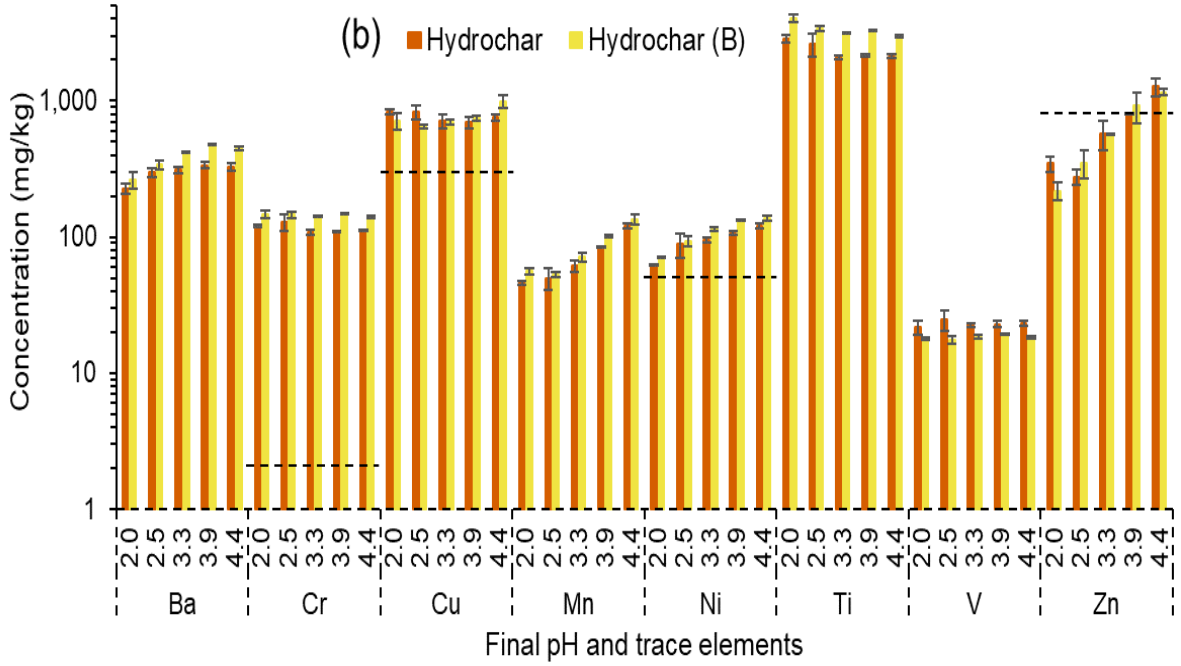

Figure S 9: Concentration of relevant (a) major and (b) trace elements in hydrochar and hydrochar (B) samples. The horizontal dashed lines represent the maximum allowable limit for concentration in organic fertilizer as per EU regulation (no specification for Ba, Mn, Ti, and V; Cr corresponds to Cr (VI) in the regulation). The error bar represents the standard deviation.

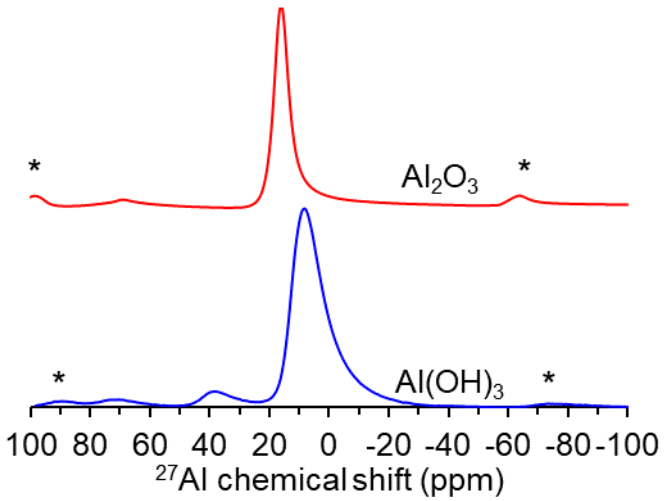

Figure S 10: SSNMR spectra of Al salts. The spinning sidebands are denoted by an asterisk (*).

REFERENCES

[1] A.R. Jupp, S. Beijer, G.C. Narain, W. Schipper, J.C. Slootweg, Phosphorus recovery and recycling – closing the loop, Chemical Society Reviews 50 (2021) 87–101. https://doi.org/10.1039/D0CS01150A.

[2] European Sustainable Phosphorus Platform - Phosphate rock in EU Critical Raw Materials list, (n.d.). https://phosphorusplatform.eu/scope-in-print/news/359-phosphate-rock-in-eu-critical-raw-materials-list (accessed May 28, 2021).

[3] R.J. Diaz, R. Rosenberg, Spreading Dead Zones and Consequences for Marine Ecosystems, Science 321 (2008) 926–929. https://doi.org/10.1126/science.1156401.

[4] L. Babcock-Jackson, T. Konovalova, J. Krogman, R. Bird, L. Lotti Diaz, Sustainable Fertilizers: Current Publication Landscape and Challenges, Chemistry, 2022. https://doi.org/10.26434/chemrxiv-2022-fxnlc.

[5] Science Breakthroughs to Advance Food and Agricultural Research by 2030, National Academies Press, Washington, D.C., 2019. https://doi.org/10.17226/25059.

[6] B.K. Mayer, L.A. Baker, T.H. Boyer, P. Drechsel, M. Gifford, M.A. Hanjra, P. Parameswaran, J. Stoltzfus, P. Westerhoff, B.E. Rittmann, Total Value of Phosphorus Recovery, Environmental Science & Technology 50 (2016) 6606–6620. https://doi.org/10.1021/acs.est.6b01239.

[7] L.E. Sommers, Chemical Composition of Sewage Sludges and Analysis of Their Potential Use as Fertilizers, Journal of Environmental Quality 6 (1977) 225–232. https://doi.org/10.2134/jeq1977.00472425000600020026x.

[8] H. Liu, G. Hu, I.A. Basar, J. Li, N. Lyczko, A. Nzihou, C. Eskicioglu, Phosphorus recovery from municipal sludge-derived ash and hydrochar through wet-chemical technology: A review towards sustainable waste management, Chemical Engineering Journal 417 (2021) 129300. https://doi.org/10.1016/j.cej.2021.129300.

[9] L. Egle, H. Rechberger, M. Zessner, Overview and description of technologies for recovering phosphorus from municipal wastewater, Resources, Conservation and Recycling 105 (2015) 325–346. https://doi.org/10.1016/j.resconrec.2015.09.016.

[10] J.R. Mihelcic, L.M. Fry, R. Shaw, Global potential of phosphorus recovery from human urine and feces, Chemosphere 84 (2011) 832–839. https://doi.org/10.1016/j.chemosphere.2011.02.046.

[11] B. Cieślik, P. Konieczka, A review of phosphorus recovery methods at various steps of wastewater treatment and sewage sludge management. The concept of "no solid waste generation" and analytical methods, Journal of Cleaner Production 142 (2017) 1728–1740. https://doi.org/10.1016/j.jclepro.2016.11.116.

[12] S.B. Tiwari, T.J.N. Hooper, A. Veksha, W.P. Chan, X. Fei, W. Liu, G. Lisak, T.-T. Lim, Sequential wet extraction of phosphorus from sewage sludge using alum sludge: Reassessing the aluminium-phosphorus speciation using experimental and simulation approach, Chemical Engineering Journal 459 (2023) 141569. https://doi.org/10.1016/j.cej.2023.141569.

[13] S.B. Tiwari, S.Y. Chin, A. Veksha, W.P. Chan, X. Fei, G. Lisak, W. Liu, T.-T. Lim, Synergistic application of alum sludge and sequential extraction for phosphorus recovery from sewage sludge char, Chemical Engineering Journal 481 (2024) 148574. https://doi.org/10.1016/j.cej.2024.148574.

[14] S. Petzet, B. Peplinski, P. Cornel, On wet chemical phosphorus recovery from sewage sludge ash by acidic or alkaline leaching and an optimized combination of both, Water Research 46 (2012) 3769–3780. https://doi.org/10.1016/j.watres.2012.03.068.
[15] Z. Fang, X. Zhuang, X. Zhang, Y. Li, R. Li, L. Ma, Influence of paraments on the transformation behaviors and directional adjustment strategies of phosphorus forms during different thermochemical treatments of sludge, Fuel 333 (2023) 126544. https://doi.org/10.1016/j.fuel.2022.126544.
[16] H. Nakagawa, J. Ohta, Phosphorus Recovery from Sewage Sludge Ash: A Case Study in Gifu, Japan, in: H. Ohtake, S. Tsuneda (Eds.), Phosphorus Recovery and Recycling, Springer, Singapore, 2019: pp. 149–155. https://doi.org/10.1007/978-981-10-8031-9_9.
[17] F.H. Westheimer, Why Nature Chose Phosphates, Science 235 (1987) 1173–1178. https://doi.org/10.1126/science.2434996.
[18] M.A. de Boer, L. Wolzak, J.C. Slootweg, Phosphorus: Reserves, Production, and Applications, in: H. Ohtake, S. Tsuneda (Eds.), Phosphorus Recovery and Recycling, Springer, Singapore, 2019: pp. 75–100. https://doi.org/10.1007/978-981-10-8031-9_5.
[19] M.B. Geeson, C.C. Cummins, Let's Make White Phosphorus Obsolete, ACS Cent. Sci. 6 (2020) 848–860. https://doi.org/10.1021/acscentsci.0c00332.
[20] R.W. Scholz, A.H. Roy, D.T. Hellums, Sustainable Phosphorus Management: A Transdisciplinary Challenge, in: Sustainable Phosphorus Management, Springer, Dordrecht, 2014: pp. 1–128. https://doi.org/10.1007/978-94-007-7250-2_1.
[21] S.M. Powers, T.W. Bruulsema, T.P. Burt, N.I. Chan, J.J. Elser, P.M. Haygarth, N.J.K. Howden, H.P. Jarvie, Y. Lyu, H.M. Peterson, A.N. Sharpley, J. Shen, F. Worrall, F. Zhang, Long-term accumulation and transport of anthropogenic phosphorus in three river basins, Nature Geosci 9 (2016) 353–356. https://doi.org/10.1038/ngeo2693.
[22] K. Richardson, W. Steffen, W. Lucht, J. Bendtsen, S.E. Cornell, J.F. Donges, M. Drüke, I. Fetzer, G. Bala, W. von Bloh, G. Feulner, S. Fiedler, D. Gerten, T. Gleeson, M. Hofmann, W. Huiskamp, M. Kummu, C. Mohan, D. Nogués-Bravo, S. Petri, M. Porkka, S. Rahmstorf, S. Schaphoff, K. Thonicke, A. Tobian, V. Virkki, L. Wang-Erlandsson, L. Weber, J. Rockström, Earth beyond six of nine planetary boundaries, Science Advances 9 (2023) eadh2458. https://doi.org/10.1126/sciadv.adh2458.
[23] P.R. Rout, M.K. Shahid, R.R. Dash, P. Bhunia, D. Liu, S. Varjani, T.C. Zhang, R.Y. Surampalli, Nutrient removal from domestic wastewater: A comprehensive review on conventional and advanced technologies, Journal of Environmental Management 296 (2021) 113246. https://doi.org/10.1016/j.jenvman.2021.113246.
[24] S. Comber, M. Gardner, K. Georges, D. Blackwood, D. Gilmour, Domestic source of phosphorus to sewage treatment works, Environmental Technology 34 (2013) 1349–1358. https://doi.org/10.1080/09593330.2012.747003.
[25] APHA, AWWA, WEF, Standard Methods for the Examination of Water and Wastewater, 22nd Edition, American Public Health Association, 2012.
[26] G. Hanrahan, T. SalmassiI, C. Khachikian, K. Foster, Reduced inorganic phosphorus in the natural environment: significance, speciation and determination, Talanta 66 (2005) 435–444. https://doi.org/10.1016/j.talanta.2004.10.004.

[27] B.L. Turner, B.J. Cade-Menun, L. Condron, S. Newman, Extraction of soil organic phosphorus, Talanta 66 (2005) 294–306. https://doi.org/10.1016/j.talanta.2004.11.012.
[28] G. Tchobanoglous, F.L. Burton, H.D. Stensel, M.& E. Inc, Wastewater Engineering: Treatment and Reuse, McGraw-Hill Education, 2003.
[29] D. Ragsdale, Advanced Wastewater Treatment to Achieve Low Concentration of Phosphorus, EPA, Sattle, 2007. https://www.epa.gov/sites/default/files/2019-02/documents/advanced-wastewater-treatment-low-concentration-phosphorus.pdf.
[30] S. Yeoman, T. Stephenson, J.N. Lester, R. Perry, The removal of phosphorus during wastewater treatment: A review, Environmental Pollution 49 (1988) 183–233. https://doi.org/10.1016/0269-7491(88)90209-6.
[31] C. Kazadi Mbamba, P. Grau, S. Tait, X. Flores-Alsina, I. Takács, D.J. Batstone, Precipitation and dissolution, in: D. Batstone, X. Flores-Alsina (Eds.), Generalised Physicochemical Model (PCM) for Wastewater Processes, IWA Publishing, 2022: pp. 21–38. https://doi.org/10.2166/9781780409832_0021.
[32] B. Yu, J. Luo, H. Xie, H. Yang, S. Chen, J. Liu, R. Zhang, Y.-Y. Li, Species, fractions, and characterization of phosphorus in sewage sludge: A critical review from the perspective of recovery, Science of The Total Environment 786 (2021) 147437. https://doi.org/10.1016/j.scitotenv.2021.147437.
[33] A. Bashir, L. Wang, S. Deng, J. Liu, J. Tian, B. Qiu, X. Cheng, Phosphorus release during alkaline treatment of waste activated sludge from wastewater treatment plants with Al salt enhanced phosphorus removal: Speciation and mechanism clarification, Science of The Total Environment 688 (2019) 87–93. https://doi.org/10.1016/j.scitotenv.2019.06.207.
[34] Z.-W. He, W.-Z. Liu, L. Wang, C.-C. Tang, Z.-C. Guo, C.-X. Yang, A.-J. Wang, Clarification of phosphorus fractions and phosphorus release enhancement mechanism related to pH during waste activated sludge treatment, Bioresource Technology 222 (2016) 217–225. https://doi.org/10.1016/j.biortech.2016.10.010.
[35] D.-C. Xu, C.-Q. Zhong, K.-H. Yin, S.-H. Peng, T.-T. Zhu, G. Cheng, Alkaline solubilization of excess mixed sludge and the recovery of released phosphorus as magnesium ammonium phosphate, Bioresource Technology 249 (2018) 783–790. https://doi.org/10.1016/j.biortech.2017.10.065.
[36] Z.-W. He, C.-C. Tang, L. Wang, Z.-C. Guo, A.-J. Zhou, D. Sun, W.-Z. Liu, A.-J. Wang, Transformation and release of phosphorus from waste activated sludge upon combined acid/alkaline treatment, RSC Advances 7 (2017) 35340–35345. https://doi.org/10.1039/C7RA03696E.
[37] Y. Xu, H. Hu, J. Liu, J. Luo, G. Qian, A. Wang, pH dependent phosphorus release from waste activated sludge: contributions of phosphorus speciation, Chemical Engineering Journal 267 (2015) 260–265. https://doi.org/10.1016/j.cej.2015.01.037.
[38] J. Liu, S. Deng, B. Qiu, Y. Shang, J. Tian, A. Bashir, X. Cheng, Comparison of pretreatment methods for phosphorus release from waste activated sludge, Chemical Engineering Journal 368 (2019) 754–763. https://doi.org/10.1016/j.cej.2019.02.205.
[39] T.U. Ali, D.-J. Kim, Phosphorus extraction and sludge dissolution by acid and alkali treatments of polyaluminum chloride (PAC) treated wastewater sludge, Bioresource Technology 217 (2016) 233–238. https://doi.org/10.1016/j.biortech.2016.02.017.

[40] W. Huang, W. Cai, H. Huang, Z. Lei, Z. Zhang, J.H. Tay, D.-J. Lee, Identification of inorganic and organic species of phosphorus and its bio-availability in nitrifying aerobic granular sludge, Water Research 68 (2015) 423–431. https://doi.org/10.1016/j.watres.2014.09.054.
[41] S. Li, W. Zeng, Z. Jia, G. Wu, H. Xu, Y. Peng, Phosphorus species transformation and recovery without apatite in FeCl3-assisted sewage sludge hydrothermal treatment, Chemical Engineering Journal 399 (2020) 125735. https://doi.org/10.1016/j.cej.2020.125735.
[42] P. Worsfold, I. McKelvie, P. Monbet, Determination of phosphorus in natural waters: A historical review, Analytica Chimica Acta 918 (2016) 8–20. https://doi.org/10.1016/j.aca.2016.02.047.
[43] E. Bezak-Mazur, J. Ciopińska, The Application of Sequential Extraction in Phosphorus Fractionation in Environmental Samples, Journal of AOAC INTERNATIONAL 103 (2020) 337–347. https://doi.org/10.5740/jaoacint.19-0263.
[44] V. Ruban, J.F. López-Sánchez, P. Pardo, G. Rauret, H. Muntau, P. Quevauviller, Harmonized protocol and certified reference material for the determination of extractable contents of phosphorus in freshwater sediments - A synthesis of recent works, Fresenius' Journal of Analytical Chemistry 370 (2001) 224–228. https://doi.org/10.1007/s002160100753.
[45] M.J. Hedley, J.W.B. Stewart, B.S. Chauhan, Changes in Inorganic and Organic Soil Phosphorus Fractions Induced by Cultivation Practices and by Laboratory Incubations, Soil Science Society of America Journal 46 (1982) 970–976. https://doi.org/10.2136/sssaj1982.03615995004600050017x.
[46] I.D. Mckelvie, D.M.W. Peatb, P.J. Worsfoldb, Analytical Perspective Techniques for the Quantification and Speciation of Phosphorus in Natural Waters, Analytical Proceedings Including Analytical Communications 1995 (1995) 32.
[47] J. Kruse, M. Abraham, W. Amelung, C. Baum, R. Bol, O. Kühn, H. Lewandowski, J. Niederberger, Y. Oelmann, C. Rüger, J. Santner, M. Siebers, N. Siebers, M. Spohn, J. Vestergren, A. Vogts, P. Leinweber, Innovative methods in soil phosphorus research: A review, Journal of Plant Nutrition and Soil Science 178 (2015) 43–88. https://doi.org/10.1002/jpln.201400327.
[48] T.C. Sichler, R. Becker, A. Sauer, M. Barjenbruch, M. Ostermann, C. Adam, Determination of the phosphorus content in sewage sludge: comparison of different aqua regia digestion methods and ICP-OES, ICP-MS, and photometric determination, Environmental Sciences Europe 34 (2022) 99. https://doi.org/10.1186/s12302-022-00677-1.
[49] Ph.E.A.M. Quevauviller, E.A. Maier, eds., CRMs for soil and sludge analysis, in: Techniques and Instrumentation in Analytical Chemistry, Elsevier, 1999: pp. 421–443. https://doi.org/10.1016/S0167-9244(99)80013-4.
[50] M. Palmer, Propagation of uncertainity through mathematical operations., (n.d.). http://web.mit.edu/fluids-modules/www/exper_techniques/.
[51] B.J. Cade-Menun, Characterizing phosphorus in environmental and agricultural samples by 31P nuclear magnetic resonance spectroscopy, Talanta 66 (2005) 359–371. https://doi.org/10.1016/j.talanta.2004.12.024.
[52] Y. Hu, M. Chen, J. Pu, S. Chen, Y. Li, H. Zhang, Enhancing phosphorus source apportionment in watersheds through species-specific analysis, Water Research 253 (2024) 121262. https://doi.org/10.1016/j.watres.2024.121262.

[53] S. Nanzer, A. Oberson, L. Berger, E. Berset, L. Hermann, E. Frossard, The plant availability of phosphorus from thermo-chemically treated sewage sludge ashes as studied by 33P labeling techniques, Plant Soil 377 (2014) 439–456. https://doi.org/10.1007/s11104-013-1968-6.
[54] J. Helfenstein, F. Tamburini, C. von Sperber, M.S. Massey, C. Pistocchi, O.A. Chadwick, P.M. Vitousek, R. Kretzschmar, E. Frossard, Combining spectroscopic and isotopic techniques gives a dynamic view of phosphorus cycling in soil, Nat Commun 9 (2018) 3226. https://doi.org/10.1038/s41467-018-05731-2.
[55] Y. Zhang, H. Yuan, S. Cai, Y. Zhang, D. Wang, W. Zhang, Molecular transformation pathway and bioavailability of organic phosphorus in sewage sludge under hydrothermal treatment: Importance of biopolymers interactions, Journal of Cleaner Production 385 (2023) 135746. https://doi.org/10.1016/j.jclepro.2022.135746.
[56] G.C. Campbell, L.G. Galya, A.J. Beeler, A.D. English, Effect of RF Inhomogeneity upon Quantitative Solid-State NMR Measurements, Journal of Magnetic Resonance, Series A 112 (1995) 225–228. https://doi.org/10.1006/jmra.1995.1035.
[57] G.H. Major, N. Fairley, P.M.A. Sherwood, M.R. Linford, J. Terry, V. Fernandez, K. Artyushkova, Practical guide for curve fitting in x-ray photoelectron spectroscopy, Journal of Vacuum Science & Technology A 38 (2020) 061203. https://doi.org/10.1116/6.0000377.
[58] P. Cornel, C. Schaum, Phosphorus recovery from wastewater: needs, technologies and costs, Water Science and Technology 59 (2009) 1069–1076. https://doi.org/10.2166/wst.2009.045.
[59] T.-T. Qian, H. Jiang, Migration of Phosphorus in Sewage Sludge during Different Thermal Treatment Processes, ACS Sustainable Chemistry & Engineering 2 (2014) 1411–1419. https://doi.org/10.1021/sc400476j.
[60] Solubility Rules for Ionic Compounds, (n.d.). https://www.sigmaaldrich.com/IN/en/technical-documents/technical-article/materials-science-and-engineering/solid-state-synthesis/solubility-rules-solubility-of-common-ionic-compounds (accessed June 29, 2024).
[61] K. Venkiteshwaran, P.J. McNamara, B.K. Mayer, Meta-analysis of non-reactive phosphorus in water, wastewater, and sludge, and strategies to convert it for enhanced phosphorus removal and recovery, Science of The Total Environment 644 (2018) 661–674. https://doi.org/10.1016/j.scitotenv.2018.06.369.
[62] L. Fang, J. Li, M.Z. Guo, C.R. Cheeseman, D.C.W. Tsang, S. Donatello, C.S. Poon, Phosphorus recovery and leaching of trace elements from incinerated sewage sludge ash (ISSA), Chemosphere 193 (2018) 278–287. https://doi.org/10.1016/j.chemosphere.2017.11.023.
[63] E. Levlin, B. Hultman, Phosphorus recovery from sewage sludge - ideas for further studies to improve leaching, Report No.12.Integration and Optimization of Urban Sanitation Systems, 2004.
[64] K. Stark, Phosphorus release from sewage sludge by use of acids and bases, Joint Polish - Swedish Reports, TRITA-AMI REPORT 3088, 2001.
[65] N.C. Shiba, F. Ntuli, Extraction and precipitation of phosphorus from sewage sludge, Waste Management 60 (2017) 191–200. https://doi.org/10.1016/j.wasman.2016.07.031.
[66] X.H. Zhao, Y.Q. Zhao, P. Kearney, Phosphorus recovery as AlPO 4 from beneficially reused aluminium sludge arising from water treatment,

Environmental Technology 34 (2012) 263–268. https://doi.org/10.1080/09593330.2012.692714.
[67] N. Semerci, S. Ahadi, S. Coşgun, Comparison of dried sludge and sludge ash for phosphorus recovery with acidic and alkaline leaching, Water and Environment Journal 35 (2021) 359–370. https://doi.org/10.1111/wej.12633.
[68] C.-G. Lee, P.J.J. Alvarez, H.-G. Kim, S. Jeong, S. Lee, K.B. Lee, S.-H. Lee, J.-W. Choi, Phosphorous recovery from sewage sludge using calcium silicate hydrates, Chemosphere 193 (2018) 1087–1093. https://doi.org/10.1016/j.chemosphere.2017.11.129.
[69] X.H. Zhao, Y.Q. Zhao, Investigation of phosphorus desorption from P-saturated alum sludge used as a substrate in constructed wetland, Separation and Purification Technology 66 (2009) 71–75. https://doi.org/10.1016/j.seppur.2008.11.020.
[70] B. Kim, M. Gautier, A. Simidoff, C. Sanglar, V. Chatain, P. Michel, R. Gourdon, pH and Eh effects on phosphorus fate in constructed wetland's sludge surface deposit, Journal of Environmental Management 183 (2016) 175–181. https://doi.org/10.1016/j.jenvman.2016.08.064.
[71] M. López Torres, Ma. del C. Espinosa Lloréns, Effect of alkaline pretreatment on anaerobic digestion of solid wastes, Waste Management 28 (2008) 2229–2234. https://doi.org/10.1016/j.wasman.2007.10.006.
[72] H. Li, Y. Jin, R. Mahar, Z. Wang, Y. Nie, Effects and model of alkaline waste activated sludge treatment, Bioresource Technology 99 (2008) 5140–5144. https://doi.org/10.1016/j.biortech.2007.09.019.
[73] C. Luedecke, S.W. Hermanowicz, D. Jenkins, PRECIPITATION OF FERRIC PHOSPHATE IN ACTIVATED SLUDGE: A CHEMICAL MODEL AND ITS VERIFICATION, in: Water Pollution Research and Control Brighton, Elsevier, 1988: pp. 325–337. https://doi.org/10.1016/B978-1-4832-8439-2.50035-3.
[74] B. Xiao, J. Liu, Study on treatment of excess sludge under alkaline condition, Huan Jing Ke Xue= Huanjing Kexue 27 (2006) 319–23.
[75] W. Bi, Y. Li, Y. Hu, Recovery of phosphorus and nitrogen from alkaline hydrolysis supernatant of excess sludge by magnesium ammonium phosphate, Bioresource Technology 166 (2014) 1–8. https://doi.org/10.1016/j.biortech.2014.04.092.
[76] N. Gao, K. Kamran, C. Quan, P.T. Williams, Thermochemical conversion of sewage sludge: A critical review, Progress in Energy and Combustion Science 79 (2020) 100843. https://doi.org/10.1016/j.pecs.2020.100843.
[77] W.D. Chanaka Udayanga, A. Veksha, A. Giannis, G. Lisak, V.W.C. Chang, T.-T. Lim, Fate and distribution of heavy metals during thermal processing of sewage sludge, Fuel 226 (2018) 721–744. https://doi.org/10.1016/j.fuel.2018.04.045.
[78] S.S.A. Syed-Hassan, Y. Wang, S. Hu, S. Su, J. Xiang, Thermochemical processing of sewage sludge to energy and fuel: Fundamentals, challenges and considerations, Renewable and Sustainable Energy Reviews 80 (2017) 888–913. https://doi.org/10.1016/j.rser.2017.05.262.
[79] M. Praspaliauskas, N. Pedišius, N. Striūgas, Elemental Migration and Transformation from Sewage Sludge to Residual Products during the Pyrolysis Process, Energy Fuels 32 (2018) 5199–5208. https://doi.org/10.1021/acs.energyfuels.8b00196.
[80] Y. Zhu, Y. Zhai, S. Li, X. Liu, B. Wang, X. Liu, Y. Fan, H. Shi, C. Li, Y. Zhu, Thermal treatment of sewage sludge: A comparative review of the

conversion principle, recovery methods and bioavailability-predicting of phosphorus, Chemosphere 291 (2022) 133053. https://doi.org/10.1016/j.chemosphere.2021.133053.
[81] R. Huang, C. Fang, X. Lu, R. Jiang, Y. Tang, Transformation of Phosphorus during (Hydro)thermal Treatments of Solid Biowastes: Reaction Mechanisms and Implications for P Reclamation and Recycling, Environmental Science & Technology 51 (2017) 10284–10298. https://doi.org/10.1021/acs.est.7b02011.
[82] H. Han, S. Hu, Y. Zhang, L. He, S.A. Abdullahi, S. Ma, Z. Deng, Y. Wang, S. Su, J. Xiang, Roles of dehydration conditioners on the formation of apatite phosphorus during the pyrolysis of various sludge, Journal of Environmental Chemical Engineering 9 (2021) 105248. https://doi.org/10.1016/j.jece.2021.105248.
[83] D. Sun, L. Hale, G. Kar, R. Soolanayakanahally, S. Adl, Phosphorus recovery and reuse by pyrolysis: Applications for agriculture and environment, Chemosphere 194 (2018) 682–691. https://doi.org/10.1016/j.chemosphere.2017.12.035.
[84] G. Chen, J. Wang, F. Yu, X. Wang, H. Xiao, B. Yan, X. Cui, A review on the production of P-enriched hydro/bio-char from solid waste: Transformation of P and applications of hydro/bio-char, Chemosphere 301 (2022) 134646. https://doi.org/10.1016/j.chemosphere.2022.134646.
[85] N. Skoglund, Ash chemistry and fuel design focusing on combustion of phosphorus-rich biomass, Department of applied physics and electronics, Umeå universitet, 2014.
[86] T. Qian, Q. Yang, D.C.F. Jun, F. Dong, Y. Zhou, Transformation of phosphorus in sewage sludge biochar mediated by a phosphate-solubilizing microorganism, Chemical Engineering Journal 359 (2019) 1573–1580. https://doi.org/10.1016/j.cej.2018.11.015.
[87] M.K. Hossain, V. Strezov, K.Y. Chan, A. Ziolkowski, P.F. Nelson, Influence of pyrolysis temperature on production and nutrient properties of wastewater sludge biochar, Journal of Environmental Management 92 (2011) 223–228. https://doi.org/10.1016/j.jenvman.2010.09.008.
[88] R. Huang, Y. Tang, Speciation Dynamics of Phosphorus during (Hydro)Thermal Treatments of Sewage Sludge, Environmental Science & Technology 49 (2015) 14466–14474. https://doi.org/10.1021/acs.est.5b04140.
[89] J. Li, Y. Li, F. Liu, X. Zhang, M. Song, R. Li, Pyrolysis of sewage sludge to biochar: Transformation mechanism of phosphorus, Journal of Analytical and Applied Pyrolysis 173 (2023) 106065. https://doi.org/10.1016/j.jaap.2023.106065.
[90] S. Tang, F. Yan, C. Zheng, Z. Zhang, Novel Calcium Oxide-Enhancement Phosphorus Recycling Technique through Sewage Sludge Pyrolysis, ACS Sustainable Chemistry & Engineering 6 (2018) 9167–9177. https://doi.org/10.1021/acssuschemeng.8b01492.
[91] Z. Ren, W. Zeng, H. Liu, Y. Jia, X. Peng, Y. Peng, Enhanced bioavailability of phosphorus in sewage sludge through pyrolysis aided by calcined clam shell powder, Process Safety and Environmental Protection 156 (2021) 121–133. https://doi.org/10.1016/j.psep.2021.10.008.
[92] R. Huang, Y. Tang, Evolution of phosphorus complexation and mineralogy during (hydro)thermal treatments of activated and anaerobically digested sludge: Insights from sequential extraction and P K-edge XANES, Water

Research 100 (2016) 439–447. https://doi.org/10.1016/j.watres.2016.05.029.
[93] J. Chen, S. Tang, F. Yan, Z. Zhang, Efficient recovery of phosphorus in sewage sludge through hydroxylapatite enhancement formation aided by calcium-based additives, Water Research 171 (2020) 115450. https://doi.org/10.1016/j.watres.2019.115450.
[94] S. Lu, Q. Sheng, J. Wang, S. Yuan, B. Dong, Z. Xu, A combination of conventional extraction and advanced analytical techniques afford a comprehensive understanding of phosphorus distribution and transformation in sewage sludge biochars, Chemical Engineering Journal 477 (2023) 146954. https://doi.org/10.1016/j.cej.2023.146954.
[95] S. Adhikari, G. Gascó, A. Méndez, A. Surapaneni, V. Jegatheesan, K. Shah, J. Paz-Ferreiro, Influence of pyrolysis parameters on phosphorus fractions of biosolids derived biochar, Science of the Total Environment 695 (2019) 133846. https://doi.org/10.1016/j.scitotenv.2019.133846.
[96] Y. Zhu, Q. Zhao, D. Li, J. Li, W. Guo, Performance comparison of phosphorus recovery from different sludges in sewage treatment plants through pyrolysis, Journal of Cleaner Production 372 (2022) 133728. https://doi.org/10.1016/j.jclepro.2022.133728.
[97] N. Vali, L.-E. Åmand, A. Combres, T. Richards, A. Pettersson, Pyrolysis of Municipal Sewage Sludge to Investigate Char and Phosphorous Yield together with Heavy-Metal Removal—Experimental and by Thermodynamic Calculations, Energies 14 (2021) 1477. https://doi.org/10.3390/en14051477.
[98] Z. Fang, F. Liu, Y. Li, B. Li, T. Yang, R. Li, Influence of microwave-assisted pyrolysis parameters and additives on phosphorus speciation and transformation in phosphorus-enriched biochar derived from municipal sewage sludge, Journal of Cleaner Production 287 (2021) 125550. https://doi.org/10.1016/j.jclepro.2020.125550.
[99] J.A. Garcia-Nunez, M.R. Pelaez-Samaniego, M.E. Garcia-Perez, I. Fonts, J. Abrego, R.J.M. Westerhof, M. Garcia-Perez, Historical Developments of Pyrolysis Reactors: A Review, Energy Fuels 31 (2017) 5751–5775. https://doi.org/10.1021/acs.energyfuels.7b00641.
[100] T. Malkow, Novel and innovative pyrolysis and gasification technologies for energy efficient and environmentally sound MSW disposal, Waste Management 24 (2004) 53–79. https://doi.org/10.1016/S0956-053X(03)00038-2.
[101] W. Buss, C. Wurzer, M. Bach, J. Heberling, T. Appel, H. Gerber, O. Mašek, Highly efficient phosphorus recovery from sludge and manure biochars using potassium acetate pre-treatment, Journal of Environmental Management 314 (2022) 115035. https://doi.org/10.1016/J.JENVMAN.2022.115035.
[102] D. Müller-Stöver, R. Thompson, C. Lu, T.P. Thomsen, N. Glæsner, S. Bruun, Increasing plant phosphorus availability in thermally treated sewage sludge by post-process oxidation and particle size management, Waste Management 120 (2021) 716–724. https://doi.org/10.1016/j.wasman.2020.10.034.
[103] Y. Xiao, T. Yan, P. Yao, W. Xiang, Y. Wu, J. Li, Co-pyrolysis of sewage sludge and phosphate tailings: Synergistically enhancing heavy metal immobilization and phosphorus availability, Waste Management 181 (2024) 44–56. https://doi.org/10.1016/j.wasman.2024.04.003.

[104] L. Yang, X. Guo, S. Liang, F. Yang, M. Wen, S. Yuan, K. Xiao, W. Yu, J. Hu, H. Hou, J. Yang, A sustainable strategy for recovery of phosphorus as vivianite from sewage sludge via alkali-activated pyrolysis, water leaching and crystallization, Water Research 233 (2023) 119769. https://doi.org/10.1016/j.watres.2023.119769.
[105] Y. Zhu, Q. Zhao, D. Li, J. Li, W. Guo, Enhanced recovery of phosphorus in sewage sludge-derived biochar with CaCO3: Phosphorus speciation and slow-release phosphorus behavior, Separation and Purification Technology 311 (2023) 123325. https://doi.org/10.1016/j.seppur.2023.123325.
[106] H. Nan, F. Yang, D. Li, X. Cao, X. Xu, H. Qiu, L. Zhao, Calcium enhances phosphorus reclamation during biochar formation: Mechanisms and potential application as a phosphorus fertilizer in a paddy soil, Waste Management 162 (2023) 83–91. https://doi.org/10.1016/j.wasman.2023.03.018.
[107] Q.-S. Liu, T. Tian, Co-pyrolysis of iron-rich sewage sludge and potassium phosphate to prepare biochars: P fractionation and alleviated occlusion, Journal of Analytical and Applied Pyrolysis 159 (2021) 105285. https://doi.org/10.1016/j.jaap.2021.105285.
[108] Q. Liu, J. Li, Z. Fang, Y. Liu, Y. Xu, X. Ruan, X. Zhang, W. Cao, Behavior of fast and slow phosphorus release from sewage sludge–derived biochar amended with CaO, Environmental Science and Pollution Research (2021) 1–10. https://doi.org/10.1007/s11356-021-12725-z.
[109] Y. Xia, Y. Tang, K. Shih, B. Li, Enhanced phosphorus availability and heavy metal removal by chlorination during sewage sludge pyrolysis, Journal of Hazardous Materials 382 (2020) 121110. https://doi.org/10.1016/j.jhazmat.2019.121110.
[110] W. Buss, A. Bogush, K. Ignatyev, O. Mašek, Unlocking the Fertilizer Potential of Waste-Derived Biochar, ACS Sustainable Chemistry and Engineering 8 (2020) 12295–12303. https://doi.org/10.1021/acssuschemeng.0c04336.
[111] I. Gbouri, F. Yu, X. Wang, J. Wang, X. Cui, Y. Hu, B. Yan, G. Chen, Co-Pyrolysis of Sewage Sludge and Wetland Biomass Waste for Biochar Production: Behaviors of Phosphorus and Heavy Metals, International Journal of Environmental Research and Public Health 2022, Vol. 19, Page 2818 19 (2022) 2818. https://doi.org/10.3390/IJERPH19052818.
[112] Q. Xiong, X. Wu, H. Lv, S. Liu, H. Hou, X. Wu, Influence of rice husk addition on phosphorus fractions and heavy metals risk of biochar derived from sewage sludge, Chemosphere 280 (2021) 130566. https://doi.org/10.1016/j.chemosphere.2021.130566.
[113] D. Lachos-Perez, P.C. Torres-Mayanga, E.R. Abaide, G.L. Zabot, F.D. Castilhos, Hydrothermal carbonization and Liquefaction: differences, progress, challenges, and opportunities, Bioresource Technology 343 (2022) 126084. https://doi.org/10.1016/j.biortech.2021.126084.
[114] L. Leng, W. Zhou, Chemical compositions and wastewater properties of aqueous phase (wastewater) produced from the hydrothermal treatment of wet biomass: A review, Energy Sources, Part A: Recovery, Utilization, and Environmental Effects 40 (2018) 2648–2659. https://doi.org/10.1080/15567036.2018.1495780.
[115] A. Tangredi, C. Barca, J.-H. Ferrasse, O. Boutin, Effect of process parameters on phosphorus conversion pathways during hydrothermal treatment of sewage sludge: A review, Chemical Engineering Journal 463 (2023) 142342. https://doi.org/10.1016/j.cej.2023.142342.

[116] T. Wang, Y. Zhai, Y. Zhu, C. Li, G. Zeng, A review of the hydrothermal carbonization of biomass waste for hydrochar formation: Process conditions, fundamentals, and physicochemical properties, Renewable and Sustainable Energy Reviews 90 (2018) 223–247. https://doi.org/10.1016/j.rser.2018.03.071.
[117] O.S. Djandja, L.X. Yin, Z.C. Wang, P.G. Duan, From wastewater treatment to resources recovery through hydrothermal treatments of municipal sewage sludge: A critical review, Process Safety and Environmental Protection 151 (2021) 101–127. https://doi.org/10.1016/J.PSEP.2021.05.006.
[118] O.S. Djandja, A.A. Salami, Z.-C. Wang, J. Duo, L.-X. Yin, P.-G. Duan, Random forest-based modeling for insights on phosphorus content in hydrochar produced from hydrothermal carbonization of sewage sludge, Energy (2022) 123295. https://doi.org/10.1016/J.ENERGY.2022.123295.
[119] H.P. Ruyter, Coalification model, Fuel 61 (1982) 1182–1187. https://doi.org/10.1016/0016-2361(82)90017-5.
[120] U. Ekpo, A.B. Ross, M.A. Camargo-Valero, P.T. Williams, A comparison of product yields and inorganic content in process streams following thermal hydrolysis and hydrothermal processing of microalgae, manure and digestate, Bioresource Technology 200 (2016) 951–960. https://doi.org/10.1016/j.biortech.2015.11.018.
[121] A. Amrullah, Y. Matsumura, Sewage Sludge Gasification under a Hydrothermal Condition: Phosphorus Behavior and Its Kinetics, Energy and Fuels 33 (2019) 2301–2307. https://doi.org/10.1021/acs.energyfuels.8b04289.
[122] K. Rathika, S. Kumar, B.R. Yadav, Enhanced energy and nutrient recovery via hydrothermal carbonisation of sewage sludge: Effect of process parameters, Science of The Total Environment 906 (2024) 167828. https://doi.org/10.1016/j.scitotenv.2023.167828.
[123] M. Malhotra, A. Garg, Hydrothermal carbonization of sewage sludge: Optimization of operating conditions using design of experiment approach and evaluation of resource recovery potential, Journal of Environmental Chemical Engineering 11 (2023) 109507. https://doi.org/10.1016/j.jece.2023.109507.
[124] Q. Wang, H. Jung, B. Wan, P. Liu, P. Yang, Y. Tang, Transformation Kinetics of Phosphorus and Nitrogen in Iron-Rich Sewage Sludges during Hydrothermal Treatment and Recovery of Nutrients from Process Water, ACS Sustainable Chemistry & Engineering 9 (2021) 10630–10641. https://doi.org/10.1021/acssuschemeng.1c03452.
[125] E. Ovsyannikova, P.J. Arauzo, G.C. Becker, A. Kruse, Experimental and thermodynamic studies of phosphate behavior during the hydrothermal carbonization of sewage sludge, Science of The Total Environment 692 (2019) 147–156. https://doi.org/10.1016/j.scitotenv.2019.07.217.
[126] L. Wang, Y. Chang, Q. Liu, Fate and distribution of nutrients and heavy metals during hydrothermal carbonization of sewage sludge with implication to land application, Journal of Cleaner Production 225 (2019) 972–983. https://doi.org/10.1016/j.jclepro.2019.03.347.
[127] Y. Shi, G. Luo, Y. Rao, H. Chen, S. Zhang, Hydrothermal conversion of dewatered sewage sludge: Focusing on the transformation mechanism and recovery of phosphorus, Chemosphere 228 (2019) 619–628. https://doi.org/10.1016/j.chemosphere.2019.04.109.
[128] M. Breulmann, M. van Afferden, R.A. Müller, E. Schulz, C. Fühner, Process conditions of pyrolysis and hydrothermal carbonization affect the

potential of sewage sludge for soil carbon sequestration and amelioration, Journal of Analytical and Applied Pyrolysis 124 (2017) 256–265. https://doi.org/10.1016/j.jaap.2017.01.026.
[129] R. Zhang, H. Liu, E. Sariola-Leikas, K.-Q. Tran, C. He, Practical strategies of phosphorus reclamation from sewage sludge after different thermal processing: Insights into phosphorus transformation, Water Research 255 (2024) 121524. https://doi.org/10.1016/j.watres.2024.121524.
[130] S. Neha, L. Vergeynst, P. Biller, Evaluating hydrothermal liquefaction hydrochar from sewage sludge as a phosphorus resource through struvite production, Journal of Environmental Chemical Engineering (2024) 113014. https://doi.org/10.1016/j.jece.2024.113014.
[131] H. Liu, N. Lyczko, A. Nzihou, C. Eskicioglu, Incorporating hydrothermal liquefaction into wastewater treatment – Part II: Characterization, environmental impacts, and potential applications of hydrochar, Journal of Cleaner Production 383 (2023) 135398. https://doi.org/10.1016/j.jclepro.2022.135398.
[132] A. Matayeva, S.R. Rasmussen, P. Biller, Distribution of nutrients and phosphorus recovery in hydrothermal liquefaction of waste streams, Biomass and Bioenergy 156 (2022) 106323. https://doi.org/10.1016/j.biombioe.2021.106323.
[133] F. Conti, S.S. Toor, T.H. Pedersen, T.H. Seehar, A.H. Nielsen, L.A. Rosendahl, Valorization of animal and human wastes through hydrothermal liquefaction for biocrude production and simultaneous recovery of nutrients, Energy Conversion and Management 216 (2020) 112925. https://doi.org/10.1016/j.enconman.2020.112925.
[134] A.A. Shah, S.S. Toor, F. Conti, A.H. Nielsen, L.A. Rosendahl, Hydrothermal liquefaction of high ash containing sewage sludge at sub and supercritical conditions, Biomass and Bioenergy 135 (2020) 105504. https://doi.org/10.1016/j.biombioe.2020.105504.
[135] E. Ovsyannikova, A. Kruse, G.C. Becker, Feedstock-Dependent Phosphate Recovery in a Pilot-Scale Hydrothermal Liquefaction Bio-Crude Production, Energies 13 (2020) 379. https://doi.org/10.3390/en13020379.
[136] P. Das, S. Khan, M. AbdulQuadir, M. Thaher, M. Waqas, A. Easa, E.S.M. Attia, H. Al-Jabri, Energy recovery and nutrients recycling from municipal sewage sludge, Science of The Total Environment 715 (2020) 136775. https://doi.org/10.1016/j.scitotenv.2020.136775.
[137] G. Weijin, Z. Zizheng, L. Yue, W. Qingyu, G. Lina, Hydrogen production and phosphorus recovery via supercritical water gasification of sewage sludge in a batch reactor, Waste Management 96 (2019) 198–205. https://doi.org/10.1016/j.wasman.2019.07.023.
[138] W. Zhu, Z.R. Xu, L. Li, C. He, The behavior of phosphorus in sub- and super-critical water gasification of sewage sludge, Chemical Engineering Journal 171 (2011) 190–196. https://doi.org/10.1016/j.cej.2011.03.090.
[139] A. Amrullah, Y. Matsumura, Supercritical water gasification of sewage sludge in continuous reactor, Bioresource Technology 249 (2018) 276–283. https://doi.org/10.1016/j.biortech.2017.10.002.
[140] C. Peng, J.P. Crawshaw, G.C. Maitland, J.P. Martin Trusler, D. Vega-Maza, The pH of CO2-saturated water at temperatures between 308 K and 423 K at pressures up to 15 MPa, The Journal of Supercritical Fluids 82 (2013) 129–137. https://doi.org/10.1016/j.supflu.2013.07.001.
[141] C.I. Aragón-Briceño, O. Grasham, A.B. Ross, V. Dupont, M.A. Camargo-Valero, Hydrothermal carbonization of sewage digestate at wastewater

treatment works: Influence of solid loading on characteristics of hydrochar, process water and plant energetics, Renewable Energy 157 (2020) 959–973. https://doi.org/10.1016/j.renene.2020.05.021.
[142] Y. Xue, Z. Wang, Y. Wu, R. Wu, F. Zhao, Migration and Conversion of Phosphorus in Hydrothermal Carbonization of Municipal Sludge with Hydrochloric Acid, Sustainability 15 (2023) 6799. https://doi.org/10.3390/su15086799.
[143] X. Zheng, M. Shen, Z. Ying, Y. Feng, B. Wang, B. Dou, Correlating phosphorus transformation with process water during hydrothermal carbonization of sewage sludge via experimental study and mathematical modelling, Science of The Total Environment 807 (2022) 150750. https://doi.org/10.1016/J.SCITOTENV.2021.150750.
[144] S.B. Tiwari, A. Veksha, W.P. Chan, X. Fei, W. Liu, G. Lisak, T.T. (T T.) Lim, Directional Sewage Sludge Transformation Using Acidic Hydrothermal Carbonization for Enhanced Alkaline Extraction of Phosphorus, (2024). https://doi.org/10.2139/ssrn.4848678.
[145] M. Gong, H. Chu, Q. Xu, Influences of reaction parameters and complexation pretreatments on the distribution of phosphorus during hydrothermal carbonization of dewatered sewage sludge, Journal of Water Process Engineering 60 (2024) 105209. https://doi.org/10.1016/j.jwpe.2024.105209.
[146] A. Sarrion, M.A. de la Rubia, N.D. Berge, A.F. Mohedano, E. Diaz, Comparison of Nutrient-Release Strategies in Hydrothermally Treated Digested Sewage Sludge, ACS Sustainable Chem. Eng. (2023). https://doi.org/10.1021/acssuschemeng.2c05870.
[147] K. Liu, Y. Xue, Y. Zhai, L. Zhou, J. Kang, Hydrochloric Acid Catalyzed Hydrothermal Treatment to Recover Phosphorus from Municipal Sludge, Catalysts 14 (2024) 65. https://doi.org/10.3390/catal14010065.
[148] R. Liu, Y. Xu, J. Cao, H. Geng, R. Chen, H. Liu, Y. Chen, S. Yuan, X. Dai, Effects of pH-varying thermal modification on sewage sludge: a focus on releasing nitrogen- and phosphorus-containing substances, Water Research (2024) 121746. https://doi.org/10.1016/j.watres.2024.121746.
[149] T. Wang, Y. Zhai, Y. Zhu, C. Peng, T. Wang, B. Xu, C. Li, G. Zeng, Feedwater pH affects phosphorus transformation during hydrothermal carbonization of sewage sludge, Bioresource Technology 245 (2017) 182–187. https://doi.org/10.1016/j.biortech.2017.08.114.
[150] V.S. Ekanthalu, S. Narra, J. Sprafke, M. Nelles, Influence of acids and alkali as additives on hydrothermally treating sewage sludge: Influence on phosphorus recovery, yield, and energy value of hydrochar, Processes 9 (2021) 618. https://doi.org/10.3390/pr9040618.
[151] F. Lai, Y. Chang, H. Huang, G. Wu, J. Xiong, Z. Pan, C. Zhou, Liquefaction of sewage sludge in ethanol-water mixed solvents for bio-oil and biochar products, Energy 148 (2018) 629–641. https://doi.org/10.1016/j.energy.2018.01.186.
[152] Q. Xiong, J. Xia, · Xiang Wu, · Xu Wu, H. Hou, · Hang Lv, Influence of persulfate on transformation of phosphorus and heavy metals for improving sewage sludge dewaterability by hydrothermal treatment, Environmental Science and Pollution Research 2022 1 (2022) 1–11. https://doi.org/10.1007/S11356-022-18624-1.
[153] R. Wang, W. Zhu, S. Zhao, J. Cao, Hydrothermal oxidation-precipitation method for recovering phosphorus from dewatered sludge and the

mechanisms involved, Separation and Purification Technology 298 (2022) 121580. https://doi.org/10.1016/j.seppur.2022.121580.
[154] R. Dou, F. Gao, Y. Tan, H.-R. Xiong, Z.-X. Xu, S.M. Osman, L.-J. Zheng, R. Luque, Phosphorus species transformation and recovery in deep eutectic solvent-assisted hydrothermal carbonization of sewage sludge, Sustainable Chemistry and Pharmacy 37 (2024) 101408. https://doi.org/10.1016/j.scp.2023.101408.
[155] C. He, K. Wang, A. Giannis, Y. Yang, J.Y. Wang, Products evolution during hydrothermal conversion of dewatered sewage sludge in sub- and near-critical water: Effects of reaction conditions and calcium oxide additive, International Journal of Hydrogen Energy 40 (2015) 5776–5787. https://doi.org/10.1016/j.ijhydene.2015.03.006.
[156] Y. Feng, K. Ma, T. Yu, S. Bai, D. Pei, T. Bai, Q. Zhang, L. Yin, Y. Hu, D. Chen, Phosphorus Transformation in Hydrothermal Pretreatment and Steam Gasification of Sewage Sludge, Energy Fuels 32 (2018) 8545–8551. https://doi.org/10.1021/acs.energyfuels.8b01860.
[157] F. Merzari, J. Goldfarb, G. Andreottola, T. Mimmo, M. Volpe, L. Fiori, Hydrothermal Carbonization as a Strategy for Sewage Sludge Management: Influence of Process Withdrawal Point on Hydrochar Properties, Energies 13 (2020) 2890. https://doi.org/10.3390/en13112890.
[158] M. Gong, H. Chu, J. Feng, Y. Su, Regulating the distribution of phosphorus in sewage sludge hydrothermal carbonization products by complexation pretreatment, Journal of Environmental Chemical Engineering 12 (2024) 111921. https://doi.org/10.1016/j.jece.2024.111921.
[159] N. Stobernack, C. Malek, Hydrothermal carbonization combined with thermochemical treatment of sewage sludge: Effects of MgCl2 on the migration of phosphorus and heavy metal, Waste Management 165 (2023) 150–158. https://doi.org/10.1016/j.wasman.2023.04.010.
[160] G. Qi, X. Wang, Y. Shen, X. Liu, M. Asraful Alam, B. Liu, Y. Chen, Effect of different flocculants on the characteristics of hydrochar and hydroliquid derived from the hydrothermal treated active sludge. A comparative study, Journal of Environmental Chemical Engineering 10 (2022) 107514. https://doi.org/10.1016/j.jece.2022.107514.
[161] X. Zheng, Y. Ye, Z. Jiang, Z. Ying, S. Ji, W. Chen, B. Wang, B. Dou, Enhanced transformation of phosphorus (P) in sewage sludge to hydroxyapatite via hydrothermal carbonization and calcium-based additive, Science of the Total Environment 738 (2020) 139786. https://doi.org/10.1016/j.scitotenv.2020.139786.
[162] X. Zheng, Z. Jiang, Z. Ying, Y. Ye, W. Chen, B. Wang, B. Dou, Migration and Transformation of Phosphorus during Hydrothermal Carbonization of Sewage Sludge: Focusing on the Role of pH and Calcium Additive and the Transformation Mechanism, ACS Sustainable Chem. Eng. 8 (2020) 7806–7814. https://doi.org/10.1021/acssuschemeng.0c00031.
[163] A. Petrovič, T. Cenčič Predikaka, L. Škodič, S. Vohl, L. Čuček, Hydrothermal co-carbonization of sewage sludge and whey: Enhancement of product properties and potential application in agriculture, Fuel 350 (2023) 128807. https://doi.org/10.1016/j.fuel.2023.128807.
[164] J. Li, J. Jin, Y. Zhao, Z. Zou, Y. Wu, J. Sun, J. Xia, Enhancing phosphorus bioavailability in sewage sludge through co-hydrothermal treatment with biomass, Journal of Water Process Engineering 51 (2023) 103448. https://doi.org/10.1016/j.jwpe.2022.103448.

[165] S. Shaddel, H. Bakhtiary-Davijany, C. Kabbe, F. Dadgar, S. Østerhus, Sustainable Sewage Sludge Management: From Current Practices to Emerging Nutrient Recovery Technologies, Sustainability 11 (2019) 3435. https://doi.org/10.3390/su11123435.
[166] W. Zhao, H. Xie, J. Li, L. Zhang, Y. Zhao, Application of Alum Sludge in Wastewater Treatment Processes: "Science" of Reuse and Reclamation Pathways, Processes 9 (2021) 612. https://doi.org/10.3390/pr9040612.
[167] K.B. Dassanayake, G.Y. Jayasinghe, A. Surapaneni, C. Hetherington, A review on alum sludge reuse with special reference to agricultural applications and future challenges, Waste Management 38 (2015) 321–335. https://doi.org/10.1016/J.WASMAN.2014.11.025.
[168] EN 15933:2012 Sludge , treated biowaste and soil — Determination of pH, (2012).
[169] W.P. Chan, J.-Y. Wang, Comprehensive characterisation of sewage sludge for thermochemical conversion processes – Based on Singapore survey, Waste Management 54 (2016) 131–142. https://doi.org/10.1016/j.wasman.2016.04.038.
[170] EN 13656:2020 Soil, treated biowaste, sludge and waste- Digestion with a hydrochloric (HCl), nitric (HNO3) and tetrafluoroboric (HBF4) or hydrofluoric (HF) acid mixture for subsequent determination of elements, (2020).
[171] V. Ruban, J.F. López-Sánchez, P. Pardo, G. Rauret, H. Muntau, P. Quevauviller, Selection and evaluation of sequential extraction procedures for the determination of phosphorus forms in lake sediment, Journal of Environmental Monitoring 1 (1999) 51–56. https://doi.org/10.1039/a807778i.
[172] Visual MINTEQ – Visual MINTEQ – a free equilibrium speciation model, (n.d.). https://vminteq.lwr.kth.se/ (accessed August 8, 2022).
[173] M.M. Benjamin, Water Chemistry, 2nd ed., Waveland Press, Illinois, 2014.
[174] R.K. Harris, E.D. Becker, S.M. Cabral de Menezes, P. Granger, R.E. Hoffman, K.W. Zilm, Further conventions for NMR shielding and chemical shifts (IUPAC Recommendations 2008), Pure Appl. Chem. 80 (2008) 59–84. https://doi.org/10.1351/pac200880010059.
[175] R.K. Harris, E.D. Becker, S.M. Cabral de Menezes, R. Goodfellow, P. Granger, NMR Nomenclature: Nuclear Spin Properties and Conventions for Chemical Shifts: IUPAC Recommendations 2001, Solid State Nuclear Magnetic Resonance 22 (2002) 458–483. https://doi.org/10.1006/snmr.2002.0063.
[176] D. Massiot, F. Fayon, M. Capron, I. King, S. Le Calvé, B. Alonso, J.-O. Durand, B. Bujoli, Z. Gan, G. Hoatson, Modelling one- and two-dimensional solid-state NMR spectra, Magnetic Resonance in Chemistry 40 (2002) 70–76. https://doi.org/10.1002/mrc.984.
[177] Y. Jiang, C. Ren, H. Guo, M. Guo, W. Li, Speciation Transformation of Phosphorus in Poultry Litter during Pyrolysis: Insights from X-ray Diffraction, Fourier Transform Infrared, and Solid-State NMR Spectroscopy, Environmental Science & Technology 53 (2019) 13841–13849. https://doi.org/10.1021/acs.est.9b03261.
[178] H.C. Ong, W.-H. Chen, Y. Singh, Y.Y. Gan, C.-Y. Chen, P.L. Show, A state-of-the-art review on thermochemical conversion of biomass for biofuel production: A TG-FTIR approach, Energy Conversion and Management 209 (2020) 112634. https://doi.org/10.1016/j.enconman.2020.112634.

[179] P.L. Brezonik, W.A. Arnold, Water chemistry: an introduction to the chemistry of natural and engineered aquatic systems, Oxford University Press, New York, 2011.
[180] M.L. Davis, Water and Wastewater Engineering., McGraw-Hill Professional Publishing, New York, USA, 2010.
[181] E. Galarneau, R. Gehr, Phosphorus removal from wastewaters: Experimental and theoretical support for alternative mechanisms, Water Research 31 (1997) 328–338. https://doi.org/10.1016/S0043-1354(96)00256-4.
[182] G. Zhu, H. Zheng, Z. Zhang, T. Tshukudu, P. Zhang, X. Xiang, Characterization and coagulation–flocculation behavior of polymeric aluminum ferric sulfate (PAFS), Chemical Engineering Journal 178 (2011) 50–59. https://doi.org/10.1016/j.cej.2011.10.008.
[183] C. Wagner, C. Powell, J. Allison, J. Rumble, NIST X-ray photoelectron spectroscopy database 1, version 2, (1997).
[184] P. Pardo, G. Rauret, J.F. López-Sánchez, Shortened screening method for phosphorus fractionation in sediments, Analytica Chimica Acta 508 (2004) 201–206. https://doi.org/10.1016/j.aca.2003.11.005.
[185] R. Li, J. Yin, W. Wang, Y. Li, Z. Zhang, Transformation of phosphorus during drying and roasting of sewage sludge, Waste Management 34 (2014) 1211–1216. https://doi.org/10.1016/j.wasman.2014.03.022.
[186] G.L. Turner, K.A. Smith, R.J. Kirkpatrick, E. Oldfieldt, Structure and cation effects on phosphorus-31 NMR chemical shifts and chemical-shift anisotropies of orthophosphates, Journal of Magnetic Resonance 70 (1986) 408–415. https://doi.org/10.1016/0022-2364(86)90129-0.
[187] S. Hunger, H. Cho, J.T. Sims, D.L. Sparks, Direct Speciation of Phosphorus in Alum-Amended Poultry Litter: Solid-State 31 P NMR Investigation, Environmental Science & Technology 38 (2004) 674–681. https://doi.org/10.1021/es034755s.
[188] K.J.D. MacKenzie, M.E. Smith, eds., Chapter 7 - NMR of Other Commonly Studied Nuclei, in: Pergamon Materials Series, Pergamon, 2002: pp. 399–457. https://doi.org/10.1016/S1470-1804(02)80008-6.
[189] R. Lookman, P. Grobet, R. Merckx, W.H. Van Riemsdijk, Application of 31P and 27Al MAS NMR for phosphate speciation studies in soil and aluminium hydroxides: promises and constraints, Geoderma 80 (1997) 369–388. https://doi.org/10.1016/S0016-7061(97)00061-X.
[190] M. Li, Y. Tang, X.-Y. Lu, Z. Zhang, Y. Cao, Phosphorus speciation in sewage sludge and the sludge-derived biochar by a combination of experimental methods and theoretical simulation, Water Research 140 (2018) 90–99. https://doi.org/10.1016/j.watres.2018.04.039.
[191] J. Sanz, J.M. Campelo, J.M. Marinas, NMR characterization of synthetic and modified aluminum orthophosphates, Journal of Catalysis 130 (1991) 642–652. https://doi.org/10.1016/0021-9517(91)90143-R.
[192] J. Kragten, An improved procedure for the complexometric titration of aluminium, The Analyst 99 (1974) 43. https://doi.org/10.1039/an9749900043.
[193] W. Li, X. Feng, Y. Yan, D.L. Sparks, B.L. Phillips, Solid-State NMR Spectroscopic Study of Phosphate Sorption Mechanisms on Aluminum (Hydr)oxides, Environ. Sci. Technol. 47 (2013) 8308–8315. https://doi.org/10.1021/es400874s.
[194] A.A.M. Brown, T.J.N. Hooper, S.A. Veldhuis, X.Y. Chin, A. Bruno, P. Vashishtha, J.N. Tey, L. Jiang, B. Damodaran, S.H. Pu, S.G. Mhaisalkar, N.

Mathews, Self-assembly of a robust hydrogen-bonded octylphosphonate network on cesium lead bromide perovskite nanocrystals for light-emitting diodes, Nanoscale 11 (2019) 12370–12380. https://doi.org/10.1039/C9NR02566A.
[195] X. Xue, M. Kanzaki, Proton Distributions and Hydrogen Bonding in Crystalline and Glassy Hydrous Silicates and Related Inorganic Materials: Insights from High-Resolution Solid-State Nuclear Magnetic Resonance Spectroscopy, Journal of the American Ceramic Society 92 (2009) 2803–2830. https://doi.org/10.1111/j.1551-2916.2009.03468.x.
[196] E.G. Alves Filho, L.M. Alexandre e Silva, A.G. Ferreira, Advancements in waste water characterization through NMR spectroscopy: review, Magnetic Resonance in Chemistry 53 (2015) 648–657. https://doi.org/10.1002/mrc.4158.
[197] Q. Wang, C.S. Raju, N. Almind-Jørgensen, M. Laustrup, K. Reitzel, U.G. Nielsen, Variation in Phosphorus Speciation of Sewage Sludge throughout Three Wastewater Treatment Plants: Determined by Sequential Extraction Combined with Microscopy, NMR Spectroscopy, and Powder X-ray Diffraction, Environ. Sci. Technol. (2022). https://doi.org/10.1021/acs.est.2c01815.
[198] M. Uchimiya, S. Hiradate, M.J. Antal, Dissolved Phosphorus Speciation of Flash Carbonization, Slow Pyrolysis, and Fast Pyrolysis Biochars, ACS Sustainable Chemistry & Engineering 3 (2015) 1642–1649. https://doi.org/10.1021/acssuschemeng.5b00336.
[199] L. Lin, X.-Y. Li, Effects of pH adjustment on the hydrolysis of Al-enhanced primary sedimentation sludge for volatile fatty acid production, Chemical Engineering Journal 346 (2018) 50–56. https://doi.org/10.1016/j.cej.2018.04.005.
[200] L.M. Ottosen, G.M. Kirkelund, P.E. Jensen, Extracting phosphorous from incinerated sewage sludge ash rich in iron or aluminum, Chemosphere 91 (2013) 963–969. https://doi.org/10.1016/j.chemosphere.2013.01.101.
[201] P.H. Liao, D.S. Mavinic, F.A. Koch, Release of phosphorus from biological nutrient removal sludges: A study of sludge pretreatment methods to optimize phosphorus release for subsequent recovery purposes, Journal of Environmental Engineering and Science 2 (2003) 369–381. https://doi.org/10.1139/s03-044.
[202] A. Nättorp, K. Remmen, C. Remy, Cost assessment of different routes for phosphorus recovery from wastewater using data from pilot and production plants, Water Science and Technology 76 (2017) 413–424. https://doi.org/10.2166/wst.2017.212.
[203] Inflation, consumer prices (annual %) - Germany | Data, (n.d.). https://data.worldbank.org/indicator/FP.CPI.TOTL.ZG?locations=DE (accessed January 8, 2023).
[204] Hydrochloric Acid Prices: Latest Price, Pricing, Database, Market Analysis, (n.d.). https://www.procurementresource.com/resource-center/hydrochloric-acid-price-trends (accessed December 28, 2022).
[205] Sodium Hydroxide Prices: Latest Price, News, Market Analysis, Database, (n.d.). https://www.procurementresource.com/resource-center/sodium-hydroxide-price-trends (accessed December 28, 2022).
[206] Sodium hydroxide Price and Market Analysis - ECHEMI - ECHEMI.com, ECHEMI (n.d.). https://www.echemi.com/productsInformation/pd20150901041-caustic-soda-pearls.html (accessed December 28, 2022).

[207] Magnesium Chloride Prices, Price, News, Monitor | ChemAnalyst, (n.d.). https://www.chemanalyst.com/Pricing-data/magnesium-chloride-1403 (accessed January 8, 2023).
[208] Buy Wholesale Magnesium Chloride Price from Global Wholesalers - Alibaba.com, (n.d.). https://www.alibaba.com/showroom/magnesium-chloride-price.html (accessed January 8, 2023).
[209] Buy Quality Ammonium Chloride Price Per Ton At Bargain Prices - Alibaba.com, (n.d.). https://www.alibaba.com/showroom/ammonium-chloride-price-per-ton.html (accessed January 9, 2023).
[210] U. Shashvatt, J. Benoit, H. Aris, L. Blaney, CO2-assisted phosphorus extraction from poultry litter and selective recovery of struvite and potassium struvite, Water Research 143 (2018) 19–27. https://doi.org/10.1016/j.watres.2018.06.035.
[211] F. Zhu, E.K. Cakmak, Z. Cetecioglu, Phosphorus recovery for circular Economy: Application potential of feasible resources and engineering processes in Europe, Chemical Engineering Journal 454 (2023) 140153. https://doi.org/10.1016/j.cej.2022.140153.
[212] Fertilizer prices expected to remain higher for longer, (n.d.). https://blogs.worldbank.org/opendata/fertilizer-prices-expected-remain-higher-longer (accessed December 28, 2022).
[213] Q. Liu, Z. Fang, Y. Liu, Y. Liu, Y. Xu, X. Ruan, X. Zhang, W. Cao, Phosphorus speciation and bioavailability of sewage sludge derived biochar amended with CaO, Waste Management 87 (2019) 71–77. https://doi.org/10.1016/j.wasman.2019.01.045.
[214] H. Han, W. Buss, Y. Zheng, P. Song, M. Khalid Rafiq, P. Liu, O. Mašek, X. Li, Contaminants in biochar and suggested mitigation measures – a review, Chemical Engineering Journal 429 (2022) 132287. https://doi.org/10.1016/j.cej.2021.132287.
[215] W. Buss, Pyrolysis Solves the Issue of Organic Contaminants in Sewage Sludge while Retaining Carbon—Making the Case for Sewage Sludge Treatment via Pyrolysis, ACS Sustainable Chem. Eng. 9 (2021) 10048–10053. https://doi.org/10.1021/acssuschemeng.1c03651.
[216] X. Wang, C. Shi, X. Hao, M.C.M. van Loosdrecht, Y. Wu, Synergy of phosphate recovery from sludge-incinerated ash and coagulant production by desalinated brine, Water Research 231 (2023) 119658. https://doi.org/10.1016/j.watres.2023.119658.
[217] D.M. Templeton, F. Ariese, R. Cornelis, L.-G. Danielsson, H. Muntau, H.P.V. Leeuwen, R. Łobiński, Guidelines for terms related to chemical Speciation and fractionation of elements. Definitions, structural aspects, and Methodological approaches (IUPAC Recommendations 2000), 2000. http://publications.iupac.org/pac/pdf/2000/pdf/7208x1453.pdf.
[218] C. Zaiontz, Real Statistics Using Excel, (n.d.). https://real-statistics.com/ (accessed December 18, 2023).
[219] S.R. Naqvi, R. Tariq, M. Shahbaz, M. Naqvi, M. Aslam, Z. Khan, H. Mackey, G. Mckay, T. Al-Ansari, Recent developments on sewage sludge pyrolysis and its kinetics: Resources recovery, thermogravimetric platforms, and innovative prospects, Computers & Chemical Engineering 150 (2021) 107325. https://doi.org/10.1016/j.compchemeng.2021.107325.
[220] C. Barca, M. Martino, P. Hennebert, N. Roche, Kinetics and capacity of phosphorus extraction from solid residues obtained from wet air oxidation of sewage sludge, Waste Management 89 (2019) 275–283. https://doi.org/10.1016/j.wasman.2019.04.024.

[221] H. Xu, P. He, W. Gu, G. Wang, L. Shao, Recovery of phosphorus as struvite from sewage sludge ash, Journal of Environmental Sciences 2012 (n.d.) 1533–1538. https://doi.org/10.1016/S1001-0742(11)60969-8.
[222] E.O. Lidman Olsson, P. Glarborg, K. Dam-Johansen, H. Wu, Review of Phosphorus Chemistry in the Thermal Conversion of Biomass: Progress and Perspectives, Energy Fuels (2023) acs.energyfuels.2c04048. https://doi.org/10.1021/acs.energyfuels.2c04048.
[223] C.C. de Figueiredo, A. de S.P.J. Reis, A.S. de Araujo, L.E.B. Blum, K. Shah, J. Paz-Ferreiro, Assessing the potential of sewage sludge-derived biochar as a novel phosphorus fertilizer: Influence of extractant solutions and pyrolysis temperatures, Waste Management 124 (2021) 144–153. https://doi.org/10.1016/j.wasman.2021.01.044.
[224] M. Uchimiya, Changes in Nutrient Content and Availability During the Slow Pyrolysis of Animal Wastes, in: Applied Manure and Nutrient Chemistry for Sustainable Agriculture and Environment, Springer, Dordrecht, 2014: pp. 53–68. https://doi.org/10.1007/978-94-017-8807-6_3.
[225] J. Zhang, F. Lü, H. Zhang, L. Shao, D. Chen, P. He, Multiscale visualization of the structural and characteristic changes of sewage sludge biochar oriented towards potential agronomic and environmental implication, Sci Rep 5 (2015) 9406. https://doi.org/10.1038/srep09406.
[226] N. Vali, A. Combres, A. Hosseinian, A. Pettersson, The Effect of the Elemental Composition of Municipal Sewage Sludge on the Phosphorus Recycling during Pyrolysis, with a Focus on the Char Chemistry—Modeling and Experiments, Separations 10 (2023) 31. https://doi.org/10.3390/separations10010031.
[227] Y. Yao, B. Gao, J. Chen, L. Yang, Engineered Biochar Reclaiming Phosphate from Aqueous Solutions: Mechanisms and Potential Application as a Slow-Release Fertilizer, Environ. Sci. Technol. 47 (2013) 8700–8708. https://doi.org/10.1021/es4012977.
[228] H. Yin, M. Kong, Simultaneous removal of ammonium and phosphate from eutrophic waters using natural calcium-rich attapulgite-based versatile adsorbent, Desalination 351 (2014) 128–137. https://doi.org/10.1016/j.desal.2014.07.029.
[229] Phosphorus, (n.d.). http://www.xpsfitting.com/2013/01/phosphorus.html (accessed July 22, 2023).
[230] Y. Liu, K. Li, Y. Liu, L. Pu, Z. Chen, S. Deng, The high-performance and mechanism of P-doped activated carbon as a catalyst for air-cathode microbial fuel cells, J. Mater. Chem. A 3 (2015) 21149–21158. https://doi.org/10.1039/C5TA04595A.
[231] X. Wu, L.R. Radovic, Inhibition of catalytic oxidation of carbon/carbon composites by phosphorus, Carbon 44 (2006) 141–151. https://doi.org/10.1016/j.carbon.2005.06.038.
[232] C. Powell, X-ray Photoelectron Spectroscopy Database XPS,Version 4.1, NIST Standard Reference Database 20, (1989). https://doi.org/10.18434/T4T88K.
[233] A.M. Puziy, O.I. Poddubnaya, A.M. Ziatdinov, On the chemical structure of phosphorus compounds in phosphoric acid-activated carbon, Applied Surface Science 252 (2006) 8036–8038. https://doi.org/10.1016/j.apsusc.2005.10.044.
[234] D. Steckenmesser, C. Vogel, C. Adam, D. Steffens, Effect of various types of thermochemical processing of sewage sludges on phosphorus speciation,

solubility, and fertilization performance, Waste Management 62 (2017) 194–203. https://doi.org/10.1016/j.wasman.2017.02.019.
[235] J.S. Robinson, K. Baumann, Y. Hu, P. Hagemann, L. Kebelmann, P. Leinweber, Phosphorus transformations in plant-based and bio-waste materials induced by pyrolysis, Ambio 47 (2018) 73–82. https://doi.org/10.1007/s13280-017-0990-y.
[236] M. Uchimiya, S. Hiradate, Pyrolysis Temperature-Dependent Changes in Dissolved Phosphorus Speciation of Plant and Manure Biochars, J. Agric. Food Chem. 62 (2014) 1802–1809. https://doi.org/10.1021/jf4053385.
[237] S.L. Miller, M. Parris, Synthesis of Pyrophosphate Under Primitive Earth Conditions, Nature 204 (1964) 1248–1250. https://doi.org/10.1038/2041248a0.
[238] Q. Fang, B. Chen, Y. Lin, Y. Guan, Aromatic and Hydrophobic Surfaces of Wood-derived Biochar Enhance Perchlorate Adsorption via Hydrogen Bonding to Oxygen-containing Organic Groups, Environ. Sci. Technol. 48 (2014) 279–288. https://doi.org/10.1021/es403711y.
[239] P. Sannigrahi, E. Ingall, Polyphosphates as a source of enhanced P fluxes in marine sediments overlain by anoxic waters: Evidence from 31P NMR, Geochemical Transactions 6 (2005) 52. https://doi.org/10.1186/1467-4866-6-52.
[240] W.F. Bleam, P.E. Pfeffer, J.S. Frye, 31P solid-state nuclear magnetic resonance spectroscopy of aluminum phosphate minerals, Phys Chem Minerals 16 (1989) 455–464. https://doi.org/10.1007/BF00197015.
[241] G. Xu, Y. Zhang, H. Shao, J. Sun, Pyrolysis temperature affects phosphorus transformation in biochar: Chemical fractionation and 31P NMR analysis, Science of The Total Environment 569–570 (2016) 65–72. https://doi.org/10.1016/j.scitotenv.2016.06.081.
[242] S.J. Duffy, G.W. vanLoon, Investigations of aluminum hydroxyphosphates and activated sludge by 27Al and 31P MAS NMR, Can. J. Chem. 73 (1995) 1645–1659. https://doi.org/10.1139/v95-204.
[243] H. Nagashima, C. Martineau-Corcos, G. Tricot, J. Trébosc, F. Pourpoint, J.-P. Amoureux, O. Lafon, Chapter Four - Recent Developments in NMR Studies of Aluminophosphates, in: G.A. Webb (Ed.), Annual Reports on NMR Spectroscopy, Academic Press, 2018: pp. 113–185. https://doi.org/10.1016/bs.arnmr.2017.12.004.
[244] C.S. Blackwell, R.L. Patton, Aluminum-27 and phosphorus-31 nuclear magnetic resonance studies of aluminophosphate molecular sieves, J. Phys. Chem. 88 (1984) 6135–6139. https://doi.org/10.1021/j150669a016.
[245] R. Dupree, M.H. Lewis, M.E. Smith, Structural characterization of ceramic phases with high-resolution 27Al NMR, Journal of Applied Crystallography 21 (1988) 109–116. https://doi.org/10.1107/S0021889887010069.
[246] C.V. Chandran, C.E.A. Kirschhock, S. Radhakrishnan, F. Taulelle, J.A. Martens, E. Breynaert, Alumina: discriminative analysis using 3D correlation of solid-state NMR parameters, Chem. Soc. Rev. 48 (2019) 134–156. https://doi.org/10.1039/C8CS00321A.
[247] S. Xu, N.R. Jaegers, W. Hu, J.H. Kwak, X. Bao, J. Sun, Y. Wang, J.Z. Hu, High-Field One-Dimensional and Two-Dimensional 27Al Magic-Angle Spinning Nuclear Magnetic Resonance Study of θ-, δ-, and γ-Al2O3 Dominated Aluminum Oxides: Toward Understanding the Al Sites in γ-Al2O3, ACS Omega 6 (2021) 4090–4099. https://doi.org/10.1021/acsomega.0c06163.

[248] D. Müller, E. Jahn, G. Ladwig, U. Haubenreisser, High-resolution solid-state 27Al and 31P NMR: correlation between chemical shift and mean Al-O-P angle in AlPO4 polymorphs, Chemical Physics Letters 109 (1984) 332–336. https://doi.org/10.1016/0009-2614(84)85596-7.
[249] J. Klein, M. Ushio, L.S. Burrell, B. Wenslow, S.L. Hem, Analysis of aluminum hydroxyphosphate vaccine adjuvants by 27Al MAS NMR, Journal of Pharmaceutical Sciences 89 (2000) 311–321. https://doi.org/10.1002/(SICI)1520-6017(200003)89:3<311::AID-JPS3>3.0.CO;2-8.
[250] X. He, T. Zhang, Y. Niu, Q. Xue, E.F. Ali, S.M. Shaheen, D.C.W. Tsang, J. Rinklebe, Impact of catalytic hydrothermal treatment and Ca/Al-modified hydrochar on lability, sorption, and speciation of phosphorus in swine manure: Microscopic and spectroscopic investigations, Environmental Pollution 299 (2022) 118877. https://doi.org/10.1016/j.envpol.2022.118877.
[251] X-ray Photoelectron Spectroscopy (XPS) Reference Pages, (n.d.). http://www.xpsfitting.com/search/label/Aluminum (accessed July 23, 2023).
[252] Aluminum & Aluminum Compounds, (2022). https://xps-database.com/aluminum-al-z13-chemicals/ (accessed July 23, 2023).
[253] G. Xu, J. Zou, G. Li, Ceramsite Made with Water and Wastewater Sludge and its Characteristics Affected by SiO2 and Al2O3, Environ. Sci. Technol. 42 (2008) 7417–7423. https://doi.org/10.1021/es801446h.
[254] M. Liu, X. Liu, W. Wang, J. Guo, L. Zhang, H. Zhang, Effect of SiO2 and Al2O3 on characteristics of lightweight aggregate made from sewage sludge and river sediment, Ceramics International 44 (2018) 4313–4319. https://doi.org/10.1016/j.ceramint.2017.12.022.
[255] I. Chen, S.K. Hwang, S. Chen, Chemical kinetics and reaction mechanism of thermal decomposition of aluminum hydroxide and magnesium hydroxide at high temperature (973-1123 K), Ind. Eng. Chem. Res. 28 (1989) 738–742. https://doi.org/10.1021/ie00090a015.
[256] M. Li, Y. Tang, N. Ren, Z. Zhang, Y. Cao, Effect of mineral constituents on temperature-dependent structural characterization of carbon fractions in sewage sludge-derived biochar, Journal of Cleaner Production 172 (2018) 3342–3350. https://doi.org/10.1016/j.jclepro.2017.11.090.
[257] C. Qin, H. Wang, X. Yuan, T. Xiong, J. Zhang, J. Zhang, Understanding structure-performance correlation of biochar materials in environmental remediation and electrochemical devices, Chemical Engineering Journal 382 (2020) 122977. https://doi.org/10.1016/j.cej.2019.122977.
[258] Y. Lin, P. Munroe, S. Joseph, R. Henderson, A. Ziolkowski, Water extractable organic carbon in untreated and chemical treated biochars, Chemosphere 87 (2012) 151–157. https://doi.org/10.1016/j.chemosphere.2011.12.007.
[259] M.C. Biesinger, Accessing the robustness of adventitious carbon for charge referencing (correction) purposes in XPS analysis: Insights from a multi-user facility data review, Applied Surface Science 597 (2022) 153681. https://doi.org/10.1016/j.apsusc.2022.153681.
[260] Carbon & Carbon Compounds, (2022). https://xps-database.com/carbon-c-z6-carbon-compounds/ (accessed July 23, 2023).
[261] X-ray Photoelectron Spectroscopy (XPS) Reference Pages, (n.d.). http://www.xpsfitting.com/search/label/carbon (accessed July 23, 2023).
[262] E. Leng, Y. Zhang, Y. Peng, X. Gong, M. Mao, X. Li, Y. Yu, In situ structural changes of crystalline and amorphous cellulose during slow

pyrolysis at low temperatures, Fuel 216 (2018) 313–321. https://doi.org/10.1016/j.fuel.2017.11.083.
[263] A. Zielińska, P. Oleszczuk, B. Charmas, J. Skubiszewska-Zięba, S. Pasieczna-Patkowska, Effect of sewage sludge properties on the biochar characteristic, Journal of Analytical and Applied Pyrolysis 112 (2015) 201–213. https://doi.org/10.1016/j.jaap.2015.01.025.
[264] X. Jian, M. Uchimiya, A. Orlov, Particle Size- and Crystallinity-Controlled Phosphorus Release from Biochars, Energy Fuels 33 (2019) 5343–5351. https://doi.org/10.1021/acs.energyfuels.9b00680.
[265] V. Gómez-Serrano, F. Piriz-Almeida, C.J. Durán-Valle, J. Pastor-Villegas, Formation of oxygen structures by air activation. A study by FT-IR spectroscopy, Carbon 37 (1999) 1517–1528. https://doi.org/10.1016/S0008-6223(99)00025-1.
[266] M. Uchimiya, I. Noda, A. Orlov, G. Ramakrishnan, In Situ and Ex Situ 2D Infrared/Fluorescence Correlation Monitoring of Surface Functionality and Electron Density of Biochars, ACS Sustainable Chem. Eng. 6 (2018) 8055–8062. https://doi.org/10.1021/acssuschemeng.8b01720.
[267] G. Haberhauer, B. Rafferty, F. Strebl, M.H. Gerzabek, Comparison of the composition of forest soil litter derived from three different sites at various decompositional stages using FTIR spectroscopy, Geoderma 83 (1998) 331–342. https://doi.org/10.1016/S0016-7061(98)00008-1.
[268] H. Lu, W. Zhang, S. Wang, L. Zhuang, Y. Yang, R. Qiu, Characterization of sewage sludge-derived biochars from different feedstocks and pyrolysis temperatures, Journal of Analytical and Applied Pyrolysis 102 (2013) 137–143. https://doi.org/10.1016/j.jaap.2013.03.004.
[269] R. Hamdan, H.M. El-Rifai, A.W. Cheesman, B.L. Turner, K.R. Reddy, W.T. Cooper, Linking Phosphorus Sequestration to Carbon Humification in Wetland Soils by 31P and 13C NMR Spectroscopy, Environ. Sci. Technol. 46 (2012) 4775–4782. https://doi.org/10.1021/es204072k.
[270] G. Fraissler, M. Jöller, H. Mattenberger, T. Brunner, I. Obernberger, Thermodynamic equilibrium calculations concerning the removal of heavy metals from sewage sludge ash by chlorination, Chemical Engineering and Processing: Process Intensification 48 (2009) 152–164. https://doi.org/10.1016/j.cep.2008.03.009.
[271]B. Galey, M. Gautier, B. Kim, D. Blanc, V. Chatain, G. Ducom, N. Dumont, R. Gourdon, Trace metal elements vaporization and phosphorus recovery during sewage sludge thermochemical treatment – A review, Journal of Hazardous Materials 424 (2022) 127360. https://doi.org/10.1016/j.jhazmat.2021.127360.
[272] Z. Zhang, R. Ju, H. Zhou, H. Chen, Migration characteristics of heavy metals during sludge pyrolysis, Waste Management 120 (2021) 25–32. https://doi.org/10.1016/j.wasman.2020.11.018.
[273] Z. Fan, X. Zhou, Z. Peng, S. Wan, Z.F. Gao, S. Deng, L. Tong, W. Han, X. Chen, Co-pyrolysis technology for enhancing the functionality of sewage sludge biochar and immobilizing heavy metals, Chemosphere 317 (2023) 137929. https://doi.org/10.1016/j.chemosphere.2023.137929.
[274] Regulation (EU) 2019/1009 of the European Parliament and of the Council of 5 June 2019 laying down rules on the making available on the market of EU fertilising products and amending Regulations (EC) No 1069/2009 and (EC) No 1107/2009 and repealing Regulation (EC) No 2003/2003 (Text with EEA relevance)Text with EEA relevance, 2023.

http://data.europa.eu/eli/reg/2019/1009/2023-03-16/eng (accessed April 14, 2024).
[275] G.Q. Lu, J.C.F. Low, C.Y. Liu, A.C. Lua, Surface area development of sewage sludge during pyrolysis, Fuel 74 (1995) 344–348. https://doi.org/10.1016/0016-2361(95)93465-P.
[276] H. Ohtake, S. Tsuneda, Phosphorus Recovery and Recycling, Springer Singapore, Singapore, 2019. https://doi.org/10.1007/978-981-10-8031-9.
[277] N. Rathnayake, S. Patel, P. Halder, S. Aktar, J. Pazferreiro, A. Sharma, A. Surapaneni, K. Shah, Co-pyrolysis of biosolids with alum sludge: Effect of temperature and mixing ratio on product properties, Journal of Analytical and Applied Pyrolysis 163 (2022) 105488. https://doi.org/10.1016/j.jaap.2022.105488.
[278] M. Bagheri, E. Wetterlund, Introducing hydrothermal carbonization to sewage sludge treatment systems—a way of improving energy recovery and economic performance?, Waste Management 170 (2023) 131–143. https://doi.org/10.1016/j.wasman.2023.08.006.
[279] C.I. Aragón-Briceño, A.K. Pozarlik, E.A. Bramer, L. Niedzwiecki, H. Pawlak-Kruczek, G. Brem, Hydrothermal carbonization of wet biomass from nitrogen and phosphorus approach: A review, Renewable Energy 171 (2021) 401–415. https://doi.org/10.1016/j.renene.2021.02.109.
[280] Y. Xu, F. Yang, L. Zhang, X. Wang, Y. Sun, Q. Liu, G. Qian, Migration and transformation of phosphorus in municipal sludge by the hydrothermal treatment and its directional adjustment, Waste Management 81 (2018) 196–201. https://doi.org/10.1016/j.wasman.2018.10.011.
[281] Y. Yu, X. Yang, Z. Lei, R. Yu, K. Shimizu, N. Chen, C. Feng, Z. Zhang, Effects of three macroelement cations on P mobility and speciation in sewage sludge derived hydrochar by using hydrothermal treatment, Bioresource Technology Reports 7 (2019) 100231. https://doi.org/10.1016/j.biteb.2019.100231.
[282] Used Water Treatment, PUB, Singapore's National Water Agency (n.d.). http://www.pub.gov.sg/Professionals/Requirements/Used-Water/Treatment (accessed March 19, 2024).
[283] Water Treatment, PUB, Singapore's National Water Agency (n.d.). http://www.pub.gov.sg/Public/WaterLoop/Water-Treatment (accessed March 19, 2024).
[284] ISO 17294-1:2006 Water quality — Application of inductively coupled plasma mass spectrometry (ICP-MS), (2007). https://doi.org/10.3403/03163790.
[285] C. He, A. Giannis, J.-Y. Wang, Conversion of sewage sludge to clean solid fuel using hydrothermal carbonization: Hydrochar fuel characteristics and combustion behavior, Applied Energy 111 (2013) 257–266. https://doi.org/10.1016/j.apenergy.2013.04.084.
[286] X. Fu, W.P. Chan, V. Chin, Y.Z. Boon, W. Chen, Y. Zhao, S. Heberlein, Y. Gu, J. Oh, G. Lisak, Converting sludge to slag through a high temperature slagging co-gasification process: An evaluation based on a demonstration trial and life cycle assessment, Chemical Engineering Journal 468 (2023) 143475. https://doi.org/10.1016/j.cej.2023.143475.
[287] H. Huang, X. Yuan, The migration and transformation behaviors of heavy metals during the hydrothermal treatment of sewage sludge, Bioresource Technology 200 (2016) 991–998. https://doi.org/10.1016/j.biortech.2015.10.099.

[288] Justin Gorham, NIST X-ray Photoelectron Spectroscopy Database - SRD 20, (2012). https://doi.org/10.18434/T4T88K.
[289] NCERT, The p-Block Elements, in: Chmistry Part I, 2022nd ed., National Council of Educational Research and Training, New Delhi, n.d. https://ncert.nic.in/textbook.php?lech1=7-9.
[290] Chemistry of Phosphorus (Z=15), Chemistry LibreTexts (2013). https://chem.libretexts.org/Bookshelves/Inorganic_Chemistry/Supplemental_Modules_and_Websites_(Inorganic_Chemistry)/Descriptive_Chemistry/Elements_Organized_by_Block/2_p-Block_Elements/Group_15%3A_The_Nitrogen_Family/Z015_Chemistry_of_Phosphorous (accessed August 19, 2023).
[291] The Chemistry of Nitrogen and Phosphorous, (n.d.). https://chemed.chem.purdue.edu/genchem/topicreview/bp/ch10/group5.php#phos (accessed August 19, 2023).
[292] ISO 11464:2006 Soil quality — Pretreatment of samples for physico-chemical analyses, (2006).
[293] ISO 12404:2021 Soil quality — — Guidance on the selection and application of screening methods, (2011).
[294] ISO, ISO 16720:2007 Soil quality-pretreatment of samples by freeze-drying for subsequent analysis, (2006).
[295] ISO 11465:1993 Soil quality — Determination of dry matter and water content on a mass basis — Gravimetric method, (1993).
[296] Water quality, determination of alkalinity. Part 1, Determination of total and composite alkalinity. (British standard: BS EN ISO 9963-1 : 1996), (1996).
[297] ASTM D7582-15 Standard Test Methods for Proximate Analysis of Coal and Coke by Macro Thermogravimetric Analysis, (2015). https://doi.org/10.1520/D7582-15.
[298] ISO 29541:2010 Solid mineral fuels — Determination of total carbon , hydrogen and nitrogen content — Instrumental method, (2010).
[299] EN 15170:2008 Characterization of sludges — Determination of calorific value, (2009).
[300] ISO / TR 20736 : 2021 BSI Standards Publication Sludge recovery , recycling , treatment and disposal — Guidance on thermal treatment of sludge, (2021).
[301] ISO 18227:2014 Soil quality — Determination of elemental composition by X- ray fluorescence, (2014).
[302] Water quality. Determination of selected elements by inductively coupled plasma optical emission spectrometry (ICP-OES) (ISO 11885:2007), (2009).
[303] ISO / TS 16965 : 2013 Soil quality — Determination of trace elements using inductively coupled plasma mass spectrometry (ICP-MS), (2013).
[304] ISO 54321 : 2021 Soil , treated biowaste , sludge and waste — Digestion of aqua regia soluble fractions of elements, (2021).
[305] ISO 16729:2013 Soil quality — Digestion of nitric acid soluble fractions of elements, (2013). https://doi.org/10.3403/30242164U.
[306] ISO 14869-2:2002 Soil quality — Dissolution for the determination of total element content — Part 2: Dissolution by alkaline fusion, (2001).
[307] 14:00-17:00, ISO 6878:2004 Water quality — Determination of phosphorus — Ammonium molybdate spectrometric method, (n.d.). https://www.iso.org/standard/36917.html (accessed June 6, 2024).

[308] 14:00-17:00, ISO 10304-1:2007 Water quality — Determination of dissolved anions by liquid chromatography of ions (Part 1: Determination of bromide, chloride, fluoride, nitrate, nitrite, phosphate and sulfate), (n.d.). https://www.iso.org/standard/46004.html (accessed June 6, 2024).